Biogas Upgrading and Solvent Regeneration in Monoethanolamine and Ionic Liquids for Carbon Dioxide Utilisation

by

Adam Raphael Samuel

A report submitted as a requirement for the degree of

Doctor of Philosophy

at the Department of Chemical and Biological Engineering,
University of Sheffield

December, 2014

EPSRC
Engineering and Physical Sciences
Research Council

4CU
Foreseeing
a future
using CO_2

E-Futures

Abstract

Biogas is a renewable energy source, consisting primarily of methane and carbon dioxide (CO_2), which can be upgraded by stripping the CO_2 to produce biomethane. One of the standard industrial solvents used in biogas upgrading is monoethanolamine (MEA). Despite the effective CO_2 capture capability of MEA, it is energy intensive to regenerate since it requires heating the solvent to approximately 120 ºC. Additional issues with MEA include material losses due to degradation and evaporation. This work investigates methods for improving the biogas upgrading process by utilising microbubbles and comparing ionic liquid solvents to MEA. It is also examined whether CO_2 can be released from a solvent with high enough purity to be utilised directly in conjunction with carbon dioxide utilisation (CDU) processes.

The study is in two parts: the first investigates a new regeneration method through computational modelling, termed Direct Contact Regeneration (DCR), whereby a superheated bubble in contact with the solvent desorbs CO_2 locally from the liquid with minimal bulk liquid heating. The second experimentally investigates factors influencing bubble size and absorption of CO_2 by ionic liquids with a view to biogas upgrading.

It was found that DCR is technically feasible with MEA if a bubble of superheated nitrogen is used; however, the efficiency of regeneration would be lower than that using temperature swing methods. In contrast, DCR with the ionic liquid [C_2mim][NTf_2] is feasible and can be used in tandem with CDU processes by replacing superheated nitrogen with pure CO_2 in order to produce an outlet stream with high purity.

It was found that bubble size in the majority of ionic liquids tested was far greater than that in aqueous glycerol mixtures of similar viscosity; however, three of the ionic liquids tested had a similar bubble size. Further analysis showed that rather than viscosity, the surface tension of the ionic liquid has the most significant influence on bubble size due to its stabilising effect on the homogeneous regime in bubble columns.

30 wt.% aqueous MEA solution was shown to have a significantly greater rate of mass transfer than the ionic liquids tested due to its greater absorption capacity, greater diffusivity and tendency to form smaller bubbles. Of the ionic liquids tested, the greatest absorption capacity was exhibited by [C_2mim][NTf_2] and the greatest volumetric mass transfer coefficient by [C_2mim][$EtSO_4$].

Acknowledgments

I would firstly like to thank my supervisor, Prof. Will Zimmerman for supervising me throughout this project and for supporting me in my decisions.

To the EPSRC and the 4CU project for the financial support they have provided me to carry out my research.

To my friends in the research group, particularly Dr. Stuart Brittle, Tom Holmes, Don Willey, Fahad Rehman, Dan Wesley, and Gareth Medley for providing motivation, guidance and support throughout this project.

Prof. Geraint Jewell and Dr. Neil Lowrie for providing financial support and respecting my decisions.

Dr. Corinne Howse for providing the financial and practical support needed to carry out my research, supporting me in my decisions, and offering me guidance when it was needed.

Dr. Rachael Elder, for helping me with the structure and planning of my thesis.

To everyone on the 4CU project who has offered their guidance and shared their knowledge in order to speed up the project.

To all the technicians and supporting staff without whom I would not have been able to carry out any of my research.

To all my friends who have kept me motivated throughout the duration of the PhD. Especially to Jon Davison, Dave Anderson, Pete Weston, Tom Young, and James Craven.

To Prof. Rabi Baliga, McGill University, for igniting my interest in scientific research in 2009.

And last but not least, to my parents, siblings, and the rest of my family for helping me through the degree and supporting me in all my decision making. I look forward to working with them in the future.

Table of Contents

List of Figures

List of Tables

Nomenclature

Parameter	**Description**	**Value / Units**
a	Specific interfacial area	m^2/m^3
A	Cross-sectional area of column	m^2
A_P	Projected area of particle	m^2
c	Concentration	mol/m^3
c_p	Specific heat capacity	J/kg/K
d	Bubble diameter	m
$\bar{d}$	Mean bubble diameter	m
D	Diffusion coefficient	m^2/s
e	Specific energy requirement	J/tonne-CO_2
E	Energy	J
f_c	Conversion factor	m/pixel
f_H	Heywood shape coefficient	Dimensionless
g	Acceleration due to gravity	9.81 m/s^2
h	Heat transfer coefficient	$W/m^2/K$
H	Henry's constant	atm
ΔH_r	Enthalpy of reaction	J/g
ΔH_r	Enthalpy of vapourisation	J/g
J	Molar flux	$mol/m^2/s$
k_G	Individual gas-side mass transfer coefficient	$mol/m^2/Pa/s$
k_L	Individual liquid-side mass transfer coefficient	m/s
K_Ga	Volumetric gas-side mass transfer coefficient	$mol/m^3/Pa/s$
K_La	Volumetric liquid-side mass transfer coefficient	1/min
m	Mass	kg
M	Molecular mass	g/mol
n	Number of bubbles	Dimensionless
$\dot{n}$	Rate of mass transfer	mol/s
N_A	Molar flux	$mol/m^2/s$
p,P	Pressure	Pa
P_{atm}	Atmospheric pressure	101325 Pa
P_P	Particle perimeter	m
q	Heat flux	W/m^2

Q	Heat addition due to heat source/sink	W
r, θ	Spherical co-ordinates	m, degrees
r, z	Cylindrical co-ordinates	m, m
R	Bubble radius	m
R_G	Universal gas constant	8.3145 J/mol/K
Rs	Rate of production of species by chemical reaction	mol/s
t	Time	s
T	Temperature	K, °C
u	Velocity	m/s
T_C	Critical Temperature of water	647 K
U_G	Superficial gas velocity	m/s
U_{slip}	Bubble slip velocity	m/s
U_T	Bubble terminal velocity	m/s
V	Volume	m^3
$\dot{V}$	Volume flow rate	m^3/s

Greek Letters

Parameter	**Description**	**Value / Units**
α	CO_2 Loading	mol-CO_2/mol-MEA
γ	Surface tension	N/m
ε	Gas Holdup	Dimensionless
η	Efficiency	%
θ	Contact angle	Degrees
κ	Thermal conductivity	W/m/K
μ	Viscosity	Pa·s
ρ	Density	kg/m^3

Subscripts

Parameter	**Description**
CH_4	Methane
CO_2	Carbon Dioxide
g	Glycerol

G	Gas
i	Interface
i	Inlet
L	Liquid
MEA	Monoethanolamine
MEA_{aq}	30 wt.% aqueous monoethanolamine
o	Outlet
w	Water
0	Initial

Superscripts

Parameter	**Description**
i	Inside the bubble
o	Outside the bubble
*	In equilibrium with the other phase

Dimensionless Numbers

Parameter	**Description**
Bo	Bond Number
Ca	Capillary Number
Eo	Eotvos Number
Fr	Froude Number
Ga	Galilei Number
Mo	Morton Number
Nu	Nusselt Number
Pe	Péclet Number
Pr	Prandtl Number
Ra	Rayleigh Number
Re	Reynolds Number
Sc	Schmidt Number
Sh	Sherwood Number

A complete description of these dimensionless numbers is presented in Appendix A

1. Introduction

1.1. Motivation for This Work

Biogas is a renewable energy source that can be harvested to reduce greenhouse gas emissions into the atmosphere and prevent climate change.

Climate change and energy security have come to the forefront of global politics in recent years, indicating their increasing importance on global welfare and economic growth (DTI, 2007). There are fears that our strive for economic growth since the beginning of the industrial revolution has resulted in unintended consequences on our planet that could potentially lead to irreparable damage, e.g. flooding, drought, and loss of animal habitats (Stern, 2007). Among scientists, this is widely thought to be due to the emission of large quantities of greenhouse gases – in particular CO_2 – into the atmosphere since the revolution began. It has been predicted that if these emissions continue, entire ecosystems could change due to animal extinction.

There are a number of options scientists and politicians have explored for reducing greenhouse gas emissions whilst improving standards of living and reducing dependencies on foreign imports for energy; the main ones being renewable energy, nuclear energy, carbon capture and storage (CCS), and more recently, carbon dioxide utilisation (CDU) (MacKay, 2008, Styring et al., 2011). While all of these face public opposition to varying degrees, they each have their pros and cons: Renewables, e.g. solar, wind, geothermal, etc., can theoretically produce energy for free once they have been installed; however, they currently have a low power density and high cost compared with fossil fuel plants. Additionally, without the necessary infrastructure in place, their energy supply is very intermittent. Nuclear energy, which is being widely used in France, has a significantly higher power density than renewable energy and may become very economical in the future if nuclear fusion becomes practical; however, nuclear waste is, at present, very expensive to dispose of safely; additionally, there are public fears of radiation leakage due to the disasters at Three Mile Island (1979), Chernobyl (1986), and more recently at Fukushima (2011). CCS, while being an easy retrofit to existing power plants, is very expensive, primarily due to the high cost of releasing the CO_2 from a capture solvent in order to pump it underground (IPCC, 2005); it also does not provide increased energy security. CDU, akin to CCS, is also very expensive; however, it has greater potential to become economical as the CO_2 is converted into useful products/services.

Unfortunately, a detailed discussion of the pros and cons of each of these low-carbon technologies is not within the scope of this work; however, what it does suggest is that none of the low-carbon technologies at present have yet to provide serious competition to fossil fuels in terms of supplying energy at a high power density, when it is needed, at a comparable cost, and with less public opposition.

The motivation for this thesis is therefore to help contribute towards finding a suitable alternative to fossil fuel energy in order to prevent irreparable damage to the planet, whilst increasing energy security and maintaining a high standard of global welfare. This work will focus on obtaining energy from biogas by capturing the CO_2 in solvents, and subsequently releasing it for CDU. This work will be undertaken as part of the 4CU project, which will be discussed in the next section.

1.2. Carbon Dioxide Utilisation (CDU)

4CU is a collaboration project between the University of Sheffield, University of Manchester, University College London, and Queens University Belfast, whose aim is to capture CO_2 from renewable energy sources and waste streams, such as biogas, and convert it into fuels. An overview of the 4CU project is depicted in Figure 1.1 with the contribution of this work highlighted in red.

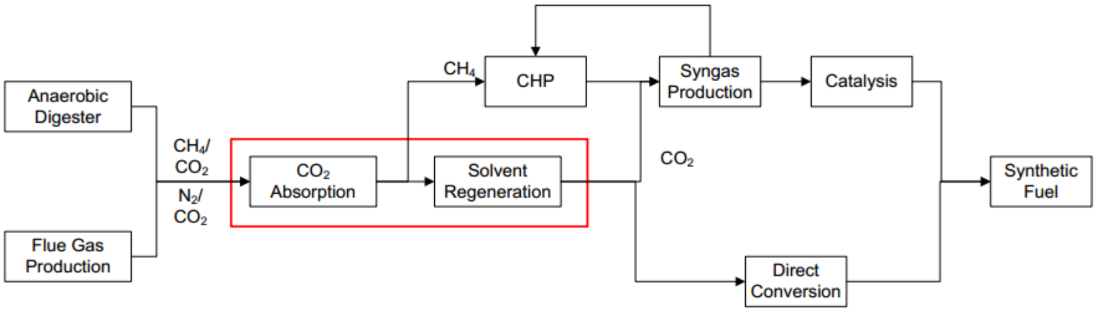

Figure 1.1. An overview of the 4CU project

This work will primarily focus on capturing CO_2 from biogas by absorption into solvents and releasing it (i.e. regenerating the solvent) as a very pure CO_2 stream such that it can be easily utilised. Furthermore, this work will compare two classes of solvent: monoethanolamine (MEA) – a solvent that is typically used to capture CO_2 in industrial applications; and ionic liquids – a new class of solvent that is gaining increasing popularity among researchers.

CDU, as mentioned earlier, is the process of converting CO_2 into useful products/services. It is already being implemented on a small scale for making products such as urea, pigments, construction materials, and methanol (Mikkelsen et al., 2010). Such products and services help to offset the cost of capturing the CO_2. Additionally, unlike with CCS, there is no need for a complex transport infrastructure as the CO_2 can be converted locally or sometimes *in situ*. It is estimated that global CO_2 emissions could be reduced by up to 10% if CO_2 could be converted into synthetic fuels (Aresta, 2007, Styring et al., 2011).

1.3. Biogas Upgrading

Biogas is a gas which derives from the anaerobic digestion of organic material by micro-organisms (Petersson and Wellinger, 2009). The main sources of biogas are: agricultural waste, food waste, and sewage sludge. Although its constituents depend largely on the biogas source, in general, it consists of approximately 60% methane, 40% CO_2, and traces of impurities, such as water vapour and hydrogen sulphide (Palmeri et al., 2008, Bidart et al., 2011, Privalova et al., 2013a).

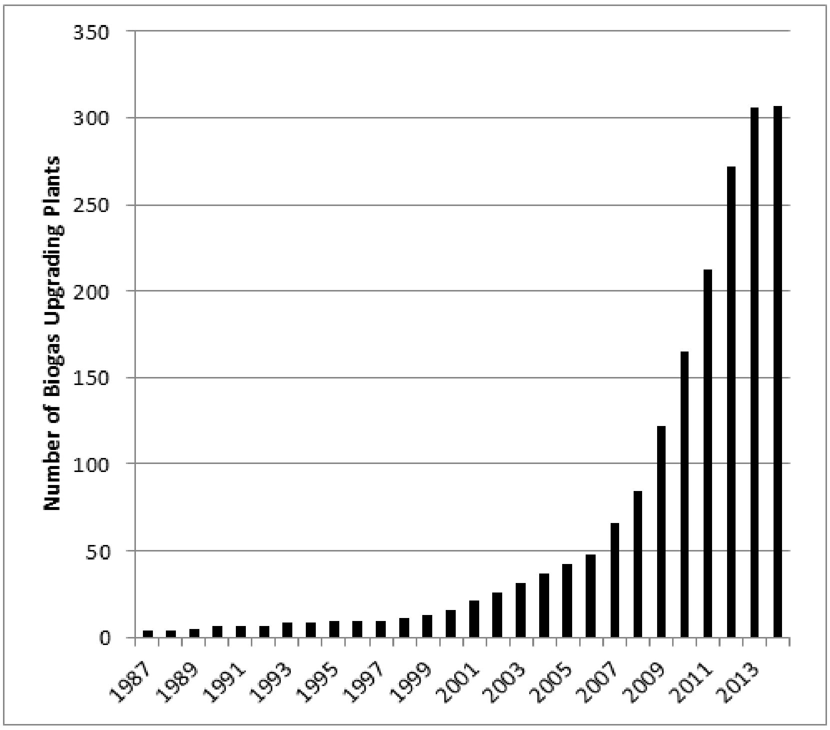

Figure 1.2. Number of biogas upgrading plants by year (data source: (IEA, 2013) date: 12/08/2014)

The methane present in biogas has a high energy content (~55 MJ/kg) making it a suitable source of heat and/or power. While biogas can be burnt at the site of production to provide heat and/or power locally, it can also be upgraded into biomethane, which typically has a methane content of ~96 % by volume (Ryckebosch et al., 2011), by removing most of the CO_2 and contaminants. This opens up the possibilities of injecting the gas into the gas grid – an option which is currently being employed in countries such as Germany, France, the UK, and the USA – or using it to power transport vehicles, which is being widely utilised in Sweden and Germany.

Since biogas derives from biological matter which has taken CO_2 out of the atmosphere during its growth, using it as an alternative energy source to fossil fuels would help contribute towards reducing CO_2 emissions into the atmosphere. Additionally, as it can be produced wherever there is agricultural, human, or industrial waste, it can improve energy security and has the advantage over most other renewable technologies that it can be burnt when it is needed. For these reasons, biomethane is becoming increasingly used as an energy source, as shown in Figure 1.2, indicating its potential to compete with other low carbon technologies, with the majority of interest stemming from Europe and the USA (see Figure 1.3).

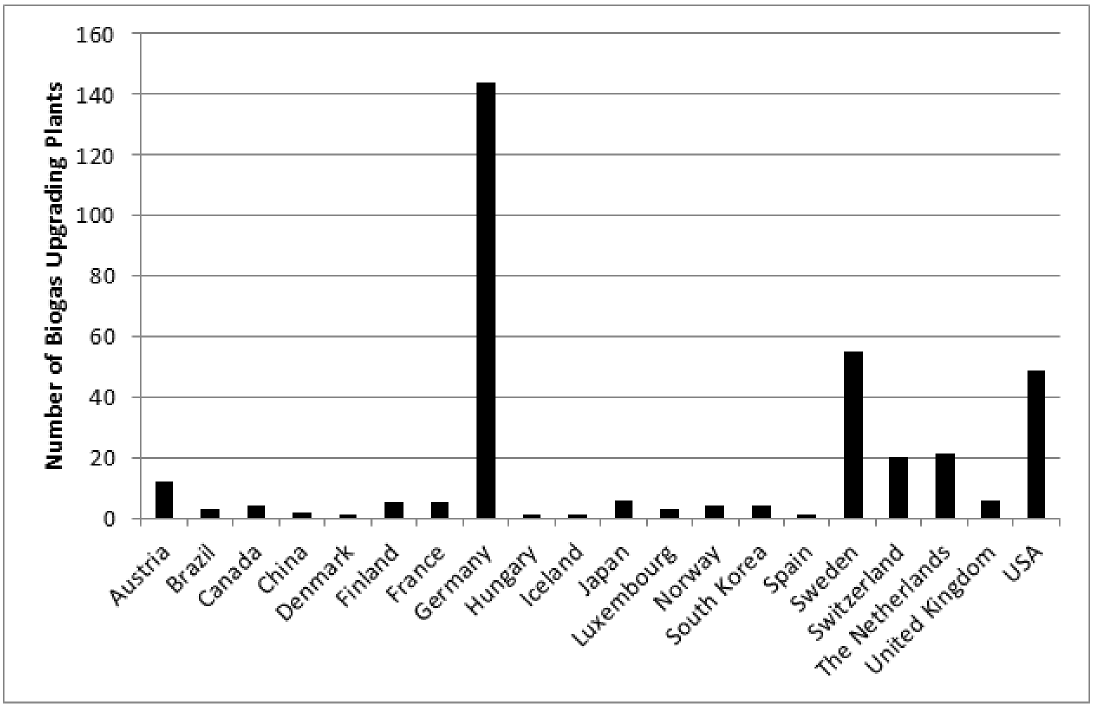

Figure 1.3. Number of biogas upgrading plants by country (data source: (IEA, 2013) date: 12/08/2014)

There are a number of methods for upgrading biogas into biomethane (Petersson and Wellinger, 2009):

- Water scrubbing – absorbing the CO_2 in water under pressure and releasing it by pressure reduction
- Absorption into physical solvents (by physisorption) and chemical solvents (by chemical reaction); the CO_2 is released by heating the liquid
- Pressure swing adsorption (PSA) – adsorbing the CO_2 onto solid particles and releasing it by pressure reduction
- Membrane separation – trapping the CO_2 in fine membranes under pressure and releasing it by pressure reduction
- Cryogenic separation – separating the gases by condensing one or more of the phases

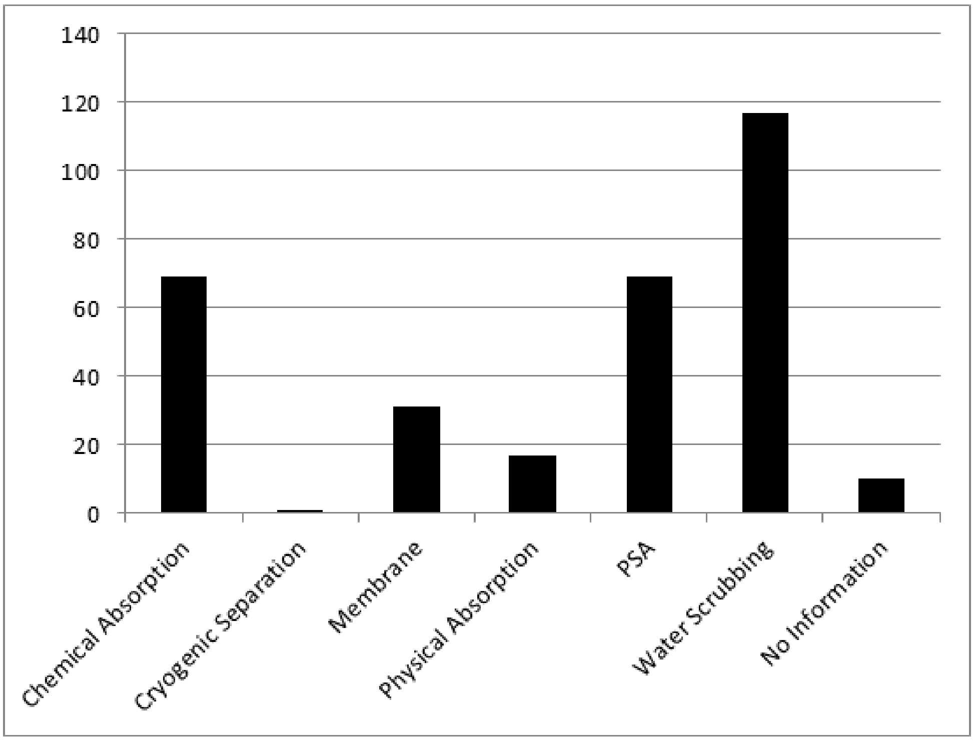

Figure 1.4. Number of biogas upgrading plants by upgrading method (data source: (IEA, 2013) date: 12/08/2014)

The most common method of upgrading biogas is water scrubbing (Figure 1.4), followed by PSA and chemical absorption. While each technology has its advantages and disadvantages and the choice of plant depends largely on the plant capacity and biomethane purity requirement, this work will focus on biogas upgrading using chemical and physical solvents, which are typically used when the purity of the biomethane needs to be particularly high (>99% methane). An overview of the absorption process is provided below.

The most common chemical solvent used in biogas upgrading is monoethanolamine (MEA) due to its high absorption capacity and low cost. A typical flow diagram of the amine treatment process is shown in Figure 1.5; the upgrading process operates as follows (Kohl and Nielsen, 1997, Mokhatab et al., 2006):

1. Prior to absorption, sulphur containing compounds must be removed from the biogas
2. The desulphurised gas is then passed into an absorber, operating under atmospheric pressure, where the CO_2 reacts with the amine solvent
3. The treated gas leaves the top of the absorber while a rich (loaded) solvent enters a flash tank to remove hydrocarbons

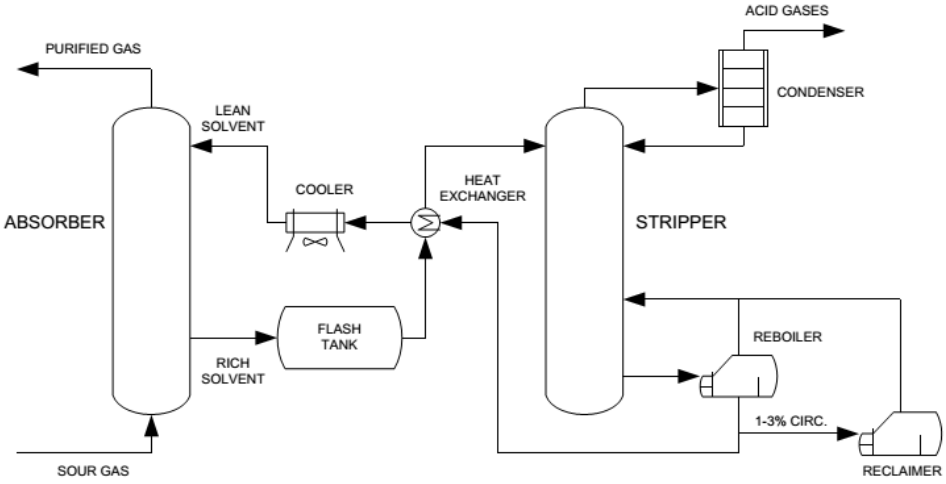

Figure 1.5. Schematic of an amine treatment plant (adapted from Mokhatab, 2012)

4. The rich solvent is then pumped to the top of a stripper column via a heat exchanger (to reduce the process energy requirement) in order to remove acid gases from the solvent. The words ‘stripping’, ‘regeneration’, and ‘desorption’ are typically used to describe this process
5. A reboiler heats some of the loaded solvent to between 107 - 127°C; the steam thus generated flows counter-currently to the loaded solvent in the stripper column, providing enough heat to reverse the CO_2-MEA reaction
6. The acid gases leaving the top of the stripper are passed to a condenser, which removes water vapour and adds it back into the top of the stripper column

7. Lean (unloaded) solvent leaving the stripper column is cooled via a heat exchanger and cooler before being pumped back into the top of the absorber
8. A reclaimer is often added to the process after the reboiler to remove heat stable salts, which are produced when the amine reacts with impurities in the gas stream

Typically, up to 80% of the energy requirement of the amine treatment process is consumed in the regeneration stage due to the large heat requirement of the reboiler (Chakma, 1997).

It is common for either trays or packing structures to be placed in the absorber and stripper columns in order to increase the interfacial area and residence time for mass transfer to occur.

In this work, novel methods for improving the biogas separation process will be investigated, such as the use of a novel regeneration technique termed Direct Contact Regeneration, the use of microbubbles to increase the interfacial area for gas absorption, and the use of ionic liquids to absorb CO_2. The use of these novel materials and techniques will be outlined in the next section and discussed in more detail in the literature review in Chapter 2.

1.4. Novelty in this Work

1.4.1. Direct Contact Regeneration

Earlier it was mentioned that the energy requirement of regenerating MEA contributes approximately 80% towards the entire upgrading process, primarily due to the high energy requirement of heating the liquid to desorb the CO_2. Here, it will be hypothesised that the aqueous MEA can be regenerated by bubbling a superheated gas into it, thus providing a locally high temperature at the bubble interface for desorption to take place. This technique will be termed Direct Contact Regeneration (DCR). If this is possible, the sensible heat requirement– which equates to about 42% that of the regeneration process (Dugas, 2006) – could be significantly reduced. The high surface area of microbubbles makes them a useful tool for testing this hypothesis.

In order for CDU to be economical, the CO_2 input stream usually needs to have a high purity. For this reason, in order to integrate DCR with CDU, the gas fed in to the column would have to be CO_2. This would likely inhibit desorption; however, in theory, if the bubble temperature is hot enough then the thermodynamics would still favour the desorption reaction.

1.4.2. Microbubble-Mediated Mass Transfer

Microbubbles are bubbles of diameter between 1 – 1,000 microns (Zimmerman et al., 2011). They are known to exhibit excellent mass transfer properties for absorbing gases into liquids. The reasons for this are:

- They have a high surface area for mass transfer to take place
- They have a high internal pressure
- Their low buoyancy promotes a long residence time for mass transfer

By exploiting these mass transfer characteristics of microbubbles for use in biogas upgrading, the rate of mass transfer can be increased, enabling more biogas to be upgraded using a smaller plant. In this work, a fluidic oscillator will be used to create microbubbles (see Section 2.3.2); such a device has been used by other researchers at the University of Sheffield for producing microbubbles in water, e.g. (Hanotu et al., 2012).

1.4.3. Ionic Liquids

Ionic Liquids are salts that exist in the liquid state below 100 °C (Blath et al., 2011). They are known to have excellent CO_2 absorption properties and are typically easy to regenerate, releasing nearly all of the CO_2 at about 80°C. Additionally, they don't evaporate at room temperature and pressure (Brennecke and Maginn, 2001) meaning that these liquids can essentially be used indefinitely (provided they don't degrade).

However, they typically have complex molecular structures making them very expensive to produce, as well as low diffusion coefficients making mass transfer slow. Despite these drawbacks, since they don't evaporate and therefore do not require replenishment, they may still be more economical than using chemical solvents over the plant lifetime.

1.5. Overall Goals of This Work

The overall goals of this work are as follows:

- Investigate the feasibility of using Direct Contact Regeneration for regenerating aqueous MEA and ionic liquids

- Investigate whether Direct Contact Regeneration can be integrated with CDU technologies using MEA and ionic liquids
- Investigate the physical properties of ionic liquids that are ideal for producing microbubbles
- Determine the suitability of upgrading biogas in aqueous MEA and ionic liquids using microbubbles

1.6. Specific Objectives

In order to achieve these overall goals, the following objectives will be achieved:

- Produce a numerical model to determine the feasibility of desorbing CO_2 into a bubble from both aqueous MEA and ionic liquids using DCR
    - Simulations will be conducted using COMSOL Multiphysics by modelling a superheated microbubble inside a liquid of fixed concentration
- Determine the effects of bubble size, temperature, and CO_2 loading on the rate of desorption
- Use the aforementioned model to examine whether DCR can be used in conjunction with CDU technologies
- Conduct experiments to determine whether a fluidic oscillator can be used to produce microbubbles in ionic liquids from a single orifice
    - Determine the effect of oscillation frequency on bubble size
- Obtain experimental data using air in water-glycerol mixtures to examine how the viscosity, surface tension, and density of the liquid affects bubble size and gas holdup from a microporous diffuser
- Determine the effects of liquid viscosity, surface tension, density, and gas flow rate on the bubble size and gas holdup in ionic liquids and compare the results with those in water-glycerol mixtures
- Examine the effect of drying ionic liquids on the production of microbubbles in a bubble column
- Conduct experiments to compare the suitability of aqueous MEA and various ionic liquids for upgrading biogas using microbubbles
- Investigate how the properties of ionic liquids affect mass transfer

1.7. Thesis Overview

The importance of biogas upgrading and CDU in a global setting, as well as the motivation for using microbubbles in aqueous MEA and ionic liquids has been explained in this chapter (Chapter 1); subsequently the overall goal and objectives of this work were outlined. Chapter 2 presents a review of the relevant literature surrounding this work, highlighting where this work fits in. The experimental apparatus and techniques used in this work are presented in Chapter 3. In Chapters 4 and 5, the setup and results of a numerical simulation on the feasibility of DCR using aqueous MEA and ionic liquids are presented. An experimental investigation into bubble size and gas holdup in ionic liquids is presented in Chapter 6. Following that, the results of an experimental investigation of biogas upgrading using microbubbles in aqueous MEA and ionic liquids are presented in Chapter 7. Finally, in Chapter 8, the conclusions of this work are presented.

2. Literature Review

In this chapter, a review of the relevant literature surrounding this work will be discussed. First, a comparison between aqueous MEA and ionic liquids for gas upgrading will be presented, outlining the advantages and disadvantages of each solvent. Then, a review of biogas upgrading using aqueous MEA and ionic liquids will be presented. Following this, a review of bubble size, gas holdups, and mass transfer coefficients in ionic liquids and common solvents will be discussed. Finally, a summary of the literature review will be presented, noting the gap in the literature where this work fits in.

2.1. MEA vs. Ionic Liquids

Monoethanolamine (MEA) is a chemical solvent commonly used for upgrading gas streams containing acid gases such as CO_2 (Kohl and Nielsen, 1997). It is typically used to purify natural gas (Mokhatab et al., 2006); however it can also viably be used to purify other gas streams such as flue gas (Alie et al., 2005) and biogas (Privalova et al., 2013b, Palmeri et al., 2008).

The main advantages of using MEA for CO_2 absorption processes are its high absorption capacity and low cost; in a typical amine treatment process, one mole of MEA is used to capture 0.2 moles of CO_2 (Abu-Zahra et al., 2007a, Abu-Zahra et al., 2007b). This equates to about 6.9 g of MEA per gram of CO_2 captured.

The main disadvantages of MEA are its high corrosivity, high energy requirement for regeneration, and high vapour losses during regeneration. Regeneration of MEA typically comprises around 49% of the total energy requirement of the capture process (Rao and Rubin, 2002); however, some authors have quoted figures as high as 80% (Chakma, 1997). The standard method for regenerating MEA is to heat a rich aqueous MEA solution to temperatures of around 120 °C in a stripper column (Mokhatab et al., 2006, Abu-Zahra et al., 2007a), providing enough energy to reverse the CO_2-MEA reaction (see Appendix B: MEA-CO_2 Reaction) and to release the CO_2 from the solvent. Due to its high corrosivity, a 30 wt.% aqueous MEA solution is typically used, rather than pure MEA (Abu-Zahra et al., 2007b). As a result of the high temperatures as well as impurities in the gas stream, evaporation and degradation losses occur and so some of the MEA has to be replenished, increasing plant operating costs; it is estimated that the replenishment rate of MEA is between 179 – 307 kg-MEA/tonne-CO_2 captured (Zhu et al., 2013).

Many of the problems that MEA suffers from highlight the benefits of ionic liquids. Ionic liquids are salts that exist in the liquid phase below 100 °C (Kaji et al., 2009, Blath et al., 2011, Kerlé et al., 2009). They typically have high CO_2 absorption capacities (up to about 1 mole-CO_2/mole-IL/atm), don't evaporate under atmospheric conditions (Brennecke and Maginn, 2001), and have a high thermal stability (Privalova et al., 2013a). (Zhang et al., 2012b) report that the best performing ionic liquids require 4.88 g of solvent to capture 1 g of CO_2 – that is about one fifth of the mass of aqueous MEA required[1]. Additionally, many ionic liquids have a low enthalpy of absorption of CO_2 (approx. 10-120 kJ/mol-CO_2 (Zhang et al., 2012b)) compared with MEA (~85 kJ/mol-CO_2 (Kim and Svendsen, 2007)), thus reducing the energy requirement for regeneration. As a result, they have gained increasing popularity among researchers, as shown in Figure 2.1.

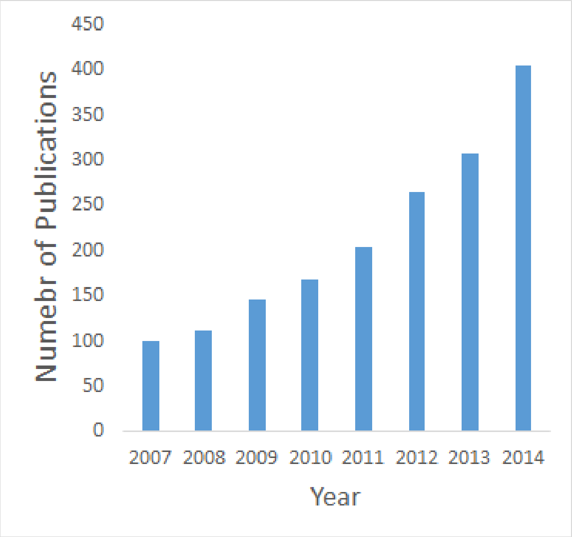

Figure 2.1. Publications per year containing 'ionic liquids' and 'CO2' in the title, subject, or keywords between 2007-2014 (from Web of Science search)

However, there are several disadvantages of ionic liquids which underline why they are not used on an industrial scale. Firstly, they are difficult to synthesise, making them very expensive (Keskin et al., 2007). They also typically have high viscosities and low CO_2 diffusivities, making mass transfer slow. Thirdly, they are very hygroscopic; the absorption of even a small amount of water is known to significantly affect both the

---

[1] Calculated assuming a 30 wt.% aqueous MEA solution with rich and lean loadings of 0.4 and 0.2 mol-CO_2/mol-MEA respectively

physical and absorption properties of ionic liquids (Gallagher et al., 2014, Zhang et al., 2013).

(Keskin et al., 2007) report that the cost of ionic liquids is about 30,000 times that of typical chemical solvents. It is estimated that this cost can be reduced to about $33/kg once they benefit from economies of scale. However, this is still about 25 times greater than the cost of MEA ($1.298/kg (Kohl and Nielsen, 1997)).

Additionally, their high viscosities – typically upwards of 0.01 Pa·s – inhibit the production of small bubbles (Lange et al., 2013), which are desirable for higher mass transfer rates in bubble columns. (Hou and Baltus, 2007) showed that the CO_2 diffusivity in ionic liquids also decreases with increasing viscosity, further inhibiting mass transfer.

Although ionic liquids are very hygroscopic, this is not necessarily a disadvantage in terms of their carbon capture capabilities (Aki et al., 2004). However, it means that in order to get meaningful research data from them, they either have to be dried thoroughly immediately before use or the moisture content needs to be accurately determined.

2.1.1. **Regeneration**

As mentioned in Section 2.1, one of the main disadvantages of using MEA for CO_2 capture is the high regeneration energy requirement; this is estimated to be around 4 GJ/tonne-CO_2 captured (see Table 2.1).

The total amount of energy required for regenerating a solvent, comprises the enthalpy of reaction, the sensible heat requirement, and the latent heat of vapourisation (Chakma, 1997, Song et al., 2008). (Dugas, 2006) studied a typical pilot plant and found that the largest constituent is the sensible heat requirement which contributes approximately 42% of the regeneration thermal energy requirement. This was followed by the heat of reaction, cooling requirement, and heat losses, which comprise 24%, 20%, and 14% respectively.

Various efforts have been made to reduce the regeneration energy requirement of aqueous MEA solutions. Such efforts include the use of amine mixtures such as MEA/MDEA (e.g. (Chakma, 1997, Idem et al., 2006)), the use of additives (e.g. (Dang and Rochelle, 2003)) and non-amine-based solvents (e.g. (Bishnoi and Rochelle, 2000)), experimenting with different packings and column arrangements (e.g. (Dugas, 2006, Jassim and Gary, 2006, Oyenekan and Rochelle, 2007), and investigating the effects of different solution loadings and MEA concentrations (e.g. (Abu-Zahra et al., 2007a)).

Table 2.1. Reported regeneration energy of rich aqueous MEA solutions

Author(s)	**Method**	**Process/ Solvent**	**Power Plant Type**	**Regeneration Energy Requirement (GJ/t-CO_2)**
(Suda et al., 1992)	Experimental	Econamine FG™	Natural Gas boiler	4.1
(Mimura et al., 1997)	Experimental	Aqueous MEA (30 wt. %)	Natural Gas, Coal	3.8
(Chapel et al., 1999)	Review	Econamine FG™	Various	4.2
(Singh et al., 2003)	Numerical	MEA	Coal	3.8
(IPCC, 2005)	Review	Econamine FG™	Coal	3.2
(IPCC, 2005)	Review	Econamine FG™	Natural Gas	3.7
(Alie et al., 2005)	Numerical	Aqueous MEA (30 wt. %)	Cement, Coal, Natural Gas	4.0-4.5
(Abu-Zahra et al., 2007a)	Numerical	Aqueous MEA (20-40 wt. %)	Coal	3.0-3.9

While the aforementioned studies have successfully found ways of reducing the energy requirement for regeneration, it must be noted that many of these methods compromise another aspect of the process: for example, mixing MEA with other amines often reduces the absorption capacity and increasing amine concentrations so as to reduce the sensible heat requirement can lead to increased corrosion.

It is evident that MEA requires a lot of energy to regenerate, largely due to the sensible heat requirement. The next sub-section will introduce Direct Contact Regeneration (DCR) – a method devised in this work for regenerating a solvent with minimal heating of the bulk liquid.

2.1.1.1. *Direct Contact Regeneration (DCR)*

In this work, a model will be developed to examine the feasibility of regenerating MEA and an ionic liquid using Direct Contact Regeneration (DCR). The idea is to sparge hot microbubbles into the solvent so as to locally desorb CO_2 at the bubble interface without heating the bulk liquid. Such a technique may negate some of the sensible heat requirement – the largest energy contributor to regeneration.

Although this is a new idea, its concept derives from Direct Contact Evaporation (DCE), whereby hot bubbles are sparged into a liquid in order to evaporate it – a technique that has been around for centuries. This technique is known to produce heat transfer efficiencies as high as 95% (Ribeiro and Lage, 2005, Zimmerman et al., 2013) due to low heat losses.

Schematics of a DCE column and DCR column are provided in Figure 2.2 to highlight their similarities together with a photograph of the bubble column used in this work. In a DCE column, a superheated gas is sparged into a liquid. The liquid evaporates and diffuses into the gas phase and is then extracted at the top of the column when the bubbles burst.

Comparatively, in a DCR column, a superheated gas is sparged into a solution. In this work the solution will consist of either aqueous MEA and CO2 or an ionic liquid and CO2. The heat from the gas causes the solute – in this case CO2 – to desorb out of the solution and enter the gas phase. When the bubbles burst at the surface, the solute is extracted at the top of the column.

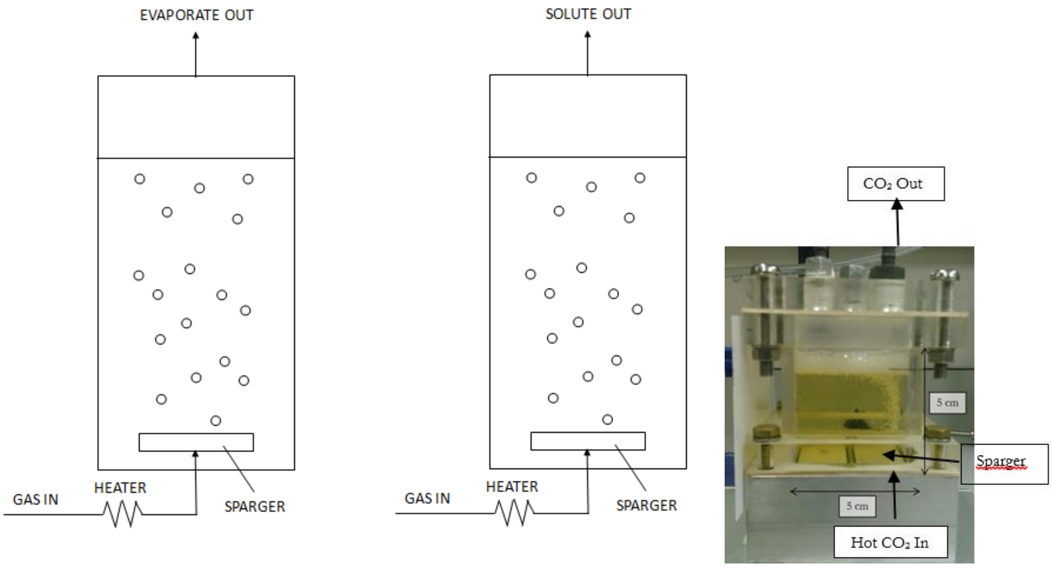

Figure 2.2. Schematic of a Direct Contact Evaporator (left), a Direct Contact Regenerator (centre), and a photograph of the bubble column used in this work (right)

In the numerical model, a single bubble will be simulated with the partial pressure of CO_2, MEA, and water at the bubble interface assumed to flash to saturation. This is in accordance with the model of (Zimmerman et al., 2013) for water evaporation into a bubble, except with CO_2 and MEA as additional parameters. [C_2mim][NTf_2] will be used as an example to compare with aqueous MEA since the partial pressure of CO_2 in this ionic liquid has been studied for a range of temperatures (300 – 500 K) (Finotello et al., 2008, Kerlé et al., 2009) and the enthalpy of reaction between [C_2mim][NTf_2] and CO_2 is also known (Cadena et al., 2004, Blath et al., 2011).

2.2. Biogas Upgrading

Biogas is becoming an increasingly attractive form of renewable energy to harvest. A typical biogas mixture consists of about 60% CH_4, 40% CO_2, and traces of water vapour, volatile organic compounds (VOCs), and H_2S (Palmeri et al., 2008, Bidart et al., 2011, Privalova et al., 2013a). In order to increase its calorific value, biogas is often upgraded to biomethane by removing most of the CO_2 and VOCs.

While water scrubbing, used in approximately 35% of biogas upgrading plants, is the most common method of upgrading biogas, chemical scrubbing and pressure swing adsorption are also often used, especially when a high purity of methane is required, such as for injection into the gas grid or for use as vehicle fuel (see Figure 2.3).

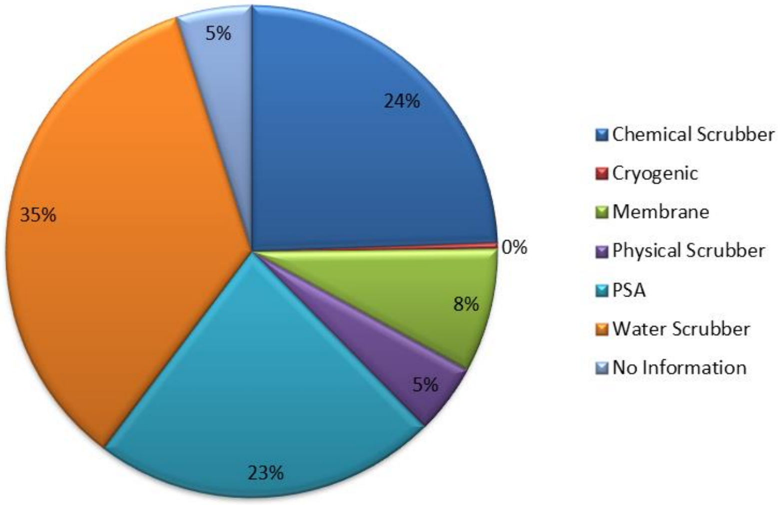

Figure 2.3. Biogas upgrading plants from IEA 37 member countries sorted by technology (IEA, 2013) (2014)

Many studies have been conducted to determine the solubility of CO_2 in ionic liquids, e.g. (Finotello et al., 2008, Kerlé et al., 2009, Carvalho et al., 2010); however, very few have compared ionic liquids with either water or chemical solvents for biogas upgrading.

(Privalova et al., 2013a) compared the capture capabilities of imidazolium-based ionic liquids ([C_4mim][BF_4], [C_4mim][DCA], [C_4mim][PF_6], [C_4mim][AcO]) with water and aqueous MEA (15 wt.%) from both an artificial biogas mixture and a real biogas mixture. They found that while water absorbed 1.62 L-CO_2/L-solvent, three of the ionic liquids ([C_4mim][BF_4], [C_4mim][DCA], [C_4mim][PF_6]) performed only slightly better, absorbing between 2.63-3.31 litres of CO_2/L-solvent. However, [C_4mim][AcO] – a chemical solvent – was capable of absorbing 48.85 L-CO_2/L-solvent, which was comparable to the MEA solution (50.12 L-CO_2/L-solvent).

(Bidart et al., 2011) examined the feasibility of upgrading biogas using two imidazolium-based ionic liquids ([C_4mim][Br], [pamim][Br]) and compared them with aqueous MEA (15 wt.%) in a packed column. However, due to their high viscosities, the ionic liquids had to be diluted with water. They found that the ionic liquids only absorbed about one third the amount of CO_2 compared with the MEA solution (per kg of solvent); however, adding MEA to the ionic liquid was shown to increase its absorption capacity.

Despite their increasing popularity among researchers, due to their high cost and difficulty in handling, there is still very little data on biogas upgrading using ionic liquids in absorption columns. Moreover, much of the data focuses on CO_2 solubility; none of the papers have calculated mass transfer rates, which are vitally important for plant design, especially if the biomethane purity requirement is pre-defined.

In this work, several ionic liquids will be investigated for biomethane production and mass transfer rates will be calculated from experiments.

2.3. Bubble Size and Gas Holdup

Knowledge of bubble size and gas holdup is important for determining the amount of surface area for mass transfer and will therefore be reviewed here.

A bubble column is one of the simplest contactors used for absorbing gases into liquids. It consists of a column of liquid with a porous sparger (or set of orifices) located at or near the bottom (see Figure 2.4).

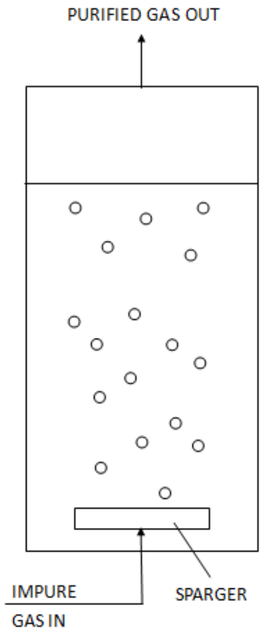

Figure 2.4. Schematic of a bubble column

In general, there are three bubble regimes that exist in a bubble column: these are: the bubble-flow regime, churn turbulent regime, and slug flow regime (Shah et al., 1982, Deckwer, 1991). These are shown schematically in Figure 2.5. The bubble flow regime is sometimes termed the homogenous regime since the bubbles are all of a similar size and shape. Conversely, the churn-turbulent and slug-flow regimes are referred to as heterogeneous regimes. In general, bubbly flow with small bubbles is desirable for mass transfer processes.

There are many factors that affect the size of a bubble from a submerged orifice; these include: liquid viscosity, gas-liquid surface tension, liquid density, gas density, orifice shape, orifice diameter, orifice chamber volume, orifice submergence, orifice contact angle, orifice orientation, orifice material, and gas flow rate (Kulkarni and Joshi, 2005). In the case of forming bubbles from a diffuser with multiple pores, additional factors may affect not only the initial bubble size, but also the amount of bubble coalescence. Such factors include: the shape of the column, the distance between pores, the position of the diffuser in relation to the column walls, and the regularity of the pore size and shape. If one is using a fluidic oscillator, such as that described in Section 2.3.2, to aid microbubble production then the pressure drop across the diffuser and the flexibility of the diffuser also makes a significant difference.

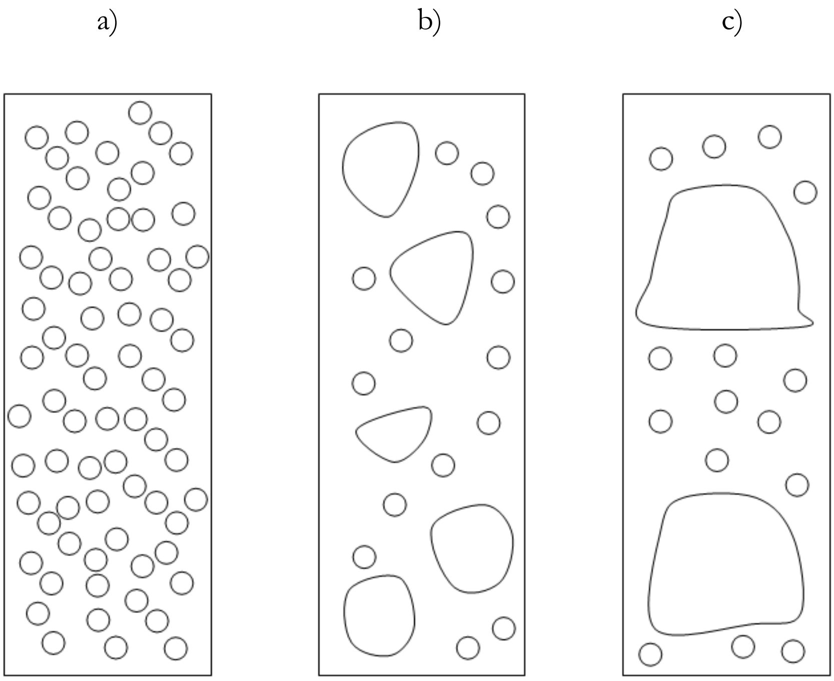

Figure 2.5. Bubble regimes in bubble columns: a) bubble flow regime; b) churn-turbulent regime; c) slug flow regime

An important parameter often used to measure the effectiveness of bubble columns is the gas holdup, ε, as defined by (Kantarci et al., 2005):

$$\varepsilon = \frac{Volume\ of\ Gas}{Total\ Volume} \tag{2.3.1}$$

It is often calculated using the equation:

$$\varepsilon = \frac{U_G}{U_{slip}} \tag{2.3.2}$$

were, U_{slip} is the bubble slip velocity, defined by the velocity difference between the bubble and the liquid and U_G is the superficial gas velocity as defined by:

$$U_G = \frac{\dot{V}}{A} \tag{2.3.3}$$

where $\dot{V}$ is the volume flow rate of gas and A is the area of the column (Hughmark, 1967).

It is desirable for the gas holdup to be high and the bubble diameter to be small, so as to maximise the surface area (per unit volume) for mass transfer, a, which is given by:

$$a = \frac{6\varepsilon}{\bar{d}} \tag{2.3.4}$$

where $\bar{d}$ is the mean bubble diameter (Shah et al., 1982, Kantarci et al., 2005).

2.3.1. Microbubble-Mediated Mass Transfer

Microbubbles are bubbles of diameter between 1-1,000 μm (Zimmerman et al., 2011). Many authors have found microbubbles to have excellent mass transfer properties in numerous applications, such as water aeration (Motarjemi and Jameson, 1978, Zimmerman et al., 2009c), wastewater treatment (Terasaka et al., 2011), gas fermentation (Bredwell and Worden, 1998), and drug delivery (Unger et al., 2001). The reasons for this are outlined in this section.

2.3.1.1. Surface Area

The surface area to volume ratio (SVR) of a sphere of radius R is given by (Zimmerman et al., 2009a):

$$SVR = \frac{4\pi R^2}{4/3\,\pi R^3} = \frac{3}{R} \tag{2.3.5}$$

This means that if the bubble size is reduced, for example by a factor of 10, and the total volume of gas is kept constant, there will be 10 times more surface area for mass transfer to take place.

2.3.1.2. Internal Pressure

The pressure inside a bubble is given by the Young-Laplace Equation (Young, 1805, Laplace, 1805):

$$\Delta P = \frac{2\gamma}{R} \tag{2.3.6}$$

where ΔP is the pressure difference between the inside and outside of the bubble, γ represents the surface tension of the liquid, and R is the bubble radius.

Therefore, if the bubble radius is reduced, the pressure inside the bubble will be greater, thus increasing the driving force for mass transfer.

2.3.1.3. Residence Time

There are a few equations provided in the literature for the terminal velocity of a bubble, U_T. The terminal velocity of a spherical bubble rising in an infinite fluid region is given by the Hadamard-Rybczinski equation (Zimmerman et al., 2013):

$$U_T = \frac{1}{6}\frac{gd^2(\rho_L - \rho_G)}{\mu_L}\frac{\mu_L + \mu_G}{2\mu_L + 3\mu_G} \tag{2.3.7}$$

where g is the acceleration due to gravity, d is the bubble diameter, ρ and μ denote density and viscosity respectively and the subscripts, L and G, represent the liquid and gas phases respectively. Often, the viscosity of the gas is considered to be negligible and the equation is simplified to:

$$U_T = \frac{1}{12}\frac{gd^2(\rho_L - \rho_G)}{\mu_L} \tag{2.3.8}$$

The Hadamard-Rybczinski equation is derived from the Navier-Stokes equation and takes into account internal circulation within the bubble (Clift et al., 1978).

For a bubble rising in the Stokes flow regime (Re<<1), the terminal velocity can be calculated by equating the buoyancy force with the Stokes drag force, thus giving the equation:

$$U_T = \frac{1}{18}\frac{gd^2(\rho_L - \rho_G)}{\mu_L} \tag{2.3.9}$$

In practice, the bubble rise velocity often lies somewhere in between the Hadamard-Rybczinski and Stokes terminal velocities. However, the Hadamard-Rybczinski equation is more commonly used for bubbles.

In both equations, it can be seen that as the bubble diameter is reduced, the terminal velocity decreases and so the bubble stays in the liquid for longer. This demonstrates that microbubbles have a longer residence time than fine bubbles, providing more time for mass transfer to occur.

2.3.1.4. Compounding Effects

Points 1 – 3 convey why mass transfer is higher in smaller bubbles. As mass is transferred from the bubble to the liquid, the bubble shrinks in size. This promotes further mass transfer causing the bubble to shrink further. In some instances, the effects of mass transfer will be so great that the bubble will collapse (Xu et al., 2008).

For these reasons, it is of fundamental importance that the bubble size is sufficiently small for mass transfer applications; otherwise the column would have to be made bigger or liquid would have to be pumped faster, which would increase operating costs.

2.3.2. **Fluidic Oscillator**

In this work, it will be investigated whether a fluidic oscillator can be used to produce microbubbles in ionic liquids. Such a device has been used to produce microbubbles in other works conducted in the Microfluidics Group, University of Sheffield using water (al-Mashhadani et al., 2011, Zimmerman et al., 2009b, Hanotu et al., 2012). The main advantage of using a fluidic oscillator over other microbubble-generation techniques is that it contains no moving parts, thus reducing the risk of damage due to wear.

The main effect that causes the fluid to oscillate inside a fluidic oscillator is the Coandă effect. This states that a jet of fluid flowing near a solid surface has a tendency to follow the shape of the surface rather than continuing along its trajectory. The reason for this is because when a fluid jet flows near a solid surface, the fluid in between the surface and the jet becomes entrained. Due to Bernoulli's Principle, this causes the pressure between the surface and the fluid jet to be reduced, thus creating a pressure imbalance on either side of the jet and resulting in the fluid being diverted towards the surface. The operation of the fluidic oscillator is presented in Figure 2.6; it works as follows (Tesař et al., 2006, Tesař and Bandalusena, 2010):

a) A fluid is fed into the supply terminal, S, and travels through the oscillator. If the Reynolds number is high enough (typically >1,000), then the fluid will be diverted towards one of the outlet terminals, Y. This diversion is a result of the Coandă effect which causes a fluid to become entrained as it flows past a solid surface.
b) Since the fluid path is now asymmetric, a pressure difference results between the control terminals, X_1 and X_2, which are connected by a feedback loop.

c) This causes a fraction of the fluid to move towards the opposite flow terminal, thus increasing the pressure and diverting the main jet towards the opposite outlet terminal. A fluidic valve connecting the two outlet terminals is used to aid the fluid towards a single outlet terminal and prevent undesirable spillover.

d) A pressure difference between the two control terminals is reproduced, however in the opposite direction, diverting the fluid back to the other supply terminal

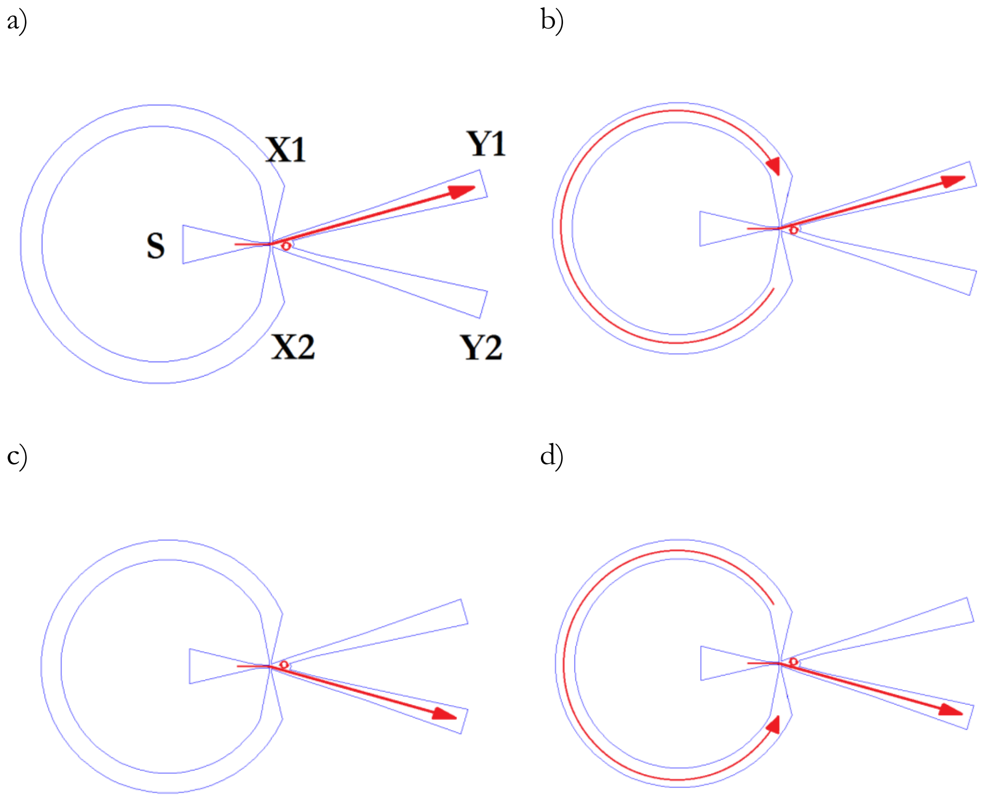
a)
b)
c)
d)

Figure 2.6. Operation of the fluidic oscillator

Typically, a bubble will break off when the buoyancy force exceeds the surface tension and drag forces. The fluidic oscillator works by pulsing a gas into a liquid with a high inertia compared with steady flow, using the inertia of the gas to break off the bubbles while they are small (Zimmerman et al., 2009b, Hanotu et al., 2012).

Other researchers in the Microfluidics Group at the University of Sheffield have found that if the gas pressure at the inlet to a diffuser or orifice is oscillated, there exists a particular oscillation frequency (usually around 150 Hz) at which the bubble size is significantly reduced (Brittle, 2014). The reason for this is because if the frequency is too high, each pulse of gas is not strong enough to make the bubble detach – the gas flow tends towards a steady flow approximation as the frequency tends to infinity;

alternatively, if the oscillation frequency is too low, each pulse of gas will be sufficiently great to make a large bubble detach; thus, a frequency in the middle is optimal.

2.3.3. Bubble Size and Gas Holdup in Bubble Columns

Bubble diameter and gas holdup are affected by a number of parameters, the main ones being: liquid viscosity, gas-liquid surface tension, liquid density, gas density, orifice diameter, contact angle, sparger design, and gas flow rate. These parameters affect the bubble size in the following ways:

- Liquid viscosity: this is a measure of the amount of drag acting on the bubble both during and after bubble formation. A greater liquid viscosity causes the bubble to form slower as the viscous drag force acting on the bubble is larger. This means that there is more time for gas to enter the bubble while it is being formed, causing the bubble size to increase.

- Gas-liquid surface tension: this is the force that holds the bubble together after formation but also anchors it to the diffuser surface during formation. If the gas-liquid surface tension is increased, the force anchoring the bubble to the diffuser surface will be greater. This means that more buoyancy is required to break the bubble away from the surface therefore increasing the bubble size.

- Liquid density: A greater liquid density means that there is more pressure acting on the bubble during formation, thus causing the bubble size to be reduced.

- Gas density: A greater gas density reduces the buoyancy force on the bubble, thus increasing the bubble size and increasing the gas holdup. However the effect of this parameter is usually very small compared with the liquid density (as the gas density is usually only a small fraction of the liquid density) and so it is often neglected.

- Contact angle (wettability): This is a measure of how attracted the liquid molecules are to the solid surface compared with their attraction to the gas. If the liquid is highly attracted to the surface then the contact angle is small and the wettability is high. If the wettability is high, the bubble will not spread very far over the pore area during formation; however, if the wettability is low then the bubble will spread over an area much larger than the pore. A lower wettability therefore increases the anchoring force caused by the surface tension and therefore a larger buoyancy force is required to break the bubble away from the surface, thus resulting in a greater bubble diameter.

- Gas flow rate: The greater the gas flow rate, the faster the gas can get into the bubble before the bubble is able to detach from the surface. Therefore, a higher gas flow rate results in an increase in bubble diameter.

- Orifice diameter: The smaller the orifice diameter, the smaller the bubbles that will be produced as the anchoring force acting on the bubble will be smaller.

The aforementioned factors affecting bubble size affect gas holdup as follows:

- Any factor that causes the bubble size to increase causes the buoyancy force on the bubble to increase. This increases the bubble rise velocity and therefore reduces the gas holdup as the bubbles remain in the liquid for a shorter time period. Conversely, any factor that causes the bubble size to reduce results in the bubble rise velocity being reduced and the gas holdup to increase. The buoyancy force increases with the cube of the bubble diameter and the bubble rise velocity increases with the square of the bubble diameter.

- Liquid viscosity: Since a greater liquid viscosity results in a greater drag force acting on the bubble, the rise velocity will be slower in a viscous liquid than a non-viscous liquid (for the same size bubble) resulting in a larger gas holdup.

- Liquid density: A greater liquid density increases the buoyancy force acting on the bubble, thus increasing the rise velocity and reducing gas holdup.

- Gas density: A greater gas density reduces the buoyancy force acting on the bubble, thus decreasing the rise velocity and increasing gas holdup. Again, this effect is usually very small in comparison to the effect of liquid density.

- Gas flow rate: A greater gas flow rate increases the superficial gas velocity, UG, thus increasing the value of the gas holdup if the bubble size remains the same. However, if the increase in gas flow rate causes the bubble rise velocity to increase by more than the superficial gas velocity then the gas holdup will actually be reduced.

- Release velocity: It is often assumed that the bubble travels at its terminal velocity inside a bubble column. However, depending on the gas flow rate and fluid parameters, the bubble can be released at different speeds. If the gas flow rate is small then the bubble will be released at a velocity lower than its terminal velocity and speed up. However, if the flow rate is sufficiently high then the bubble may be released at a velocity greater than its terminal velocity and slow down. This may result in an underestimation of the rise velocity and hence an overestimation of the gas holdup.

The only studies on bubble columns using ionic liquids are those by (Zhang et al., 2012a) and (Kaji et al., 2009). (Zhang et al., 2012a) conducted experiments with [C$_4$mim][EtSO$_4$] at different temperatures using a sparger consisting of four needles. The viscosity of the ionic liquid in their experiments ranged between 0.066-0.188 Pa·s. They found that the liquid viscosity had a much larger effect on the mean bubble diameter than the surface tension and that higher superficial gas velocities resulted in more bubble coalescence, thus increasing the bubble size. A low liquid viscosity and high surface tension were shown to produce smaller bubbles.

(Kaji et al., 2009) carried out experiments using a porous sparger with [C$_2$mim][EtSO$_4$], which has a viscosity of 0.12 Pa·s. They found that the bubble size was similar to that of an aqueous glycerol mixture of similar viscosity, suggesting that viscosity is the dominant parameter for determining the bubble size.

A few other studies have been conducted using bubbles in ionic liquids from a single orifice. (Wang et al., 2010b) studied bubble size in [C$_4$mim][BF$_4$], [C$_4$mim][BF$_6$], and [C$_8$mim][BF$_4$]. At higher liquid temperatures, the bubble diameter decreased. They concluded that both viscosity and surface tension are important for determining bubble size; however, the relative importance of these were not quantified.

(Wang et al., 2010a) conducted a separate study on mass transfer in bubble columns. Although bubble sizes were not reported the interfacial area was less than 100 m^2/m^3 and gas holdups of less than 0.01 were reported. This is far less than gas holdups achievable in common solvents, which are of the order of 0.1 (Akita and Yoshida, 1973, Chaumat et al., 2007).

Other authors have conducted experiments in bubble columns using common solvents to examine the effects of liquid physical properties and gas flow rate on bubble size. Most authors have used a correlation based on dimensionless numbers, which can be expressed as:

$$\bar{d} \propto {\mu_L}^A \gamma^B {\rho_L}^C {U_G}^D \tag{2.3.10}$$

where $\bar{d}$ is the mean bubble diameter, μ_L, γ, and ρ_L, are the viscosity, surface tension, and density of the liquid respectively, and U_G represents the superficial gas velocity.

Table 2.2 Exponential dependences of bubble diameter on liquid properties and superficial gas velocity in a bubble column: d $\propto \mu_L^A \gamma^B \rho_L^C U_G^D$ (adapted from (Pohorecki et al., 2005))

Reference	Viscosities Studied (Pa·s)	A	B	C	D
(Hughmark, 1967)	0.0009-0.152		0.60	-0.20	
(Van Dierendonck, 1970)	0.04-0.65		0.50	-0.50	
(Akita and Yoshida, 1974)	0.0006-0.002	0.24	0.50	-0.74	-0.12
(Kumar et al., 1976)	0.001-0.012		0.25	-0.25	0.43
(Wilkinson et al., 1994)	0.0004-0.021	0.22	0.34	-0.45	-0.02
(Pohorecki et al., 2005)	0.0005-0.005	-0.05	0.44	-0.55	-0.12
(Zhang et al., 2012a)	0.066-0.188	0.14	-0.10	0.07	0.28

The exponents from Eqn. 2.3.10 have been obtained by other authors investigating common solvents; these are presented in Table 2.2, which has been adapted from (Pohorecki et al., 2005).

The general consensus seems to be that a greater liquid viscosity, greater surface tension, and lower liquid density all lead to the production of larger bubbles, although (Pohorecki et al., 2005) observed a slight reduction in bubble size with increasing viscosity and (Zhang et al., 2012a) observed a slight reduction in bubble size with increasing surface tension. There seems to be some disagreement as to whether a greater superficial gas velocity causes the bubble size to increase or decrease. While (Zhang et al., 2012a) observed an increase in bubble size with increasing viscosity in ionic liquids, they found surface tension and liquid density to have the opposite effect on bubble size compared with previous studies.

Other authors have conducted studies in bubble columns without using the correlation in Eq. 2.3.10. For example, (Schäfer et al., 2002) conducted experiments in bubble columns using liquids of viscosity between 0.001-0.04 Pa·s. They found that a greater liquid viscosity, greater surface tension and greater superficial gas velocity all led to the production of larger bubbles, which is in general agreement with the works of the authors presented in Table 2.2.

These studies imply that ionic liquids with lower viscosities, lower surface tensions and higher densities will produce smaller bubbles, which will aid mass transfer. However, the gas-liquid interface of ionic liquids is known to behave very differently to that in common solvents due to the high density of ions (Dong et al., 2010). Additionally, most of these studies focus on liquids with much lower viscosities than most ionic liquids. Therefore, although they give some insight into how the liquid physical properties might affect the bubble size in ionic liquids, they are by no means definitive. This is evident by the fact that (Zhang et al., 2012a) found surface tension and liquid density to have the opposite effect on bubble size in ionic liquids compared with the other studies.

A similar equation to Eqn. 2.3.10 is often used to describe gas holdup, ε:

$$\varepsilon \propto {\mu_L}^A \gamma^B {\rho_L}^C {U_G}^D \tag{2.3.11}$$

The values of the exponents from Eqn. 2.3.11, determined from experiments by other authors, have been summarised in Table 2.3. Although many studies have been undertaken to investigate gas holdup in common solvents, the studies mentioned here have been selected from the literature since they specifically investigated gas holdup in more viscous liquids (>0.01 Pa·s) and can be written in the form shown in Eqn. 2.3.11. A review of other gas holdup studies can be found in (Shah et al., 1982) and (Kantarci et al., 2005).

Table 2.3. Exponential dependences of gas holdup on liquid properties and superficial gas velocity in a bubble column: $\varepsilon \propto {\mu_L}^A \gamma^B {\rho_L}^C {U_G}^D$

Reference	Bubble Regime	Viscosities Studied (Pa·s)	A	B	C	D
(Hikita et al., 1980)	N/A	0.0006-0.017	-0.05	-0.19	-0.19	0.58
(Godbole et al., 1982)	Slug flow	0.001-0.246				0.63
(Haque et al., 1986)	Churn-turbulent		-0.22			0.60
(Kawase and Moo-Young, 1987)	N/A	0.001-0.034				0.67
(Schumpe and Deckwer, 1987)	Slug flow		-0.22	0.13	0.09	0.54
(Vatai and Tekić, 1989)	Slug flow	0.002-0.067				0.53
(Kang et al., 1999)	Bubbly and Churn-turbulent flow	0.001-0.038	-0.20		0.20	0.20
(Mouza et al., 2005)	Bubbly flow	0.001-0.023	-0.13	-1.5	1.6	0.67

The authors presented in Table 2.3 generally agree that gas holdup increases with reducing viscosity and increasing superficial gas velocity. However, there is some disagreement over whether surface tension and density increase or decrease gas holdup. In theory, a lower surface tension should produce smaller bubbles with lower terminal velocities, thus increasing gas holdup (Davidson and Schüler, 1960). However, (Ruzicka et al., 2003) found that a stable homogeneous regime exists for liquid viscosities between 0.001-0.003 Pa·s using aqueous glycerol mixtures, causing gas holdup to be high in this region. (Chaumat et al., 2007) noted that in pure organic liquids the stable homogeneous regime does not exist in this region; it is therefore difficult to predict the liquid parameters that produce the highest gas holdup.

To summarise, none of the aforementioned studies investigated gas holdups in ionic liquids so it is not clear from previous research what the ideal properties of ionic liquids are for producing high gas holdups. It is evident from (Wang et al., 2010a) that the gas holdups they achieved were very low; however, they did not compare them with common solvents under the same conditions. In general, lower viscosity liquids and greater gas flow rates have been found to increase gas holdup, indicating that low viscosity ionic liquids are likely to produce greater gas holdups.

2.3.4. Bubble Size from an Orifice in Viscous Liquids

(Davidson and Schüler, 1960) showed that a different mathematical model is required to model bubbles in viscous liquids compared with inviscid liquids due to their slow formation. It is clear that much of the research done related to bubble size distributions in bubble columns is for low viscosity liquids (<0.1 Pa·s), since most common solvents lie within this range. Due to the lack of literature data on bubble columns using liquids of comparable viscosity to ionic liquids (>0.01 Pa·s), it is necessary to divert the reader's attention towards studies in viscous liquids from a single orifice to examine how liquid properties affect bubble size in highly viscous liquids.

The seminal work of (Davidson and Schüler, 1960) investigated bubble formation in aqueous glycerol mixtures of viscosity between 0.5-1.04 Pa·s. They note that for a constant gas flow rate, viscosity and density of the liquid have a large effect on bubble diameter, whereas the surface tension does not. They found that a greater liquid viscosity, lower liquid density and greater superficial gas velocity all increased bubble size.

(Ramakrishnan et al., 1969, Satyanarayan et al., 1969, Khurana and Kumar, 1969) developed a two-stage model taking into account buoyancy, surface tension, drag, and inertial forces. Experiments were conducted using liquids with viscosities up to 0.552 Pa·s. Although their equation makes it difficult to determine the relative effects of physical properties, they concluded that in highly viscous liquids, the flow rate has to be very small for the surface tension to have an effect. Whilst viscosity was shown to increase the bubble size, it had a much larger influence when the flow rate was high and when the surface tension was low. Since ionic liquids have a low surface tension (~0.03 N/m), viscosity is likely to have a large influence on bubble size.

(Swope, 1971) derived a fifth order equation to determine bubble size from an orifice as a function of fluid and setup properties. This was achieved by balancing the buoyancy and pressure forces with the drag and surface tension forces. However, it is difficult to determine the relative importance of the fluid parameters that affect bubble size from their equation.

(Park et al., 1977) noted that at low flow rates, the bubble size can simply be determined by equating the buoyancy force with the surface tension force. Hence, increasing the surface tension or decreasing the liquid density both act in favour of increasing the bubble size.

(Gaddis and Vogelpohl, 1986) found that the bubble diameter increased with increasing viscosity, surface tension and flow rate and with decreasing liquid density. Their experiments were conducted with liquids of viscosity between 0.001-1 Pa·s.

(Terasaka and Tsuge, 1990) found that the bubble diameter increased with both the liquid viscosity and orifice diameter.

(Jamialahmadi et al., 2001) obtained an equation for bubble diameter based on the Eotvos, Froude and Gallilei numbers in liquids of viscosity between 0.001-0.09 Pa·s. They found that the bubble size increased with increasing surface tension, flow rate, and liquid viscosity and with decreasing liquid density.

(Zhang et al., 2013) investigated the effect of water content and temperature on the bubble size in [C_4mim][BF_4]. Since higher temperatures and water concentrations in the ionic liquid reduced the viscosity, both led to the production of smaller bubbles. They found that the viscosity was the more dominant contributor to the bubble behaviour in the liquid. Additionally, a small amount of water (<10,000 ppm) was shown to decrease the viscosity and density of the ionic liquid, whilst increasing the surface tension.

Table 2.4. Effect of Liquid Properties and Gas Flow Rate on Bubble Size

Reference	Viscosities Studied (Pa·s)	Viscosity	Surface Tension	Density	Flow Rate
(Davidson and Schüler, 1960)	0.5-1.04	↑	↑	↓	↑
(Ramakrishnan et al., 1969, Satyanarayan et al., 1969, Khurana and Kumar, 1969)	0.001-0.552	↑	↑	↓	↑
(Park et al., 1977)	0.005-0.522		↑	↓	
(Gaddis and Vogelpohl, 1986)	0.001-1.0	↑	↑	↓	↑
(Terasaka and Tsuge, 1990)	0.001-1.1	↑			
(Jamialahmadi et al., 2001)	0.001-0.09	↑	↑	↓	↑
(Zhang et al., 2013)	0.0068-0.088	↑	↑	↓	↑

A summary of the effects of the liquid viscosity, surface tension, density, and superficial gas velocity from the aforementioned studies is provided in Table 2.4. The authors presented in Table 2.4 unanimously agree that greater liquid viscosities, greater liquid surface tensions, greater gas flow rates, and lower liquid densities all increase the bubble size from an orifice.

Some of the authors in Table 2.4 have determined correlations for bubble size in the form of Eqn. 2.3.10. The exponents from these correlations have been summarised in Table 2.5:

Table 2.5. Effect of liquid physical properties and superficial gas velocity on bubble diameter from a single orifice: $d \propto \mu_L^A \gamma^B \rho_L^C U_G^D$

Reference	Viscosities Studied (Pa·s)	A	B	C	D
(Davidson and Schüler, 1960)	0.5-1.04	0.25		-0.25	0.25
(Park et al., 1977)	0.005-0.522		0.33	-0.33	
(Zhang et al., 2013)	0.0068-0.088	0.06	0.29	-0.35	0.06

From Table 2.5 and Table 2.4, it is clear that the bubble size from a single orifice increases with increasing liquid viscosity, surface tension and superficial gas velocity and with decreasing liquid density. It appears that density and surface tension have the largest effect on bubble size in viscous liquids. This generally agrees with the correlations obtained for bubble columns. However, the stable gas holdup regime in bubble columns has caused some confusion.

Based on the literature, it appears that the ideal ionic liquid for producing small bubbles is one which has a low viscosity, a low surface tension, and a high density. Since viscosity can vary by several orders of magnitude between ionic liquids while surface tension and density do not, it is likely that viscosity will have the largest effect on bubble size.

2.4. Mass Transfer Coefficients

Knowledge of mass transfer coefficients is vital for designing capture plants and will therefore be determined in this work for ionic liquids. A review of mass transfer coefficients in bubble columns is presented here.

Whitman's two-film theory is the most widely accepted model of mass transfer between a gas and a liquid (Lewis and Whitman, 1924). It states that at a gas-liquid interface, there are two films present – a gas film and a liquid film – each of which possess a finite resistance to mass transfer. A schematic of this is shown in Figure 2.7.

In equation form, the two-film theory can be written as:

$$k_L(c_i - c) = k_G(p - p_i) = N_A \tag{2.4.1}$$

where k_L [m/s] and k_G [mol/m^2/Pa/s] represent the individual liquid- and gas-side mass transfer coefficients respectively, c [mol/m^3] and p [Pa] denote the gas concentration in the bulk liquid phase and gas partial pressure in the bulk gas phase respectively, c_i [mol/m^3] and p_i [Pa] denote the gas concentration and gas partial pressure at the interface, and N_A [mol/m^2/s] is the quantity of gas absorbed per unit time per unit area.

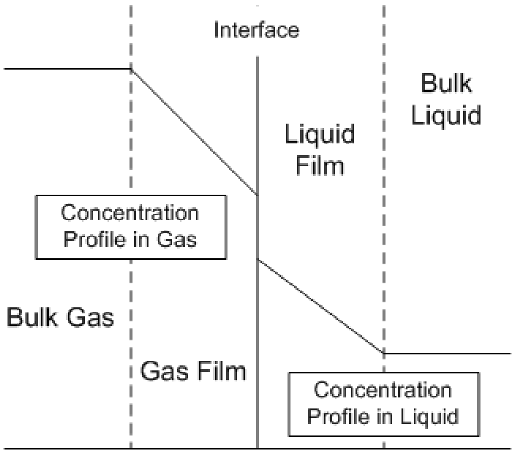

Figure 2.7. Two-film theory schematic

Since the gas partial pressure and concentration at the interface are often unknown, the volumetric liquid- and gas-side mass transfer coefficients, K_La and K_Ga are often used, where:

$$K_L a(c^* - c) = K_G a(p - p^*) = N_A a \qquad (2.4.2)$$

Here, the superscript, *, denotes 'in equilibrium with the other phase' and a [m^2/m^3] is the interfacial area per unit volume. The bracketed parameters in Eqn. 2.4.2 can be thought of as the driving force for mass transfer.

When the solubility of the gas in the liquid is sufficiently low (<0.1 mol/L), the gas-side resistance to mass transfer can be considered negligible (Coulson and Richardson, 1998). When this is the case, the overall liquid-side mass transfer coefficient is approximately equal to the individual liquid-side mass transfer coefficient. i.e. $k_L \sim K_L$. This assumption has been used by many authors for CO_2 absorption in water (Akita and Yoshida, 1973).

Despite the high number of publications regarding ionic liquids, few studies have been undertaken with regard to mass transfer coefficients. (Wang et al., 2010a) carried out simulations to observe mass transfer in [C_4mim][PF_6] in a bubble column. Mass transfer coefficients between $1 \cdot 10^{-5} – 6 \cdot 10^{-5}$ s^{-1} were achieved, although the bubbles were quite large (between 2.5 – 5 cm in diameter). Greater K_La values were obtained at a temperature of 300 K compared with 320 K despite the bubbles having larger diameters. Although the value of k_L was lower at 300 K, the viscosity was higher; hence the bubbles rose more slowly and higher gas holdups and interfacial areas were obtained. This indicates that it is worth studying higher viscosity ionic liquids in bubble columns.

(Galán Sánchez et al., 2011, Zhang et al., 2014) carried out mass transfer coefficient studies on ionic liquids in stirred cell reactors. Galán Sánchez increased the temperature of the ionic liquid, $[C_4mim][BF_4]$, to change the viscosity while (Zhang et al., 2014) added water to the ionic liquids $[C_4mim][NO_3]$ and $[C_4mim][BF_4]$. Both studies found that the individual liquid-side mass transfer coefficient, k_L, increases as viscosity decreases. K_La values of $0.98\cdot10^{-4} – 3.27\cdot10^{-4}$ s^{-1} were achieved by (Galán Sánchez et al., 2011) while k_L values of $0.55\cdot10^{-5} – 2.45\cdot10^{-5}$ m/s were achieved by (Zhang et al., 2014). (Zhang et al., 2014) also compared a 30 wt.% aqueous MEA solution with various MEA-IL-H_2O mixtures. They found that both the mass transfer coefficient and CO_2 diffusion coefficient were greater in the aqueous MEA solution than in the ternary mixtures.

(Zhang et al., 2011) studied mass transfer in $[C_4mim][PF_6]$ in a rotating packed bed. K_La was found to be between 0.01 – 0.04 s^{-1} and increased only slightly with superficial gas velocity. The volumetric mass transfer coefficient was also correlated against the physical properties of the ionic liquid:

$$K_L a \propto \mu^{-0.24} \rho^{-0.10} \gamma^{-0.34} D^{0.5} \tag{2.4.3}$$

Many correlations have been reported in the literature for both the individual liquid-side mass transfer coefficient, k_L, and the volumetric liquid-side mass transfer coefficient, K_La, as a function of fluid and system properties. This section introduces some of these correlations which will later be compared with the correlations produced in this work using ionic liquids.

2.4.1. **Bubble Columns**

Table 2.6 and Table 2.7 present correlations found in the literature for the liquid-side mass transfer coefficient and the overall volumetric liquid side mass transfer coefficient in bubble columns respectively. These tables have been adapted from the works of (Shah et al., 1982, Behkish et al., 2002, Kantarci et al., 2005). The dimensionless numbers are defined in Appendix A: List of Dimensionless Numbers for the reader.

Table 2.6. Review of the correlations for the overall volumetric liquid side mass transfer coefficient in bubble columns

Reference	Correlations	Validity
(Akita and Yoshida, 1973)	$K_L a = \frac{0.6D}{{d_c}^2} Sc^{0.5} Bo^{0.62} Ga^{0.81} \varepsilon^{1.1}$	μ_L: 0.0006 – 0.021 Pa·s
(Hikita et al., 1981)	$K_L a = \frac{14.9g}{U_G} Ca^{1.76} Mo^{-0.248} Sc^{-0.604} \left(\frac{\mu_G}{\mu_L}\right)^{0.243}$	μ_L: 0.001 – 0.011 Pa·s
(Öztürk et al., 1987)	$K_L a = \frac{D}{d^2} 0.62 \cdot Sc^{0.5} Bo^{0.33} Ga^{0.29} Fr^{0.68} \left(\frac{\rho_G}{\rho_L}\right)^{0.04}$	μ_L: 0.0003 – 0.02 Pa·s
(Kawase et al., 1987)	$K_L a = \frac{0.45D}{{d_c}^2} Sc^{0.5} Re^{0.75} Bo^{0.60} Fr^{0.12}$	Non-Newtonian fluids
(Kang et al., 1999)	$K_L a = 0.00083 d_c Re^{0.254}$	μ_L: 0.001 – 0.038

It is clear from these tables that even the studies that have been undertaken in higher viscosity liquids, e.g. (Calderbank and Moo-Young, 1961, Kang et al., 1999), have only investigated viscosities as high as the least viscous ionic liquids. The main reason for this is because most industrial processes use liquids of low viscosity (e.g. water scrubbing). It is therefore most likely that none of these correlations will be suitable for use with ionic liquids. However, it is still useful to review them to provide some insight into the effects of fluid properties on mass transfer.

Table 2.7. Review of the correlations for the individual liquid-side mass transfer coefficient in bubble columns

Reference	Correlation	Validity
(Frössling, 1938)	$k_L = \frac{D}{d}\left(2.0 + 0.552 \cdot Re^{1/2} Sc^{1/3}\right)$	d: < 0.15 mm
(Calderbank and Moo-Young, 1961)	$k_L = 0.42 \left(\frac{\mu_L}{\rho_L D}\right)^{-0.5} \left(\frac{(\rho_L - \rho_G)\mu_L g}{{\rho_L}^2}\right)^{0.33}$	d: > 2.5 mm μ_L: 0.0006 – 0.09 Pa·s
(Calderbank and Moo-Young, 1961)	$k_L = 0.31 \left(\frac{\mu_L}{\rho_L D}\right)^{-0.67} \left(\frac{(\rho_L - \rho_G)\mu_L g}{{\rho_L}^2}\right)^{0.33}$	d: < 2.5 mm μ_L: 0.0008 – 0.001 Pa·s

Reference	Correlation	Validity
(Hughmark, 1967)	$k_L = \frac{D}{d}\left(2.0 + 0.0187\left((Re^{0.484}Sc^{0.339})\left(\frac{dg^{0.33}}{D^{0.67}}\right)^{0.072}\right)^{1.61}\right)$	μ_L: 0.009 – 0.152 Pa·s
(Oellrich et al., 1973)	$k_L = \frac{D}{d}\left(1 + (1 + 0.564 \cdot Pe^{2/3})^{3/4}\right)$	Valid for all Pe
(Sherwood et al., 1975)	$k_L = \frac{D}{d} \cdot Pe^{1/3}$	d: < 1 mm
(Akita and Yoshida, 1974)Akita and Yoshida (1974)	$k_L = \frac{D}{d} 0.5 \cdot Sc^{0.5} Ga^{0.25} Bo^{0.38}$	μ_L: 0.0006 – 0.02 Pa·s
(Schumpe and Deckwer, 1982)	$k_L = 0.0545 {U_G}^{0.08} {\mu_L}^{-0.32}$	Non-Newtonian fluids
(Öztürk et al., 1987)	$k_L = \frac{D}{d} 0.62 \cdot Sc^{0.5} Bo^{0.33} Ga^{0.29} Fr^{0.68} \left(\frac{\rho_G}{\rho_L}\right)^{0.04}$	d: ~ 3 mm μ_L: 0.0003 – 0.02 Pa·s

Many authors choose to correlate these parameters as functions of dimensionless numbers for simplicity; however, there does not seem to be any agreement between the dimensionless numbers used by different authors. Therefore, the equations will be re-written in the form:

$$
\begin{gathered}
K_L a \propto \mu^A \gamma^B \rho^C D^D \\
k_L a \propto \mu^A \gamma^B \rho^C D^D
\end{gathered}
\tag{2.4.4}
$$

The values of the exponents are presented in

Table 2.8 and Table 2.9. This should provide some indication into how the liquid properties affect the rate of mass transfer in ionic liquids.

Table 2.8. Exponential dependence of k_L on liquid properties and gas flow rate

Reference	Viscosity	Surface tension	Density	Diffusivity	Flow rate
(Calderbank and Moo-Young, 1961)	-0.17		0.17	0.5	
(Calderbank and Moo-Young, 1961)	-0.34		0.34	0.67	
(Sherwood et al., 1975)				0.67	0.33
(Akita and Yoshida, 1974)		-0.38	0.38	0.5	
(Schumpe and Deckwer, 1982)	-0.32				0.08
(Öztürk et al., 1987)	-0.08	-0.33	0.37	0.5	0.68

Table 2.9. Exponential dependence of K_La on liquid properties and gas flow rate

Reference	Viscosity	Surface tension	Density	Diffusivity	Flow rate
(Akita and Yoshida, 1973)	-0.12	-0.62	-0.5	0.5	
(Hikita et al., 1981)	-0.08	-1.02	0.85	0.6	0.76
(Öztürk et al., 1987)	-0.08	-0.33	0.37	0.5	0.68
(Kawase et al., 1987)	-0.25	-0.6	0.85	0.5	0.99
(Kang et al., 1999)	-0.25		0.25		0.25

Table 2.8 and Table 2.9 suggest that the mass transfer coefficients increase with:

- Decreasing liquid viscosity
- Decreasing gas-liquid surface tension
- Increasing density
- Increasing diffusivity
- Increasing flow rate

Moreover, it suggests that surface tension, gas diffusivity, and flow rate are the more dominant contributors to the mass transfer coefficient, followed by liquid density, then by the liquid viscosity. While ionic liquids generally have a low surface tension, which should increase the mass transfer coefficient, they have high viscosities and low diffusivities, which are both detrimental for mass transfer. Additionally, viscosity can vary by a few orders of magnitude between ionic liquids while surface tension and density do not. Therefore, viscosity is likely to have the largest effect on mass transfer coefficient in ionic liquids.

Since diffusivity is important, it is necessary to compare the diffusivities of CO_2 in aqueous MEA and ionic liquids. Bishnoi and Rochelle reported a diffusivity of CO_2 in aqueous MEA of about $1.9 \cdot 10^{-9}$ m^2/s. Comparatively, the diffusion coefficient of CO_2 in ionic liquids is typically between $1 \cdot 10^{-11}$ - $1 \cdot 10^{-10}$ m^2/s (Hou and Baltus, 2007, Shiflett and Yokozeki, 2005, Morgan et al., 2005, Ferguson and Scovazzo, 2007).

From the above literature review, it seems that the less viscous ionic liquids would be the most suitable for CO_2 capture. There are numerous reasons for this:

- Decreasing liquid viscosity increases the mass transfer coefficient
- Decreasing liquid viscosity leads to higher diffusivities, further increasing the mass transfer coefficient
- Less viscous liquids produce smaller bubbles, providing higher interfacial areas and gas holdups in a bubble column

(Wang et al., 2010a) produced the only study to date on the mass transfer coefficient of CO_2 in an ionic liquid in a bubble column. The ionic liquid used was $[C_4mim][PF_6]$, which has a viscosity of 0.0885 Pa·s. The highest mass transfer coefficient achieved was 0.000015 s^{-1}, which occurred at a column height of 12 cm and a superficial gas velocity of using 0.001 m/s. However, the bubbles in their experiments were produced from relatively large nozzles and thus had fairly large diameters (~3 mm).

In this work, experiments will be conducted using microbubbles in order to try to increase the rate of CO_2 absorption into the ionic liquid.

2.5. Summary

Biogas upgrading is proving to be an attractive form of renewable energy and few studies have been conducted to upgrade biogas using ionic liquids.

Regeneration of MEA solutions is very energy intensive, particularly due to the large sensible heat requirement. Direct Contact Regeneration (DCR) is a novel idea that has never been investigated before and could possibly regenerate solvents with a reduction in the amount of energy transferred as sensible heat.

It is clear that despite there being a lot of interest in ionic liquids, there is very little data regarding bubble size, gas holdups and mass transfer in ionic liquids. While MEA solutions appears to have better absorption capabilities than many ionic liquids and higher CO_2 diffusion coefficients, mass transfer in ionic liquids may still be fast if microbubbles can be made in them. It is therefore important to determine the properties of ionic liquids that produce the smallest bubbles.

3. Experimental Apparatus and Techniques

In this chapter, details of the materials, experimental setups, apparatus, methods, and procedures are presented.

3.1. Liquids and Gases

In order to determine how the physical properties of liquids affect bubble size in bubble columns, ten ionic liquids were obtained along with deionised water and glycerol.

For examining the feasibility of using ionic liquids for biogas upgrading, seven of the ten ionic liquids were selected and compared with a 30 wt.% aqueous MEA solution – a common chemical solvent for biogas upgrading. An artificial biogas mixture was used to simulate the flow of biogas into the column.

The physical properties of these liquids and gases are provided in this section.

3.1.1. Ionic Liquids and their Properties

In this work, several imidazolium- and phosphonium-based room temperature ionic liquids will be studied in order to determine how the physical properties of ionic liquids affect bubble size. The following ionic liquids, obtained from Rebecca Taylor, Queen's University Belfast, were selected due to their wide range of physical properties:

- 1-Ethyl-3-methylimidazolium dicyanamide ($[C_2mim][DCA]$)
- 1-Ethyl-3-methylimidazolium bis(trifluoromethylsulfonyl)imide ($[C_2mim][NTf_2]$)
- 1-Butyl-3-methylimidazolium bis(trifluoromethylsulfonyl)imide ($[C_4mim][NTf_2]$)
- 1-Butyl-3-methylimidazolium trifluoroacetate ($[C_4mim][TFA]$)
- 1-Ethyl-3-methylimidazolium ethyl sulfate ($[C_2mim][EtSO_4]$)
- Trihexyl(tetradecyl)phosphonium bis(trifluoromethylsulfonyl)imide ($[P_{66614}][NTf_2]$)
- Trihexyl(tetradecyl)phosphonium dicyanamide ($[P_{66614}][DCA]$)
- Trihexyl(tetradecyl) phosphonium decanoate ($[P_{66614}][C_{10}H_{19}O_2]$)
- Tetradecyl(trihexyl) phosphonium chloride ($[P_{66614}][Cl]$)
- Tetradecyl(trihexyl) phosphonium bromide ($[P_{66614}][Br]$)

The latter four ionic liquids are known to have purities of 96.5%, 94%, 97.7%, and 96.7% respectively, measured by Phosphorus-31 NMR spectroscopy.

Molecular drawings of these ionic liquids are presented in Figure 3.1 for the interested reader.

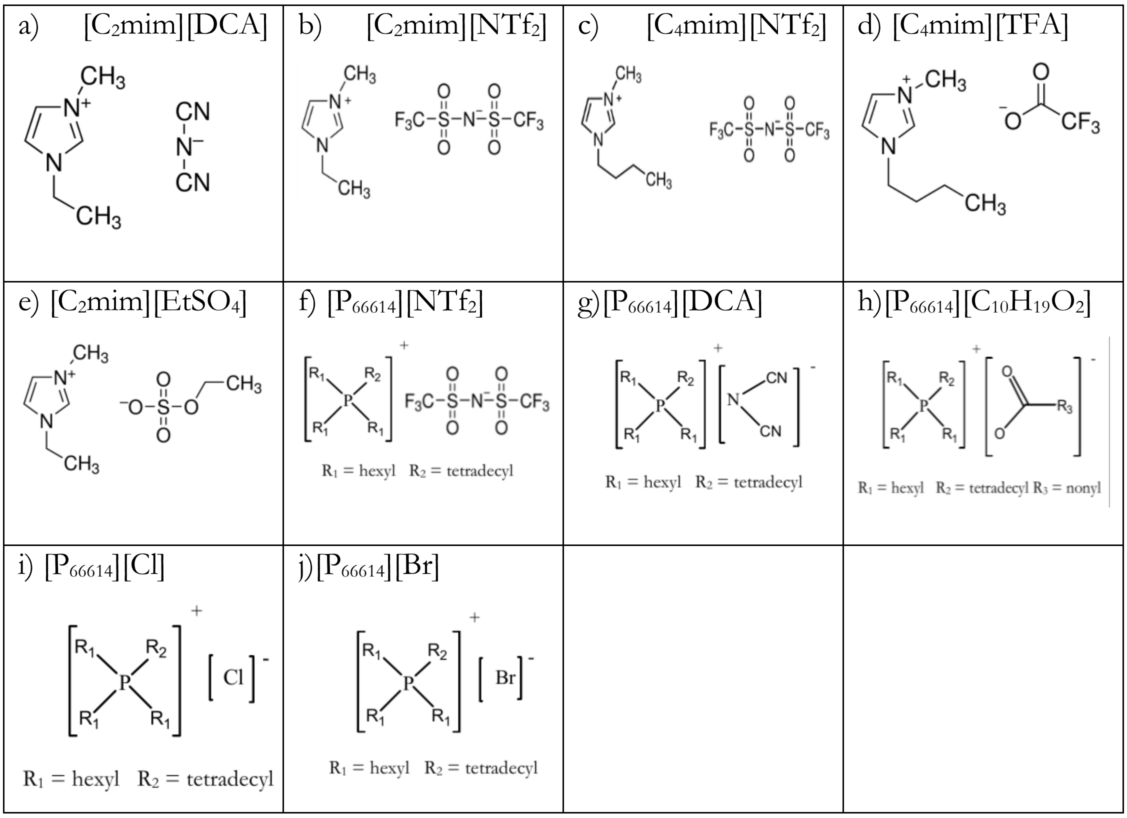

Figure 3.1. Molecular drawings of the ionic liquids used in this work

In order to determine how the physical properties of ionic liquids affect bubble size and mass transfer rates, the densities, viscosities, surface tensions, and molecular weights of the aforementioned ionic liquids have been tabulated in Table 3.1 with relevant citations.

Table 3.1. Physical properties of the ionic liquids used in this work

Solvent	**Viscosity, μ [Pa·s]**	**Surface tension, γ [N/m]**	**Density, ρ [kg/m^3]**	**Molecular weight [g/mol]**
[C$_2$mim][DCA]	0.0159 [a] 20	0.060 [j] 25	1095.3 [a] 20	177.21
[C$_2$mim][NTf$_2$]	0.0325 [a] 20	0.0369 [k] 20	1515.4 [a] 20	391.39
[C$_4$mim][NTf$_2$]	0.0520 [b] 20	0.0336 [k] 20	1440 [o] 20	419.36
[C$_4$mim][TFA]	0.0530 [c] 30	0.0347 [l] 25	1220 [c] 25	252.23
[C$_2$mim][EtSO$_4$]	0.120 [d]	0.047 [d]	1241 [d]	236.29
[P$_{66614}$][NTf$_2$]	0.165 [b] 20	0.0301 [m] 25	1064 [p] 25	764.01

Solvent	**Viscosity, μ [Pa·s]**	**Surface tension, γ [N/m]**	**Density, ρ [kg/m³]**	**Molecular weight [g/mol]**
$[P_{66614}][DCA]$	0.280 [e] 25	0.0323 [m] 25	898.5 [e] 25	549.9
$[P_{66614}][C_{10}H_{19}O_2]$	0.319 [f] 25	0.029 [m] 25	887.9 [f] 25	655.11
$[P_{66614}][Cl]$	1.82 [g] 25	0.0306 [m] 25	881.9 [g] 25	519.31
$[P_{66614}][Br]$	2.09 [h] 25	0.0309 [m] 25	954.6 [h] 25	563.76
30 wt.% MEA	0.0021 [i] 30	0.0615 [n] 25	1003	

(*data from (Gallagher et al., 2014) [a], (Zhang et al., 2006) [b], (Palgunadi et al., 2010) [c], (Kaji et al., 2009) [d], (Cytec, 2008d) [e], (Cytec, 2008c) [f], (Cytec, 2008b) [g], (Cytec, 2008a) [h], (Li and Lie, 1994) [i], (Klomfar et al., 2011) [j], (Carvalho et al., 2008) [k], (Restolho et al., 2009a) [l], (Almeida et al., 2013) [m], (Vazquez et al., 1997) [n], (Sigma-Aldrich, 2012a) [o], (Fraser and MacFarlane, 2009) [p])

It is clear from Table 3.1 that, of the three physical parameters compared, the most significant difference between 30 wt. % aqueous MEA and ionic liquids is the viscosity; while the density of the aforementioned ionic liquids differs from that of the MEA solution by ±51% and the surface tension is up to 53% lower than that of the MEA solution, the viscosity of the ionic liquids is up to three orders of magnitude greater. Additionally, other authors (Kaji et al., 2009, Lange et al., 2013) have recommended using low viscosity ionic liquids in order to produce smaller bubbles. For these reasons, the effect of viscosity will be largely the focus in this work.

Of the aforementioned ionic liquids, $[C_2mim][DCA]$, $[C_2mim][NTf_2]$, $[C_4mim][NTf_2]$, $[C_4mim][TFA]$, $[C_2mim][EtSO_4]$, $[P_{66614}][NTf_2]$, and $[P_{66614}][Cl]$ will be compared with a 30 wt.% aqueous MEA solution for biogas upgrading. In order to determine the effects of fluid parameters on the rate of CO_2 absorption in ionic liquids, the CO_2 solubility and diffusivity in these ionic liquids is provided in Table 3.2.

Table 3.2. CO_2 solubility, diffusion coefficient, enthalpy of absorption, and cost of ionic liquids and 30 wt.% aqueous MEA (Numbered index represents temperature in °C)

Solvent	**CO_2 Solubility [mol/L-solvent]**	**CO_2 Solubility [g-CO_2/g-solvent]**	**CO_2 Diffusivity, D $\cdot 10^9$ [m^2/s]**	**Enthalpy of Absorption of CO_2 [kJ/mol]**	**Cost (£/g)**
[C_2mim][DCA]	0.076 [a]^{40}	0.00261 [a]^{40}			1.59 (>95% NMR) [l]
[C_2mim][NTf_2]	0.108 [a]^{25}	0.00312 [a]^{25}	0.660 [f]^{30}	14.2 [i]	0.97 (>98% NMR) [l]
[C_4mim][NTf_2]	0.107 [a]^{25}	0.00328 [a]^{25}	0.851 [g]^{30}	12.0 [g]	1.06 (>98% NMR) [l]
[C_4mim][TFA]	0.101 [b]^{25}	0.00365 [b]^{25}			12.40 (>97% NMR) [l]
[C_2mim][$EtSO_4$]	0.055 [c]^{30}	0.00195 [c]^{30}	2.190 [c]^{30}	10.5 [j]	0.22 (>95% NMR) [l]
[P_{66614}][NTf_2]	0.075 [a]^{25}	0.00311 [a]^{25}			4.16 (>95% NMR) [m]
[P_{66614}][Cl]	0.049 [d]^{30}	0.00245 [d]^{30}	0.220 [f]^{30}		1.30 (>95% NMR) [m]
30 wt.% MEA	3.42 [e]^{25}	0.15 [e]^{25}	1.95 [h]^{25}	85 [k]	0.04 (>98%) [n]

(*data from (Bara et al., 2009) [a], (Yokozeki et al., 2008) [b], (Jalili et al., 2010) [c], (Ferguson and Scovazzo, 2007) [d], (Jou et al., 2009) [e], (Morgan et al., 2005) [f], (Hou and Baltus, 2007) [g], (Bishnoi and Rochelle, 2000) [h], (Cadena et al., 2004) [i], (Xie et al., 2014) [j], (Kim and Svendsen [k]), (Sigma Aldrich, 2015a) [l], (Sigma Aldrich, 2015b) [m], (Sigma Aldrich, 2015c [n]))

Since the CO_2 diffusivity in [C_2mim][DCA] and [C_4mim][TFA] have not previously been studied, they were estimated from the correlation obtained by (Hou and Baltus, 2007):

$$D = 6.7 \cdot 10^{-5} \cdot \mu^{-0.66} M^{-0.89} \rho^{4.8} T^{-3.3} \qquad (3.1.1)$$

where D is the diffusion coefficient of CO_2 in the ionic liquid, μ, M, and ϱ, are the viscosity, molecular weight, and density of the ionic liquid respectively, and T is the temperature in Kelvin. This equation used data from similar imidazolium based ionic liquids ([C_4mim][NTf_2], [C_4mim][BF_4]) and was also shown to agree with diffusivity data for [C_2mim][NTf_2] produced by (Camper et al., 2006). One would expect the diffusivity to be inversely proportional to the molar volume (and therefore proportional to liquid density) since it would be more difficult for the gas to diffuse through the liquid if the space between the molecules is larger. However Eqn 3.1.1 implies a power relationship between diffusivity and liquid density. Although this seems strange, the equation agrees with 24 data points from four different imidazolium-based ionic liquids to with 15% of the experimental values.

Similarly, the CO_2 diffusivity in $[P_{66614}][NTf_2]$ was estimated from the correlation obtained by (Morgan et al., 2005):

$$D = 3.7 \cdot 10^{-3} \cdot {\mu_L}^{-0.59} {M_L}^{-1.0} {\rho_L}^{1.0} {\rho_G}^{-2.0} \tag{3.1.2}$$

This equation was used as it was made using data from both imidazolium- and phosphonium-based ionic liquids.

In order to upgrade biogas, it is also important to use a solvent that does not absorb a lot of methane. Therefore, the CO_2/CH_4 selectivity of these ionic liquids are compared with a 30 wt.% aqueous MEA solution in Table 3.3.

Table 3.3. CO_2/CH_4 Selectivity in ionic liquids and 30 wt.% aqueous MEA

Solvent	**CO_2 Solubility [mol/L]**	**CH_4 Solubility [mol/L]**	**CO_2/CH_4 Selectivity**
$[C_2mim][DCA]$	0.076 [a]	0.004 [a]	21.2
$[C_2mim][NTf_2]$	0.108 [a]	0.007 [a]	15.4
$[C_4mim][NTf_2]$	0.107 [a]	0.002 [a]	50.5
$[C_2mim][EtSO_4]$	0.055 [b] 30		25.5 [g]
$[P_{66614}][Cl]$	0.049 [c]	<0.01 [e] 30	>4.9
30 wt.% MEA	3.42 [d]	0.0015 [f] 25	102

(*data from (Bara et al., 2009) [a], (Jalili et al., 2010) [b], (Ferguson and Scovazzo, 2007) [c], (Jou et al., 2009) [d], (Morgan et al., 2005) [e], (Carroll et al., 1998) [f] – for 18.3 wt.% solution, (Bermejo et al., 2013) [g] at 5 bar)

It appears that aqueous MEA has a higher CO_2 capacity, lower diffusion coefficient and higher CO_2/CH_4 selectivity than the ionic liquids used in this work and so will probably have a higher rate of mass transfer. However, as mentioned previously, it requires a lot of energy to regenerate.

3.1.2. Aqueous Glycerol Mixtures

Aqueous glycerol mixtures were obtained by mixing glycerol, obtained from Sigma-Aldrich (>99.5 % purity) with de-ionised water, obtained from the Department of Chemical and Biological Engineering, University of Sheffield.

The viscosity of the glycerol-water mixtures, μ_m, were calculated using the empirical formula of (Cheng, 2008), which has an error of ±8.5%:

$$\mu_m = \mu_w{}^{\alpha} \cdot \mu_g{}^{(1-\alpha)} \tag{3.1.3}$$

where μ_w and μ_g are the respective viscosities of water and glycerol (equal to 0.001 Pa·s and 1.412 Pa·s respectively) and α is a variable given by:

$$\alpha = 1 - c_g + \frac{a \cdot b \cdot c_g \cdot (1 - c_g)}{a \cdot c_g + b \cdot (1 - c_g)} \tag{3.1.4}$$

In Eqn. 3.1.4, c_g represents the mass concentration of glycerol and a and b are temperature dependent variables given by:

$$\begin{gathered} a = 0.705 - 0.0017 \cdot T \\ b = 4.9 + 0.36 \cdot T \cdot a^{2.5} \end{gathered} \tag{3.1.5}$$

where T is the temperature in °C.

The density of the mixture, ρ_m, was approximated using a weighted average of the mass concentrations of water and glycerol:

$$\rho_m = \rho_g c_g + \rho_w \cdot (1 - c_g) \tag{3.1.6}$$

where ρ_g and ρ_w represent the densities of glycerol and water respectively (equal to 1260 kg/m^3 and 1000 kg/m^3 respectively) in accordance with (Cheng, 2008). This equation has an error of ±0.8%.

The surface tensions of the mixtures were calculated using the formula of (Khossravi and Connors, 1993):

$$\gamma_m = \gamma_w + (\gamma_g - \gamma_w) \cdot 11.35 \cdot \frac{c_g/M_g}{(1 - c_g)/M_w + 11.35 \cdot c_g/M_g} \tag{3.1.7}$$

where γ_m, γ_w, and γ_g represent the surface tensions of the mixture, water and glycerol respectively; and M_w and M_g are the molecular weights of water and glycerol, equal to 92.09 g/mol and 18.02 g/mol respectively. The surface tensions of water and glycerol are 0.072 and 0.064 N/m respectively. Eqn. 3.1.7 is known to have a standard deviation of 0.0001 N/m.

3.1.3. **30 wt.% Aqueous MEA**

30 wt. % aqueous monoethanolamine (MEA) was made gravimetrically using MEA obtained from Sigma-Aldrich (>98% purity) and de-ionised water, obtained from the Kroto Research Institute, University of Sheffield. In order to minimise CO_2 uptake into the MEA solution from the atmosphere, a new mixture was made for each experiment.

Physical properties of MEA, deionised water, and a 30 wt.% aqueous MEA solution are provided in Table 3.4:

Table 3.4. Properties of MEA, deionised water, and 30 wt.% aqueous MEA

Liquid	Density, ρ [kg/m^3]	Viscosity, μ [Pa·s]	Surface Tension [N/m]
MEA	1012 [a]	0.015 [b]	48.95 [c]
Deionised water	1000	0.001	0.072
30 wt.% MEA	1003	0.0021 [b]	0.0604 [c]

(*data from (Sigma-Aldrich, 2012c) [a], (Li and Lie, 1994) [b], (Vazquez et al., 1997) [c])

The density of the 30 wt.% MEA solution was estimated using a volume-weighted average approach.

3.1.4. **Gases**

The gases used in this work were compressed air, nitrogen and an artificial biogas mixture containing 60 vol.% CH_4 and 40 vol.% CO_2. The biogas mixture and nitrogen were obtained from The BOC Group and had purities >99%. The densities of these gases were calculated using the ideal gas law:

$$\rho = \frac{PM}{R_g T} \tag{3.1.8}$$

where P is the pressure of the gas, M is the molecular weight of the gas, R_g represents the universal gas constant (8.3145 J/mol/K), and T denotes the gas temperature in Kelvin. The molecular weights of air, nitrogen, CH_4 and CO_2 are 28.97, 28.01, 16.04, and 44.01 g/mol respectively.

Any impurities present in the gas stream, in particular water vapour' can significantly alter the physical properties of the ionic liquid upon sparging. The moisture content in the nitrogen cylinder used in this work was less than 3 ppm (BOC Gases, 2015).

In the case of the biogas mixture, a volume-weighted average was used to calculate the mixture density:

$$\rho_m = \rho_{CO2}V_{CO2} + \rho_{CH4}V_{CH4} \tag{3.1.9}$$

3.2. Gas Flow Rates

In the bubble sizing experiments, the following gas flow rates were used to determine how flow rate affects bubble size: 3, 5, 7, 10, 15, 20, 30, 50, 80 mL/min. However, in cases where the liquid foamed, only the lower flow rates were studied. For bubble sizing experiments using aqueous glycerol mixtures, a gas flow rate of 3 mL/min was used since the mixture produced a foam above this flow rate.

A flow rate of 10 mL/min was used for biogas upgrading experiments with different ionic liquids. In addition to this, flow rates of 5, 15, and 20 mL/min were used to determine the effect of flow rate on mass transfer coefficients.

3.3. Overview of Experimental Setups

In this section, overviews of the setup used for the frequency study (Section 3.3.1), bubble sizing experiments (Section 3.3.2) and biogas upgrading experiments (Section 3.3.3) are presented. Descriptions of the apparatus used in these setups are described in Section 3.4.

3.3.1. Frequency Study

The experimental setup presented in Figure 3.2 was used to study the effect of pressure oscillation frequency on mean bubble size from an orifice in ionic liquids; the results of which are presented in Section 6.1. The experimental setup was designed by Pratik Desai, University of Sheffield, and the frequency has been shown to significantly affect the bubble size in inviscid liquids, such as ethanol and water (Desai, 2014).

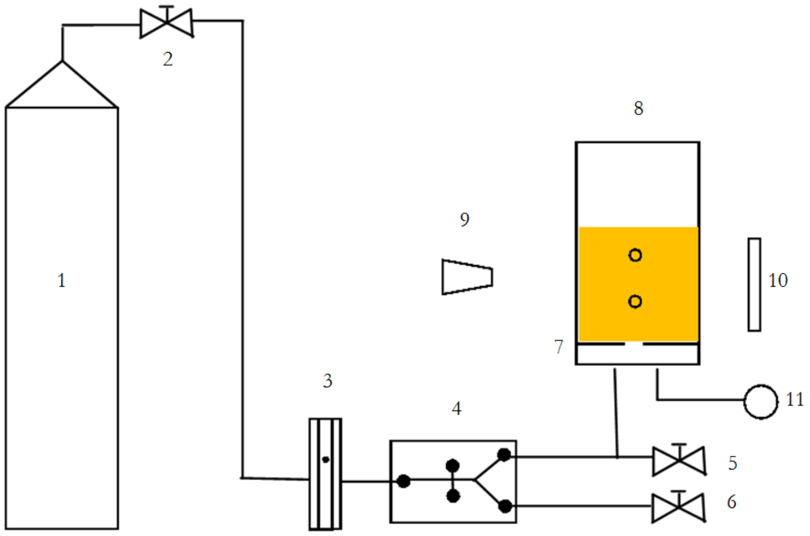

Figure 3.2. Schematic of the setup used during bubble sizing experiments from an orifice: 1 – compressed air; 2 – pressure regulator; 3 - rotameter; 4 - fluidic oscillator; 5 & 6 bleed valves; 7 – orifice; 8 – bubble column; 9 – camera; 10 – LED light source; 11 – pressure transducer

In this experimental setup, compressed air (1), was passed into a fluidic oscillator (4) at a flow rate of 85 LPM. The flow rate was controlled by a pressured regulator (2) and measured using a rotameter (3). From the fluidic oscillator, the air was passed into a bubble column (8) via an orifice of diameter 30 µm (7), measured by Pratik Desai under a microscope. The frequency of the air pressure at the orifice inlet was varied by changing the length of the feedback loop on the fluidic oscillator (see Section 3.4.1) while the amount of air going into the bubble column was controlled using bleed valves (5&6). Images of the bubbles were captured using a high speed camera (9) and an LED light source (10). For each different length of feedback loop, the oscillation frequency was measured using a pressure transducer (11), located inside the chamber of the bubble column.

Ideally, it would have been more useful to measure the pressure directly inside the bubble, however due to the size of the orifice this was not possible. It was therefore decided to measure the pressure at a location as close to the bubble as was reasonably practical, which was in the chamber underneath the orifice. Since the orifice diameter was so small, it is likely that the pressure oscillation would have been partially damped before reaching the bubble and therefore the measured frequency of oscillation cannot be assumed equal to that inside the bubble. However since P. Desai found the fluidic oscillator to significantly affect bubble size using the same setup, albeit with less viscous liquids, it is known that the pressure oscillation is not completely damped by this orifice.

3.3.2. Bubble Sizing Experimental Setup

An overview of the experimental setups used for the bubble sizing experiments and the biogas upgrading experiments is presented in Figure 3.3. The results of these experiments are provided in Section 6.2 and Sections 7.3 respectively.

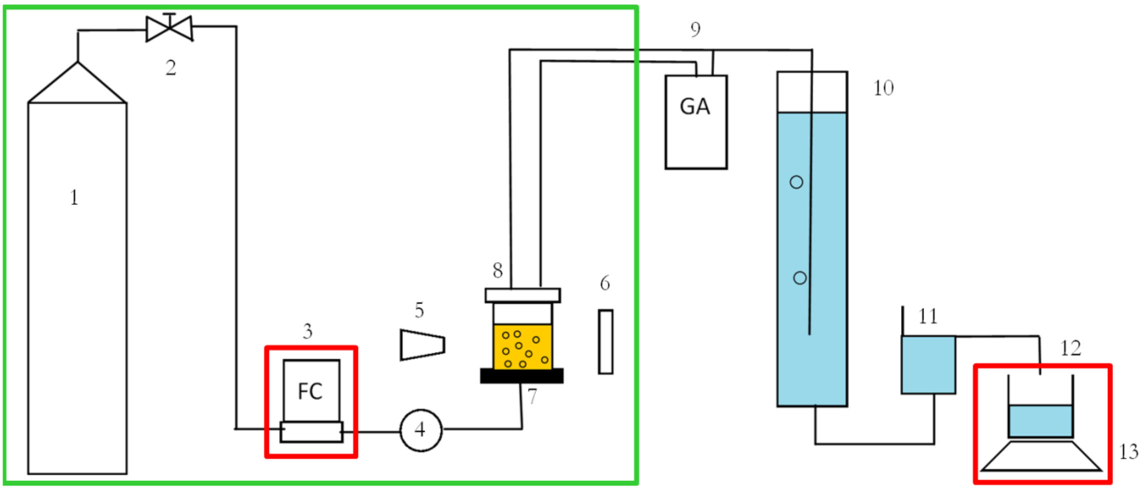

Figure 3.3. Overview of Experimental Setup: 1 – Compressed gas, 2 – pressure regulator, 3 – mass flow controller, 4 – pressure gauge, 5 – camera, 6 – LED light source, 7 – diffuser, 8 – bubble column, 9 – gas analyser, 10 – biogas collector, 11 – pressure equalisation column, 12 – beaker, 13 – mass balance

For the bubble sizing experiments, only the components inside the green box (numbered 1-8) were used and the gas used was compressed nitrogen. Using a pressure regulator (2), the compressed nitrogen (1) was fed into a flow controller (3) at a pressure of 2.0 bar and the desired flow rate was set on a computer. From the flow controller, nitrogen was passed into a bubble column (8) via a ceramic diffuser (7). Once the pressure in the diffuser plenum stabilised (measured using a pressure gauge (4)), images of the bubbles were taken using a high speed camera (5). An LED light source (6) was used to provide enough light into the camera so that the exposure time could be reduced to 0.1 ms to produce clear images.

3.3.3. Biogas Upgrading Experiments

3.3.3.1. Preliminary Experiments

For the preliminary biogas upgrading experiments, the setup presented in Figure 3.3 was used; however, the mass flow controller (3), beaker (12), and mass balance (13) were not part of the setup. The results of the preliminary experiments are presented in Section 7. 1.

In this setup, an artificial biogas mixture containing 60 vol.% methane and 40 vol.% CO_2 (1) was passed into the bubble column (8) via a ceramic diffuser (7). A pressure regulator (2) and pressure gauge (4) were used to control and measure the pressure at the inlet to the bubble column. Images of the bubbles were captured using a high speed camera (5) and a light source (6). The CH_4 and CO_2 concentrations at the outlet of the column were measured using a GasData GFM416 infra-red (IR) gas analyser (9). From the analyser, the off-gas from the bubble column was bubbled into a biogas collector column (10), displacing deionised water into a pressure equalisation column (11).

3.3.3.2. *Refined Experiments*

In the refined biogas upgrading experiments, the results of which are presented in Sections 7.2-7.8, all of the components shown in Figure 3.3 were used. The mass flow controller (3) and mass balance (13) were incorporated into the setup to improve the accuracy and repeatability of the experiment. The incorporation of these pieces of equipment allowed measurement of the flow rates both into and out of the bubble column, allowing both CO_2 and CH_4 uptake in the ionic liquids to be calculated.

3.4. Experimental Apparatus

Details of the experimental apparatus used in this work, as shown schematically in Section 3.3, are presented in this section.

3.4.1. **Fluidic Oscillator**

There are a few methods of generating microbubbles in liquids. In this work, a fluidic oscillator was used due to the array of the expertise in the research group and the advantage that it contains no moving parts.

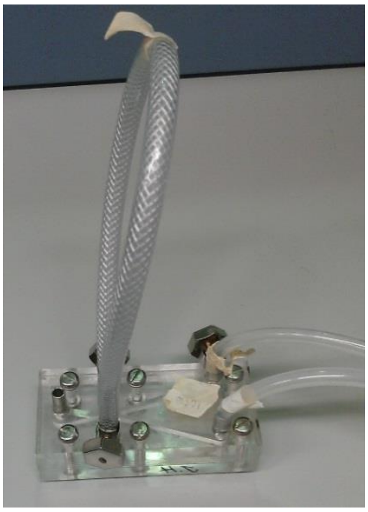

Figure 3.4. A photograph of the fluidic oscillator used in this work

A photograph of the fluidic oscillator used in this work is presented in Figure 3.4. When in operation, the control ports are connected using a Spiropolous-type feedback loop, whose length can be varied to change the frequency of oscillation.

The fluidic oscillator consists of four PMMA plates of thickness 2 mm, sandwiched between two solid plates with holes drilled for the inlet (S), outlets (Y1 and Y2) and control ports (X1 and X2). A 2D CAD drawing showing the inside of a fluidic oscillator is depicted in Figure 3.5 with major dimensions labelled.

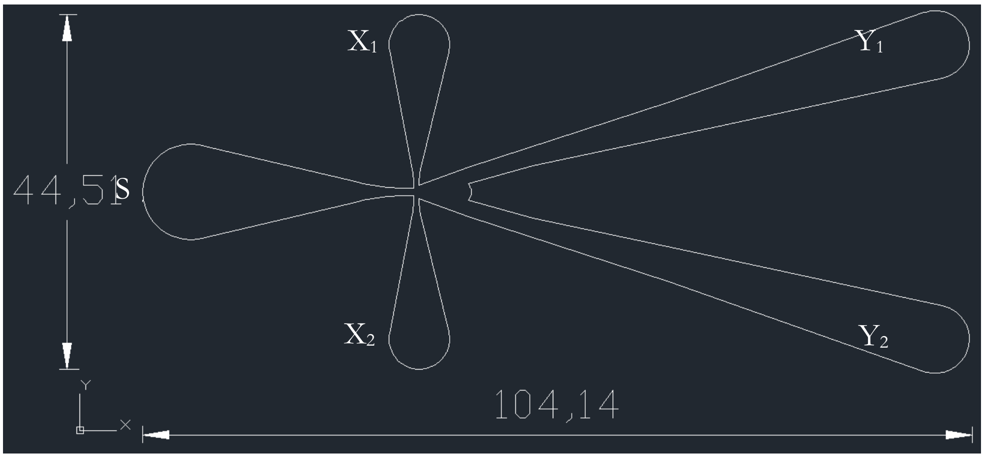

Figure 3.5. A 2D schematic of the fluidic oscillator used in this work (dimensions in mm)

3.4.2. Pressure Transducer

The frequency of oscillation was measured using an Impress IMP-G1000 pressure transducer, a photograph of which is shown in Figure 3.6.

Figure 3.6. Photograph of Impress IMP-G1000 pressure transducer

This transducer has a range of 0-1 bar (gauge pressure), an accuracy of ±250 Pa and a response time of 1 ms. A LabView program, written by Pratik Desai, took a 30 s sample of the output signal from the transducer and performed a Finite Fourier Transform on the signal in order to determine the frequency. The measured frequency was compared with that measured by an accelerometer which had an independently written source code. The difference in frequency between these two measurements was less than 1 Hz. This is clearly an error in the measurement device and confirms that the source code used in this work is correct.

3.4.3. **Mass Flow Controller**

The gas flow rate was controlled using a Bronkhorst EL-Flow controller with a range of 0-200 mL/min and an accuracy of ±0.2 mL/min ±0.5% reading. The flow controller contains a normally closed solenoid valve which is opened when activated and adjusted until the desired flow rate is reached.

Figure 3.7. Bronkhorst flow controller used in this work

It operates by heating the gas inside a tube and measuring the change in temperature of the gas, from which the mass flow rate can be calculated.

3.4.4. **Bubble Columns**

3.4.4.1. Preliminary Experiments

Figure 3.8 shows a photograph of the bubble column and diffuser used in preliminary experiments. The inner dimensions of this bubble column are 5.6 cm x 5.6 cm x 15 cm.

The diffuser, made of alumina, obtained from Point Four Inc., is square in cross section with a side length of 5.2 cm and a thickness of 1.0 cm (see Section 3.4.5). It was glued with an epoxy resin into a housing made of type-304 stainless steel; this material was chosen due to its resistance to MEA (Kohl and Nielsen, 1997). The walls of the column were made of clear, flat PMMA (Perspex) so that images of the bubbles could be taken without distortion. The column walls were connected to the diffuser housing using a silicon sealant to prevent any leakages while the lid of the column, also made of PMMA, was attached to the column with screws and a rubber gasket seal.

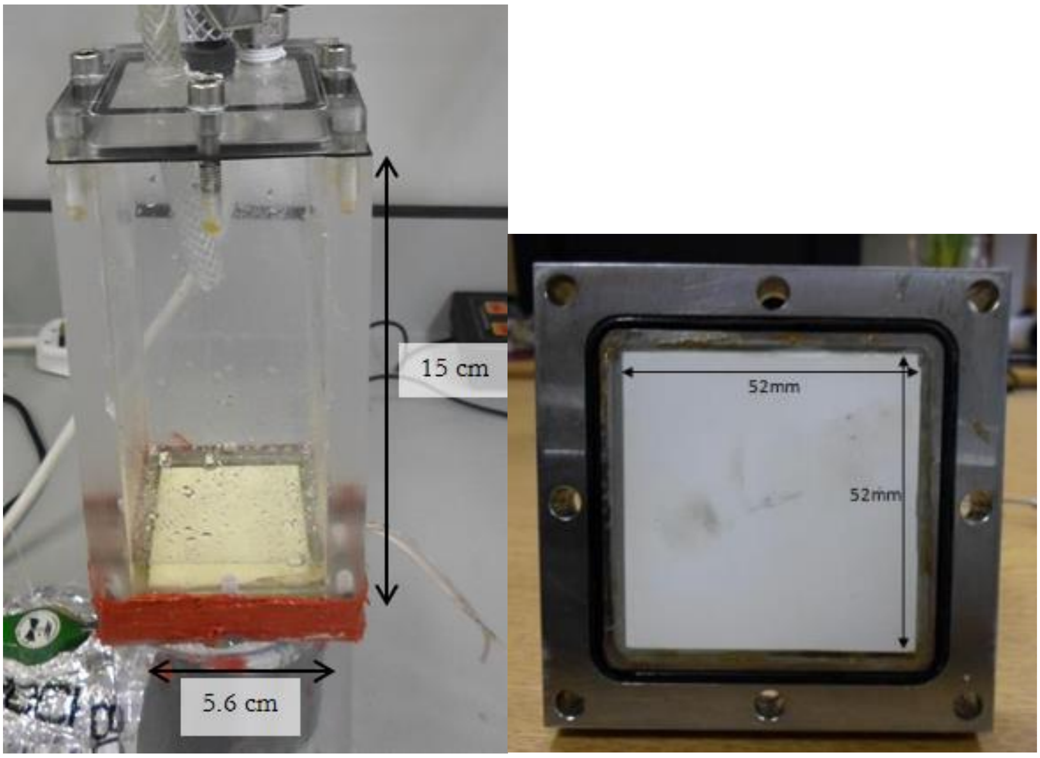

Figure 3.8. Bubble column used in preliminary biogas upgrading experiments (left) and diffuser close-up (right)

3.4.4.2. Refined Experiments

Figure 3.9 shows photographs of the bubble column and diffuser used in the refined experiments, the results of which are presented in Sections 6.2.2 and 7.2.2-7.2.11. The main differences between the preliminary design and the final design were:

1. The column was reduced from a height of 15 cm to 5 cm in order to reduce the amount of time the gas spends in the column headspace; and
2. The diffuser was separated into two rectangles (with separate chambers underneath) in order to reduce bubble coalescence due to liquid currents whilst also making it easier to capture images of the bubbles

When in operation, only one of the rectangular diffusers was used.

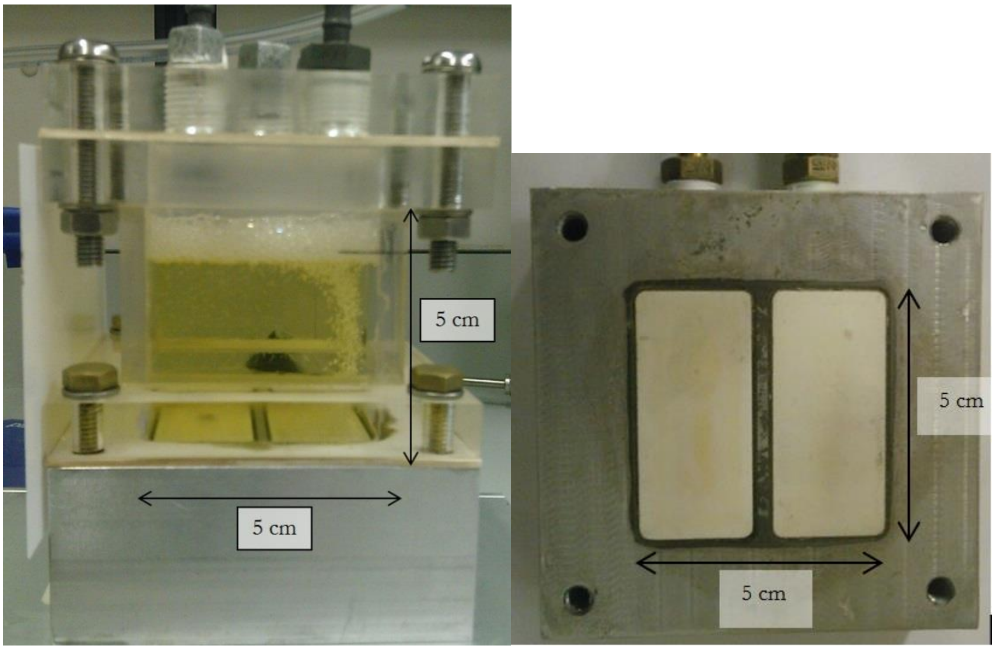

Figure 3.9. Photograph of the bubble column and diffuser used in the refined experiments

3.4.5. Ceramic Diffuser

A ceramic diffuser, obtained from Point Four Systems Inc., made of sintered alumina, was used to produce microbubbles in the solvents during the bubble sizing and biogas upgrading experiments. This type of diffuser was chosen as it is known to produce bubbles of diameter less than 100 microns in water (Rehman, 2014, Desai, 2014).

The mean pore size and porosity of the diffuser has been determined by mercury porosimetry to be 0.6 μm and 0.348 respectively.

3.4.6. Gas Analyser

A GasData GFM416 biogas analyser was used for measuring the concentrations of CH_4 and CO_2 at the outlet of the bubble column with an accuracy of ±1 vol.% and a precision of ±0.1 vol.% for each channel. A photograph of this gas analyser is provided in Figure 3.10.

Figure 3.10. GasData GFM416 Infra-Red Biogas Analyser

The concentrations of CH_4 and CO_2 at the outlet of the column were measured by connecting the column outlet to the inlet of the gas analyser via a plastic tube and recording the measurements displayed on the analyser screen. Jubilee clips were positioned at each end of the tube to ensure that no air from the surroundings was sucked into the analyser.

The gas analyser was calibrated at the start of each biogas upgrading experiment by passing an artificial biogas mixture (60% CH_4, 40% CO_2) from a gas cylinder into the gas analyser. A bleed valve was used, diverting some of the flow to atmosphere, such that the gas fed into the analyser was at atmospheric pressure. Once the readings stabilised, the analyser was calibrated for 60% CH4 and 40% CO2 by pressing 'Calibrate'. Using a nitrogen cylinder, the analyser was calibrated for 0% CH4 and 0% CO2 using the same method.

The concentrations of CH_4 and CO_2 in the gas cylinder was measured at the start and end of three experiments and a maximum instrument drift of ±1% was recorded for each channel.

3.4.7. Cameras

In the aqueous glycerol bubble sizing experiments presented in Section 3.3.2, a Pixelink PL-B749F 1.3 MegaPixel camera was used to take images of the bubbles. In the nitrogen bubble sizing experiments and biogas upgrading experiments presented in Section 3.3.2 and Section 3.3.3, a Pixelink PL-D725MU 5.3 MegaPixel camera was used. In all of the experiments, a Navitar 1-6015 lens adapter and Navitar 1-60135a lens were used to reduce the field of view and to focus on the bubbles. A photograph of the camera-lens arrangement is shown in Figure 3.11.

Figure 3.11. Photograph of the Pixelink 5.3 MegaPixel camera with Navitar lens and lens adapter

The magnification on the camera was adjusted in each experiment depending on the bubble size such that the mean bubble diameter was approximately one tenth of the height of the field of view. This was done so as to reduce the experimental error which would be present if the bubbles were too small on the screen. Table 3.5 shows the number of microns per pixel and the mean bubble diameter recorded at a gas flow rate of 3mL/min.

Table 3.5. Number of microns per pixel in reference images

Ionic Liquid	**µm/pixel - from Reference**	**Mean bubble diameter @ 3mL/min (µm)**	**1 pixel (% of bubble diameter)**
[C_2mim][DCA]	4.73	115	4.10%
[C_2mim][NTf_2]	4.76	558	0.85%
[C_4mim][NTf_2]	4.85	586	0.83%
[C_4mim][TFA]	2.87	130	2.22%
[C_2mim][$EtSO_4$]	1.47	98.8	1.48%
[P_{66614}][NTf_2]	3.89	701	0.55%
[P_{66614}][DCA]	4.95	483	1.02%
[P_{66614}][$C_{10}H_{19}O_2$]	7.08	1020	0.69%
[P_{66614}][Cl]	7.11	1360	0.52%
[P_{66614}][Br]	7.08	860	0.82%

It can be seen that with the exception of [C_2mim][DCA], one pixel was less than 2.22% of the bubble diameter in all of the ionic liquids. With [C_2mim][DCA], one pixel was 4.10% of the bubble diameter. At higher flow rates, this value would be even lower, indicating that the resolution of the images is sufficient for determining the mean bubble diameter accurately.

3.4.8. Biogas Collector and Pressure Equalisation Columns

The biogas collector and pressure equalisation columns, photographed in Figure 3.12, were designed and used by Mahmood al-Mashhadani, University of Sheffield. A photograph of these columns is presented in Figure 3.12.

Figure 3.12. Photograph of the biogas collector and pressure equalisation columns

The biogas collector was a cylinder of diameter 12 cm and height 50 cm. The pressure equalisation column, of diameter 10 cm was open to atmosphere at the top. It was placed on a lab jack so that it could be raised and lowered, allowing the pressure in the absorption column to be controlled. It is estimated that the pressure could be controlled to within about 1 mm of water, which is equivalent to 9.8 Pa. This means that the pressure in the bubble column would have been at 1 atm ±0.01 atm.

3.4.9. Mass Balance

A Kern EMS 6K0.1 mass balance was used to measure the mass of water leaving the pressure equalisation column and to make 30 wt.% aqueous MEA solutions. The accuracy and precision of this balance is ±0.1 g, which equates to approximately ±0.1 mL.

Figure 3.13. Photograph of Kern EMS 6K0.1 mass balance used to measure mass of water and MEA

3.4.10. Tensiometer

An Attension Theta tensiometer was used to measure the contact angle between the ionic liquids and alumina with an accuracy of ±0.1°. The tensiometer was calibrated before use using a 4 mm ball bearing. A photograph of this tensiometer is provided in Figure 3.14.

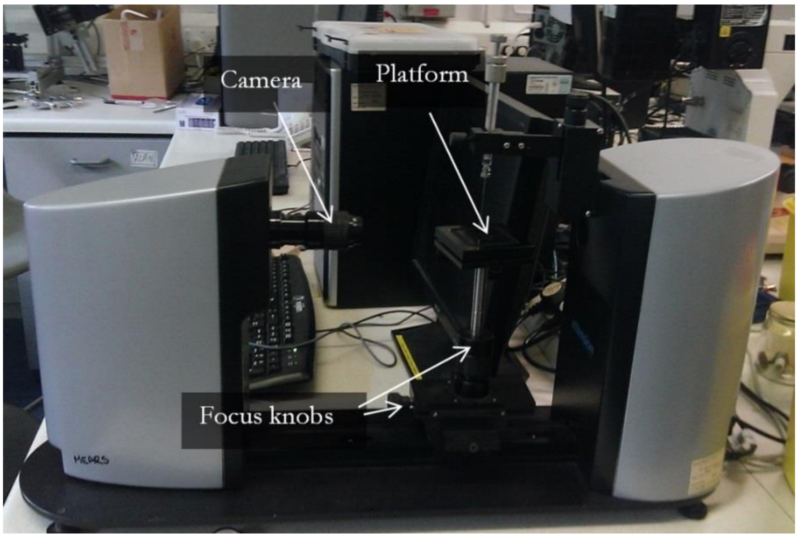

Figure 3.14. Photograph of Attension Theta tensiometer used in this work

3.5. Experimental Methods

The experimental methods used for determining the diffuser pore size, mean bubble diameter, gas holdups, gas concentrations in the liquid and mass transfer coefficients are presented in this section.

3.5.1. Determination of Pore Size and Porosity

The pore size and porosity of the diffuser were determined using mercury porosimetry. This technique forces mercury into the pores of a sample by incrementally increasing the pressure; the total intrusion volume for each pressure increase is calculated by measuring the capacitance across the penetrometer stem and the diameter of pores filled, D [m], is calculated using the Washburn Equation:

$$D = \frac{1}{P} 4\gamma cos\theta \tag{3.5.1}$$

where P denotes the applied pressure [Pa], γ represents surface tension [N/m], and θ is the contact angle between mercury and the sample, which was assumed to be that of alumina (141 degrees (Klobes et al. (2006)).

A schematic of a penetrometer is shown in Figure 3.15.

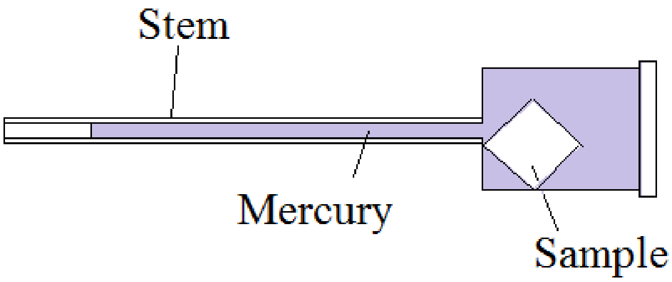

Figure 3.15. A schematic of a penetrometer

3.5.2. Determination of Bubble Diameter, *d*

Photographs of the bubbles were analysed using a LabVIEW program written by Dr. Brittle, University of Sheffield (see Appendix D: Bubble Sizing Software). The LabView program consists of four main components, as shown in Figure 3.16.

The components are as follows:

a. Upload image and convert to greyscale

b. Apply a threshold to convert the image to binary
c. Fill in holes
d. Remove border objects and particles with a high Heywood shape coefficient

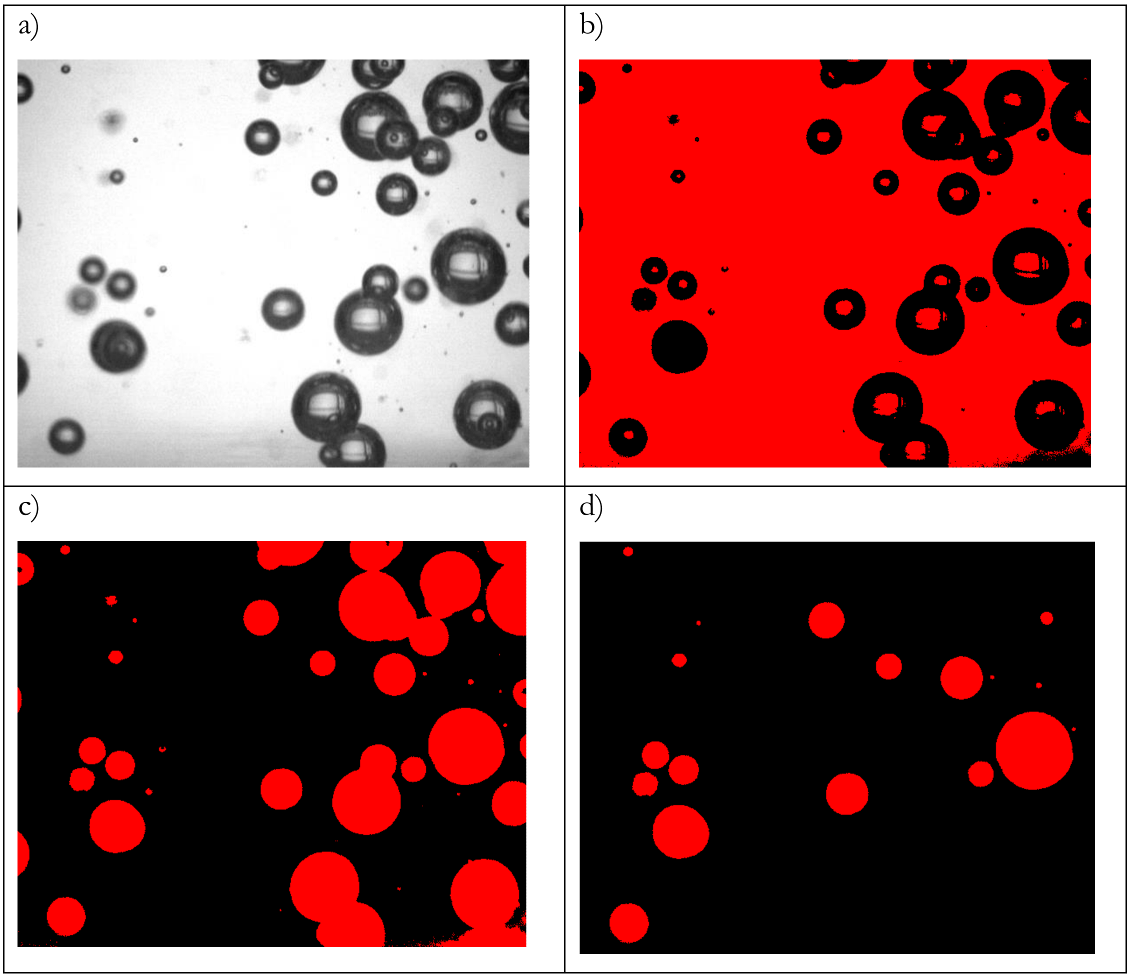

Figure 3.16. Labview bubble sizing program: a) greyscale image b) binary image c) fill holes d) apply roundness factor

For each flow rate, a set of over 30 images were captured, each containing tens of bubbles. A manual threshold was then applied to a representative image from the set using a trial and improvement method such that the final image displayed the best representation of the bubbles in the greyscale image.

The Heywood shape factor, f_H, as defined by:

$$f_H = \frac{P_P}{2\sqrt{\pi A_P}} \tag{3.5.2}$$

where P_P is the particle perimeter and A_P is the projected area of the particle, was varied using trial and improvement on the same image. This was done to remove any bubbles that were overlapping, which would provide the user with a false reading of the bubble size.

In addition to this, a size threshold was applied to the image to remove the smallest and largest particles. The lower threshold was applied to remove any noise from the image, while the upper threshold was used to remove any clouds of overlapping bubbles that were not removed by the Heywood shape factor.

After uploading a set of images to LabView and running the program, a text file was produced containing all of the bubble areas in pixels that were present in each of the final images. In order to achieve the mean bubble diameter in microns, a reference image was taken of an object with known dimensions using the same magnification as that used to take images of the bubbles. An example of such a reference image is shown in Figure 3.17.

Figure 3.17. Example of a reference image for bubble sizing

Using the image analysis software, ImageJ, a conversion factor, f_c, between pixels and microns was obtained and the mean bubble diameter was calculated from:

$$\bar{d} = \frac{f_c}{n}\sum\sqrt{\frac{4A_P}{\pi}} \tag{3.5.3}$$

where n is the number of bubbles and A_P is the bubble area in pixels.

The majority of the error in this technique stems from the user's choice of values for the minimum threshold, Heywood shape coefficient, and decision to remove how many of the largest and smallest objects from the image (if any). Ideally, these settings would be changed for each individual image; however, in order to use a large sample size of bubbles, appropriate values for these settings were investigated using two images for each experiment and the settings were applied to each of the other images in that set.

3.5.3. Determination of Gas Holdup, ε

As mentioned in Section 2.3, the gas holdup, ε, is equal to the volume of gas divided by the volume of liquid. Assuming all bubbles rise at the bubble terminal velocity, UT, inside a stagnant liquid, the time a bubble spends inside the column is equal to h/UT where h is the height of liquid in the column. In this time, the volume of gas entering the column is equal to $\dot{V}$h/U_T where $\dot{V}$ is equal to the gas volume flow rate. This is equal to the volume of gas in the column at any given time.

Here, it is useful to introduce the term 'superficial gas velocity', UG, which is equal to the volume flow rate of gas divided by the area of the column, A:

$$U_G = \frac{\dot{V}}{A} \tag{3.5.4}$$

The volume of gas in the column at any given time can therefore be expressed as U_GAh/U_T. Since the gas holdup is equal to the volume of gas divided by the volume of liquid (equal to Ah), the gas holdup is given by (Hughmark, 1967, Akita and Yoshida, 1973):

$$\varepsilon = \frac{U_G}{U_T} \tag{3.5.5}$$

In this work, the bubble rise velocity was calculated from the Hadamard-Rybczinski equation for the terminal velocity of a rising bubble (Zimmerman et al., 2013):

$$U_T = \frac{d^2 g(\rho_l - \rho_g)}{12 \cdot \mu_L} \tag{3.5.6}$$

where d is the bubble diameter, g represents acceleration due to gravity (equal to 9.81 m/s^2), ρ_L and ρ_G represent the densities of the liquid and gas phases respectfully, and μ_L denotes the liquid viscosity. In this work, the mean bubble diameter, $\bar{d}$, was used instead of d. The Hadamard-Rybczinski terminal velocity was used rather than the Stokes terminal velocity as it is more commonly used with bubbles since it takes into account internal circulation.

3.5.4. Determination of Gas Concentrations in Liquid

Since there were two gases present in the biogas mixture, the gas concentrations in the liquid could not be measured directly, e.g. using a conductivity probe. Therefore, they had to be inferred by measuring what was present in the gas phase using an infra-red gas analyser. Such methods have been used by (Bishnoi and Rochelle, 2000, Dang and Rochelle, 2003, Dugas and Rochelle, 2009) for measuring CO_2 concentrations in aqueous MEA and piperazine solutions.

3.5.4.1. Preliminary Experiments

The flow rate into the absorption column was calculated by measuring the change in the liquid level in the biogas collector over a five minute period once the ionic liquid ($[P_{66614}][Cl]$) became saturated (assumed to be when the CH_4 and CO_2 readings on the gas analyser read 60.0% ±0.1% and 40.0% ±0.1% respectively). It was assumed that a negligible amount of methane was absorbed into the ionic liquid, since it is known that the methane solubility in $[P_{66614}][Cl]$ is very low - <0.01 mol/L (Morgan et al., 2005).

The rate of CO_2 capture, $\dot{n}_{CO2}$, in the ionic liquid could thus be calculated from the ideal gas law using the following equation:

$$\dot{n}_{CO2} = \frac{P_{atm}\dot{V}}{R_g T}\left(0.4 - 0.6\left(\frac{1 - c_{CH4}}{c_{CH4}}\right)\right) \tag{3.5.7}$$

where P_{atm} represents atmospheric pressure, R_g is the universal gas constant, T is the temperature (assumed to be 298 K), $\dot{V}$ represents the inlet biogas flow rate, and c_{CH4} is the volumetric concentration of CH_4 in the off-gas, as given by:

$$c_{CH4} = \frac{c_{CH4\_o}}{c_{CH4\_o} + c_{CO2\_o}} \tag{3.5.8}$$

In Eqn 3.5.8, c_{CH4_o} and c_{CO2_o} are the volumetric concentrations of CH_4 and CO_2 at the outlet of the absorption column respectively.

Once the CH_4 and CO_2 readings on the gas analyser reached 60.0% ±0.1% and 40.0% ±0.1% respectively (the same as the inlet concentration), the ionic liquid was assumed to be saturated. At this point, the volume flow rate out of the column (assumed to be equal to the inlet volume flow rate at standard pressure) was calculated by measuring the change in the water level in the biogas collector over a five minute period.

Since the CO_2 and CH_4 concentrations at the inlet and outlet of the bubble column were known, as well as the CO_2 flow rate at the inlet and CH_4 flow rate at the outlet, the CO_2 concentration in the liquid, c_{CO2}, was calculated from the difference between the amount of CO_2 that went into and came out of the bubble column:

$$c_{CO2} = \frac{P_{atm} \cdot \dot{V}_{in} \cdot t}{RTV_L}\left(0.4 - \frac{c_{CO2\_o}}{c_{CH4\_o}} \cdot 0.6\right) \tag{3.5.9}$$

Here, P_{atm} represents atmospheric pressure, $\dot{V}_{in}$ represents the gas flow rate into the column, t denotes time, R and T represent the universal gas constant and gas temperature respectively (assumed to be 20 °C), and c_{CO2_o} and c_{CH4_o} represent the CO_2 and CH_4 concentration readings on the gas analyser. The constants, 0.4 and 0.6, represent the inlet concentrations of CO_2 and CH_4 into the column respectively.

3.5.4.2. Refined Experiments

In the final experiments, since a mass flow controller was added to the setup, the flow rate into the column was known. The flow rate out of the column was measured by weighing the mass of water in the beaker at minute intervals.

The CO_2 and CH_4 flow rates into and out of the column were thus equal to:

$$\begin{aligned} \dot{V}_{CO2,i} &= 0.4 \cdot \dot{V}_i \\ \dot{V}_{CH4,i} &= 0.6 \cdot \dot{V}_i \\ \dot{V}_{CO2,o} &= c_{CO2,o} \cdot \dot{V}_o \\ \dot{V}_{CH4,o} &= c_{CH4,o} \cdot \dot{V}_o \end{aligned} \tag{3.5.10}$$

where c represents the concentration of a gas species in the liquid and $\dot{V}_o$ is the volume flow rate out of the bubble column as given by:

$$\dot{V}_o = \frac{\Delta m_w}{\rho_w \Delta t} \tag{3.5.11}$$

Here, Δm_w is the change in mass of water over a time period Δt (one minute) and ρ_w is the density of water, which was calculated using the equation:

$$\rho_w[\frac{kg}{m^3}] = 1002.9 - 0.2349T[°C] \tag{3.5.12}$$

where T is the temperature of the water in degrees Celsius. The temperature of the water was measured using a calibrated K-type thermocouple and thermocouple reader.

Eqn. 3.5.12 was obtained by plotting the density of water between 19 – 27°C, as shown in Figure 3.18, the data for which was obtained in Perry's Chemical Engineer's Handbook (Perry and Green, 2008).

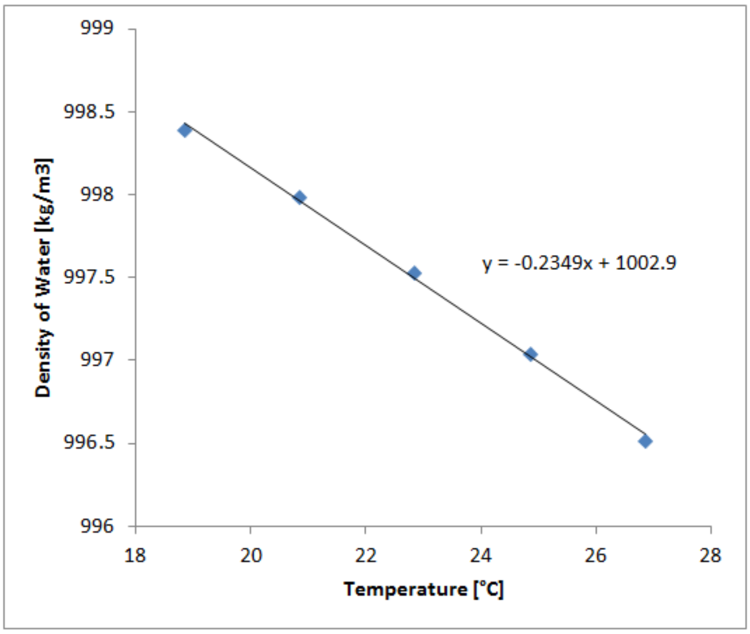

Figure 3.18. Density of pure water between 18 – 27°C

The number of moles of each species, j, captured by the solvent during each time interval was calculated from Eqn. 3.5.13:

$$n_j = \frac{P_{atm}(\dot{V}_{j,o} - \dot{V}_{j,i})\Delta t}{RT} \tag{3.5.13}$$

The concentration of each component, c_j, in the liquid at any given time was given by:

$$c_j = \frac{1}{V_L}\sum \frac{P_{atm}(\dot{V}_{j,o} - \dot{V}_{CO2,i})\Delta t}{RT} \tag{3.5.14}$$

3.5.5. Determination of Volumetric Liquid-Side Mass Transfer Coefficient, *K_La*

The volumetric mass transfer coefficient, K_La, is given by the two-film theory equation (Lewis and Whitman, 1924):

$$K_L a(c^* - c) = \frac{dc}{dt} \tag{3.5.15}$$

where dc/dt is the rate of mass transfer per unit volume, a is the interfacial area per unit volume, and c* and c represent the equilibrium concentration and actual concentration of CO_2 in the ionic liquid respectively.

Integrating with respect to time and re-arranging gives:

$$K_L a = \ln\left(\frac{c^* - c_0}{c^* - c}\right)/t \tag{3.5.16}$$

where c* is the saturation concentration of gas in the liquid, c_0 is the initial concentration, and c is the concentration at time t. The liquid-side mass transfer coefficient can thus be calculated from the gradient of a graph with $ln\left(\frac{c^*-c_0}{c^*-c}\right)$ on the ordinate axis and a·t along the abscissa, an example of which is presented in Figure 3.19.

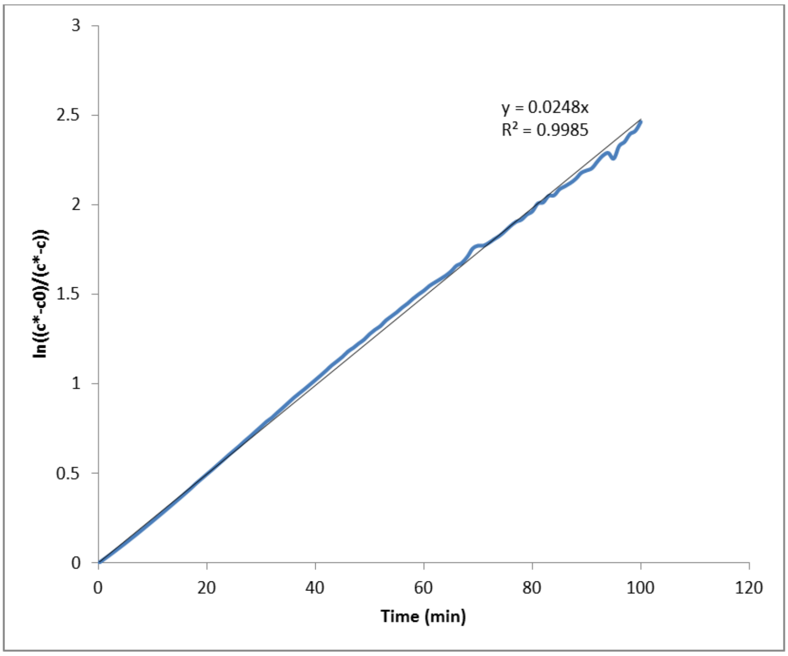

Figure 3.19. Example of a graph for calculating the volumetric mass transfer coefficient; K_La is equal to the gradient

In this work, the solubility of CO_2 in the ionic liquid, c*, was estimated for each experimental run by plotting a graph such as the one in Figure 3.19 and using trial and improvement to determine which equilibrium concentration provided the greatest R-squared value in a linear regression fit. Using this method, the solubility was estimated to two significant figures.

3.5.6. Determination of Individual Liquid-Side Mass Transfer Coefficient, k_L

The liquid-side mass transfer coefficient, k_L, was calculated by assuming that the gas-side resistance was negligible (Akita and Yoshida, 1973).

In order to determine the mass transfer coefficient, the total surface area of bubbles in the column had to be determined. The total bubble surface area per unit volume, a, is given by:

$$a = \frac{6\varepsilon}{d} \tag{3.5.17}$$

where ε is the gas holdup an d is the bubble diameter. In this work, the mean bubble diameter was used.

The individual liquid-side mass transfer coefficient, k_L, is thus given by:

$$k_L = \frac{K_L a}{a} \tag{3.5.18}$$

3.5.7. Determination of Correlation Coefficients

In this work, correlations were obtained of the form:

$$A = \alpha B^{\beta} C^{\gamma} D^{\delta} \dots \tag{3.5.19}$$

where A, B, C, and D are arbitrary variables and α, β, γ, and δ, are constants.

Taking the natural logarithm of both sides gives:

$$\ln(A) = \ln(\alpha) + \beta ln(B) + \gamma ln(C) + \delta ln(D) + \cdots \tag{3.5.20}$$

In this work, the values of ln(A), ln(B), ln(C), ln(D), etc. were tabulated in Microsoft Excel and the in-built multiple regression feature was used to find the values of α, β, γ, δ, etc.

3.6. Experimental Procedures

3.6.1. Leak Testing

In the experimental setups described in 3.2, several precautions were taken to ensure that leaks were minimised as these would distort the readings. Firstly, PTFE tape was used on all screw threads to make them air-tight. Secondly, a soapy water mixture was squirted onto any connections. If bubbles started to form, the connection was tightened, either by tightening Swagelok fittings, or by tightening a jubilee clip on the connection.

3.6.2. Drying Ionic Liquids

It is well known that even a small amount of water can significantly affect the physical properties of ionic liquids (e.g. (Zhang et al., 2013)), in particular the viscosity. The common procedure for drying ionic liquids is to hold them under vacuum under moderate temperature for at least 48 hours (e.g. (Carvalho et al., 2008, Almeida et al., 2013)). However, it is also known that it can take several days for all of the water to be completely desorbed (Keskin et al., 2007).

In this work, due to the large amount of ionic liquid being used and the difficulty in transferring the ionic liquid into the bubble column without it absorbing water, the ionic liquids were dried under high vacuum for at least 48 hours in a vacuum dessicator prior to first use (see Figure 3.20). An Edwards E2M18 vacuum pump was used to provide the vacuum, which has a capacity of 0.001 mbar. The pressure inside the dessicator was measured using a pressure gauge to be -1.0 bar (gauge). The ionic liquid was then transferred into the bubble column and sparged with nitrogen for at least 12 hours before experiments commenced. For subsequent experiments, the ionic liquid was kept in the bubble column and sparged with nitrogen for at least 12 hours.

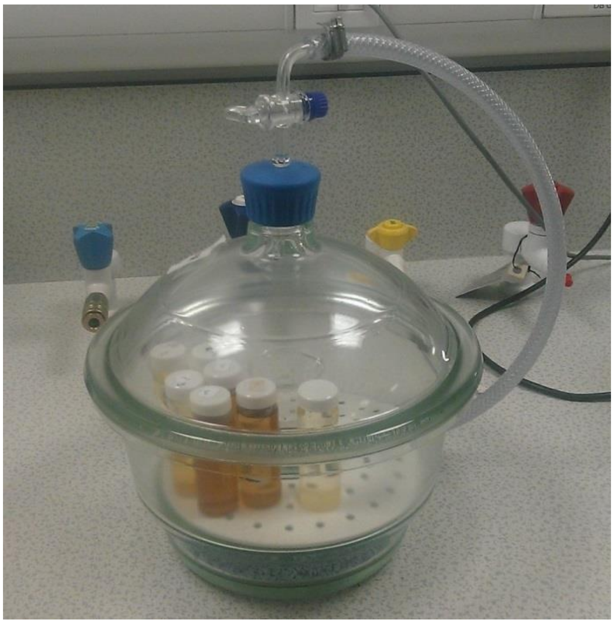

Figure 3.20. Ionic liquid samples stored in a vacuum dessicator

3.6.3. Contact Angle Measurements

The experimental procedure for the contact angle measurements was as follows:

1. Open Attension Theta software
2. Place 4 mm ball bearing on platform
3. Adjust focus knobs such that the ball bearing is in focus with the camera
4. Press calibrate
5. Place a drop of liquid onto a clean piece of alumina tile and place the tile on the platform
6. Take an image of the drop
7. Inform the computer where the surface of the tile is and the angle of tilt and click 'Execute'

8. Check that the software has followed the shape of the drop to provide the user with the correct contact angle. An example image from the software is shown in Figure 3.21
9. Repeat steps 5-8 three times and compute the mean contact angle

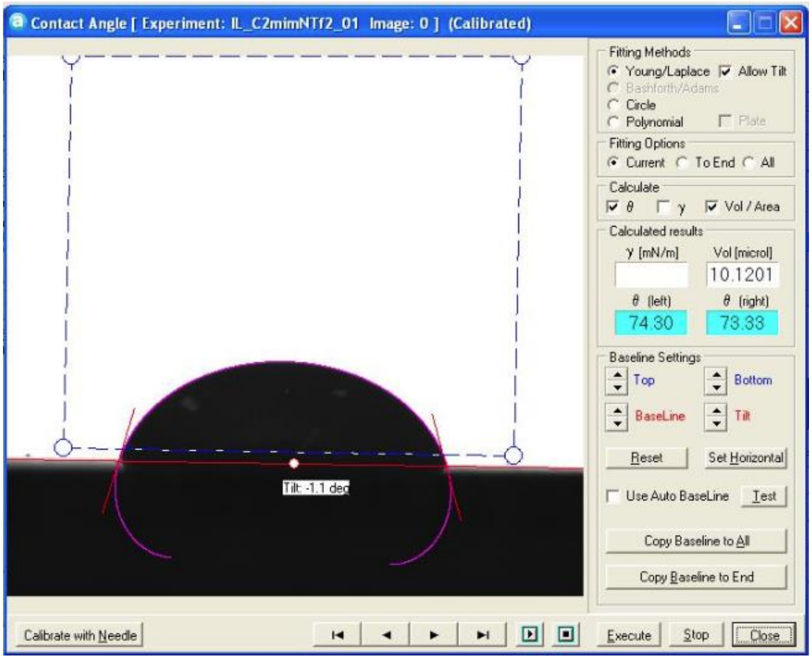

Contact Angle [Experiment: IL_C2mimNTf2_01 Image: 0] (Calibrated)

Fitting Methods
● Young/Laplace ☑ Allow Tilt
○ Bashforth/Adams
○ Circle
○ Polynomial ☐ Plate

Fitting Options
● Current ○ To End ○ All

Calculate
☑ θ ☐ γ ☑ Vol / Area

Calculated results
γ [mN/m]:
Vol [microl]: 10.1201
θ (left): 74.30
θ (right): 73.33

Baseline Settings
☐ Use Auto BaseLine

Tilt: -1.1 deg

Figure 3.21. Sample image from the Attension Theta software for measuring contact angle (ionic liquid=[C_2mim][NTf_2])

3.6.4. Frequency Study

The experimental procedure for the frequency study was as follows:

1. Pour ionic liquid into the column up to the 100 mL line
2. Place a feedback loop on the fluidic oscillator
3. Turn on the air supply
4. Adjust the pressure regulator such that the rotameter reads 85 mL/min
5. Allow 30 seconds for the oscillation to stabilise
6. Record the oscillation frequency using the LabView program which performs a Finite Fourier Transform on the signal from the pressure transducer
7. Take 100 photographs of the bubbles
8. Place next feedback loop on the oscillator
9. Repeat steps 6-9 until all feedback loops have been used
10. Turn off air supply
11. Use the methods discussed in Section 3.5.2 to determine the mean bubble diameter for each length of feedback loop

3.6.5. Water-Glycerol Bubble Sizing Experiment

The following experimental procedure was used for the water-glycerol bubble sizing experiments:

1. Open the air supply to a pressure of 2.0 bar
2. Set the air flow rate to 3 mL/min on the mass flow controller
3. Pour glycerol into bubble column up to 100 mL (4 cm) line
4. Turn on LED light source and camera
5. Wait until the pressure stabilises on the pressure gauge
6. Adjust the magnification, focus, and exposure time such that the bubbles can be seen clearly; the exposure time should be high enough such that the image is not too dark to analyse but low enough such that the bubbles are not blurry
7. Adjust the frame rate such that different bubbles are captured in each image
8. Capture 45 images of bubbles
9. Take an aliquot of glycerol out of column using a pipette and replace with an equally sized aliquot of deionised water
10. Repeat steps 5-8 until all desired mixtures have been studied
11. Empty the column and fill with de-ionised water
12. Repeat steps 4-7 using de-ionised water

3.6.6. Ionic Liquid Bubble Sizing Experiment

The following experimental procedure was used for the ionic liquid bubble sizing experiments:

1. Pour ionic liquid into bubble column up to 100 mL (4cm) line
2. Open the valve on the nitrogen cylinder
3. Turn on LED light source and camera
4. Adjust the magnification, focus and exposure time such that the bubbles can be seen clearly
5. Adjust the frame rate such that different bubbles are captured in each image
6. Set desired gas flow rate on the mass flow controller
7. Wait until the pressure stabilises on the pressure gauge
8. Capture 45 images of bubbles
9. Repeat steps 6-8 until all desired flow rates have been studied
10. Repeat steps 6-9 such that each flow rate has been studied three times
11. Turn off the nitrogen supply and pour the ionic liquid out of the column

12. Clean the column thoroughly, several times, with ethanol (>99.9% purity).
13. Analyse the bubble size using the methods described in Section 3.5.2
14. Calculate the mean bubble size at each flow rate from the three repeats

3.6.7. **Biogas Upgrading Experiments**

The following experimental procedure was used for the biogas upgrading experiments

1. Fill biogas collector completely with deionised water and close all valves to atmosphere
2. Adjust the height of the pressure equalisation column such that the pressure in the bubble column is atmospheric. This was done by lowering it until bubbles were produced in the biogas collector column and then raising it to the point where the bubbles stopped being formed
3. Place a 2 L beaker on the mass balance and tare
4. Fill the absorption column up to the 100 mL line with solvent
5. Place the lid on bubble column and connect the bubble column to the biogas collector using flexible tubing
6. Connect the IR analyser to the headspace of the bubble column and turn it on
7. Open the pressure regulator on the biogas cylinder to 2 bar
8. Set the flow rate on the mass flow controller to 50 mL/min until the desired pressure is reached and then turn down immediately to the desired flow rate
9. Start a timer and record the CH_4 and CO_2 concentrations at the outlet and the mass of water in the beaker
10. Take concentration and mass readings every minute for 100 minutes
11. After 100 minutes, close the pressure regulator on the biogas cylinder
12. Close the valve connecting the biogas collector to the pressure equalisation column
13. Disconnect the bubble column from the biogas collector
14. When using ionic liquids, purge the ionic liquid with nitrogen for at least 12 hours
15. Pour the ionic liquid out of the bubble column and clean the column thoroughly, several times, with ethanol (>99.9% purity).
16. Allow 12 hours for the ethanol to evaporate

4. Numerical Methods: Direct Contact Regeneration of MEA and Ionic Liquids

4.1. Introduction

A computer generated numerical model was created using the software COMSOL Multiphysics v.4.3b to examine the feasibility of regenerating a partially loaded 30 wt.% aqueous MEA solution using Direct Contact Regeneration (DCR). It was then adapted to investigate whether DCR can be used to regenerate ionic liquids. Additionally, the model was used to investigate whether the DCR method can be integrated with CDU processes by using a bubble of CO_2 such that the outlet gas from the column would be almost pure CO_2. It must be noted that the purpose of these models was to examine whether the DCR technique is theoretically feasible, rather than to make a fully predictive model.

The main reasons why it was decided to conduct a numerical study initially, as opposed to an experimental study, are:

- The fundamental physics involved – heat transfer and diffusion – are well understood and hence a reasonably accurate model can be produced
- To provide an indication of the ideal bubble size, gas temperature and liquid level required for the direct contact regeneration technique to work
- Any experimental setup would inevitably contain a large amount of error for the following reasons:
    - The transient temperature of the gas inside a microbubble cannot be accurately measured
    - If the gas were to be hot upon entering the liquid, the orifice material would also have to be hot. If this is the case, it is possible that some solvent would be regenerated simply by being in contact with the orifice material; it would therefore not be known whether it was the bubble or the orifice that caused the release of CO_2 from the solvent
    - The liquid would heat up over the course of the experiment, thus releasing CO_2
    - Some heat and mass transfer would occur while the bubble is forming

4.2. Objectives

The specific objectives of the work undertaken in Chapters 4 and 5 are:

- Create a numerical model to examine the feasibility of DCR and validate the model
- Determine conditions under which a 30 wt.% aqueous MEA can be regenerated using DCR with nitrogen
- Determine the effects of bubble size, bubble temperature, and CO_2 loading in the liquid on the rate of desorption of CO_2 into the bubble
- Determine whether DCR can be integrated with CDU processes using a CO_2 bubble in both aqueous MEA and ionic liquids
- Conduct an energy assessment of regenerating MEA and [C_2mim][NTf_2] using both the DCR and temperature swing desorption methods

4.3. Model 1: Direct Contact Regeneration of Aqueous MEA

A superheated microbubble of diameter 100 μm consisting of either pure CO_2 or pure N_2 was modelled inside a 30 wt. % aqueous MEA solution. The liquid phase was not included in the model; instead it was assumed that the CO_2 loading in the aqueous MEA solution was constant. At the interface, the CO_2, water, and MEA vapour concentrations were assumed to flash to saturation in accordance with the model of (Zimmerman et al., 2013), such that the partial pressures of the vapours were equal to their equilibrium values. Conduction and convection from the bubble to the liquid was accounted for using Newton's Law of Cooling. Additionally, heat transfer due to the evaporation of aqueous MEA and the reversal of the CO_2-MEA reaction was calculated using a heat flux at the bubble interface. Sections 4.3.1 – 4.3.6 describe the setup of the model, including the geometry, governing equations, list of assumptions, initial conditions, boundary conditions, and the mesh.

4.3.1. Geometry

A 2D axisymmetric geometry was used in this model, consisting of a circle of diameter *d*, centred at the origin, with axial symmetry about the $r=0$ axis. The circle was then sectioned to produce a semi-circle in order to reduce the computational time (see Figure 4.1).

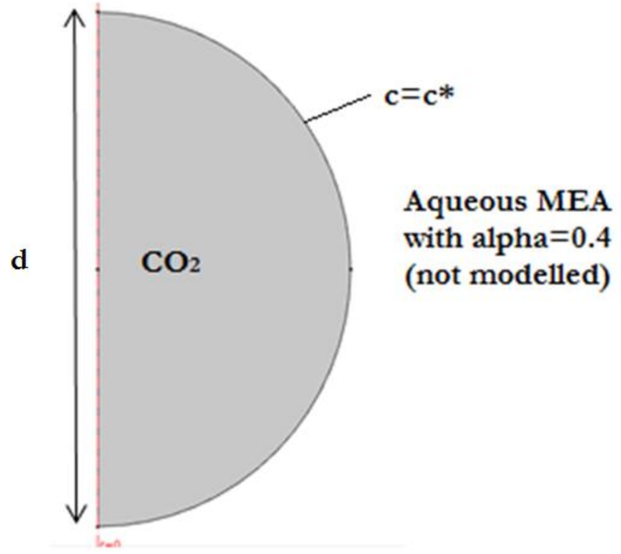

Figure 4.1. Geometry used in the DCR model

Initially, the vapour phase contained pure CO_2, such is the requirement for integration with CDU processes, and the CO_2 concentration at the interface was assumed to be saturated (c=c*). Another model was created in which the vapour phase contained pure N_2 initially in order to increase the rate of CO_2 desorption into the bubble.

4.3.2. **Governing Equations**

The model utilised both heat and mass transfer equations. In the case of mass transfer, the transfer of water vapour, MEA vapour, and CO_2 was considered.

The equation that governs heat transfer is the temperature-form of the energy equation (Bird et al., 2007):

$$\rho c_p \frac{\partial T}{\partial t} = -\rho c_p \boldsymbol{u} \cdot \nabla T + \nabla \cdot \kappa \nabla T + Q_s$$

Net rate of increase in energy density	=	Rate of increase in energy density by convection	+	Rate of increase in energy density by conduction	+	Rate of increase in energy density from an external heat source	(4.3.1)

Here ϱ, c_p, and $\varkappa$ are the material density, specific heat capacity, and thermal conductivity respectively, $\partial T/\partial t$ and ∇T represent the time- and spacial-derivative of temperature respectively, and Q_s represents the rate of change of energy due to any external heat sources/sinks.

The heat transfer coefficient, h, between the bubble and the liquid was calculated from the empirical correlation of (Calderbank and Moo-Young, 1961), which is valid for bubbles of diameter between 100 μm and 2,500 μm:

$$Nu = 2.0 + 0.31 \cdot Ra^{1/3} \tag{4.3.2}$$

Here, Nu and Ra refer to the Nusselt and Rayleigh numbers, as given by:

$$\begin{gathered} Nu = \frac{hd}{D} \\ Ra = \frac{d^3(\rho_L - \rho_G)\rho_L c_{p\_L} g}{\mu_L \kappa_L} \end{gathered} \tag{4.3.3}$$

where d refers to the bubble diameter, D represents the diffusivity of the gas in the liquid, ϱ_L and ϱ_G are the densities of the liquid and gas phases respectively, c_{p_L}, μ_L and $\varkappa_L$ represent the specific heat capacity, viscosity, and thermal conductivity of the liquid respectively, and g denotes the acceleration due to gravity.

Mass transfer was governed by the mass-form of the continuity equation, also known as the convection-diffusion equation (Bird et al., 2007):

$$\frac{\partial c}{\partial t} = \nabla \cdot (D\nabla c) - \mathbf{u} \cdot \nabla c + \mathrm{R}_s$$

$$\begin{array}{c} \text{Net rate of} \\ \text{increase in} \\ \text{concentration} \end{array} = \begin{array}{c} \text{Rate of increase} \\ \text{in concentration} \\ \text{by diffusion} \end{array} + \begin{array}{c} \text{Rate of increase} \\ \text{in concentration} \\ \text{by advection} \end{array} + \begin{array}{c} \text{Rate of} \\ \text{production of} \\ \text{species by} \\ \text{reaction} \end{array} \tag{4.3.4}$$

Here $\partial c/\partial t$ and ∇c represent the time- and spacial-derivative of a species' concentration respectively, $\mathbf{u}$ represents the fluid velocity, D is the diffusion coefficient, and R_s denotes the rate of production of the species by reaction.

One can see that the total mass flux, ***J***, of a species is equal to the sum of the diffusive and advective mass fluxes:

$$\boldsymbol{J} = -D\nabla \mathrm{c} + \mathbf{u}\mathrm{c} \tag{4.3.5}$$

The heat fluxes from the gas to the liquid due to evaporation, q_e, conduction, q_c, and the heat of reaction, q_r, are thus given by:

$$\begin{gathered} q_e = \hat{\boldsymbol{n}} \cdot \boldsymbol{J_{MEA}} \Delta H_{v,MEA} + \hat{\boldsymbol{n}} \cdot \boldsymbol{J_{H2O}} \Delta H_{v,H2O} \\ q_c = h(T_i - T_L) \\ q_r = \hat{\boldsymbol{n}} \cdot \boldsymbol{J_{CO2}} \Delta H_r \end{gathered} \tag{4.3.6}$$

where ΔH_v and ΔH_r denote the latent heat of vapourisation of the liquid phase and the enthalpy of reaction between CO_2 and MEA respectively and $\mathbf{n}$ represents a unit vector normal to the bubble interface.

4.3.3. **List of Assumptions**

The following assumptions have been used in the numerical model, which have been validated in Section 4.5.4:

- The bubble is spherical
- The bubble is of constant diameter
- There are no surface contaminants on the bubble affecting fluid flow, heat or mass transfer
- The bubble rises in the vertical direction at its Hadamard-Rybczinski terminal velocity
- The gas viscosity is negligible
- The liquid is stationary
- The liquid surrounding the bubble does not heat up significantly

- CO_2, water, and MEA on the vapour-liquid interface flash to saturation
- The CO_2 loading in the liquid surrounding the bubble is constant
- The gas is ideal
- The partial pressure of CO_2 in aqueous MEA can be extrapolated to temperatures up to 600 K

4.3.4. Initial Conditions

- The bubble consists of pure CO_2 or pure N_2
- The initial temperature of the liquid is 298 K
- The velocity field inside the bubble is governed by Stokes flow such that the bubble is assumed to be rising at the Hadamard-Rybczinski terminal velocity (Eqn's 4.3.7-4.3.8)

$$u_r{}^i = \frac{U}{2}\left(1 - \left(\frac{r}{R}\right)^2\right)\cos(\theta) \tag{4.3.7}$$

$$u_\theta{}^i = -\frac{U}{2}\left(1 - 2\left(\frac{r}{R}\right)^2\right)\sin(\theta) \tag{4.3.8}$$

- The partial pressures of CO_2, water, and MEA at the vapour-liquid interface are equal to zero
  - In order to stabilise the model, a smooth step function was implemented such that the concentrations of CO_2, H_2O, and MEA at the vapour-liquid interface had initial concentrations of 0 and increased to their saturation concentrations within 10^{-8} s.
- The pressure in the bubble is equal to:

$$P^i = P_{atm} + \frac{2\gamma}{R} \tag{4.3.9}$$

in accordance with the Young-Laplace equation

4.3.5. Boundary Conditions

- Axial symmetry exists along the r=0 axis
- Heat transfer by conduction from the bubble to the liquid is modelled by a heat sink equal with a heat flux equal to $h \cdot (T_i - T_L)$ where the heat transfer coefficient, h, is determined using the correlation of (Calderbank and Moo-

Young, 1961); T_i and T_L represent the interface and bulk liquid temperatures respectively.

- There exists a heat source on the bubble interface to account for evaporation and condensation of water and MEA, equal to $\hat{\boldsymbol{n}} \cdot \boldsymbol{J_{MEA}} \Delta H_{v,MEA} + \hat{\boldsymbol{n}} \cdot \boldsymbol{J_{H2O}} \Delta H_{v,H2O}$
- Since CO_2 is being desorbed from the liquid, a heat sink exists on the vapour-liquid interface with a heat flux equal to $\hat{\boldsymbol{n}} \cdot \boldsymbol{J_{CO2}} \Delta H_r$ where $\mathbf{J}_{CO2}$ is the total mass flux of CO_2 into the bubble and ΔH_r is equal to the heat of reaction between CO_2 and MEA
- The concentration of CO_2 at the vapour-liquid interface is equal to the saturation concentration:

$$p^*[kPa] = exp(-1225.41 + \frac{36508}{T} - 2.4931 \cdot 10^{-4} \cdot T^2 + 195.87 \cdot log(T) + 14.150 \cdot \alpha) \quad (4.3.10)$$

The above correlation, based on the extended Antoine equation, has been produced with an additional term for CO_2 loading, α, using the data from (Jou et al., 2009) for temperatures between 298.15 – 423.15 K and CO_2 loadings between 0.18 – 0.44 moles-CO_2/mole-MEA and has an R squared value of 0.999.

One can see from Figure 4.2 that the predicted partial pressure from Equation 4.3.10 shows good agreement with the measured data of (Jou et al., 2009).

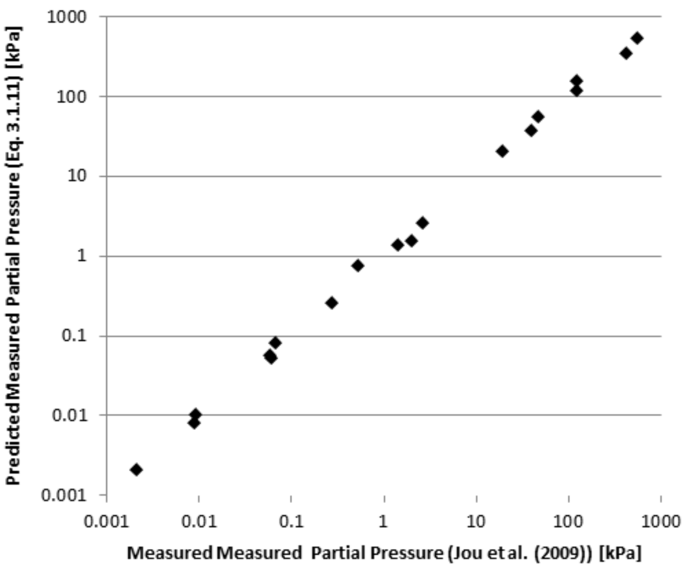

Figure 4.2. Measured CO_2 partial pressure in MEA (Jou et al. (2009)) vs. predicted partial pressure (Eq. 4.3.10)

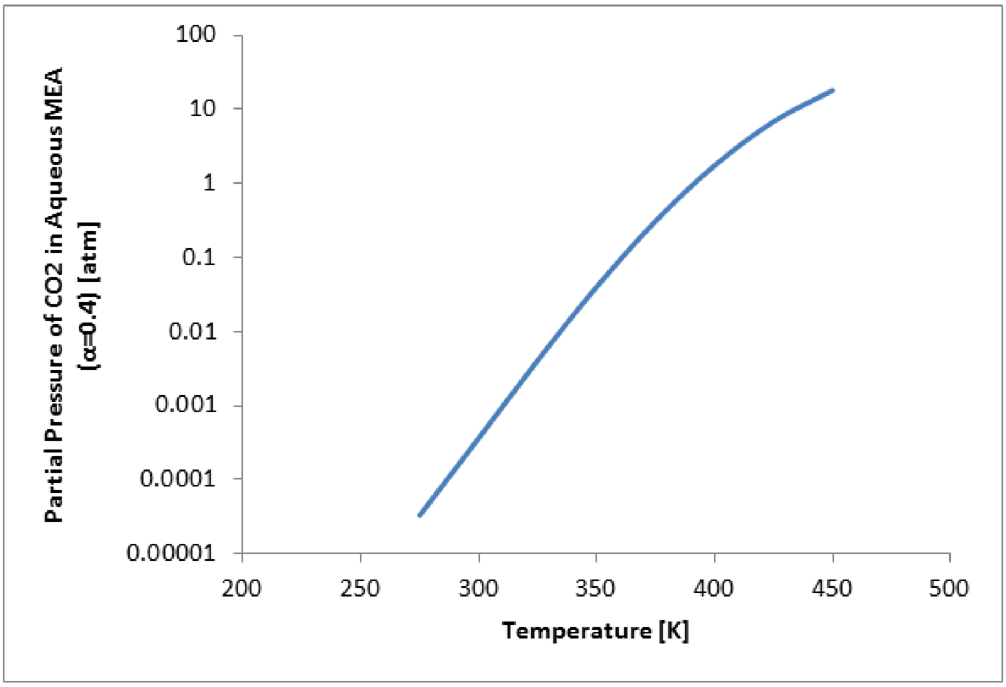

Figure 4.3. Partial pressure of CO_2 vs. temperature in 30 wt. % aqueous MEA (α=0.4)

The partial pressure of CO_2 in a 30 wt. % aqueous MEA solution, as determined from Eq. 4.3.10, has been plotted in Figure 4.3 for a CO_2 loading of 0.4 mol-CO_2/mol-MEA (a typical rich loading). It can be seen that in order for desorption to occur, the surface temperature of the bubble must remain above 390 K, such that the partial pressure of CO_2 in the liquid is above 1 atm.

- The vapour-liquid interface is represented by a moving wall with a velocity field equal to that described by Eqns. 4.3.11-4.3.12:

$$u_r = \frac{U}{2}\sin(\theta)\cos(\theta) \tag{4.3.11}$$

$$u_z = \frac{U}{2}(-\cos^2(\theta)) \tag{4.3.12}$$

These equations have been derived in Appendix C: Stokes Flow Inside and Outside of a Bubble.

4.3.6. **Mesh**

A free quad mesh was used with a maximum element size of d/100 where d is the bubble diameter. A boundary layer mesh was used at the gas-liquid interface due to the greater concentration and temperature gradients that exist at that location. A screenshot of this mesh is presented in Figure 4.4.

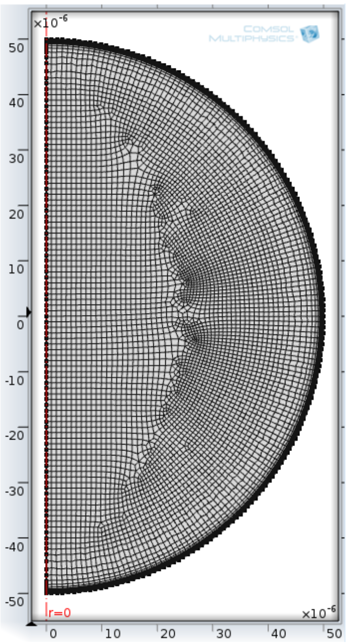

Figure 4.4. A screen shot of the mesh used in the DCR model

This mesh size has been deemed suitable for the purpose of this model following a mesh resolution study, which is presented in Section 4.5.2.

4.3.7. List of Parameters

The parameters used in the direct contact regeneration model are listed in this section. The parameters chosen for the DCR model are depicted in Table 4.1:

Table 4.1. Parameters chosen for the DCR model

Parameter [Units]	Description	Value
d [μm]	Bubble diameter	50, 100, 500, 1000
T_G [K]	Initial gas temperature	600, 500, 400, 298
α [mol-CO_2/mol-MEA]	CO_2 loading	0.2, 0.25, 0.3, 0.35, 0.4
T_L [K]	Initial liquid temperature	298

It was decided not to go above 600 K for the initial gas temperature since this approaches the critical temperature of water (647 K) and therefore some equations used in the model become invalid, e.g. the equation for the latent heat of vapourisation.

4.3.7.1. Global Parameters

The global parameters used in the direct contact regeneration model are presented in Table 4.2:

Table 4.2. Global parameters used in DCR model

Parameter [Units]	Description	Value / Formula	Reference
D [m^2/s]	Diffusion coefficient of vapour into bubble	$1 \cdot 10^{-5}$	(Zimmerman et al., 2013)
g [m/s^2]	Acceleration due to gravity	9.81	N/a
p_{atm} [kPa]	Atmospheric pressure	101.325	N/a
M_{N2} [g/mol]	Molecular mass of nitrogen	28.02	N/a
M_{CO2} [g/mol]	Molecular mass of CO_2	44.01	N/a
R_g [J/kmol/K]	Universal gas constant	8314.5	N/a
$T_{c,H2O}$ [K]	Critical temperature of water	647.096	(Perry and Green, 2008)

Parameter [Units]	Description	Value / Formula	Reference
$T_{c,MEA}$ [K]	Critical temperature of MEA	678.2	(Hilliard, 2008)
U [m/s]	Terminal velocity of bubble	$U = \frac{gR^2(\rho_L - \rho_G)}{3 \cdot \mu_L}$	(Zimmerman et al., 2013)
γ [N/m]	Surface tension of liquid	0.0604	(Vazquez et al., 1997)
μ_L [Pa·s]	Dynamic viscosity of liquid	0.0021	(Li and Lie, 1994)
$c_{p,L}$ [J/kg/K]	Specific heat capacity of aqueous MEA	3418	(Weiland et al., 1997)
ϱ_L [kg/m^3]	Density of aqueous MEA	1003	
ϱ_G [kg/m^3]	Density of gas	$\frac{(p_{atm} + 2\gamma/R)M_G}{R_G T_G}$	
$\varkappa_L$ [W/m/K]	Thermal conductivity of 30 wt.% aqueous MEA	0.48	(Pant and Srivastava, 2007)
x_{MEA}	Mole fraction of MEA	0.12	
x_{H2O}	Mole fraction of H_2O	0.88	

4.3.7.2. *Variable Fluid Parameters*

The variable parameters used in the direct contact regeneration model are presented in Table 4.3:

Table 4.3. Variable parameter values used in this work

Parameter [Units]	Description	Value / Formula	Reference
μ_{CO2} [Pa·s]	Dynamic viscosity of CO_2	$-1.485\cdot10^{-6} + 6.468\cdot10^{-8}\cdot T - 3.662\cdot10^{-11}\cdot T^2 + 1.245\cdot10^{-14}\cdot T^3$	(COMSOL, 2013)
$\varkappa_{CO2}$ [W/m/K]	Thermal conductivity of CO_2	$-0.001325 + 4.140\cdot10^{-5}\cdot T + 6.709\cdot10^{-8}\cdot T^2 - 2.111\cdot10^{-11}\cdot T^3$	(COMSOL, 2013)
$c_{p,CO2}$ [J/kg/K]	Specific heat capacity of CO_2	$459.9 + 1.865\cdot T - 0.002129\cdot T^2 + 1.225\cdot10^{-7}\cdot T^3$	(COMSOL, 2013)

Parameter [Units]	Description	Value / Formula	Reference
μ_{N2} [Pa·s]	Dynamic viscosity of nitrogen	$-1.772\cdot10^{-6} + 6.724\cdot10^{-8}\cdot T - 3.473\cdot10^{-11}\cdot T^2 + 1.012\cdot10^{-14}\cdot T^3$	(COMSOL, 2013)
κ_{N2} [W/m/K]	Thermal conductivity of nitrogen	$3.697\cdot10^{-4} + 9.744\cdot10^{-5}\cdot T - 4.076\cdot10^{-8}\cdot T^2 + 7.685\cdot10^{-12}\cdot T^3$	(COMSOL, 2013)
$c_{p,N2}$ [J/kg/K]	Specific heat capacity of nitrogen	$1088 - 0.3659\cdot T + 7.887\cdot10^{-4}\cdot T^2 - 3.749\cdot10^{-7}\cdot T^3 + 3.176\cdot10^{-11}\cdot T^4$	(COMSOL, 2013)
ρ_G [kg/m^3]	Density of gas	$P\cdot M/8.314/T$	(COMSOL, 2013)
p_{MEA}* [kPa]	Saturation vapour pressure of MEA	$x_{MEA}\cdot\exp(165.87 - 13492/T - 21.9\cdot\log(T) + 1.38\cdot10^{-5}\cdot T^2)$	(Hilliard, 2008)
p_{CO2}* [Pa]	Saturation vapour pressure of CO_2	$1000\cdot\exp(-1225.41 + 36508/T + 195.87\cdot\log(T) + 2.4931\cdot10^{-4}\cdot T^2 + 14.15\cdot\alpha)$	Eqn. 5.2.9
p_{H2O}* [Pa]	Saturation vapour pressure of H_2O	$x_{H2O}\cdot133.322\cdot10$^(7.96999-1670.45/(-44.7638+T))	(Zimmerman et al., 2013)
c* [mol/m^3]	Saturation concentration	$\frac{p^*}{R_G T}$	Ideal Gas Law
ΔH_{H2O}[J/kmol]	Enthalpy of vapourisation of water	$5.2053\cdot10^7\cdot(1-T/T_c)$^$(0.3199 - 0.212\cdot T/T_c + 0.25795\cdot(T/T_c)^2)$	(Perry and Green, 2008)
ΔH_{MEA} [J/kmol]	Enthalpy of vapourisation of MEA	$8.5465\cdot10^7\ (1-T/T_c)^{0.5102}$	(Hilliard, 2008)

4.4. Model 2: Direct Contact Regeneration of [C_2mim][NTf_2]

The governing equations, initial conditions, boundary conditions, and mesh used in this model were the same as those for Model 1 and will therefore not be repeated here. The only significant difference between the two models (apart from the physical and thermodynamic properties of the liquid) is that the rate of evaporation of the ionic liquid was assumed to be zero since ionic liquids are known to have a negligible vapour pressure at atmospheric pressure (Brennecke and Maginn, 2001).

4.4.1. List of Parameters

The physical and thermodynamic properties of $[C_2mim][NTf_2]$ are listed in Table 4.4:

Table 4.4. Physical and thermodynamic properties of $[C_2mim][NTf_2]$

Parameter [Units]	Description	Value / Formula	Reference
M_L [g/mol]	Molecular weight of $[C_2mim][NTf_2]$	391.31	(Sigma-Aldrich, 2012b)
ϱ_L [kg/m^3]	Density of $[C_2mim][NTf_2]$	1523.6	(Sigma-Aldrich, 2012b)
μ_L [Pa·s]	Dynamic viscosity of $[C_2mim][NTf_2]$	0.0386	(Sigma-Aldrich, 2012b)
$c_{p,L}$ [J/mol/K]	Specific heat capacity of $[C_2mim][NTf_2]$	525	(Ge et al., 2008)
$\varkappa_L$ [W/m/K]	Thermal conductivity of $[C_2mim][NTf_2]$	0.13	(Ge et al., 2007)

The heat of reaction between CO_2 and $[C_2mim][NTf_2]$ is -14.2 kJ/mol, which was assumed to be constant for all temperatures (Blath et al., 2011).

Henry's constant for CO_2 in $[C_2mim][NTf_2]$ has been correlated using data from (Finotello et al., 2008) and (Kerlé et al., 2009). Using their experimental data and fitting it to the Antoine equation using a linear regression, the following correlation was obtained (see Figure 4.5):

$$H[atm] = exp(-\frac{1430}{T} + 8.312) \qquad (4.4.1)$$

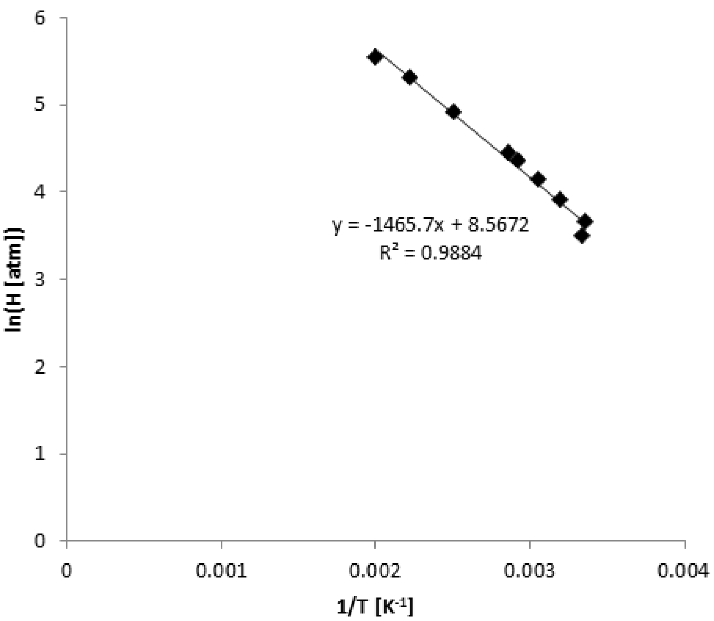

Figure 4.5. Solubilty regression fit for CO_2 in [C_2mim][NTf_2] between 300-500 K

4.5. Model Validation

First, the models will be validated using a face validation technique, whereby qualitative predictions are made and tested to see if these predictions are satisfied by the model. Secondly, the assumptions of the model will be validated.

4.5.1. Face Validation

The following hypotheses will be tested to validate the model:

- Decreasing the bubble diameter increases the rate of mass transfer of CO_2 into the bubble
- Increasing the bubble temperature increases the rate of CO_2 desorption into the bubble (or decreases the rate of absorption into the liquid)
- Increasing the CO_2 loading in the liquid increases the rate of desorption of CO_2 into the bubble
- Increasing the CO_2 concentration in the bubble reduces the rate of desorption of CO_2 into the bubble (or increases the rate of absorption of CO_2 into the liquid)

4.5.1.1. *Increasing Bubble Diameter*

Figure 5.6 and Figure 5.11 show that as the bubble diameter was increased, the maximum concentration of CO_2 in the bubble increased and the peaks occurred earlier since mass transfer was faster.

4.5.1.2. *Increasing Temperature*

Figure 5.4 and Figure 5.10 show that CO_2 was desorbed faster as the initial bubble temperature was increased. Additionally, when the gas was at the same temperature as the liquid (298 K), the CO_2 concentration in the bubble actually decreased since the liquid was not fully saturated and therefore CO_2 was absorbed into the liquid.

4.5.1.3. *CO_2 Loading*

Figure 5.8 and Figure 5.12 show that as the CO_2 loading in the liquid was increased, desorption of CO_2 into the bubble occurred faster.

4.5.1.4. *CO_2 Concentration in the Bubble*

Figure 5.1 and Figure 5.4 show that if a bubble of pure CO_2 is used for direct contact regeneration, desorption occurs far slower than if a bubble of nitrogen is used.

4.5.2. Mesh Sensitivity Analysis

A mesh sensitivity analysis was undertaken to see if the results of the model are sensitive to the mesh size. The three meshes studied are presented in Table 4.5 and are shown in Figure 4.6:

Table 4.5. Mesh Sensitivity Analysis: Mesh Size and Type

	Type	**Max. Element Size [m]**	**Total Number of Elements**
Mesh 1	Free Quad	$10\cdot10^{-7}$	17,469
Mesh 2	Free Quad	$5\cdot10^{-7}$	19,476
Mesh 3	Free Triangular	$10\cdot10^{-7}$	34,432

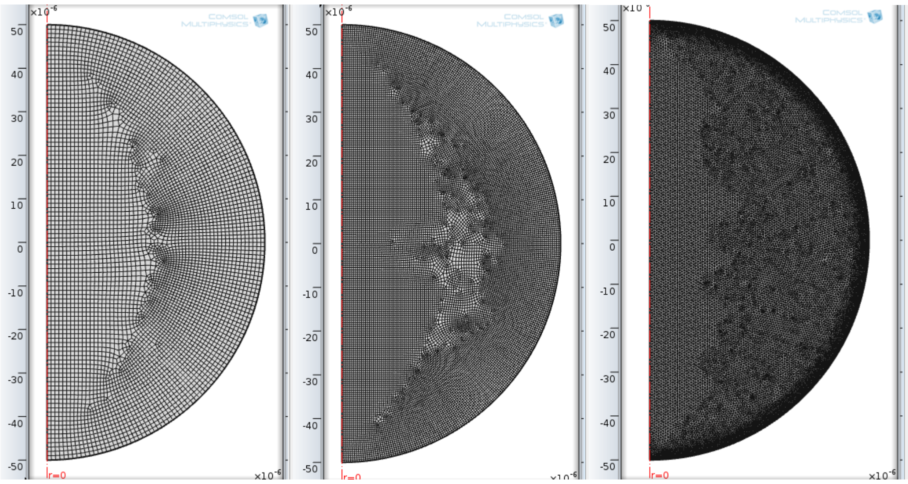

Figure 4.6. Screen shots of the three meshes tested

It is shown in Figure 4.7 that when the maximum element size is reduced by 50 %, the average concentration of CO_2 in the bubble is almost exactly the same. The maximum percentage difference between the concentration of CO_2 in the bubble for Mesh 1 and Mesh 2 was 0.949 %, which occurred at the first time step. Between Mesh 2 and Mesh 3, the maximum percentage difference in the CO_2 concentration in the bubble was 1.14 %, also occurring at the first time step.

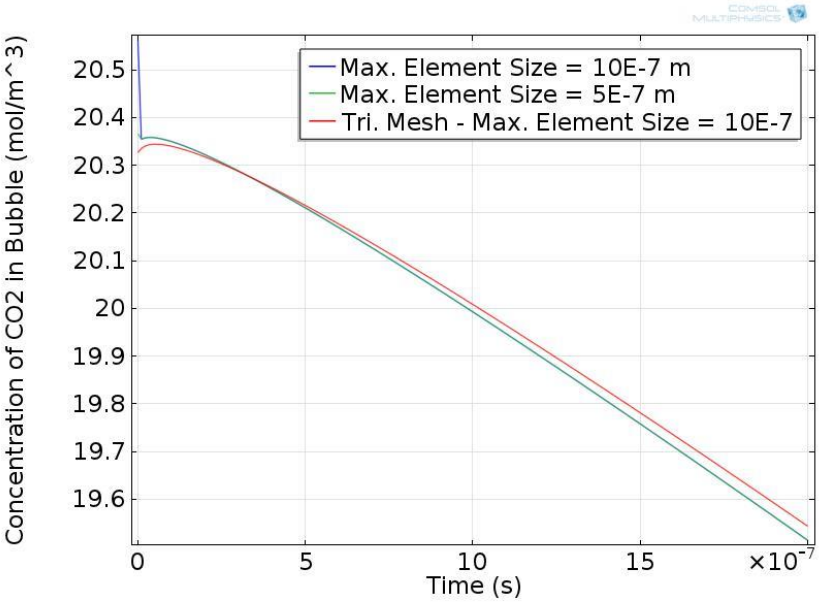

Figure 4.7. Model Validation: Mesh Sensitivity Analysis

4.5.2.1. *Validation Using Dimensionless Parameters*

Another mesh sensitivity study was undertaken using a dimensionless parameter equal to the ratio of mean CO_2 concentration in the bubble at 1 μs to that after 2 μs, referred to hereafter as c_ms. This dimensionless number was used as it takes into account propagation of error with time. This mesh sensitivity study was undertaken using a bubble of diameter 100 μm and a temperature of 600 K in [C_2mim][NTf_2] with a loading of 80% saturation.

The dimensionless parameter, c_ms, has been plotted against maximum element size in Figure 4.8. It can be seen that using both free triangular- and free quad- meshes, the dimensionless value c_ms levels off after a maximum element size of about 1 μm. Reducing the element size further results in longer computation times with only a very slight increase in the accuracy of the computation.

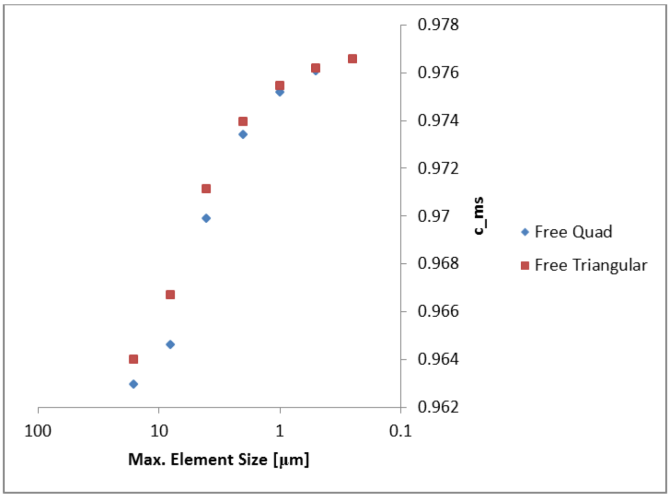

Figure 4.8. Mesh Sensitivity Analysis: c_ms vs. maximum element size

Table 4.6 shows the percentage difference in the value of c_ms as the mesh size was reduced. Starting with a free quad mesh with a maximum element size of 1 μm, the value of c_ms changed by only 0.09 % when the maximum element size was reduced to 0.5 μm. As a result of this mesh sensitivity study, it was decided to use a free quad mesh with a maximum element size of d/100. The decision to choose a free quad mesh over a free triangular mesh was made based upon two factors: firstly, the computation time was smaller for a free quad mesh; secondly, and more importantly, the large radial temperature and concentration gradients at the interface compared with the tangential gradients of these parameters mean that a mesh which has closer nodes in the radial direction than in the tangential direction is preferable; this was best achieved with a free-quad mesh with a boundary layer mesh at the interface.

Table 4.6. Mesh sensitivity analysis: percentage difference study of c_ms

Mesh Type	Max Element Size (μm)	c_CO_2_1, Mean concentration of CO_2 in bubble after 1 μs [mol/m^3]	c_CO_2_2, Mean concentration of CO_2 in bubble after 2 μs [mol/m^3]	c_CO_2_1/ c_CO_2_2	Percentage Difference from smallest mesh size (%)
Free Quad	0.5	19.9929	19.51428	0.976061	
	1	19.97219	19.47602	0.975157	0.09%
	2	19.92635	19.39605	0.973387	0.27%
	4	19.81333	19.21719	0.969912	0.63%
	8	19.53181	18.84089	0.964626	1.17%
	16	19.36824	18.6506	0.962948	1.34%
Free Triangular	0.25	20.00325	19.53421	0.976552	
	0.5	19.99498	19.51872	0.976181	0.04%
	1	19.97777	19.4871	0.975439	0.11%
	2	19.94016	19.42093	0.973961	0.27%
	4	19.85054	19.27709	0.971112	0.56%
	8	19.64548	18.99144	0.966708	1.01%
	16	19.5434	18.83954	0.963985	1.29%

4.5.3. Conservation of Energy

Another method of validating the model is to test whether energy is conserved throughout the simulation time. This was achieved by calculating the energy transferred due to conduction and convection, evaporation, and the heat of reaction, and comparing these with the internal energy of the gas inside the bubble.

The internal energy of the gas inside the bubble, E, is calculated by:

$$E = m_{CO2}c_{p\_CO2}T + m_{MEA}c_{p\_MEA}T + m_{H2O}c_{p\_H2O}T \tag{4.5.1}$$

where m, c_p, and T refer to the mass, specific heat capacity, and temperature of the gas and the subscripts CO_2, MEA, and H_2O represent the three fluids in the bubble.

The internal energy of the bubble is thus given by:

$$E = T \cdot \frac{\pi}{6} d^3 \cdot (c_{CO2}M_{CO2}c_{p_{CO2}} + c_{MEA}M_{MEA}c_{p_{MEA}} + c_{H2O}M_{H2O}c_{p_{H2O}}) \tag{4.5.2}$$

where d is the bubble diameter, c and M represent the concentration and molar mass of the gas.

The energy loss from the bubble during each time step is equal to:

$$E = \Delta t \cdot \frac{\pi}{4} d^2 \cdot (J_{CO2}\Delta H_r + J_{MEA}\Delta H_{e,MEA} + J_{H2O}\Delta H_{e,H2O} + h\Delta T) \qquad (4.5.3)$$

Where Δt is the timestep, d is the bubble diameter, J represents mass flux of a species and ΔH represents the enthalpy of absorption (CO_2) or vaporisation (MEA, H_2O) and h is the heat transfer coefficient.

By comparing the change in the internal energy of the bubble with the rate of energy loss due to heat and mass transfer, it can be seen whether energy is conserved in the model. This is shown in Figure 4.9. Here, the energy discrepancy between the two equations has been normalised by dividing by the internal energy of the gas inside the bubble at t=0 s.

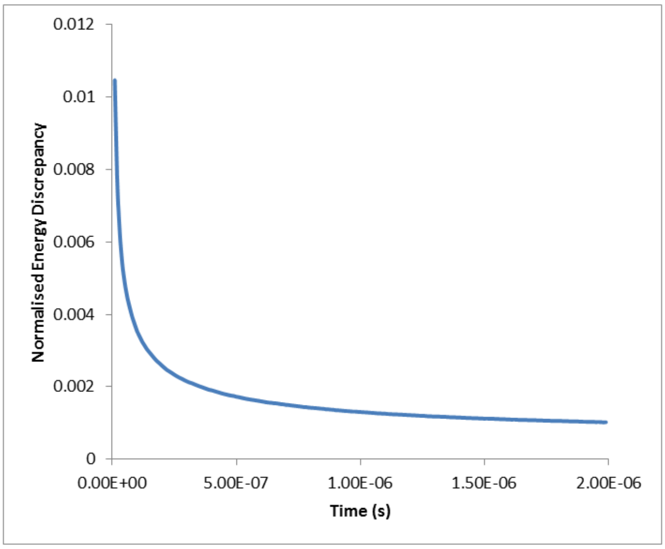

Figure 4.9. Model Validation: Conservation of Energy

It can be seen in Figure 4.9 that the energy discrepancy between the bubble internal energy and the energy loss from the bubble is less than 1.2 % of the initial bubble internal energy for all time steps considered in the simulation. Since this model is intended to determine whether the direct contact regeneration technique is theoretically feasible, rather than to provide a fully predictive model, this level of energy discrepancy is deemed suitable for its purpose.

4.5.4. **Validation of Model Assumptions**

The assumptions used in the model, outlined in Section 4.3.3, are validated here.

- The bubble is spherical

Clift et al. outlined the conditions for which a bubble is spherical. In general, this occurs when Re < 1 and/or Eö < 1. For a bubble of diameter 100 μm rising at its terminal velocity in aqueous MEA, the Reynolds number is 0.82 and the Eötvös number is equal to 0.001. In the ionic liquid [C_2mim][NTf_2], the Reynolds number and Eötvös number are 1.3 and 0.41 respectively. The bubble is clearly spherical in this regime.

- The bubble is of constant diameter

In a real system, the bubble radius, R, would change according the Rayleigh-Plesset equation:

$$\frac{d^2R}{dt^2}+\frac{3}{2R}\left(\frac{dR}{dt}\right)^2+\frac{4\mu_L}{\rho_L R^2}\frac{dR}{dt}+\frac{2\gamma}{\rho_L R^2}-\frac{P_B-P_L}{\rho_L R}=0 \qquad (4.5.4)$$

To validate the assumption of constant bubble diameter, the above equation has been solved in COMSOL Multiphysics for a bubble of initial diameter 100 μm and initial temperature of 600K in both a 30 wt.% aqueous MEA solution (Model 1) and [C_2mim][NTf_2] (Model 2). These values were chosen since they resulted in the greatest amount of mass transfer and hence are likely to produce the largest change in bubble size.

The pressure inside the bubble, P_B, is defined by:

$$P_B=\left(\frac{R_0}{R}\right)^3 R_G T(c_{CO2}+c_{H2O}+c_{MEA}+c_{N2}) \qquad (4.5.5)$$

The bubble diameter as a function of time produced from the Rayleigh-Plesset equation is shown in Figure 4.10. It can be seen that in [C_2mim][NTf_2], over the timescale of the model (10^{-4} s), the bubble diameter varied between 95 μm and 104 μm, representing a maximum variation in bubble diameter of 10 %. In aqueous MEA, the bubble diameter was found to vary between 76 μm and 100 μm over the same timescale, representing a maximum change in bubble diameter of 24%. While this is a moderately significant decrease, since the Reynolds and Péclet numbers would still be of the same order of magnitude, the governing physics would be the same; thus the assumption was deemed sufficient for the purpose of this study where the aim is to investigate the feasibility of using the DCR technique rather than to produce a fully predictive model.

It must be noted that in reality, as the bubble expands, the partial pressure inside the bubble drops, thus increasing the driving force for mass transfer. The effect of bubble size on mass transfer was considered negligible in this model. If this were taken into account, the increase in mass transfer would cause the bubble size to be reduced by a smaller amount or possibly increase.

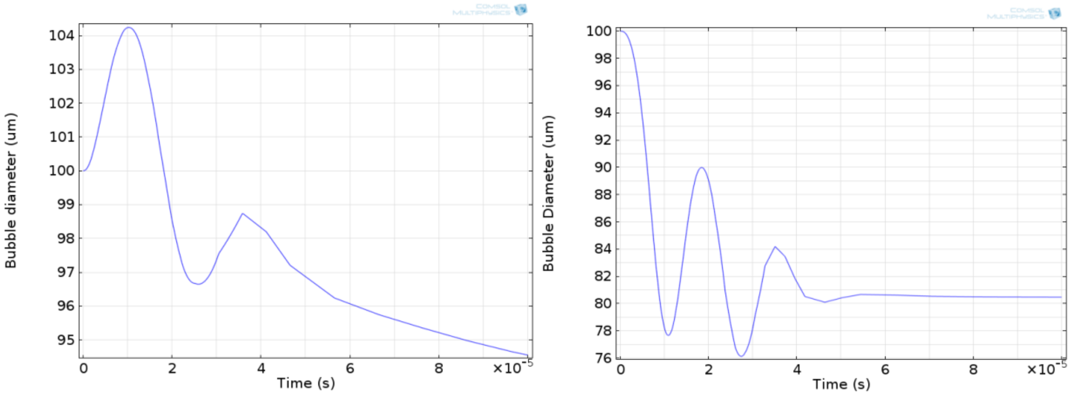

Figure 4.10. Bubble diameter as a function of time in [C_2mim][NTf_2] (left) and aqueous MEA (right); d=100 μm, T_G=600 K

A temporal oscillation in bubble diameter can be seen in Fig. 4.10. When mass transfer is present, bubbles are known to oscillate while the forces acting on the bubble are achieving equilibrium due to the nonlinearity of the Rayleigh-Plesset equation. They oscillate at their natural frequency, which varies depending on the physical properties of the liquid and the bubble size. For a bubble of diameter 100 μm in both [C_2mim][NTf_2] and 30 wt.% aqueous MEA, the time period of oscillation is 22 μs and 18 μs respectively (using the formula of Nigmatulin et al. (1981)), which is consistent with time period of oscillation as conveyed in Figure 4.10.

- There are no surface contaminants on the bubble affecting fluid flow, heat or mass transfer

This assumption would have to be verified experimentally to be certain of whether surface contaminants exist on the bubble surface.

Experiments in bubble columns have shown that bubble surface contamination occurs faster as the bubble size is reduced (Clift et al., 1978). Surface contamination is known to reduce the mobility of the bubble interface. As a result, the bubble rise velocity decreases so the bubble residence time increases. However, the reduction in mobility of the bubble interface also reduces the gas velocity inside the bubble. This means that the rate of mass transfer by convection is reduced.

It is also known that when mass transfer is present, surface tension gradients exist along the bubble interface, which can mobilise the interface and increase the rate of mass transfer. This is known as the Marangoni Effect. The assumption that the bubble is not affected by surface contamination would have to be verified experimentally. Since the bubble velocities in this work are so small, the majority of mass transfer is diffusive (see Eqn. 5.1.1).

- The bubble rises in the vertical direction at its terminal velocity

In a single bubble experimental setup, so long as the column is sufficiently large, and the liquid level is sufficiently high, the bubble can be expected to rise at its terminal velocity. In reality, in order to make the regeneration process more practical, a swarm of bubbles would be used. This may increase the velocity of the bubbles due to coalescence and the effects of bubble wakes.

It is useful to estimate the time taken for a bubble to reach its terminal velocity to determine if this assumption is accurate. For a bubble of diameter 100 μm rising in a liquid, the buoyancy force is of the order 10-8 N. Assuming Stokes drag, the drag force is likely to lie between v•10-6 N and v•10-4 N where v is the bubble velocity. By applying Newton's second law and solving the first order differential equation with the initial condition that the bubble is at rest at t=0 s, it can be shown that the time taken for the bubble to reach 95% of its terminal velocity is of the order 10-6 s. Therefore, for a column height of the order 10-3 m or greater, the bubble will be travelling close to its terminal velocity for the majority of its rise time.

However, this estimate is for a single bubble rising in a column of liquid. For a swarm of bubbles, since a rising bubble is likely to be travelling in the wake of another bubble, it is likely to be moving faster than the terminal velocity. Additionally, in swarms of bubbles, the bubbles can coalesce and breakup. At low flow rates such as the ones used in this work, the bubbles are more likely to coalesce than break up, which is likely to reduce the bubble residence time. However, the currents in the liquid can also cause the bubbles to move parallel to the diffuser as well as perpendicular, which would increase the bubble residence time.

- CO_2 and aqueous MEA on the vapour-liquid interface flash to saturation

In models such as the ones presented in this chapter, the boundary conditions are the least well known feature since they are difficult to measure experimentally. Moreover, the gas-liquid interface in a real system has a finite thickness, whereas in the aforementioned models it has been treated as being infinitesimally thin. Such an approach implies an infinite concentration gradient at the interface. Since COMSOL Multiphysics uses the Galerkin method to approximate solutions to partial differential equations, having a model with infinite gradients can be problematic. Therefore, in order to stabilise the model, a step function was used whereby the concentrations at the interface increase from zero to saturation in a finite time period. Despite the problems with this assumption, it is a common Dirichlet boundary condition used in models in order to provide a driving force for heat and mass transfer (Zimmerman et al., 2013, Incropera, 2011). Figure 4.11 shows that the timescale of the step function was appropriate since reducing the timescale by two orders of magnitude made little difference to the concentration profiles of CO_2 and H_2O in the bubble during the timescales of interest.

In practice, a bubble interface has a finite thickness, which is of the order of 1 μm for a microbubble (Bredwell and Worden, 1998), however in this model the interface was assumed to be infinitesimally thin. This assumption has been made in similar models, e.g. (Zimmerman et al., 2013). Since the concentrations at the bubble surface are assumed to flash to saturation, the mass transfer gradients and therefore the mass transfer rates predicted by this model are artificially high. Similarly predicted heat transfer rates due to conduction are also artificially high in this model.

Since conservation of energy was modelled by assuming a heat sink at the interface, the rate of heat loss from the bubble due to evaporation and desorption is therefore also artificially high. As a result, during the first few time steps of the simulation the predicted rates of heat and mass transfer at the bubble interface are likely to be greater than would be observed in practice.

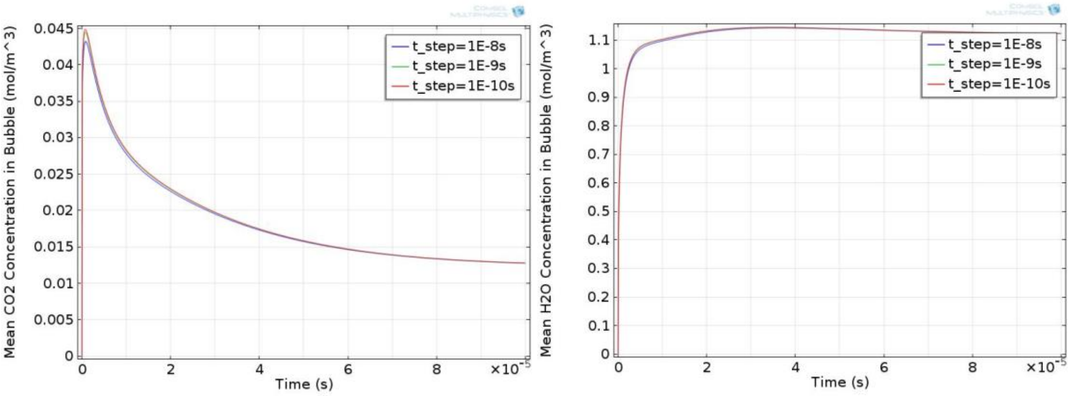

Figure 4.11. Step function validation: influence of step function time on concentrations of CO_2 and H_2O for a nitrogen bubble with d=100 μm, $T_{G,0}$=600K and loading=0.4

- The CO_2 loading in the liquid is constant

Although the CO_2 loading in the liquid will change with time during desorption, the change in concentration during the model simulation time ($\sim 1 \cdot 10^{-4}$ s) is likely to be negligible.

5. Direct Contact Regeneration of MEA and Ionic Liquids

The results of the direct contact regeneration models using 30 wt. % aqueous MEA (Model 1) and [C_2mim][NTf_2] (Model 2) are presented in sections 5.1 and 5.2. These models used the methods outlined in Sections 4.3 and 4.4 respectively.

5.1. Model 1: Direct Contact Regeneration of MEA

5.1.1. Direct Contact Regeneration of MEA using CO_2

Figure 5.1 shows the concentrations of CO_2, H_2O, and MEA in the bubble against time between 0 – 100 μs for a bubble of diameter 100 μm containing pure CO_2 at t=0 with an initial temperature of 600 K and a constant CO_2 loading of 0.4 mol-CO_2/mol-MEA in the liquid phase. The concentration of CO_2 in the bubble is initially 20.8 mol/m^3 and decreases to 0.44 mol/m^3 after 100 μs. This occurs because during the first 0.1 μs of the simulation, the mean interface temperature reduces from 598 K to 377 K (see Figure 5.2). The partial pressure of CO_2 at the interface at 377 K, as determined by Eqn 4.3.10, is equal to 36.7 kPa. Since this is less than the partial pressure of CO_2 in the bubble (102.6 kPa), absorption of CO_2 into the aqueous MEA solution occurs, rather than desorption. The rapid initial reduction in the interface temperature was primarily due to the evaporation of H_2O, as will be shown in Section 5.3.

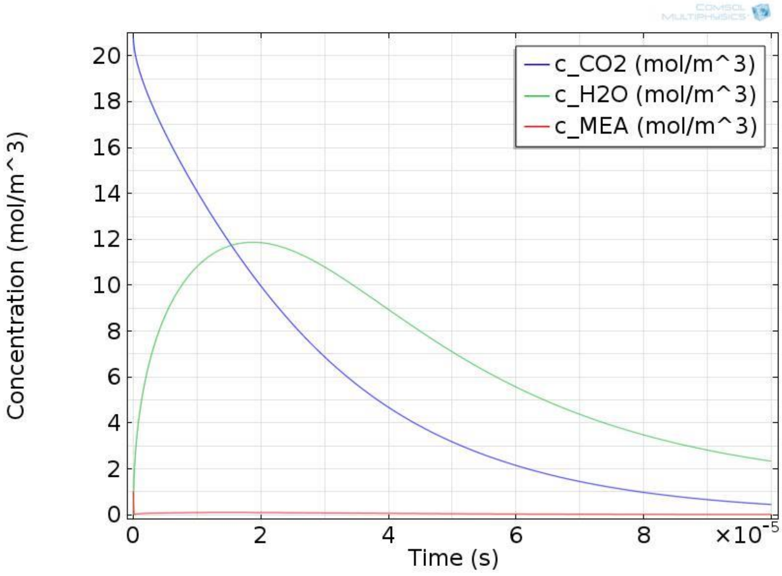

Figure 5.1. Concentration of CO_2 in vapour phase vs. time in direct contact regeneration model: CO_2 bubble

The concentration of H_2O in the bubble, which is initially 0 mol/m^3, increases to 11.87 mol/m^3 within 18.8 μs. After 18.8 μs, the temperature of the vapour decreases sufficiently that H_2O condenses. During this period, the reduction in temperature of the bubble is solely due to conduction to the liquid phase. After 100 μs, the H_2O concentration in the bubble is 2.33 mol/m^3. If the simulation were to run for longer, it would decrease gradually to 1.12 mol/m^3, which is the saturation vapour concentration of H_2O at 298 K according to the equation used in this model.

Since MEA has a much lower vapour pressure than H_2O, evaporation of MEA was almost negligible; the mean concentration of MEA in the bubble peaked at just 0.1 mol/m^3.

One can see from Figure 5.2 that there exists a discontinuity at t=0. This is caused by assumptions that the species flash to saturation on the bubble surface and that the vapour-liquid interface does not have a thickness. These assumptions have been explained in Section 4.5.4. Although a step function was introduced, such that the concentration took 10^{-8} s to reach saturation in an attempt to reduce this effect, it can be seen that it has not completely negated it. In reality, since the interface has a finite thickness, concentration and temperature gradients at the interface would likely be smaller. Hence, the rate of mass transfer is likely to be over-predicted by this model. Nevertheless, it is a reasonable first attempt to assess the feasibility of DCR.

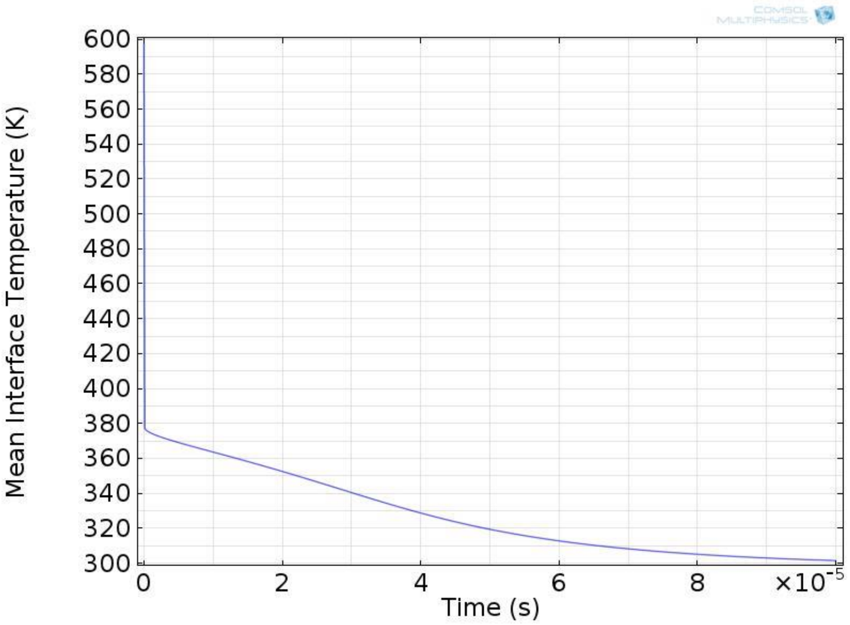

Figure 5.2. Mean surface temperature of bubble vs. time (d=100 μm, T_G=600 K, α=0.4)

Figure 5.3 illustrates the mean vapour temperature in the bubble. This was found to decrease from 600 K to 307 K within 100 μs. In contrast to the surface temperature, the mean vapour temperature decreased very gradually since the heat had to conduct away from the centre of the bubble before being transferred to the liquid.

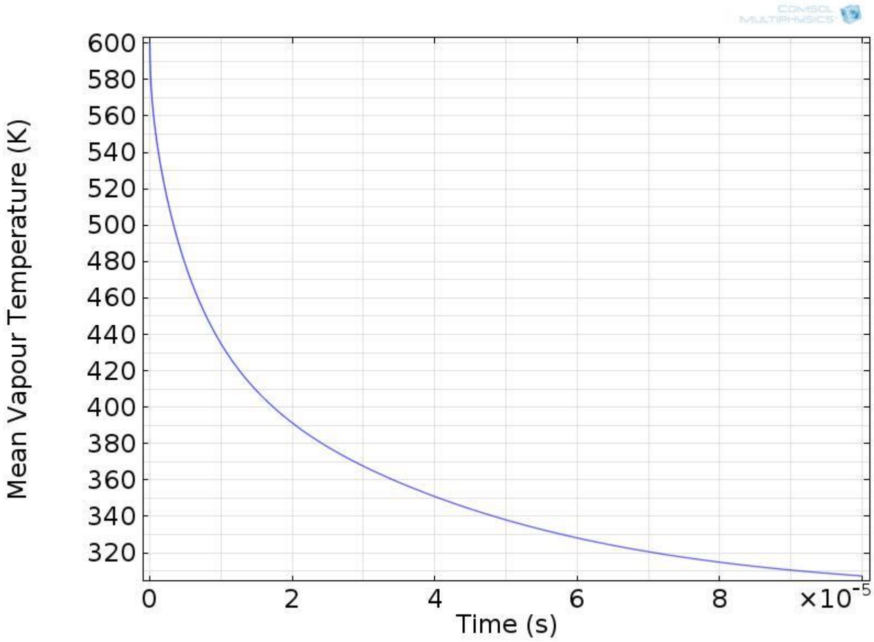

Figure 5.3. Mean temperature of vapour phase vs. time (d=100 μm, T_G=600 K, α=0.4)

Whilst in most systems mass transfer is advection dominated (since this is usually a faster mode of mass transfer), as the size of the system is reduced, mass transfer becomes increasingly dominated by diffusion (Gad-el-Hak, 2001, Tesař, 2007). The Péclet number, defined as the ratio of advective to diffusive mass transfer, can be used to identify which mode of mass transfer is dominant in a system. The terminal velocity of the bubble, according to the Hadamard-Rybczinski equation is equal to 0.0039 ms^{-1}.

The characteristic velocity to be used when calculating the Peclet number is that far from any boundaries (i.e. the bubble surface). Here, the characteristic velocity to be used for calculating the Peclet number inside the bubble is that in the centre of the bubble, which is equal to $U_T/2$.

Inside the bubble, the Péclet number is thus equal to:

$$Pe = \frac{d \cdot U_t/2}{D} = \frac{10^{-4} \cdot \frac{0.0039}{2}}{10^{-5}} = 0.02 \tag{5.1.1}$$

This low value of the Péclet number indicates that the majority of mass transfer is diffusive. Since the diffusion coefficient used in this model is equal to 10^{-5} m^2/s, one would expect the concentrations to stabilise after about 1 ms ($(10^{-4})^2/10^{-5}$). In a real system, mass transfer would be dominated by the liquid side since the gas diffusivity in the liquid is approximately four orders of magnitude slower. As a result, while evaporation of water is likely to happen on the same timescale, transfer of CO_2 into or out of the bubble is likely to be slower since the MEA-CO_2 products have to diffuse through the liquid before they reach the gas-liquid interface.

Since the diffusion coefficient in the liquid phase is much lower than that in the gas phase, CO_2 would have to diffuse through the liquid first before being transferred to the gas phase. Hence, the rate of CO_2 transfer would be liquid-side dominated. In order to model how this would affect the rate of CO_2 transfer into the bubble, a shell and core model would have to be used. It was chosen not to use such a model in this work since it would involve additional assumptions being made regarding the parameter values in either the Level Set Method or Phase Field Method.

Although the results here suggest that direct contact regeneration of MEA is unfeasible, the initial bubble temperature was only 600 K. Unfortunately, temperatures greater than this could not be modelled since the model became unstable at higher temperatures. The reason for this was because the critical point of water is 647 K, and thus water can only exist in the gas phase above this temperature. However, experimentally it may be possible to desorb CO_2 from aqueous MEA solutions at higher temperatures.

5.1.2. Direct Contact Regeneration of MEA using Nitrogen

Since regenerating MEA using a superheated CO_2 bubble appears to be unfeasible, direct contact evaporation of aqueous MEA using a nitrogen bubble will now be investigated. This has the advantage that CO_2 can be more easily desorbed from the liquid since the partial pressure of CO_2 in the bubble is lower; however, such a process for MEA regeneration would not be useful for integration with CDU processes since the gas stream exiting the column would be impure.

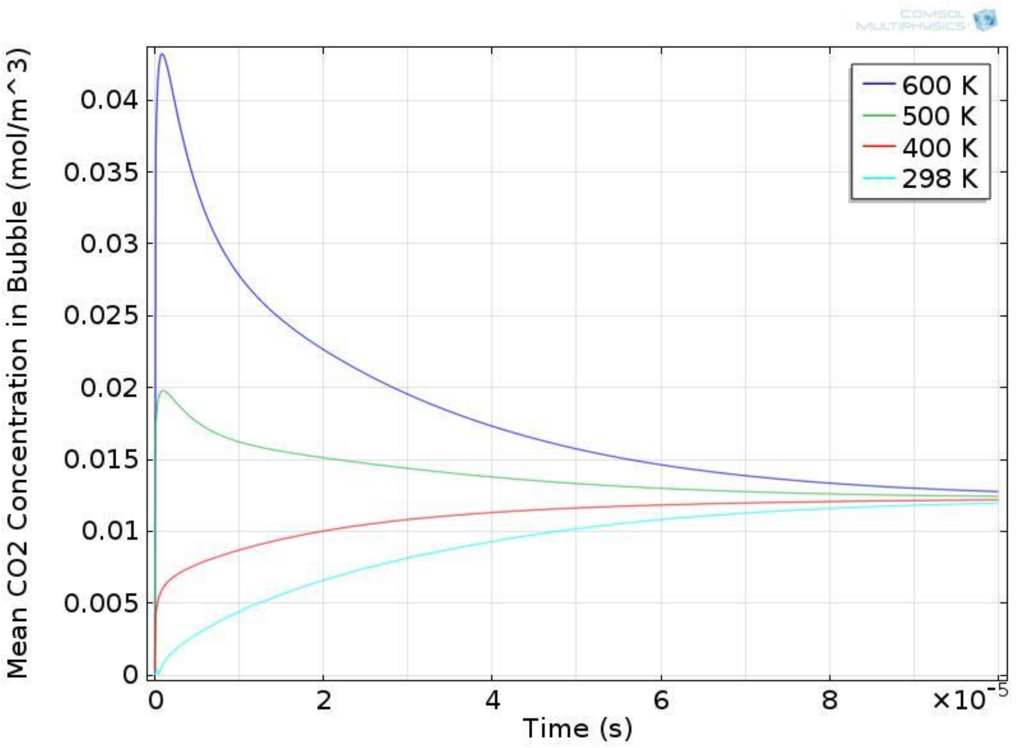

Figure 5.4. Concentration of CO_2 in vapour phase vs. time: nitrogen bubble (d=100 μm, α=0.4)

The initial bubble temperature has been varied between 298 K – 600 K to examine the effect of temperature on the rate of CO_2 desorption from a loaded MEA solution. Figure 5.4 shows that the concentration of CO_2 in the vapour phase increases when a 100 μm bubble of superheated nitrogen rises through the liquid. As expected, increasing the initial temperature of the gas has the effect of increasing the rate of CO_2 desorption; for a bubble with an initial temperature of 600 K, the maximum concentration of CO_2 in the bubble reaches 0.043 mol/m^3; reducing the initial temperature to 500 K reduces the maximum CO_2 concentration to 0.020 mol/m^3; reducing it further still to 400 K reduces the maximum CO_2 concentration to 0.012 mol/m^3. For initial bubble temperatures of 600 K and 500 K, the maximum amount of desorption occurs on a timescale less than 1 μs. It is noteworthy to mention that after 100 μs, the mean CO_2 concentration in the bubble is between 0.012-0.013 mol/m^3 for all of the initial bubble temperatures studied. Thus, the benefits gained from heating the vapour are reduced as the residence time is increased (see Figure 5.4). Therefore, a thin layer of aqueous MEA would be used in practice.

The timescales for mass transfer to occur as predicted by this model are of the order of 10^{-5} s, as can be seen in Figure 5.5. Since the terminal velocity of the bubble is 0.0039 m/s, the liquid height would have to be ~0.1 µm. This is three orders of magnitude smaller than the bubble diameter, implying that for such a process to work in practice, the bubble would not be fully formed before leaving the column. Therefore this model cannot accurately predict the rate of mass transfer in the bubble column.

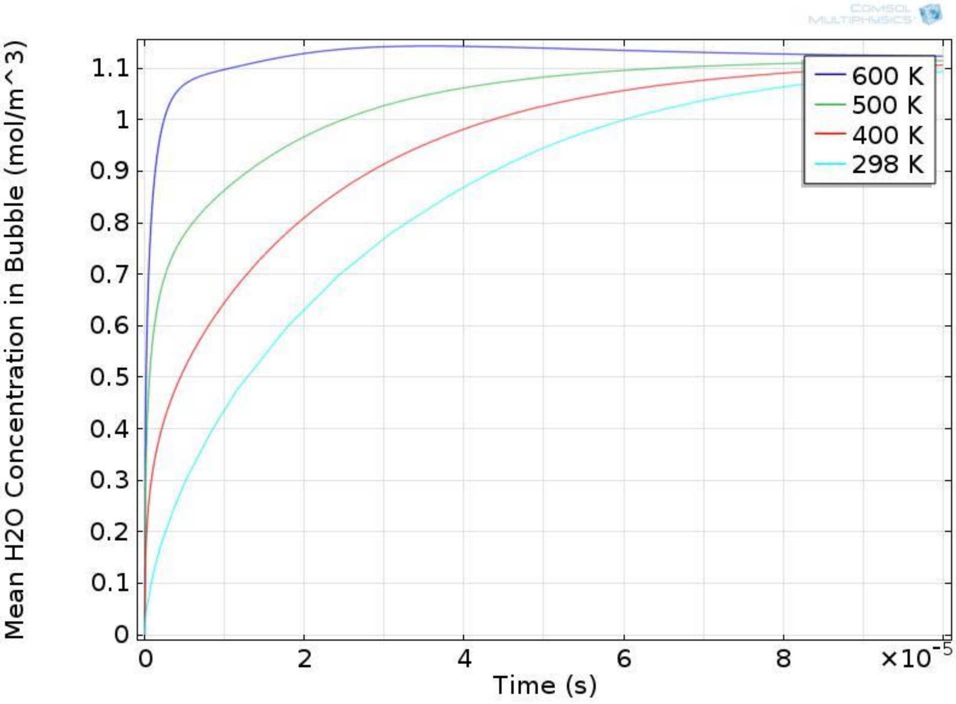

Figure 5.5. Concentration of H_2O in vapour phase vs. time: nitrogen bubble (d=100 µm, α=0.4)

The effect of initial bubble temperature on the amount of H_2O desorption into the bubble is presented in Figure 5.5. As expected, as the initial vapour temperature is increased, the rate of evaporation of H_2O into the bubble increases. This is consistent with the model of (Zimmerman et al., 2013). Although the initial rate of evaporation is greater at higher initial vapour temperatures, the mean H_2O concentration in the bubble settles at approximately 1.1 mol/m^3 after 100 µs, independent of initial vapour temperature.

The effect of bubble diameter on the mean CO_2 concentration in the bubble is presented in Figure 5.6 for an initial gas temperature of 600 K and a CO_2 loading of 0.4. It can be seen that the mean CO_2 concentration in the bubble rises to 0.042 mol/m^3, 0.037 mol/m^3, 0.019 mol/m^3, and 0.011 mol/m^3 for bubble diameters of 50 μm, 100 μm, 500 μm, and 1000 μm respectively. As the mean bubble diameter is reduced, the rate of re-absorption of CO_2 into the liquid increases. This can be explained by Figure 5.7, which shows the mean H_2O concentration in the bubble for the same bubble diameters. As the bubble size is reduced, the rate of evaporation of H_2O into the bubble increases due to the higher surface area for mass transfer. As a result, the temperature of the bubble decreases faster and therefore the rate of reabsorption of CO_2 into the liquid increases. Again, most of the heat loss from the bubble in the first few microseconds of the simulation is due to evaporation. After the initial rapid evaporation period, the energy loss from the bubble is mainly due to conduction. Since both of these means of heat transfer are dependent on surface area, the temperature of the bubble (and the mean CO_2 concentration in the bubble) decreases faster as the bubble size is reduced.

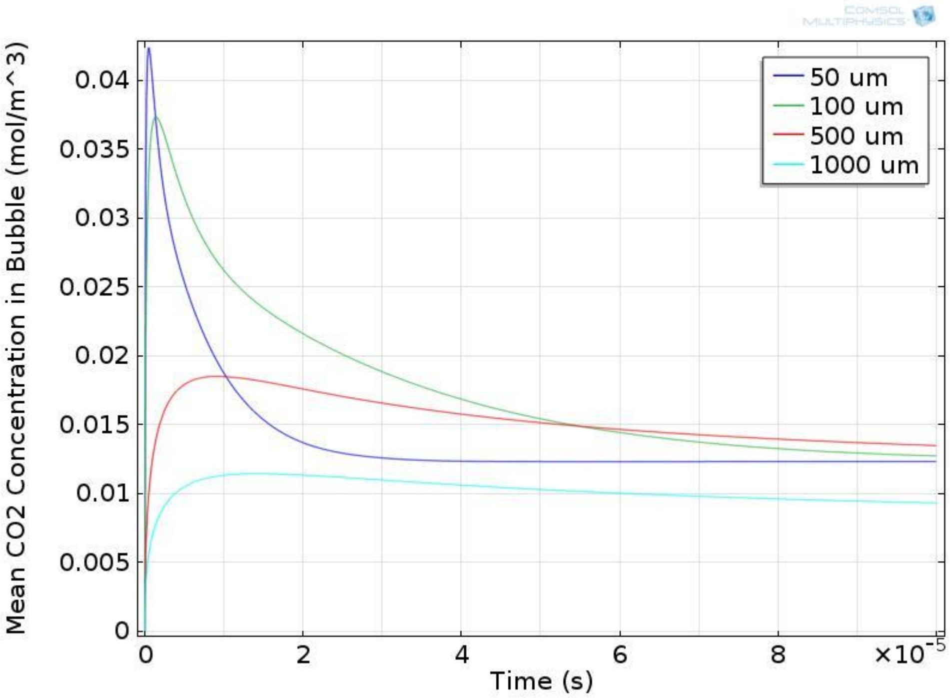

Figure 5.6. Direct contact regeneration using nitrogen: effect of bubble diameter of CO_2 desorption (T_G=600 K, α=0.4)

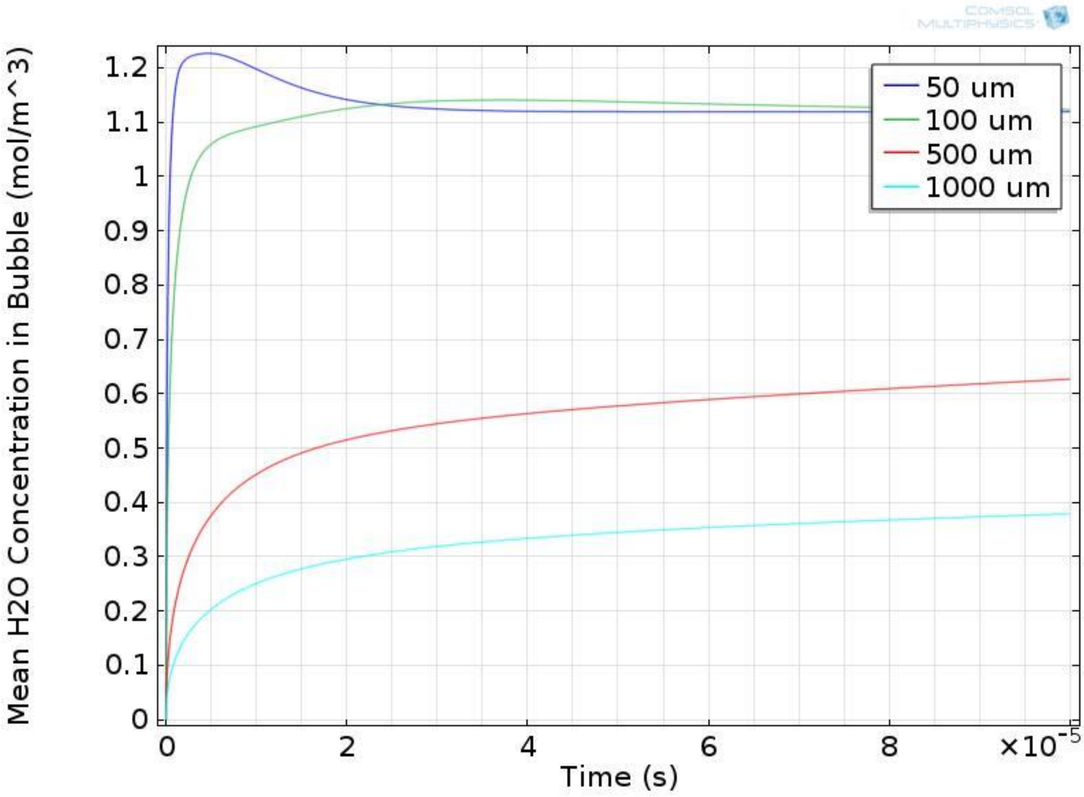

Figure 5.7. Direct contact regeneration using nitrogen: effect of bubble diameter on H_2O concentration (T_G=600 K, α=0.4)

The effect of CO_2 loading in the liquid on the amount of desorption into the bubble is presented in Figure 5.8 for an initial vapour temperature of 600 K and a bubble diameter of 100 μm. As expected, more CO_2 can be desorbed into the bubble if there is a higher CO_2 loading in the liquid phase since the partial pressure of CO_2 is greater. For loadings of 0.20, 0.25, 0.30, 0.35, and 0.40 mol-CO_2/mol-MEA the maximum CO_2 concentrations in the bubble were 0.004, 0.007, 0.013, 0.024, and 0.043 mol/m^3 respectively, with the maximum amount of desorption peaking within 1 μs of each simulation. The rate of evaporation of H_2O into the bubble is largely independent of CO_2 loading, as shown in Figure 5.9, since most of the heat loss is due to conduction and evaporation.

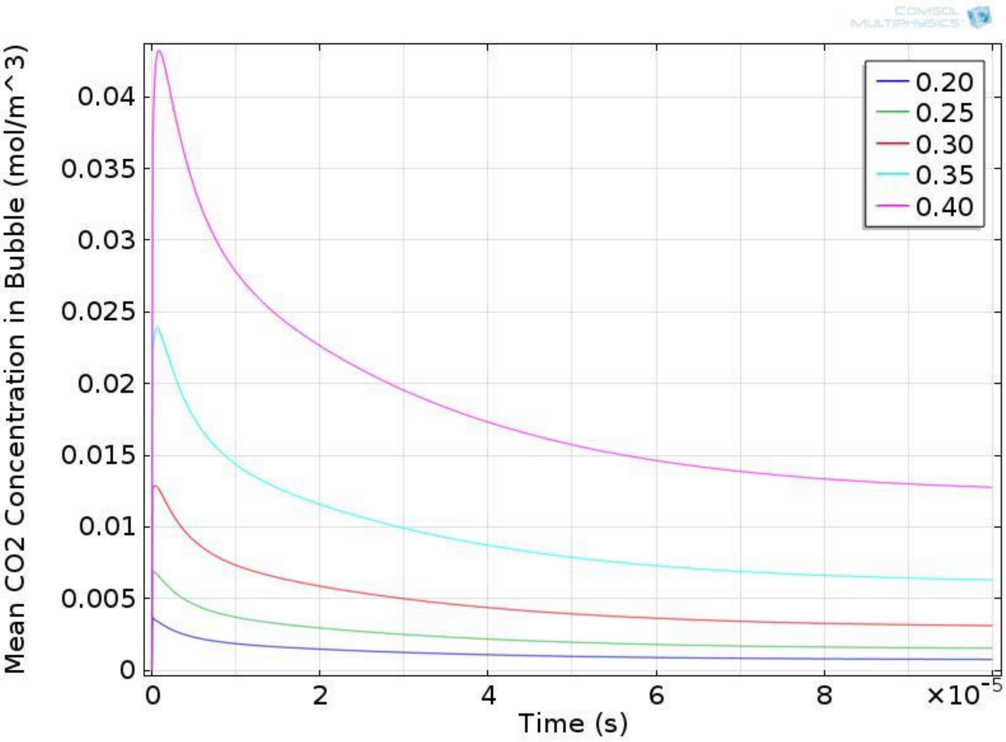

Figure 5.8. Direct contact regeneration using nitrogen: effect of CO_2 loading on rate of desorption (T_G=600 K, d=100 μm)

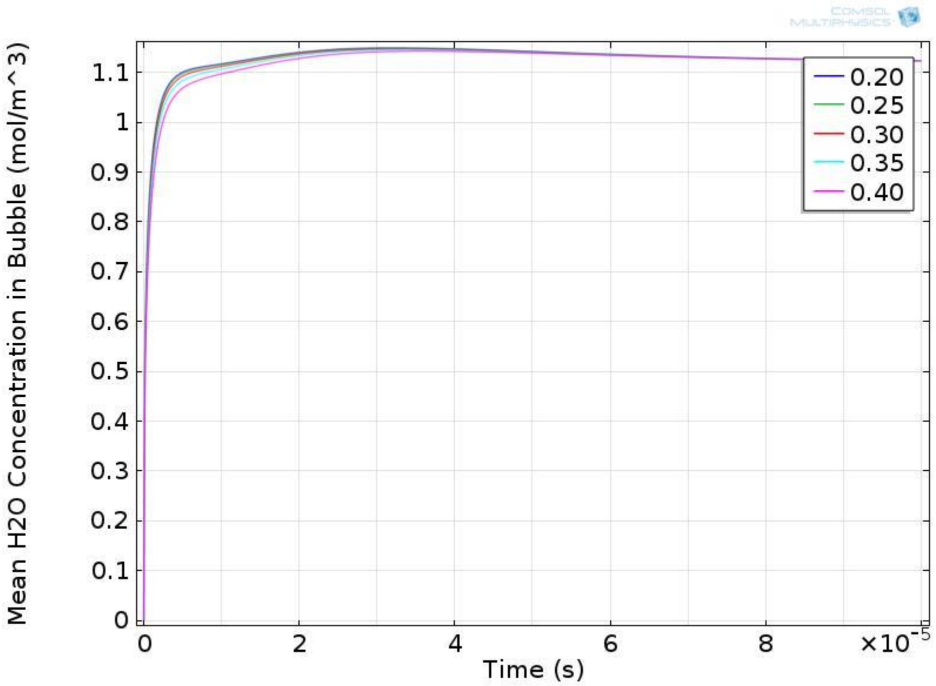

Figure 5.9. Direct contact regeneration using nitrogen: effect of CO_2 loading on H_2O concentration (T_G=600 K, d=100 μm)

5.2. Model 2: Direct Contact Regeneration of [C_2mim][NTf_2]

The rate of desorption of CO_2 from [C_2mim][NTf_2] using the direct contact regeneration method with superheated CO_2 microbubbles has been modelled here. Using CO_2 microbubbles allows for the outlet gas from the column to be pure CO_2; hence it can be used in conjunction with CCS and CDU processes.

Figure 5.10 shows how the concentration of CO_2 in the microbubble varies with time for a bubble of diameter 100 μm inside the ionic liquid. The ionic liquid is assumed to be 80% saturated with CO_2, which is approximately the same saturation percentage as a rich MEA loading. The results show that for initial temperatures of 500 K and 600 K in the vapour phase, the CO_2 concentration increases by 40% and 69% respectively in the first 50 μs before falling slowly. However, for an initial bubble temperature of 400 K, the CO_2 concentration inside the bubble does not increase significantly. As one would expect, for an initial bubble temperature of 298 K, the concentration of CO_2 in the bubble actually decreases as CO_2 is absorbed into the ionic liquid. Moreover, since desorption occurs more slowly in [C_2mim][NTf_2] than it does in the aqueous MEA solution, there is a much larger timescale for which there is net desorption into the bubble.

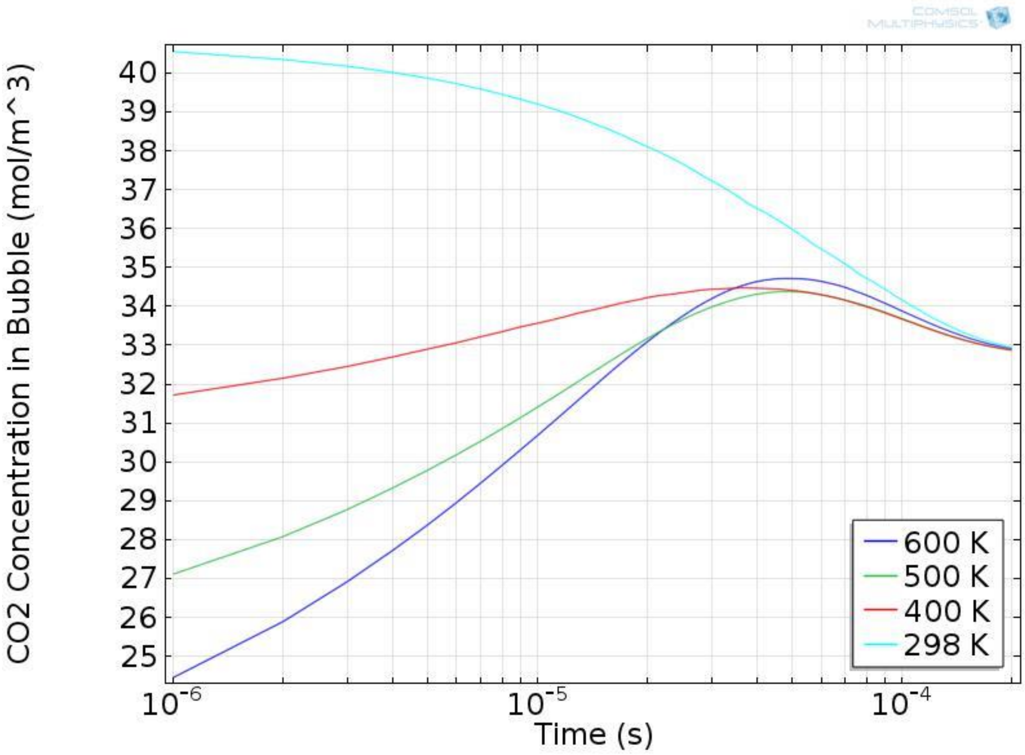

Figure 5.10. Model 2: Effect of initial bubble temperature on the rate of CO_2 desorption from [C_2mim][NTf_2] (d=100 μm; x=0.8)

It must be noted here that in reality, the bubble size would vary with time due to changes in the amount of gas and bubble temperature. In this model, since the change in bubble size is not taken into account, there is an extra resistance to mass transfer as the concentrations are artificially high. Therefore, the amount of CO_2 desorption produced by this model is likely to be underestimated.

The effect of bubble diameter on the rate of CO_2 desorption from the ionic liquid is shown in Figure 5.11 for an initial gas temperature of 600 K. For all bubble diameters studied (50 μm – 1000 μm), the CO_2 concentration in the bubble increases from its initial value of 20.3 mol/m^3 before reducing and then settling at 32.8 mol/m^3. As the bubble size is reduced, the maximum CO_2 concentration in the bubble increases and the rate of desorption increases.

At t=0, the concentration of CO_2 inside the bubble is approximately 20.3 mol/m^3 (as predicted by the Ideal Gas Law). Between t=0 and t=1 μs, the concentration value increases from this value to the values shown in Fig. 5.11.

Fig. 5.11 implies that there would not be a significant difference between using microbubbles compared with using fine bubbles since the concentration of CO2 in the bubble converges to the same value if the contact time is large enough (>1 ms). In practice the contact time is likely to be far greater than this.

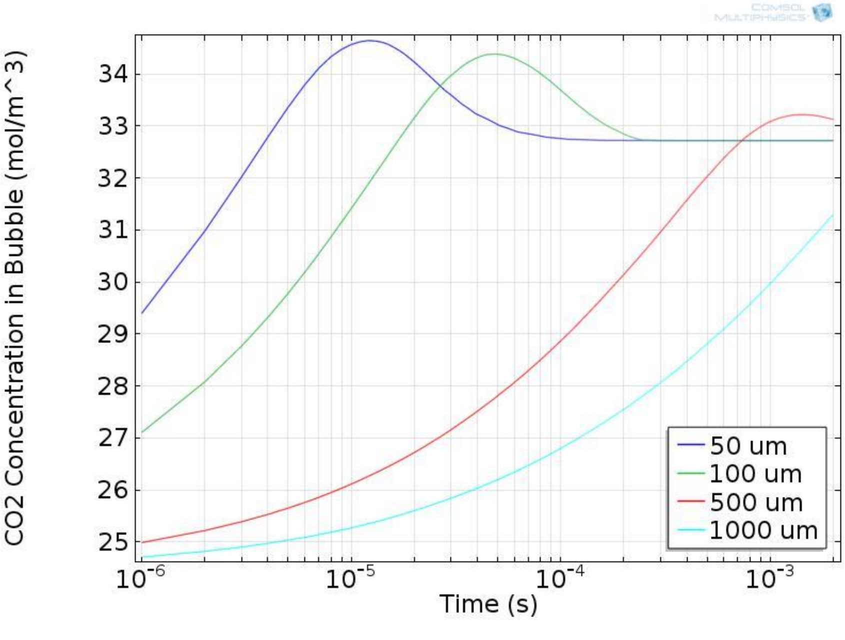

Figure 5.11. Model 3: Effect of bubble diameter on the rate of CO_2 desorption from [C_2mim][NTf_2] (T_G=600 K; x=0.8)

The effect of the level of CO_2 saturation in the ionic liquid has also been examined since there is no data in the literature which states what a reasonable level of saturation is for an ionic liquid. Ideally, one would like to completely saturate the liquid; however, the rate of absorption slows significantly as the liquid tends to saturation and thus a lower level of saturation may be desirable.

Figure 5.12 shows the results for a bubble of diameter 100 μm with an initial gas temperature of 600 K for a range of saturation levels. As the CO_2 concentration in the liquid increases, the rate of desorption increases since the partial pressure of CO_2 at the interface is greater. Also, when the CO_2 concentration in the liquid is greater, the CO_2 concentration in the bubble peaks later, allowing for a longer bubble residence time.

Fig. 5.12 implies that the liquid would need to be near fully saturated in order for a significant amount of CO2 to be desorbed using DCR. If the liquid is less than 60% saturated then DCR is likely to be unfeasible.

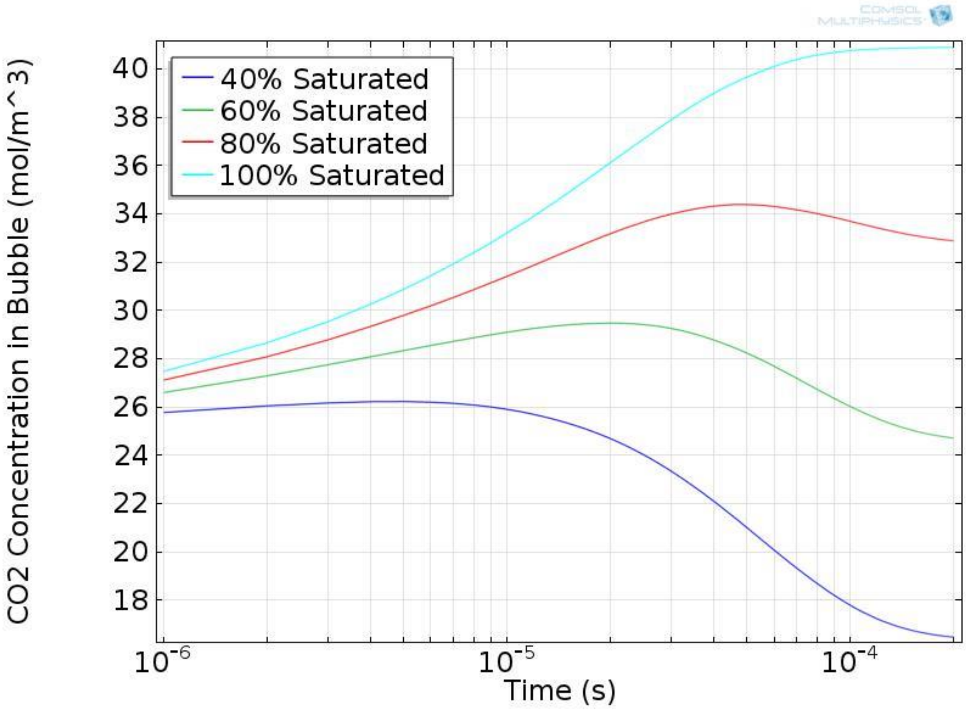

Figure 5.12. Effect of CO_2 concentration in the liquid on the rate of desorption into the bubble (d=100 μm; T_G=600 K)

5.3. Energy Assessment

5.3.1. Aqueous MEA: Direct Contact Regeneration

An energy assessment will be conducted for a nitrogen bubble with an initial temperature of 600 K and diameter of 100 μm. The efficiency of regeneration can be defined as:

$$\eta = \frac{q_r}{q_r + q_e + q_c} \tag{5.3.1}$$

where q_r, q_e, and q_c represent heat transfer due to the enthalpy of reaction between CO_2 and MEA, evaporation, and conduction respectively.

These three components of heat transfer have been plotted in Figure 5.13. It can be seen that initially, the majority – greater than 80% - of heat transfer is due to evaporation of water and MEA with some heat transfer due to desorption of CO_2 into the bubble. These components were found to decrease with time as the bubble surface cooled with the conduction component increasing. The maximum efficiency of regeneration was 14%, which occurred at t=0.003 μs. After 1 μs, of contact time, the efficiency reduced to 0% since desorption of CO_2 stopped as the bubble surface temperature cooled sufficiently.

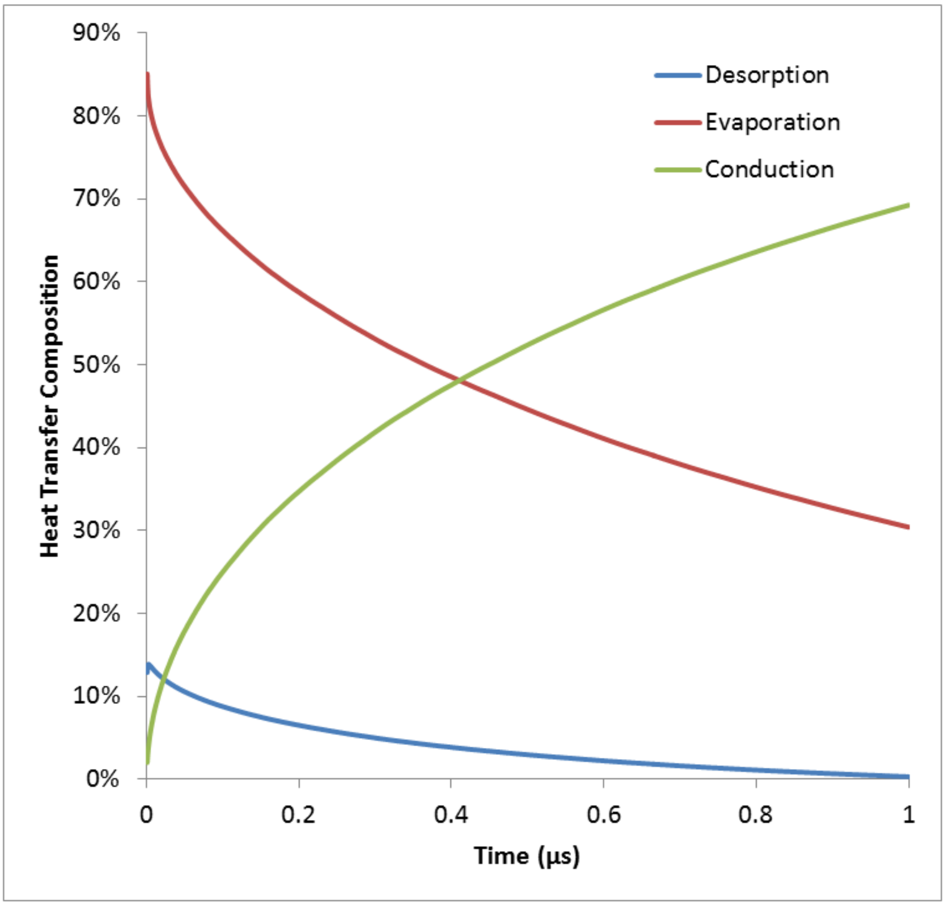

Figure 5.13. Heat transfer composition with N_2 bubble (d=100 µm; T_G=600 K)

Since the enthalpy of reaction between CO_2 and MEA is 1.915 GJ/tonne-CO_2 at 40 °C (Kim and Svendsen, 2007), a 14% efficiency implies a regeneration energy requirement of 13.7 GJ/tonne-CO_2. This is far greater than the regeneration energy requirement reported in the literature – approximately 4 GJ/tonne-CO_2 captured (Alie et al., 2005, Abu-Zahra et al., 2007a). It must be noted here that the energy requirement for regeneration could potentially be reduced if the bubble were to enter at an even hotter temperature; however, the model became unstable at temperatures greater than 600 K since this value approaches the critical temperature of water.

(Dugas, 2006) reports that about 24% of the energy input was used to reverse the CO_2-MEA reaction in a pilot plant study using a packed column. Therefore, the efficiency of the regeneration process using temperature-swing regeneration is approximately 3.4 times greater than that using direct contact regeneration.

5.3.2. [C_2mim][NTf_2]: Temperature Swing Regeneration

The energy requirement of [C_2mim][NTf_2] without direct contact regeneration has been calculated by assuming that the ionic liquid, which is fully saturated with CO_2, is heated from 20 °C and held at a raised temperature until the system reaches equilibrium. The saturation concentration of CO_2 in [C_2mim][NTf_2] is presented in Table 5.1, which has been calculated from Eqn. 4.4.1.

Table 5.1. Saturation concentration of CO_2 in [C_2mim][NTf_2] between 20 - 80 °C

Temperature (°C)	Saturation concentration (g-CO_2/g-IL)
20	0.003754
30	0.003180
40	0.002730
50	0.002366
60	0.002062
70	0.001817
80	0.001608

The energy requirement as a function of regeneration temperature has been calculated by assuming that the specific heat capacity of [C_2mim][NTf_2] is constant for all temperatures with a value of 1342 J/kg/K (Ge et al. (2008)) and the heat of reaction between CO_2 and [C_2mim][NTf_2] is constant at 0.323 kJ/g-CO_2 (Blath et al., 2011). This assumption actually produces an underestimate of the energy requirement for regeneration since the specific heat capacity of the ionic liquid increases slightly with temperature (Ge et al., 2008). The energy requirement for regeneration is plotted in Figure 5.14:

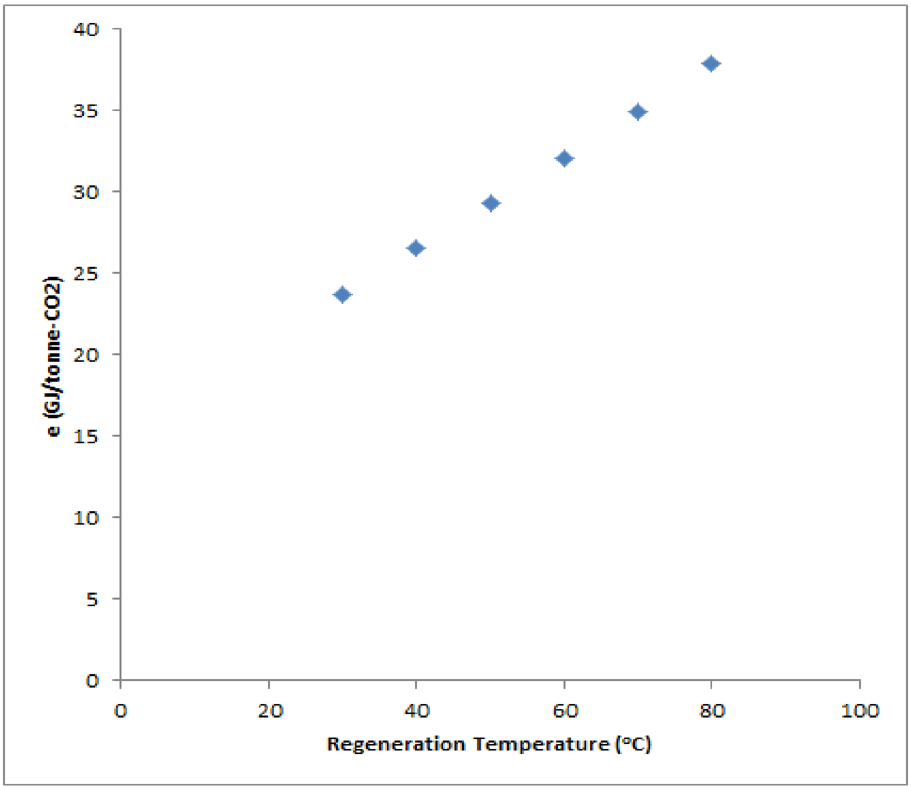

Figure 5.14. Energy requirement of regeneration of [C_2mim][NTf_2] as a function of regeneration temperature

It can be seen that for greater regeneration temperatures, the energy requirement for regeneration increases since the amount of sensible heat required increases disproportionately more than the amount of CO_2 that is released from the solvent. It thus seems best to use a low desorption temperature; however, there is a trade-off since a smaller temperature swing would equate to a smaller concentration swing in the solvent meaning that more ionic liquid would be required to capture the same amount of CO_2. The amount of solvent required to desorb 1 g of CO_2 has been plotted in Figure 5.15:

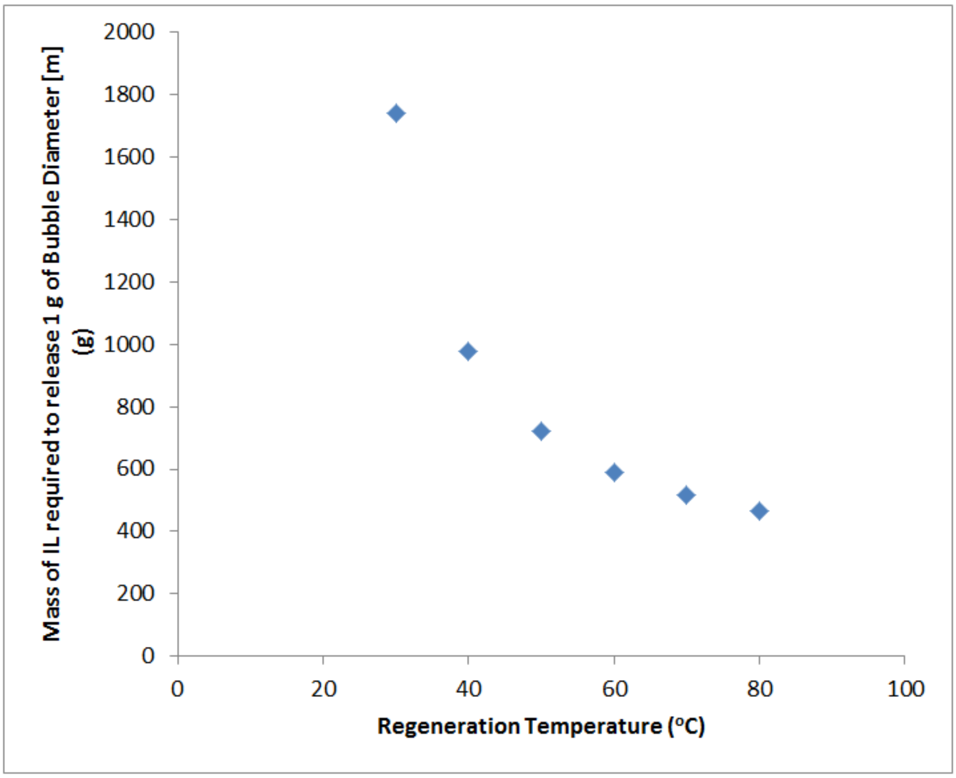

Figure 5.15. Amount of [C_2mim][NTf_2] required to capture 1 g of CO_2 for different regeneration temperatures

It can be seen that for a regeneration temperature of 30 °C, about 1.7 kg of solvent would be required to capture 1 g of CO_2 at atmospheric pressure; however, the amount of ionic liquid required decreases exponentially with increasing regeneration temperature. For a regeneration temperature of 80 °C, only 466 g of ionic liquid would be required. For comparison, since one mole of MEA is required to capture 0.2 moles of CO_2 (based on typical lean and rich solution loadings), only 23.1 g of aqueous MEA is required per gram of CO_2 captured (assuming a 30 wt.% aqueous MEA solution).

5.3.3. [C_2mim][NTf_2]: Direct Contact Regeneration

Figure 5.16 shows the heat transfer composition for direct contact regeneration with [C_2mim][NTf_2] using a CO_2 bubble with an initial temperature of 600 K. It can be seen that extremely high efficiencies can be achieved (>90%) if the contact time between the gas and liquid is of the order of 0.1 μs. The main reason for this is because ionic liquids do not evaporate and therefore more of the energy goes into desorbing CO_2 from the liquid. The efficiency decreases with contact time however, reaching 0% after approximately 33 μs; after this time, re-absorption of CO_2 into the liquid occurs.

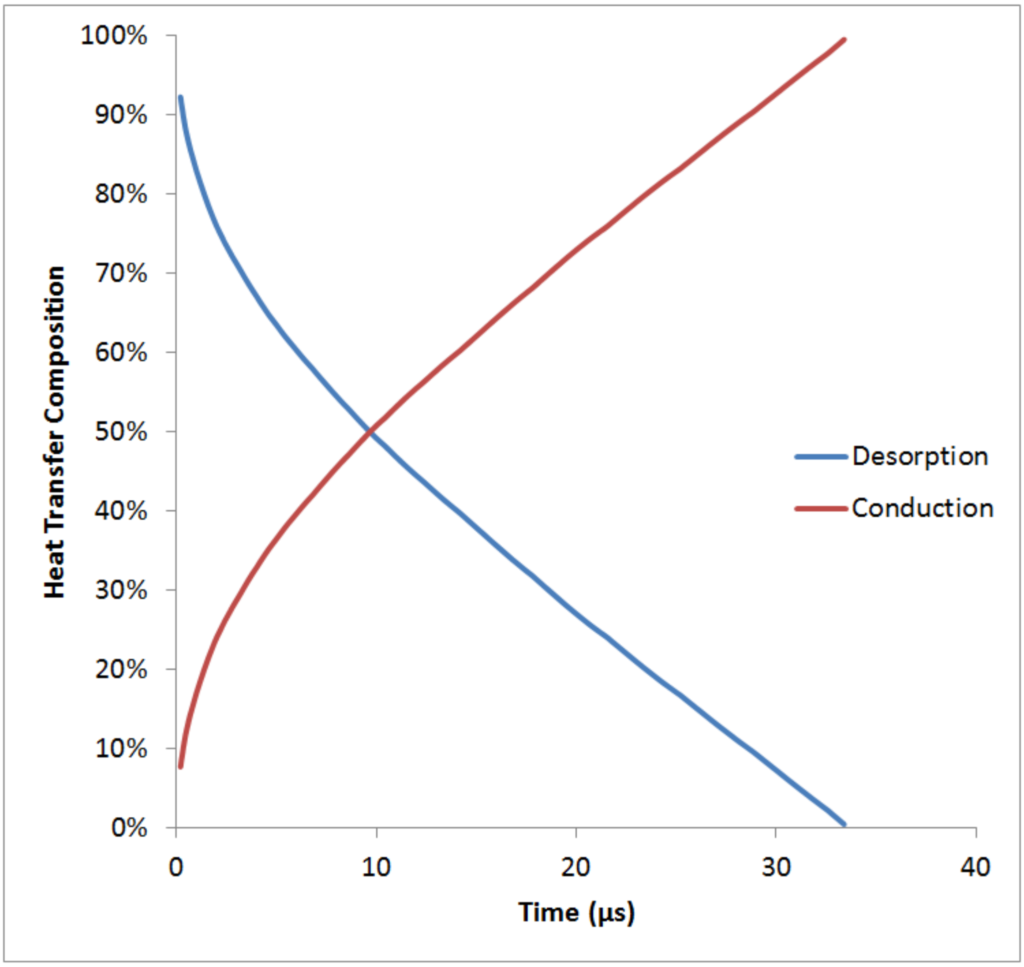

Figure 5.16. Efficiency of regeneration using DCR with CO_2 bubble in $[C_2mim][NTf_2]$ (d=100 μm, T_G=600 K)

The enthalpy of absorption between CO_2 and $[C_2mim][NTf_2]$ is 0.323 GJ/tonne-CO_2 (Blath et al., 2011). For a regeneration efficiency of 90%, the energy requirement is equal to 0.359 GJ/tonne-CO_2, which is approximately 8% of the energy requirement of regenerating MEA by temperature swing. Moreover, it is only about 1% of the energy requirement of regenerating $[C_2mim][NTf_2]$ using temperature swing methods. However, it must be noted here that due to the small timescales for which the efficiency is positive, it would be difficult to control the residence time accurately enough to achieve such a high efficiency.

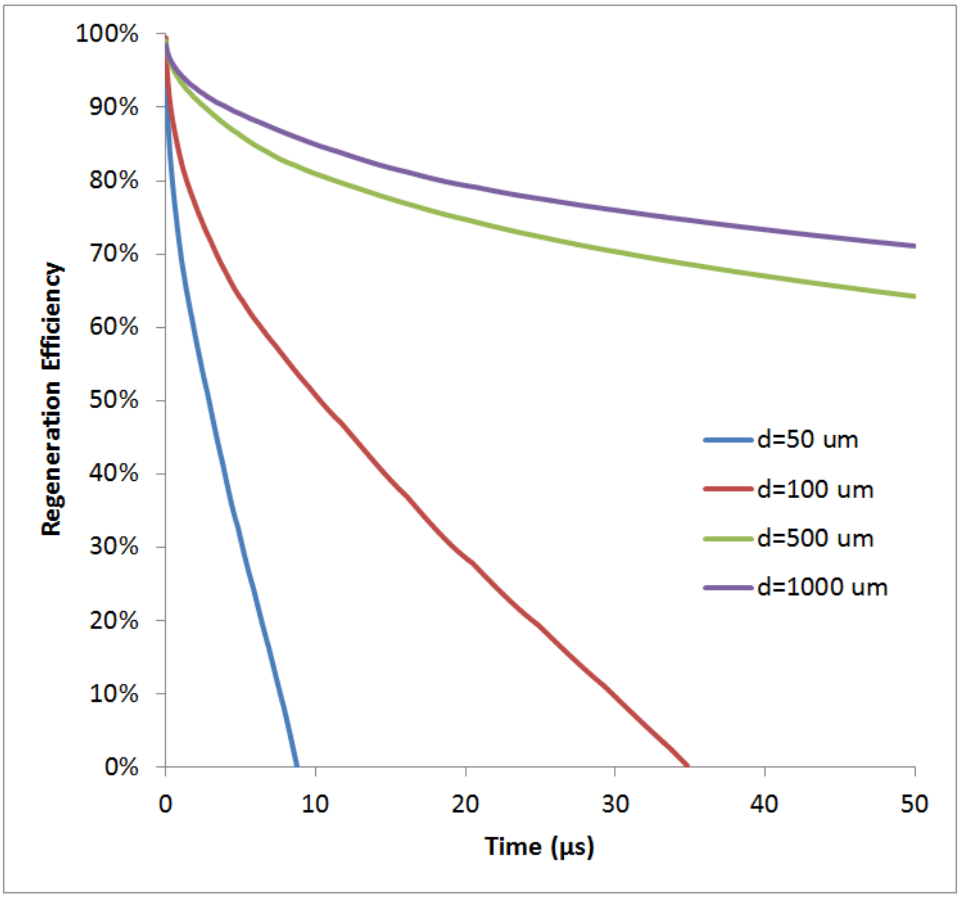

Figure 5.17. Efficiency of regeneration using DCR with a 100 μm CO_2 bubble in $[C_2mim][NTf_2]$; effect of bubble size

The efficiency of regeneration of $[C_2mim][NTf_2]$ using DCR has been plotted in Figure 5.17. Surprisingly, the efficiency increases with bubble size. There are two main reasons for this. Firstly, larger bubbles have less surface area per unit volume for conduction to occur. As a result, the bubble surface does not cool as quickly and can therefore desorb CO_2 for longer. Secondly, the model does not take into account bubble expansion and contraction. Since the CO_2 concentration in the bubble increases faster for smaller bubbles as shown in Figure 5.11, there is more resistance to mass transfer earlier on. In reality, the bubble size would change according to the Rayleigh-Plesset equation depending on the amount of gas and temperature of the gas in the bubble and so the resistance to mass transfer would be lower.

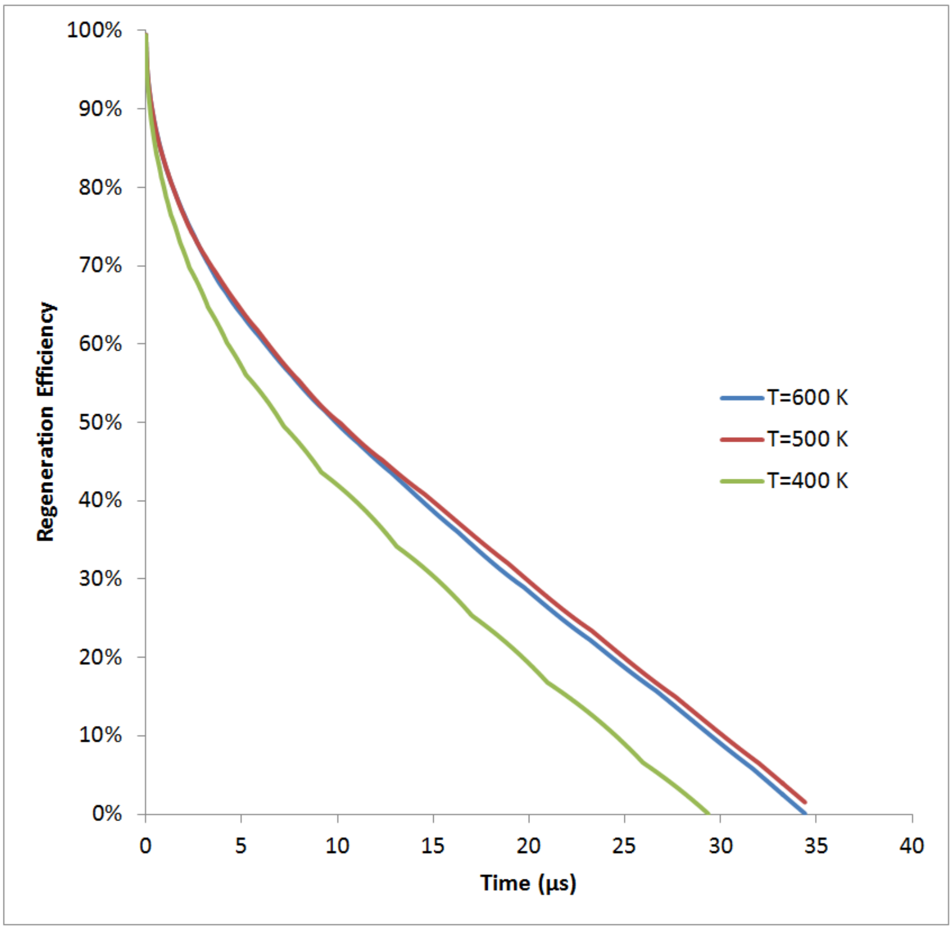

Figure 5.18. Efficiency of regeneration using DCR with 100 μm CO_2 bubble in [C_2mim][NTf_2]; effect of temperature

Figure 5.18 shows the regeneration efficiency for a bubble of diameter 100 μm in [C_2mim][NTf_2] for different initial temperatures. It can be seen that there is very little difference in the regeneration efficiency between initial gas temperatures of 600 K and 500K. However, an initial gas temperature of 400 K has slightly lower regeneration efficiency.

The reason for the small difference between regeneration temperatures of 500 K and 600 K is due to the solubility of CO_2 in [C_2mim][NTf_2] at these temperatures and is therefore specific to this ionic liquid. Figure 5.18 implies that the solubility of CO_2 in [C_2mim][NTf_2] is similar at 500 K and 600 K. It must be noted here that the results would differ if a different ionic liquid were studied.

Figures 5.13. and 5.16 imply that the lower the liquid level in the bubble column, the greater the efficiency of regeneration since more of the energy input would be used in desorbing the CO_2 from the liquid rather than for heat transfer to the liquid. This is further conveyed in Figure 5.17. The most significant observation, as shown by Figure

5.17, is that the regeneration efficiency actually increases as the bubble size increases since there is less heat loss to the liquid due to the reduction in bubble surface area. This implies that in practice, fine bubbles should be used rather than microbubbles in order to maximise the process efficiency.

With regard to bubble temperature, if [C_2mim][NTf_2] were used as the solvent, increasing the regeneration temperature would reduce the efficiency of regeneration. However it would reduce the amount of ionic liquid required which would reduce start-up costs.

5.4. Conclusions

Two models have been developed in this chapter. The first was to assess the feasibility of the direct contact regeneration technique with aqueous MEA. The second was to examine whether DCR is feasible and practical with ionic liquids and whether it can be used in conjunction with CDU processes; [C_2mim][NTf_2] was used as an example. The following conclusions can be drawn from the results of this chapter:

- Using a bubble of CO_2 to regenerate MEA using DCR and integrate the process with CDU processes is theoretically unfeasible for initial gas temperatures less than 600 K at atmospheric pressure. However, the liquid level predicted by this model for DCR to be practical is ~0.1 μm, which is three orders of magnitude smaller than the bubble diameter. This implies that this model cannot accurately predict the rate of mass transfer as the bubble would not be fully formed.
- The DCR technique is potentially feasible if the sparging gas were nitrogen, rather than CO_2, however, it would still be less efficient than conventional regeneration methods
- Increasing the temperature of the gas prior to sparging has the effect of increasing the amount and rate of CO_2 desorption from the MEA solution into the bubble. The same is true for increasing the CO_2 concentration in the liquid and reducing the bubble diameter.
- [C_2mim][NTf_2] can theoretically be regenerated using DCR with a CO_2 bubble and can thus potentially be integrated with CDU processes
- If optimised, regenerating [C_2mim][NTf_2] using DCR uses about 8% of the energy requirement of regenerating MEA using conventional techniques and

about 1% of the energy requirement of regenerating [C_2mim][NTf_2] using temperature swing methods. However, due to the small timescales, it would be difficult to optimise the process and so the efficiency is likely to be lower in practice

6. Bubble Size Measurements in Viscous Liquids

It has been shown in Chapter 5 that the Direct Contact Regeneration (DCR) technique is theoretically feasible using the ionic liquid [C_2mim][NTf_2]. Additionally, the simulations showed that smaller bubbles have faster regeneration rates when using the DCR technique. The aims of this chapter are: to produce microbubbles in ionic liquids in order to make biogas upgrading and DCR more practical; and to determine the physical properties of ionic liquids that are most ideal for producing microbubbles.

The results of the experiments conducted using the methods outlined in Sections 3.6.3-3.6.6 are presented in this chapter along with a discussion and comparison with relevant literature studies.

6.1. Bubble Size from an Orifice in Ionic Liquids: Effect of Oscillation Frequency

The results of the experiments outlined in Sections 3.3.1 and 3.6.4 are presented here. The following oscillation frequencies were studied by changing the length of the feedback loop on the fluidic oscillator: 65 Hz, 83 Hz, 113 Hz, 172 Hz, 190 Hz, 215 Hz, 319 Hz, 376 Hz, 393 Hz, 406 Hz, 416 Hz, and 770 Hz. The gas flow rate was measured *a posteriori* to be 1.2 ± 0.1 mL/min by measuring the mean bubble size and counting the number of bubbles per minute. An exemplar photograph of bubbles in the bubble column is presented in Figure 6.1.

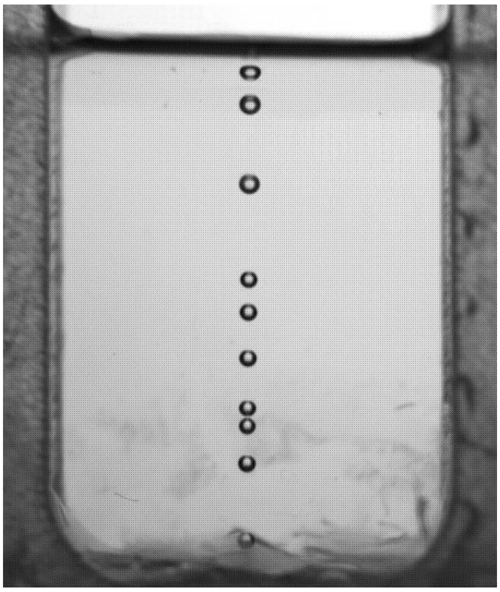

Figure 6.1. Photographs of bubbles from an orifice in [C_2mim][NTf_2] (f = 319 Hz)

The results from the single orifice experiments are presented in Figure 6.2. With the exception of [P_{66614}][Dec], where certain frequencies were shown to increase the mean bubble diameter by approximately 10%, the largest change in bubble diameter was a 4.7% increase from the mean, which occurred with [C_2mim][NTf_2]. The largest reduction in bubble diameter (relative to the mean) was 7.6%, which occurred in [P_{66614}][Dec] at a frequency of 416 Hz. Since the error in the flow rate measurement was ±8%, these variations in bubble size are insignificant. Moreover, they are far less than the reduction in bubble diameter reported by (Brittle, 2014) – a 73% reduction in bubble size in water at frequencies between 100 – 300 Hz.

It can be seen in Figure 6.1 that although the fluidic oscillator was used in these experiments, the bubbles were not produced at regular time intervals. This implies that the small pore size (30 μm) likely damped the oscillation. Figure 6.2 shows that for the experiments conducted in this work the mean variation in bubble size with oscillation frequency was almost negligible. There are two possible explanations for this. The first is that the diameter of the pore used in the experiments was too small, thus largely damping out the oscillation before the gas reaches the bubble. While this is possible, experiments conducted by P. Desai using the same experimental setup showed large variations in bubble size with oscillation frequency for bubble formation in inviscid liquids, such as water, ethanol, and methanol.

A second possible explanation is that the high viscosity of the ionic liquids induced a large drag force on the bubble during formation, which could similarly damp out the oscillation. Since the viscosity of the ionic liquids tested here is so much greater than that tested in the work of P. Desai, it is likely that liquid viscosity has a major influence on bubble size when using a fluidic oscillator. Due to the increase in drag force with liquid viscosity, this author believes that the amplitude of the oscillation needs to be increased for the fluidic oscillator to have a similar effect on ionic liquids as it has with common low-viscosity solvents.

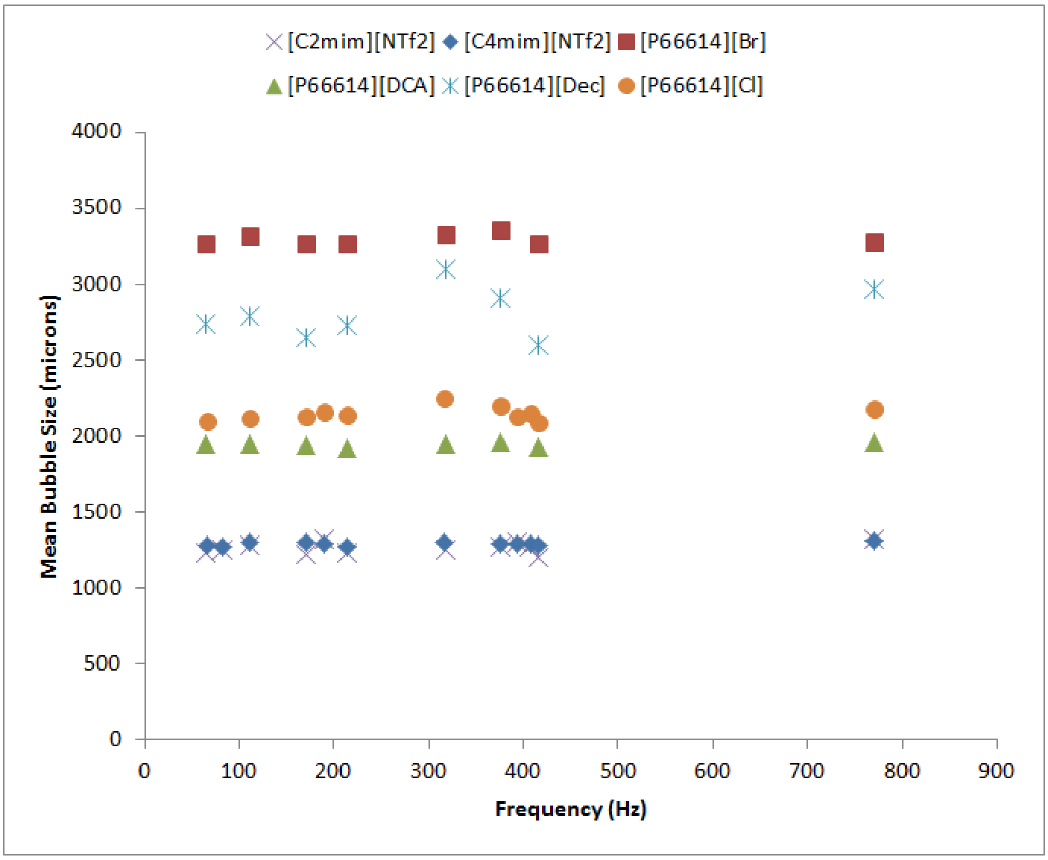

Figure 6.2. Mean bubble diameter vs. oscillation frequency in ionic liquids; flow rate = 1.2mL/min

Although many authors have found the fluidic oscillator to play a major role in reducing bubble size from a porous diffuser (Zimmerman et al., 2009a, al-Mashhadani et al., 2011, Hanotu et al., 2012), all of their experiments were tested with low viscosity liquids, such as water. Under steady flow, bubbles detach from the orifice once the sum of the buoyancy, excess pressure, and momentum forces are greater than the sum of the surface tension, inertial drag, and viscous drag forces (Gaddis and Vogelpohl, 1986). Some authors ignore the momentum and excess pressure forces since they are usually small in comparison (Ramakrishnan et al., 1969). However, under oscillatory flow, the gas moves into the bubble at a higher velocity, causing the momentum force to become more significant. Since the drag force acting on a bubble is between one and three orders of magnitude greater in ionic liquids than in water (due to the larger viscosity), a much larger oscillation would be required in order for the gas to have enough inertia to make the bubble detach.

While there may be a particular frequency for which the bubble size is significantly reduced outside of the range tested (or possibly between 400-800 Hz), there does not yet exist a methodical approach for determining the optimal frequency based on the physical properties of the liquid and gas. As a result, it was decided to produce microbubbles in ionic liquids by other means, such as changing the flow rate and using a microporous diffuser; these are presented in the next section.

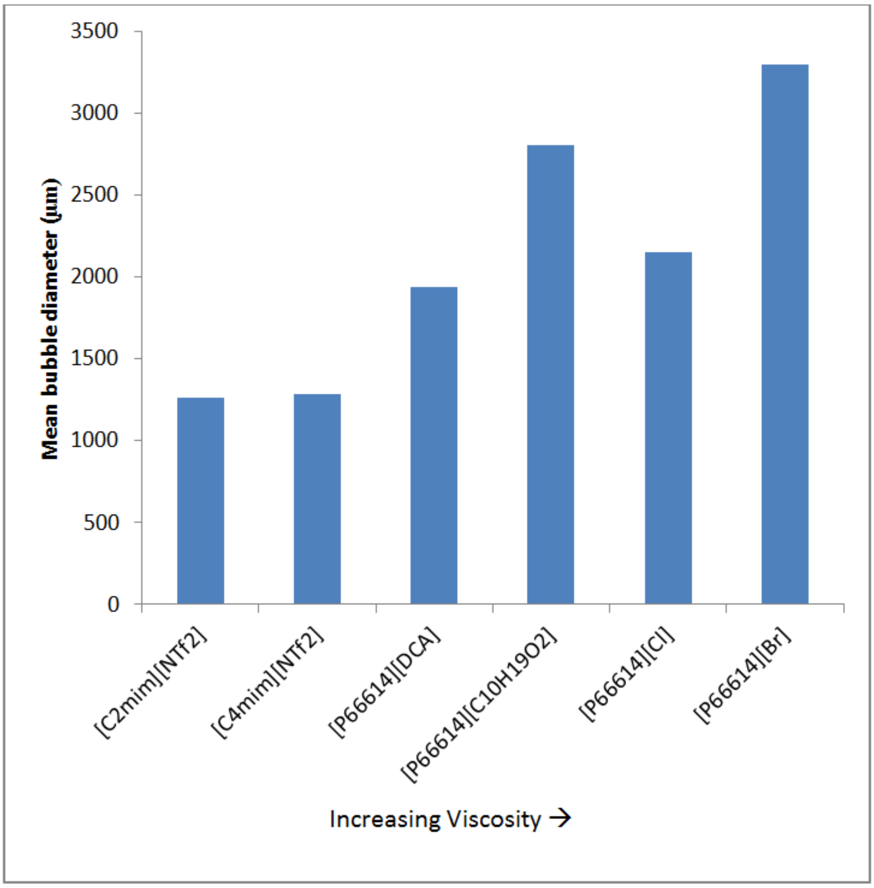

Figure 6.3. Mean bubble diameter from an orifice in ionic liquids; flow rate = 1.2 mL/min

For the experiments undertaken using oscillatory flow, the mean bubble diameter is presented in Figure 6.3 in order of increasing viscosity (left to right). It must be noted here that the order of the ionic liquids in Figure 6.3 is based upon the viscosities of dry ionic liquids; however the actual experiments were undertaken using wet ionic liquids, i.e. ones that have not been dried using the methods outlined in Section 3.6.2. As expected, the bubble diameter was smaller in the imidazolium-based ionic liquids – [C_2mim][NTf_2] and [C_4mim][NTf_2] – than in the phosphonium-based ionic liquids. This agrees with the findings of (Kaji et al., 2009, Zhang et al., 2013, Lange et al., 2013) who noted that ionic liquids with lower viscosities produce smaller bubbles. However, even in [C_2mim][NTf_2] and [C_4mim][NTf_2], the mean bubble diameter was still 1,262 µm and 1,288 µm respectively despite the orifice diameter being only 30 µm. The ionic liquid with the highest viscosity used in this work, [P_{66614}][Br], produces the largest bubbles, which have a mean diameter of 3,293 μm. However, $[P_{66614}][Cl]$, which has the second highest viscosity of the ionic liquids tested produces far smaller bubbles than $[P_{66614}][Dec]$.

Figure 6.3 shows a general upward trend between mean bubble diameter and liquid viscosity; however, it is well documented that liquid viscosity is not the only factor that affects bubble size (Ramakrishnan et al., 1969, Swope, 1971, Jamialahmadi et al., 2001). Other parameters such as surface tension, liquid density, and gas flow rate have a significant effect on the bubble diameter. The effect of the above-mentioned parameters on mean bubble diameter and gas holdup in ionic liquids and water-glycerol mixtures in bubble columns will be determined under constant flow conditions in the remainder of this chapter.

6.2. Bubble Size and Gas Holdup from a Diffuser

The results from the bubble sizing experiments outlined in Sections 3.6.5 and 3.6.6 using the experimental setup presented in Sections 3.3.2 and methods presented in Sections 3.5.2 and 3.5.3 are presented here. First, the results of the water-glycerol experiments (Section 3.6.5) are presented; following this, the results of the ionic liquid bubble sizing experiments (Section 3.6.6) are presented and compared with those from the water-glycerol experiments; then the effect of drying the ionic liquids is presented and the effect of contact angle on bubble size is examined.

6.2.1. Water-Glycerol Mixtures

An example image from this work showing bubbles in aqueous glycerol is presented in Figure 6.4. It is clear from the image that there are many overlapping bubbles in the foreground and additional bubbles in the background of the image due to the large gas holdup in the column. At greater flow rates, this effect was exacerbated and the liquid also produced a significant amount of foam. For this reason, it was not possible to determine the effect of flow rate on bubble diameter in the water-glycerol mixtures; however the effects of viscosity, surface tension, and density were still investigated.

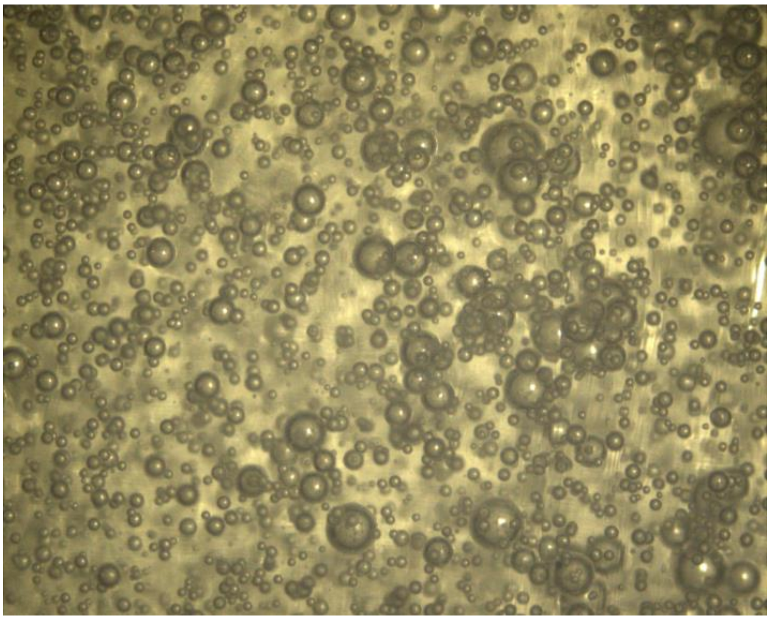

Figure 6.4. Photograph of bubbles produced in the bubble column with water-glycerol mixtures (gas flow rate = 3 mL/min)

It can be seen in Figure 6.4 that the bubbles produced in these experiments had a large range of sizes. This means that the bubbles would likely rise at different velocities inside the liquid and are therefore far more likely to coalesce. From a mass transfer perspective, this is far from ideal since the coalescence would increase the bubble size, which in turn would reduce the rate of mass transfer to the liquid. It would therefore be very useful if the fluidic oscillator were incorporated into a similar setup in order to make the bubbles more mono-disperse and uniform.

Figure 6.5 shows how the mean bubble diameter varies with liquid viscosity. The complete set of data is provided in Appendix E: Mean Bubble Diameters. In pure glycerol, the mean bubble diameter was 208 μm. As the concentration of water was increased and the viscosity reduced, the mean bubble diameter also reduced. This reduction was very gradual, reducing to 89 μm at a viscosity of 0.004 Pa·s. For pure water, which has a viscosity of 0.001 Pa·s, the mean bubble diameter was 215 μm. This is consistent with the theory and measurements of (Ruzicka et al., 2001, Ruzicka et al., 2003) who found that viscosities between 0.001-0.003 Pa·s stabilise the existence of small bubbles.

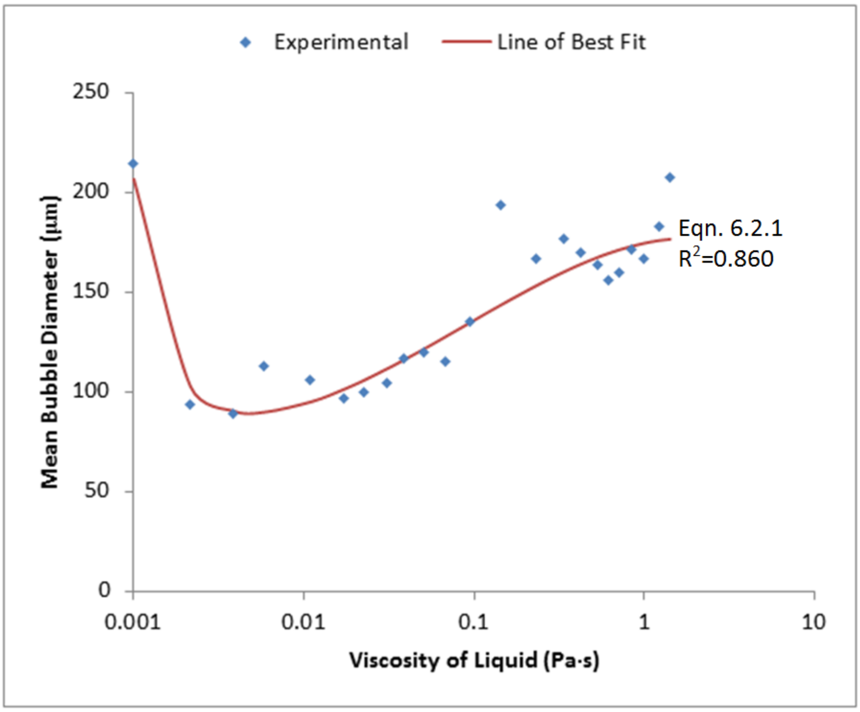

Figure 6.5. Mean bubble diameter from a ceramic diffuser vs. viscosity in water-glycerol mixtures

However, there are additional physical properties to liquid viscosity that affect bubble diameter, such as liquid density and surface tension. Since the viscosity variation with concentration of glycerol is very nonlinear, it is possible that the viscosity and surface tension are conflicting with each other as the concentration of water increases, causing the bubbles size to reduce and then increase; between the first and second point, representing pure water and 24 vol. % glycerol respectively, the viscosity increases by 115% and the surface tension decreases by 3.1 %. Many authors have noted that bubble size increases with increasing liquid viscosity and increasing surface tension in bubble columns (Ramakrishnan et al., 1969, Akita and Yoshida, 1974, Wilkinson et al., 1994). In order to determine the relative effects of viscosity, surface tension, and density of the liquid on bubble size, a multiple regression analysis has been undertaken.

Although some authors have derived equations of different forms to determine bubble diameter, e.g. (Davidson and Schüler, 1960, Gaddis and Vogelpohl, 1986, Jamialahmadi et al., 2001), many authors provide equations where the bubble diameter is expressed as a product of dimensionless numbers with exponents (Akita and Yoshida, 1974, Pohorecki et al., 2005, Zhang et al., 2013). The most common expression for bubble diameter can thus be expressed as a product of system parameters with exponents. This work will use an equation of the form:

$$\bar{d} \propto {\mu_L}^A \gamma^B {\rho_L}^C {U_G}^D$$

as suggested by (Pohorecki et al., 2005). Here, $\bar{d}$ is the mean bubble diameter, μ_L, γ, and ϱ_L are the liquid viscosity, interfacial tension and density respectively, and U_G represents the superficial gas velocity. In aqueous glycerol mixtures, the mean bubble diameter in the experiment was shown to obey the equation:

$$\bar{d} = 1.521 \cdot 10^{39} \cdot {\mu_L}^{0.56} \gamma^{35.1} \rho^{-0.36} \tag{6.2.1}$$

with an R-squared value of 0.860. This equation has been plotted in Figure 6.5 along with the experimental results for comparison. From the above equation, it is clear that surface tension has a much larger effect on mean bubble diameter than viscosity since the magnitude of the exponent is greater. This could explain why increasing the glycerol concentration from 0 – 24 vol. % results in such a large decrease in the mean bubble diameter. The addition of glycerol to water causes the viscosity and density to increase and the surface tension to decrease; since surface tension has a significantly larger effect on the mean bubble diameter than liquid viscosity and density, it is likely that the decrease in surface tension upon the addition of glycerol caused the bubble size to decrease. At greater concentrations of glycerol, the change in viscosity becomes far greater than the change in surface tension, causing viscosity to play a larger role and thus causes the bubble size to increase.

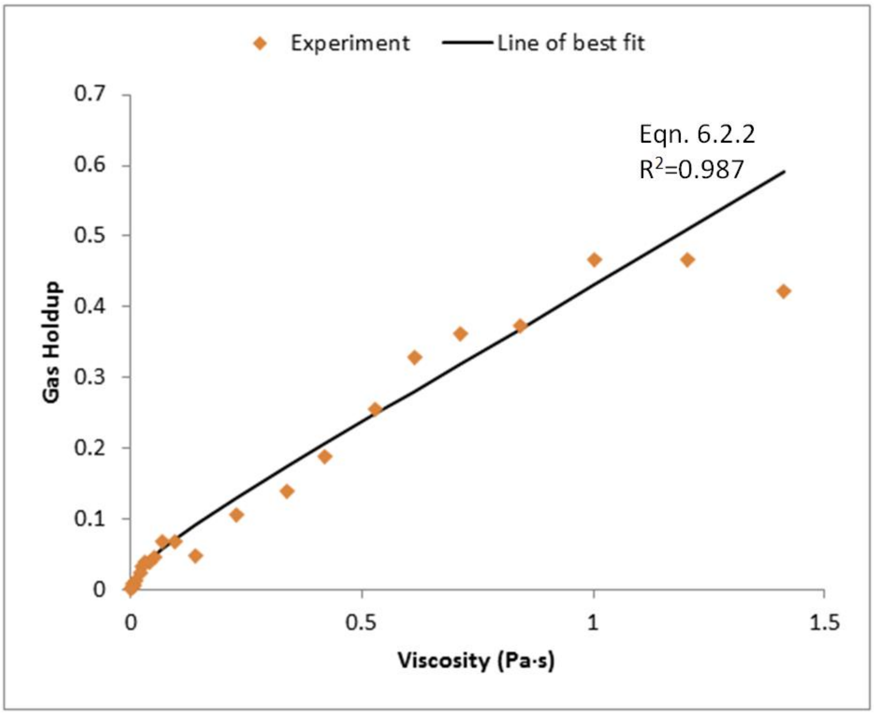

Figure 6.6. Gas holdup vs. liquid viscosity for water-glycerol mixtures

The effect of liquid viscosity, surface tension, and liquid density on gas holdup has also been studied. The change in gas holdup with liquid viscosity is presented in Figure 6.6. It appears as though, in general, the gas holdup increases with viscosity, due to the bubbles rising slower and thus staying in the liquid for longer.

Using multiple regression analysis, the effects of liquid viscosity, surface tension, and liquid density on gas holdup were investigated. The following equation was obtained with an R-squared value of 0.987:

$$\varepsilon = 7.119 \cdot 10^{-84} \cdot {\mu_L}^{-0.12} \gamma^{-70.2} \rho^{-0.28} \qquad (6.2.2)$$

The above equation shows that, contrary to what Figure 6.6 suggests, increasing liquid viscosity actually reduces gas holdup. This has been shown by many other authors (Hikita et al., 1980, Urseanu et al., 2003, Mouza et al., 2005). In fact, surface tension was shown to have a greater effect on gas holdup than both the viscosity and density of the liquid. So the reason for the increase in gas holdup with increasing glycerol concentration is mainly due to the decrease in the surface tension of the liquid mixture. This will be further discussed in Section 6.4.

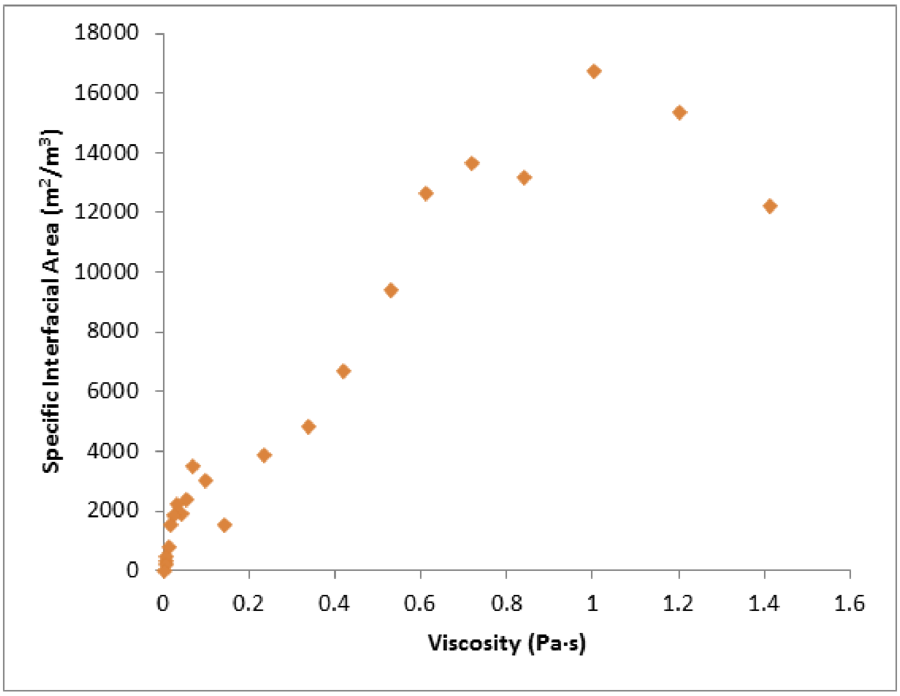

Figure 6.7. Specific interfacial area vs. viscosity for aqueous glycerol solutions

In addition to mean bubble diameter and gas holdup, the specific interfacial area – i.e. the total surface area of bubbles per unit volume of liquid – is important for mass transfer processes, such as biogas upgrading and solvent regeneration using DCR. The specific interfacial area is presented in Figure 6.7 against liquid viscosity for the experiments in aqueous glycerol solutions. It can be seen that specific interfacial area generally increases with viscosity up to approximately 1.0 Pa·s, after which it starts to decrease. The reason for this is because while the bubble size does not vary significantly as the viscosity is increased, the rise velocity is smaller due to the increased drag force acting on the bubbles. For viscosities between 1.0-1.2 Pa·s, the gas holdup reduces. This is because the bubble rise velocity increases disproportionally more than the superficial gas velocity due to the increased bubble size, thus decreasing the specific interfacial area.

It appears as though a viscosity of about 1.0 Pa·s is optimal for producing the largest interfacial area for bubbles in water-glycerol solutions. However, this does not necessarily correlate to faster mass transfer rates since the internal pressure of the bubble and diffusion coefficient in the liquid also need to be taken into account. In the next section, these experiments will be repeated with ten ionic liquids and the results will be compared and discussed in Section 6.4.

6.2.2. Dry Ionic Liquids

The mean bubble diameter in ten ionic liquids (mentioned in Section 3.1.1) is plotted against flow rate in Figure 6.8 using the data provided in Appendix E: Mean Bubble Diameter. Figure 6.8 shows that flow rate has little effect on bubble size in the ionic liquids, particularly in the less viscous ionic liquids. The smallest mean bubble diameter (93.8 µm) was recorded in [C$_2$mim][EtSO$_4$] for a gas flow rate of 7 mL/min. The mean bubble diameter in [C$_2$mim][NTf$_2$] , [C$_4$mim][NTf$_2$], and [P$_{66614}$][DCA] was approximately 600 µm and only increased slightly with flow rate. Meanwhile, the highly viscous ionic liquids – [P$_{66614}$][Dec], [P$_{66614}$][Cl], and [P$_{66614}$][Br] – produced the largest bubbles. In each of these liquids, the mean bubble diameter was greater than 1000 µm at flow rates greater than 10 mL/min indicating that viscosity has a significant effect on bubble diameter.

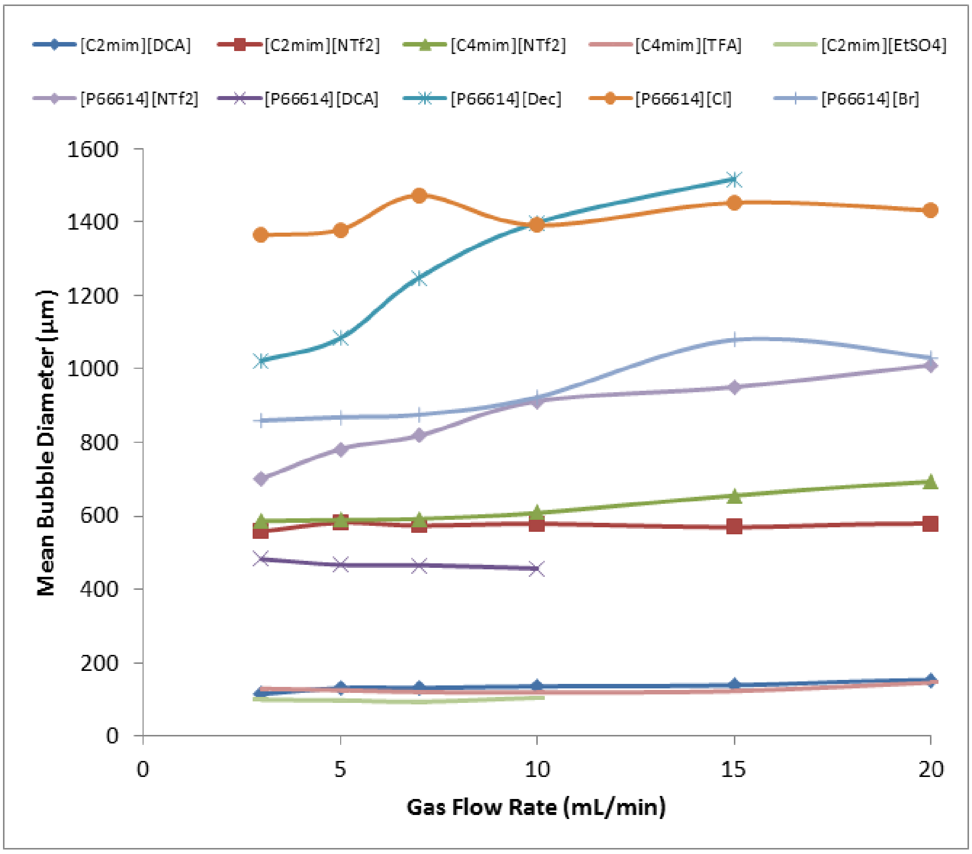

Figure 6.8. Mean diameter of bubbles produced vs. gas flow rate in various ionic liquids

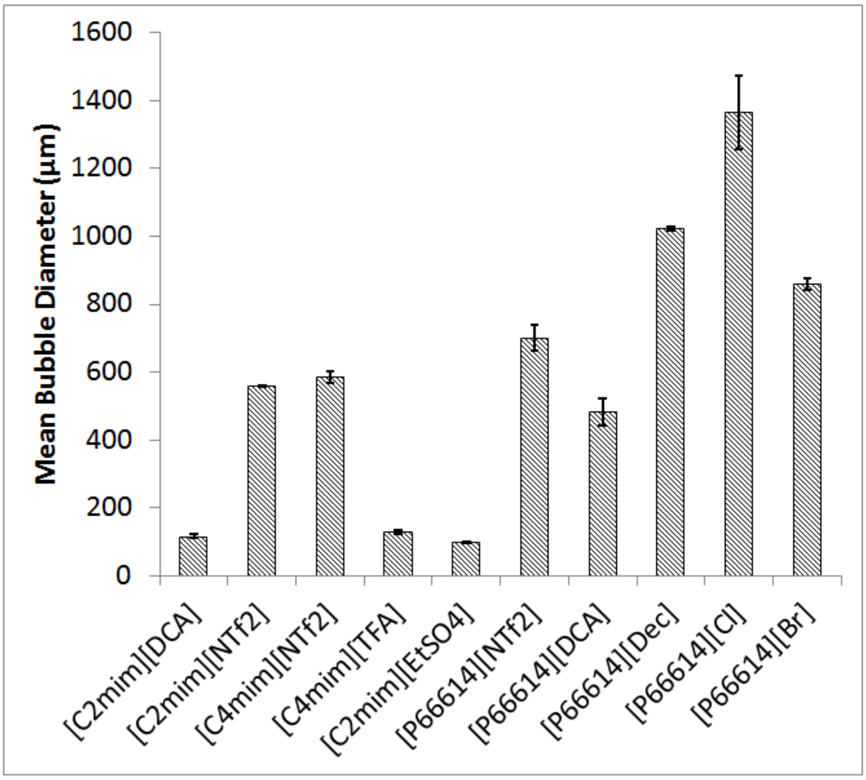

Figure 6.9. Mean diameter of bubbles produced in ionic liquids: flow rate = 3 mL/min

Since gas flow rate was shown to have little effect on mean bubble diameter, as shown in Figure 6.8, the mean bubble diameter in each of the ionic liquids for a flow rate of 3 mL/min is compared. This is presented in Figure 6.9 with the ionic liquids placed in order of increasing viscosity (left to right). It can be seen that [C$_2$mim][DCA], [C$_4$mim][TFA], and [C$_2$mim][EtSO$_4$] produce very small bubbles compared with the other ionic liquids tested. This conveys that viscosity is not the most important parameter for determining bubble diameter since the mean bubble diameter in both [C$_2$mim][NTf$_2$] and [C$_4$mim][NTf$_2$] is greater than in [C$_4$mim][TFA] and [C$_2$mim][EtSO$_4$] despite these liquids having lower viscosities. In general, bubble size does increase with viscosity however.

The gas holdup in the ionic liquids as a function of flow rate is presented in Figure 6.10. It can be seen that gas holdup increases with gas flow rate in all of the ionic liquids. However, with the exception of [C$_2$mim][EtSO$_4$], gas holdup in the ionic liquids tested is far less than that produced in the water-glycerol solutions. (Kaji et al., 2009) also found the gas holdup to be similar between [C$_2$mim][EtSO$_4$] and aqueous glycerol mixtures of similar viscosity and concluded that viscosity must be the most dominant parameter. However, this work shows that their conclusion does not hold true for other ionic liquids.

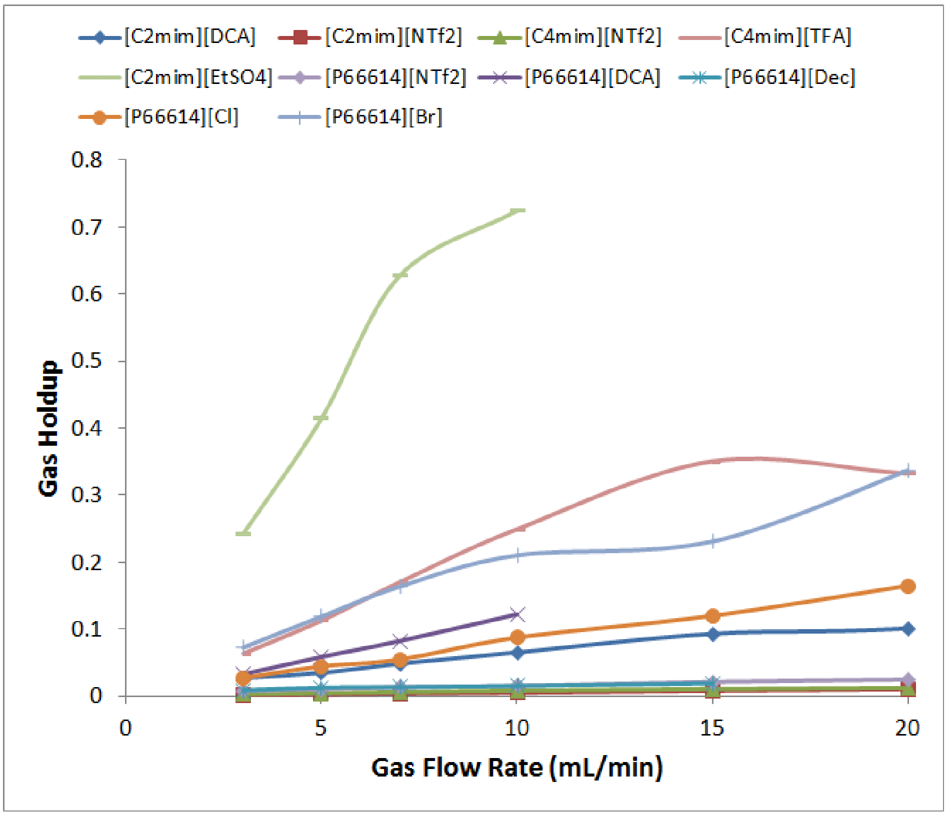

Figure 6.10. Gas holdup vs. Gas flow rate in various ionic liquids

Gas holdup in the aforementioned ionic liquids are presented in Figure 6.11 for a gas flow rate of 3 mL/min. The gas holdup in [C_2mim][$EtSO_4$] was greater than that in the other ionic liquids by between one or two orders of magnitude. Some of the more viscous ionic liquids, e.g [P_{66614}][Br], were also found to produce large gas holdups since even though the bubble size was quite large, they rose very slowly due to the high viscosity of the liquid. [C_2mim][NTf_2], [C_4mim][NTf_2], [P_{66614}][NTf_2], and [P_{66614}][Dec] were all found to produce very low gas holdups (<0.01).

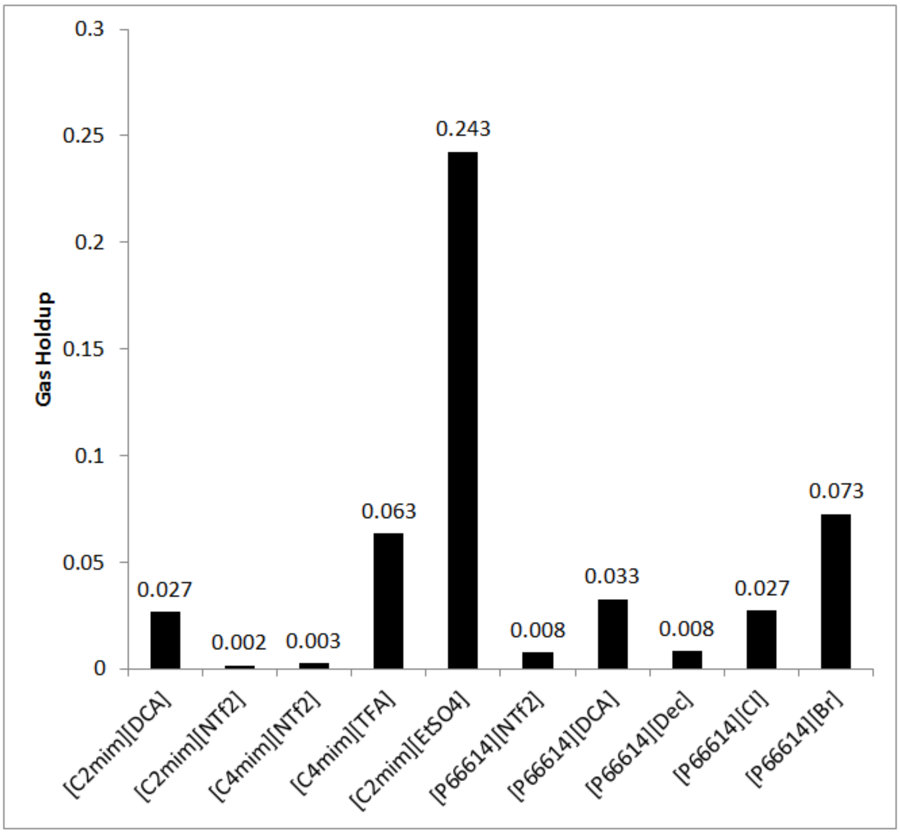

Figure 6.11. Mean gas holdup in ionic liquids: gas flow rate = 3mL/min

As mentioned previously, bubble diameter is a function of numerous physical properties, including liquid viscosity, surface tension, density, and superficial gas velocity. The mean bubble diameter and gas holdup from the experiments with ionic liquids have been correlated against these parameters using multiple regression analysis; the following equations have been produced with R-squared values of 0.812 and 0.733 respectively:

$$\bar{d} = 3.310 \cdot 10^{-6} \cdot {\mu_L}^{0.08} \gamma^{-2.88} \rho^{-0.37} {U_G}^{0.19} \qquad (6.2.3)$$

$$\varepsilon = 1.125 \cdot 10^{11} \cdot {\mu_L}^{0.84} \gamma^{5.76} \rho^{-0.26} {U_G}^{0.61} \qquad (6.2.4)$$

Equations 6.2.3 and 6.2.4 suggest that bubble diameter and gas holdup in ionic liquids is primarily determined by the surface tension of the liquid. The order of importance of the effects of the parameters studied on mean bubble diameter and gas holdup are shown below.

$$\bar{d}\colon \gamma > \rho > U_G > \mu_L$$

$$\varepsilon: \gamma > \mu_L > U_G > \rho$$

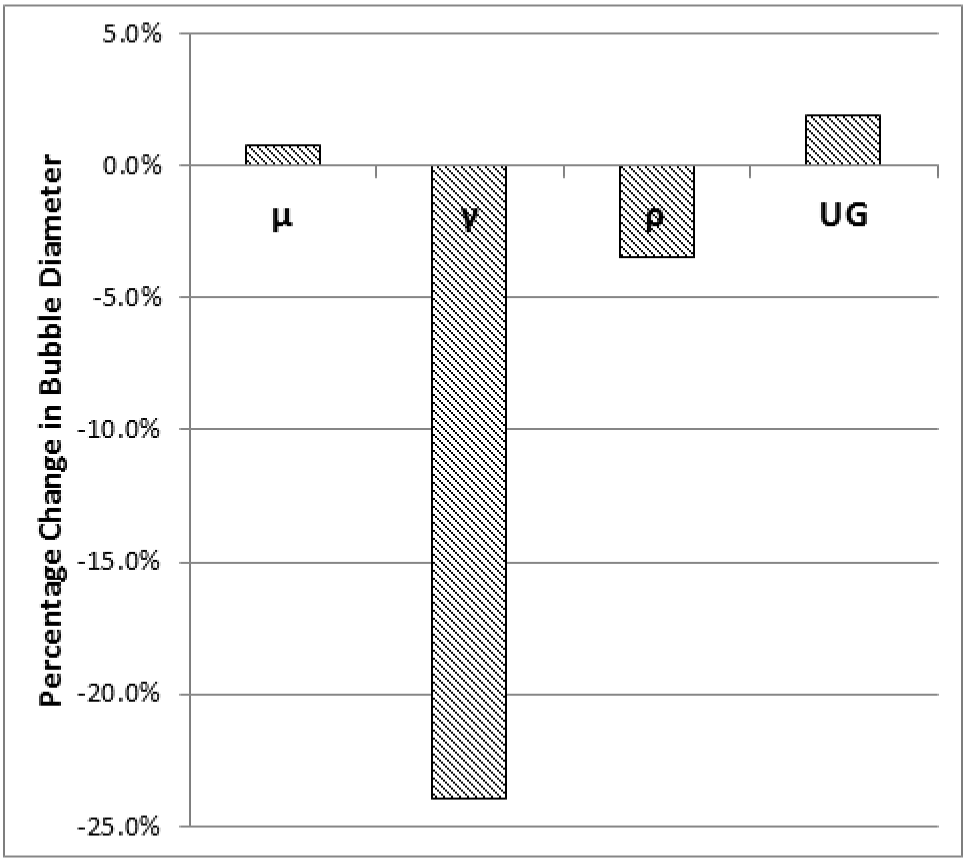

Figure 6.12. Percentage change in bubble diameter due to a 10% increase in liquid viscosity, surface tension, density, and superficial gas velocity

Figure 6.12 presents the percentage change in bubble diameter due to a 10% increase in the liquid viscosity, surface tension, liquid density, and superficial gas velocity, calculated from Eqn. 6.2.3. It can be seen that a 10% increase in surface tension reduces the mean bubble diameter by 24% while a 10% increase in liquid density reduces the mean bubble diameter by 3.5%. Increasing the superficial gas velocity and liquid density by 10% increases the mean bubble diameter by 1.8% and 0.8% respectfully. While this suggests that surface tension has the greatest effect on mean bubble diameter, since the surface tension of ionic liquids typically only varies between 0.03 – 0.06 N/m, other factors having a wider variation can be equally important. For example, the viscosity of ionic liquids can vary by several orders of magnitude and can therefore also have a significant effect on the bubble size. The density of ionic liquids typically varies between 800 – 1,600 kg/m^3 and has a smaller contribution to mean bubble diameter than surface tension so it is likely to be less important than the other two parameters.

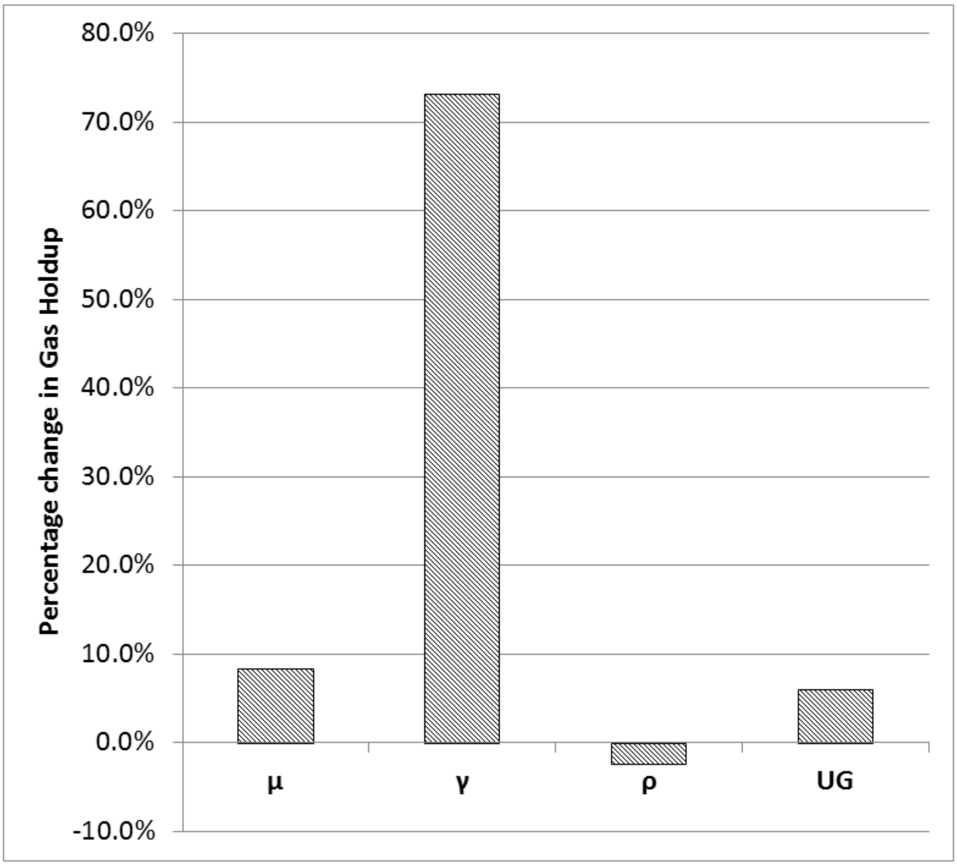

Figure 6.13. Percentage change in gas holdup due to a 10% increase in liquid viscosity, surface tension, density, and superficial gas velocity

Figure 6.13 presents the percentage change in gas holdup due to a 10% increase in liquid viscosity, surface tension, liquid density, and superficial gas velocity, calculated from Eqn. 6.2.4. A 10% increase in surface tension and viscosity are shown to increase the gas holdup by 73% and 8.3% respectively. The same increase in liquid density and superficial gas velocity results in a 2.4% decrease and a 6.0% increase in gas holdup respectively. Therefore it can be concluded that surface tension is the most dominant parameter for influencing gas holdup. However, as mentioned previously, other factors – namely viscosity – can also be as significant since they can vary by significantly more than surface tension.

Figure 6.12 and Figure 6.13 show that the surface tension of the ionic liquid has the greatest effect on both the mean bubble diameter and the gas holdup. The most likely explanation for this is because of the stabilising-destabilising effect of surface tension on the homogeneous (bubbly) regime in bubble columns. (Ruzicka et al., 2001) predicted that there is a critical value of gas holdup beyond which transition to the heterogeneous regime occurs. They later found this to be true experimentally and attributed this to viscosity (Ruzicka et al., 2003). However, in another study, the surface tension of the liquid was also found to have an important effect on the critical gas holdup (Ruzicka et al., 2008). Meanwhile, (Chaumat et al., 2007) found that the stable homogeneous regime did not exist in the same viscosity region in pure organic liquids with surface tension of approximately 0.03 N/m further indicating that surface tension significantly influences bubble diameter. (Wilkinson et al., 1992) found that increasing the surface tension of a liquid has the effect of reducing the value of the critical gas holdup, beyond which transition to the heterogeneous regime occurs. In this work the stability of the homogeneous regime appeared very apparent in [C_4mim][TFA], [C_2mim][DCA], and [C_2mim][$EtSO_4$], the latter two of which have much greater surface tensions than the other ionic liquids tested. The fact that the homogeneous regime was very stable in [C_4mim][TFA], which has a similar surface tension to the other ionic liquids suggests that it is a combination of surface tension and viscosity that provides the ideal conditions for stabilising the homogeneous regime.

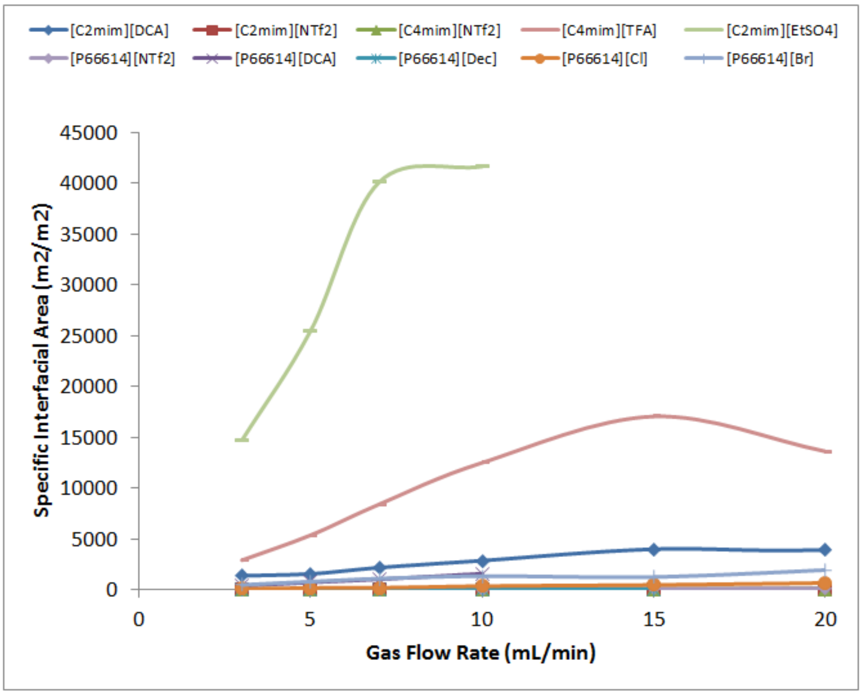

Figure 6.14. Specific interfacial area vs. Gas flow rate in ionic liquids

The specific interfacial area of bubbles in ionic liquids with respect to gas flow rate are depicted in Figure 6.14. As a result of the high gas holdups, [C_2mim][$EtSO_4$], [C_4mim][TFA], and [C_2mim][DCA] produce the largest gas-liquid interfacial areas; for a gas flow rate of 3 mL/min, these were 14,738 m^2/m^3, 2,936 m^2/m^3, and 1,396 m^2/m^3 respectively. However, with the exception of these three ionic liquids, the greatest specific interfacial area at a flow rate of 3 mL/min – the same as that used in the water-glycerol experiments – was only 507 m^2/m^3 (see Figure 6.15). In comparison, in the water-glycerol experiments, the specific interfacial area was greater than this for viscosities above 0.01 Pa·s and increased up to 16,721 m^2/m^3 at a viscosity of 1.0 Pa·s.

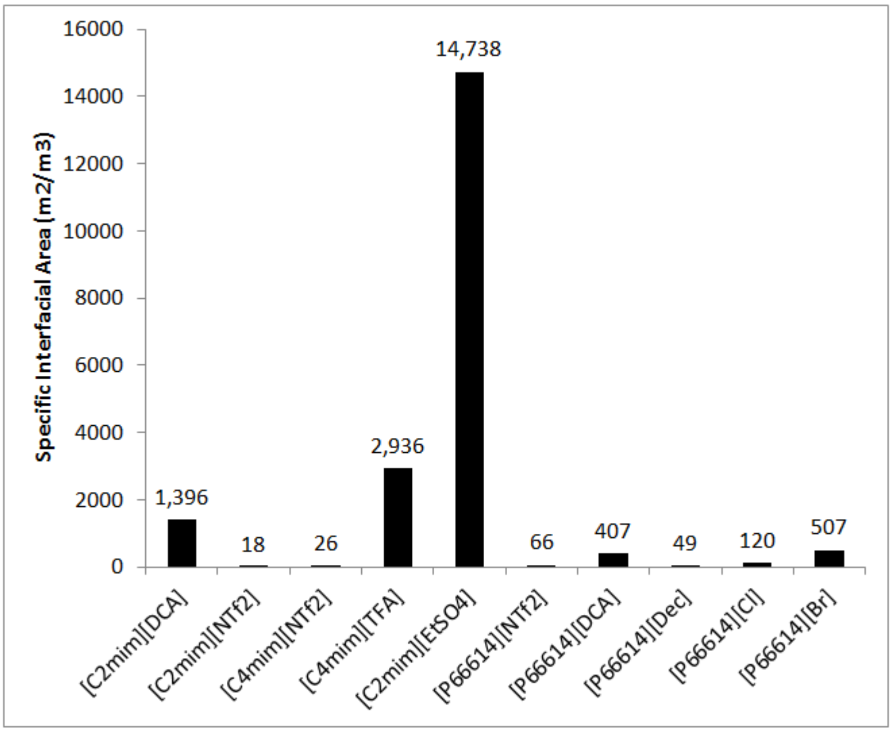

Figure 6.15. Mean specific interfacial area in ionic liquids: gas flow rate = 3mL/min

[C_2mim][$EtSO_4$] was shown to produce a relatively large specific interfacial area in combination with very small bubbles. It must be remembered that in addition to interfacial area, the internal partial pressure of CO_2 is also important for mass transfer processes and smaller bubbles have a higher internal pressure in accordance with the Young-Laplace equation. However, there are many important properties to consider when selecting a solvent for carbon capture. These include CO_2 solubility, bubble size and rate of mass transfer, selectivity between CO_2 and other gases, regeneration energy requirement and cost, production energy requirement and cost, solvent degradation and recyclability. The gas purity at the inlet of the absorption column and output purity requirements can also affect which solvent to use. Some of these properties will be discussed in relation to the ionic liquids used in this work in the paragraphs below.

The regeneration energy requirement depends on a number of factors, mainly the method used. (Xie et al. (2014)) showed that the energy requirement using a pressure swing separation process is almost two orders of magnitude less than that using a temperature swing process and approximately 20-30% of that using a combined temperature and pressure swing separation process. Using the pressure swing process alone, the most important factor to consider is the enthalpy of CO_2 absorption. There is little data regarding the enthalpy of absorption of CO_2 for the ionic liquids studied in this work, however it is known that [C_2mim][NTf_2], [C_4mim][NTf_2], and [C_2mim][$EtSO_4$] have CO_2 absorption enthalpies of 12 kJ/mol, 14.2 kJ/mol, and 10.46 kJ/mol respectively, all of which are far less than that between MEA and CO_2 (~85 kJ/mol). The enthalpies of absorption of the ionic liquids studied here are likely to be similar since the interaction between them and CO_2 uses physisorption. In comparison, Zhang et al. reported CO_2 absorption enthalpies for ionic liquids using chemisorption between 19-117 kJ/mol.

In the context of recyclability of the ionic liquids, it is known that hydrophobic ionic liquids are easier to recycle than hydrophilic ionic liquids using current technologies since the impurities can be washed out using liquid-liquid extraction with either water or other common solvents (Wu et al. (2009)). For hydrophobic ionic liquids, the recycling method is far more complex and new technologies are still being developed for this purpose. Most of the ionic liquids studied in this work are hydrophobic with the exception of [C_2mim][DCA], [C_2mim][$EtSO_4$], and [C_4mim][TFA]. Whilst this does provide some comparison between the recyclability of ionic liquids, little is known regarding the energy requirement of these processes as it is not currently implemented on a large scale.

6.3. Effect of Drying the Ionic Liquids

In this section, the effect of drying ionic liquids on mean bubble diameter and contact angle will be examined.

6.3.1. Effect on Mean Bubble Diameter

The results of the bubble sizing experiments in a bubble column using wet and dry ionic liquids are presented in Figure 6.16 for a gas flow rate of 3 mL/min. Here, a dry ionic liquid is one which has been dried using the experimental procedures outlined in Section 3.6.2 and a wet ionic liquid is simply one that has not been dried using these procedures. For each ionic liquid tested, the mean bubble diameter was greater after drying the ionic liquid. This is in agreement with the work of (Zhang et al., 2013) who found that bubble size decreases with increasing water content. They attributed this increase with the decrease in viscosity upon water absorption. Other authors have similarly found that ionic liquids with lower viscosities produce smaller bubbles (Kaji et al., 2009, Zhang et al., 2012a).

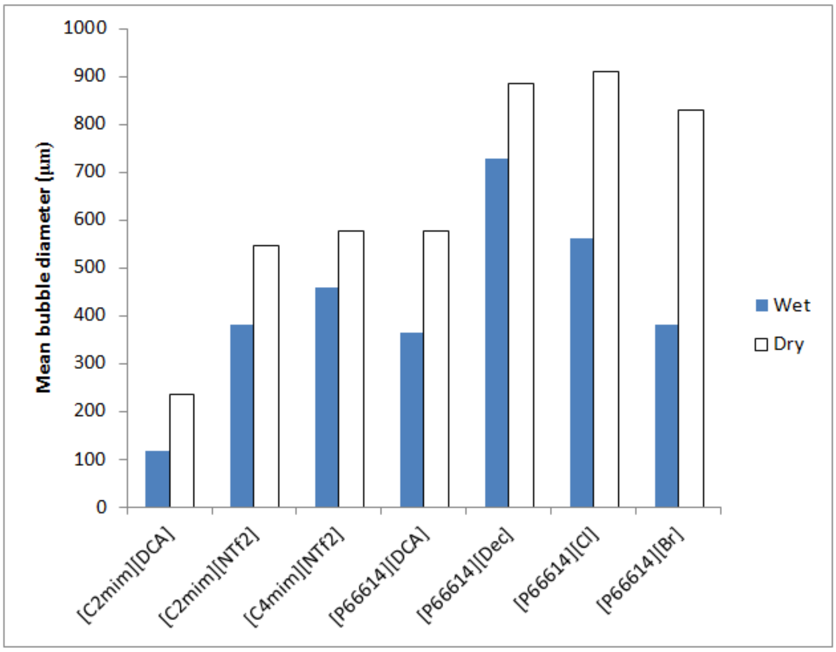

Figure 6.16. Mean bubble diameter in wet and dry ionic liquids: flow rate = 3 mL/min

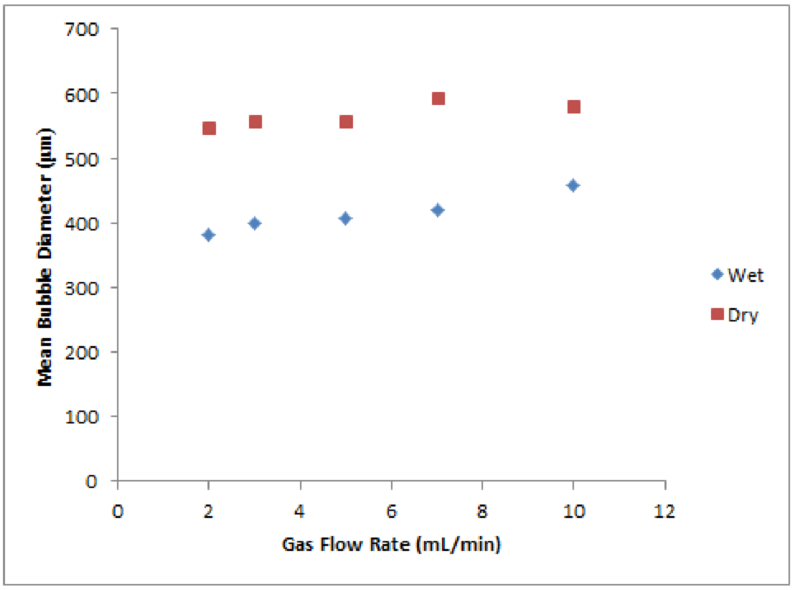

Figure 6.17. Mean bubble diameter vs. gas flow rate in wet and dry [C_2mim][NTf_2]

Figure 6.17 shows that the dry ionic liquid, [C_2mim][NTf_2], produces larger bubbles for a range of flow rates compared with the wet ionic liquid. This suggests that wet ionic liquids would be more suitable for biogas upgrading and other mass transfer processes. This is useful since it is unlikely that ionic liquids would be practical in industry if they had to be held under vacuum every time before use. However, there are some potential drawbacks to using wet ionic liquids:

- Foaming is more likely to occur

  In this work, some of the ionic liquids (namely [C_2mim][DCA] and [P_{66614}][DCA]) were shown to produce a significant amount of foam when they were wet. This was due to the water vapour acting as a surfactant on the surface of the bubbles, causing them to repel each other and thus produce a stable foam (Corning, 1991). At greater flow rates, the foaming process was exacerbated

- The solubility of CO_2 can be reduced upon absorption of water vapour. This has been found by authors such as (Goodrich et al., 2011, Stevanovic et al., 2012). However, the solubility of CO_2 in some ionic liquids has also been shown to increase with water content (Taylor et al., 2014) so this is not necessarily a drawback

It has been shown in the literature that the viscosity of ionic liquids can reduce significantly upon the absorption of a small amount of water (Gallagher et al., 2014, Zhang et al., 2013). However, the surface tension of an ionic liquid is also dependent on water concentration (Sung et al., 2005, Freire et al., 2007, Zhang et al., 2013). Surface tension however, seems to be less affected by water content than viscosity (see (Zhang et al., 2013)). Therefore the reduction in mean bubble diameter is likely to be primarily due to the decrease in viscosity with water content rather than the change in surface tension.

6.3.2. **Effect on Contact Angle**

Another factor that affects the bubble diameter is the wettability of the liquid on the solid diffuser surface (Davidson and Schüler, 1960, Gnyloskurenko et al., 2003). For this reason, the contact angle of wet and dry ionic liquids has been measured on solid alumina tiles with a 96% purity using the procedures discussed in Section 3.6.3. Alumina was chosen since it is the same material as the ceramic diffuser used in the bubble column studies. The results are presented in Figure 6.18.

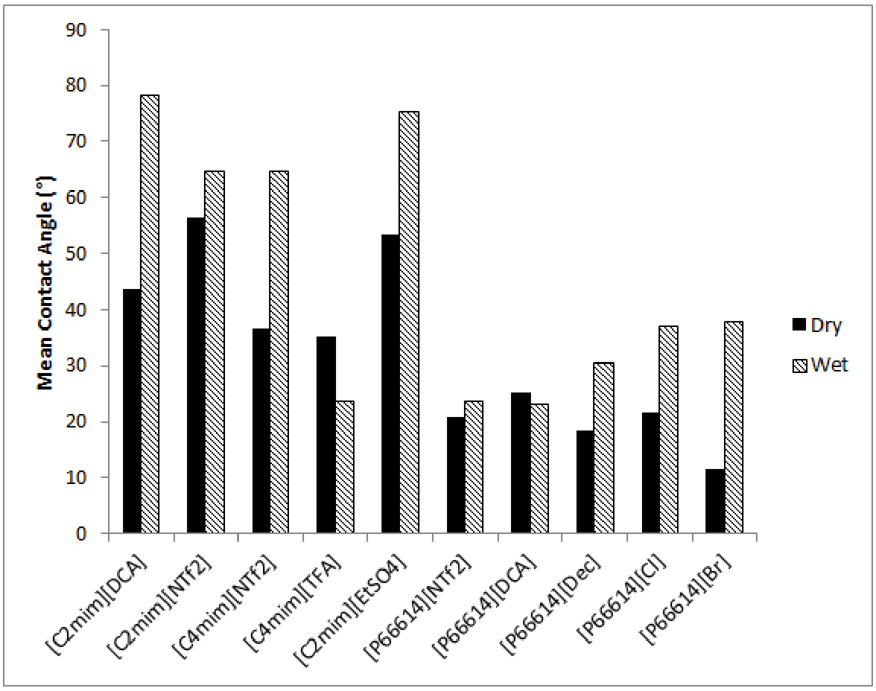

Figure 6.18. Comparison of contact angles of ILs on alumina before and after drying

It can be seen that in nearly every case, the contact angle reduces after the ionic liquid is dried. The largest change in contact angle – a 69% reduction – was experienced by [P66614][Br]. Although the viscosity decreases upon absorption of water vapour, the contact angle also decreases; these effects compete against each other when bubbles are being produced since bubble size typically increases with increasing viscosity and decreases as the contact angle is reduced.

An equation has been developed whereby the contact angle of the ionic liquid is included in an attempt to better define the relationship between mean bubble diameter and system parameters:

$$\bar{d} = 7.575 \cdot 10^{-6} \cdot {\mu_L}^{0.08} \gamma^{-2.98} \rho^{-0.54} {U_G}^{0.19} (\cos(\theta))^{-0.21} \qquad (6.2.5)$$

It was decided to use the cosine of the contact angle in Eqn. 6.2.5 since this is proportional to the wetting force. Unfortunately, the above equation has an R-squared value of 0.841, which is only slightly greater than that for the equation that omits contact angle (Eqn. 6.2.3). This form of the above equation is therefore not ideal for predicting the bubble diameter of ionic liquids.

6.4. Discussion of Bubble Size, Gas Holdup and Interfacial Area

By conducting a force balance on a bubble, as has been undertaken by many other authors, it can be noted that the main factors affecting bubble size and gas holdup are:

liquid viscosity, surface tension, liquid density, superficial gas velocity and the contact angle between the liquid and the solid diffuser surface. In this section, the effects of these parameters on bubble size and gas holdup from this study will be analysed and compared with similar literature studies.

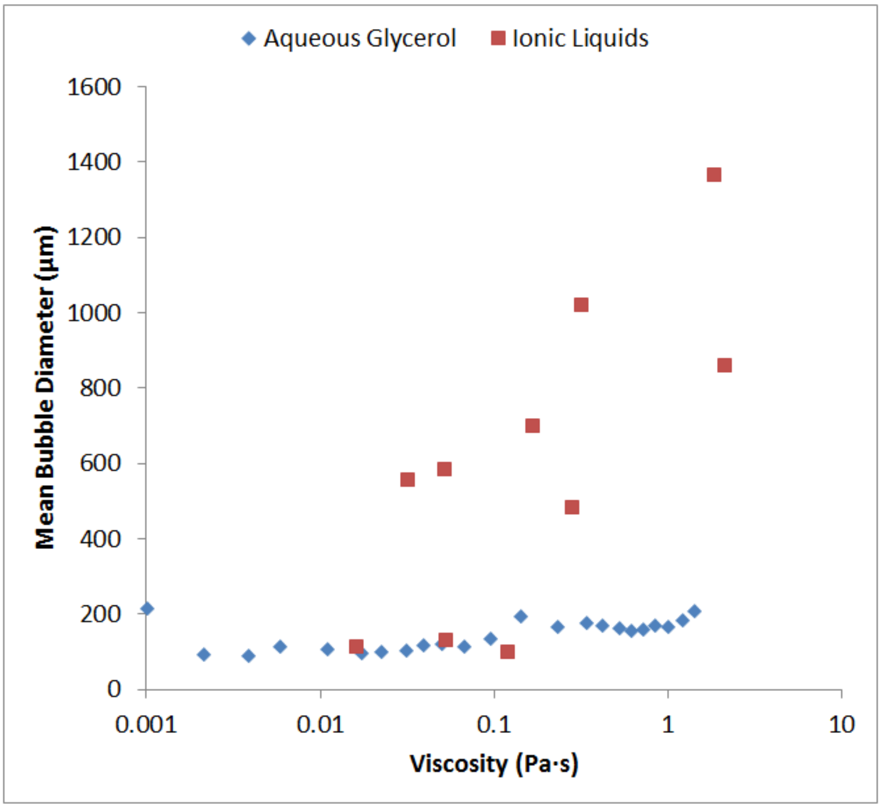

Figure 6.19. Comparison of mean bubble diameter in ionic liquids and water-glycerol mixtures vs liquid viscosity

Figure 6.19 compares the mean bubble diameter between ionic liquids and water-glycerol mixtures produced in this work at a gas flow rate of 3 mL/min. It is clear that for the same liquid viscosity, the bubble size is far smaller in the water-glycerol mixtures than in most of the ionic liquids studied with the exception of [C$_2$mim][DCA], [C$_4$mim][TFA], and [C$_2$mim][EtSO$_4$].

Correlations for the mean bubble diameter and gas holdup using data from both the ionic liquids and water-glycerol mixtures have been obtained using a multiple regression analysis with R-squared values of 0.947 and 0.781 respectively:

$$\bar{d} = 1.094 \cdot 10^{-5} \cdot {\mu_L}^{0.11} \gamma^{-2.0} \rho^{-0.31} {U_G}^{0.06} \tag{6.2.6}$$

$$\varepsilon = 1.030 \cdot 10^{10} \cdot {\mu_L}^{0.79} \gamma^{4.05} \rho^{-0.37} {U_G}^{0.89} \tag{6.2.7}$$

It can be seen from Eqns. 6.2.6 and 6.2.7 that the gas-liquid surface tension has the largest effect on both the mean bubble diameter and gas holdup since the magnitude of the exponent of the surface tension is greatest. For determining bubble diameter, the liquid density is the next most important parameter followed by viscosity and superficial gas velocity. For gas holdup, the superficial gas velocity is the next most important parameter followed by liquid viscosity and liquid density.

In this work, the physical properties of the aqueous glycerol mixtures have been calculated from empirical correlations where the authors have measured the macroscopic properties of the liquid. This assumes that the liquid is well mixed. In reality, the two liquid phases may not be so well mixed on a microscopic scale, i.e. there may be variations in these physical properties on the surface of the bubble. This could cause the bubbles to form differently to how one would expect them to form in a uniform mixture, for example gradients in surface tension are known to affect the mobility of the vapour-liquid interface, which can cause the bubbles to rise faster. Similarly, viscosity variations close to the bubble may cause the fluid flow to behave differently which could affect the shape of the bubble.

Additionally, despite the mixtures being stirred thoroughly with a glass rod, the physical properties may still vary between different areas of the column which could cause the mean bubble size to be larger in one area compared with another. This could in turn affect the currents inside the column due to the swarms of bubbles rising which could further affect bubble formation.

Many of the empirical correlations compared with this work are also based on bubble size in binary mixtures, e.g. (Davidson and Schuler, 1960, Akita and Yoshida, 1974). This means that it is very important that the mixtures were equally well mixed in these studies in order to draw an accurate comparison.

While many authors suggest that bubble size increases with surface tension in common solvents, this work found that the bubble size actually reduces with surface tension in ionic liquids. This is in agreement with the work of (Zhang et al., 2012a) – the only other study on ionic liquids in bubble columns at the time of writing that has quantified bubble size in this manner – albeit this study showed a more significant influence of surface tension. Other authors have qualitatively noted that viscosity has a larger effect than surface tension in ionic liquids; however they attribute this to the fact that water affects the viscosity of ionic liquids more than it affects surface tension (Dong et al., 2010, Zhang et al., 2013). As mentioned previously, the reason for the large influence of surface tension on mean bubble diameter is likely to be due to the stabilising effect of surface-tension on the homogeneous regime in bubble columns. Whilst (Sardeing et al., 2006) found that mean bubble diameter decreases as surface tension decreases, their work investigated the influence of surfactants on the mean bubble diameter. Many other authors have also used liquid mixtures to characterise the effects of system parameters on bubble size e.g. (Ruzicka et al., 2003). However, (Chaumat et al., 2007) undertook experiments using pure organic liquids and found that larger bubbles were produced in pure cyclohexane – an organic molecule with a low surface tension – than in pure water in bubble columns for the same gas flow rate. They attributed this to the destabilising effect of cyclohexane on the homogenous bubble regime. It is likely that a similar effect is experienced with ionic liquids since the ionic liquids with similar surface tensions to cyclohexane generally produced larger bubbles.

Another reason why surface tension might affect bubble diameter is due to its effect on contact angle; however, it has recently been discovered that the contact angle of ionic liquids decreases as surface tension decreases (Restolho et al., 2009b, Sedev, 2011). This should mean that larger bubbles would be produced for liquids with greater surface tensions (Gnyloskurenko et al., 2003).

Additionally, there may be some complex chemistry occurring at the solid-liquid interface with ionic liquids that does not occur with aqueous glycerol mixtures. One example is ion arrangement, which has been discussed by (Cremer et al., 2011), albeit not in relation to bubble formation.

In addition to the bubble size produced at the point of formation, additional factors such as bubble coalescence and break-up also largely contribute to bubble size when considering swarms of bubbles. Factors influencing the amount of bubble coalescence and break-up include: the zeta-potential of bubbles, the structure of the liquid, physical properties of the liquid, the mono-dispersity of bubbles in the column, column design, and the gas flow rate.

One factor that strongly influences bubble coalescence is the zeta potential, which is a measure of the charge caused by the arrangement of ions on the surface of the bubble.

These charges can cause bubbles to attract or repel one another. It is known than while in common solvents the cation rings are typically parallel to the bubble surface, in ionic liquids they are perpendicular to the surface. Currently there is no data on how this affects bubble coalescence in ionic liquids but it is likely to affect the attraction/repulsion between adjacent bubbles.

Physical properties, such as the low surface tension of ionic liquids can cause bubbles to coalesce and break up easier since the force holding the bubble together is smaller. Additionally, the high viscosity of ionic liquids causes bubble swarms to agglomerate since the drag forces acting on the bubbles are greater. The amount of agglomeration can be reduced by careful design of the bubble column.

The variation in bubble size is also a significant factor in determining the amount of bubble coalescence. If the bubbles are not of a similar size and are not monodisperse then they will rise at different velocities and are therefore more likely to interact with each other and coalesce. The column design can significantly affect this, e.g. a diffuser with a non-uniform pore size will likely cause more bubble coalescence than one with uniform pores.

The gas flow rate is another factor that influences bubble coalescence and break-up. A greater flow rate is likely to produce larger bubbles, however the bubbles are more susceptible to coalesce and breakup since the force holding the bubble together (surface tension) becomes relatively smaller in comparison with the other forces acting on the bubble as the bubble size increases.

Eqn. 6.2.6 also shows that bubble diameter decreases with liquid density; this is in agreement with the work of other authors experimenting with common solvents. This work also found that bubble diameter increases with viscosity and superficial gas velocity, which is in agreement with most other literature studies (Akita and Yoshida, 1974, Jamialahmadi et al., 2001, Zhang et al., 2013).

Table 6.1 and Table 6.2 convey the dependencies of bubble diameter on liquid physical properties and gas flow rate from an orifice and a bubble column respectively.

Table 6.1. Dependencies of bubble size on liquid physical properties and gas flow rate from an orifice: ↑ indicates bubble size increase, ↓ indicates bubble size decrease

Reference	Viscosities Studied (Pa·s)	Property affecting bubble size			
		Increasing Viscosity	Increasing Surface Tension	Increasing Density	Increasing Flow Rate
(Davidson and Schüler, 1960)	0.5-1.04	↑	↑	↓	↑
(Ramakrishnan et al., 1969)	0.001-0.552	↑	↑	↓	↑
(Park et al., 1977)	0.005-0.522		↑	↓	
(Gaddis and Vogelpohl, 1986)	0.001-1.0	↑	↑	↓	↑
(Terasaka and Tsuge, 1990)	0.001-1.1	↑			
(Jamialahmadi et al., 2001)	0.001-0.09	↑	↑	↓	↑
(Zhang et al., 2013)	0.0068-0.088	↑	↑	↓	↑

It is clear that all of the authors presented in Table 6.1 agree that from a single orifice, the mean bubble diameter increases with increasing viscosity, surface tension, and flow rate, and with decreasing liquid density. This has been concluded using liquids of varying viscosities from 0.001-1.1, which covers most of the ionic liquid viscosities studied in this work.

The general consensus in bubble columns is that bubble diameter increases with increasing viscosity and surface tension and with decreasing liquid density; however there are some disagreements over the effect of gas flow rate (see Table 6.2). Moreover, all of the bubble column studies have been conducted using liquids of viscosity less than 0.65 Pa·s. The results of this work, as portrayed by Eqn. 6.2.6 agrees to some extent with previous studies, primarily with regard to the effects of liquid viscosity, density and superficial gas flow rate. However, Eqn. 6.2.6 suggests that mean bubble diameter decreases with increasing liquid surface tension, which is in direct conflict with all previous works except that of (Zhang et al., 2012a). As mentioned previously, this is probably due to the stabilising effect of the homogeneous regime at higher surface tensions as found by (Ruzicka et al., 2008).

Table 6.2. Exponential dependences of bubble diameter on liquid properties and superficial gas velocity in a bubble column: d $\propto \mu_L^A \gamma^B \rho_L^C U_G^D$ (adapted from (Pohorecki et al., 2005))

Reference	Viscosities Studied (Pa·s)	A	B	C	D
(Hughmark, 1967)	0.0009-0.152		0.60	-0.20	
(Van Dierendonck, 1970)	0.04-0.65		0.50	-0.50	
(Akita and Yoshida, 1974)	0.0006-0.002	0.24	0.50	-0.74	-0.12
(Ramakrishnan et al., 1969)	0.001-0.012		0.25	-0.25	0.43
(Wilkinson et al., 1994)	0.0004-0.021	0.22	0.34	-0.45	-0.02
(Pohorecki et al., 2005)	0.0005-0.005	-0.05	0.44	-0.55	-0.12
(Zhang et al., 2012a)	0.066-0.188	0.14	-0.10	0.07	0.28
This work (water-glycerol)	0.001-1.412	0.56	35.1	-0.36	
This work (ILs)	0.016-2.094	0.08	-2.88	-0.37	0.19
This work (water-glycerol + ILs)	0.001-2.094	0.11	-2.0	-0.31	0.06

Eqn. 6.2.7 shows that gas holdup increases with increasing viscosity, increasing surface tension, decreasing density, and increasing superficial gas velocity. Most authors in the past have found viscosity to reduce the gas holdup (see Table 6.3). It was shown in Figure 6.10 that gas holdup in [C$_2$mim][DCA] is greater than that in some of the more viscous ionic liquids ([C$_2$mim][NTf$_2$] , [C$_4$mim][NTf$_2$], and [P$_{66614}$][Dec]). However, if the viscosity of the liquid is increased by two orders of magnitude (see [P$_{66614}$][Cl], [P$_{66614}$][Br]), then the bubbles rise so slowly in the liquid that gas holdup actually increases.

Table 6.3. Exponential dependences of gas holdup on liquid properties and superficial gas velocity in a bubble column: $\varepsilon \propto \mu_L^A \gamma^B \rho_L^C U_G^D$

Reference	Bubble Regime	Viscosities Studied (Pa·s)	A	B	C	D
(Hikita et al., 1980)	N/A	0.0006-0.017	-0.05	-0.19	-0.19	0.58
(Godbole et al., 1982)	Slug flow	0.001-0.246				0.63
(Haque et al., 1986)	Churn-turbulent		-0.22			0.60
(Kawase et al., 1987)	N/A	0.001-0.034				0.67
(Öztürk et al., 1987)	Slug flow		-0.22	0.13	0.09	0.54
(Vatai and Tekić, 1989)	Slug flow	0.002-0.067				0.53
(Kang et al., 1999)	Bubbly and Churn-turbulent flow	0.001-0.038	-0.20		0.20	0.20
(Urseanu et al., 2003)	Churn-turbulent	0.05-0.55	-0.12			0.58
(Mouza et al., 2005)	Bubbly flow	0.001-0.023	-0.13	-1.5	1.6	0.67
This work (water-glycerol)	Bubbly flow	0.001-1.412	-0.12	-70.2	-0.28	
This work (ILs)	Bubbly flow	0.016-2.094	0.84	5.76	-0.26	0.61
This work (water-glycerol + ILs)	Bubbly flow	0.001-2.094	0.79	4.05	-0.37	0.89

Eqn. 6.2.7 also shows that gas holdup increases with increasing surface tension and superficial gas velocity and decreasing liquid density. Previous studies agree that the gas holdup increases with superficial gas velocity, however there is some disagreement over the effects of surface tension and density. Whilst (Hikita et al., 1980) and (Mouza et al., 2005) found that gas holdup increases with decreasing surface tension using liquids such as sucrose, methanol, n-butanol, and glycerol, (Schumpe and Deckwer, 1982), who experimented with thickening agents under slug flow conditions, found the opposite.

Surface tension and density are shown to have a much larger effect on both mean bubble diameter and gas holdup than liquid viscosity in this work. While other authors have found liquid viscosity to have a reducing effect on gas holdup, this work has found the opposite. This is likely to be due to the fact that the bubbles produced in this work are significantly smaller than those produced in previous works, particularly at greater liquid viscosities. Since the terminal rise velocity of a bubble is proportional to the cube of the bubble diameter, the bubbles were able to stay in the liquid for longer even at high viscosities, resulting in an increase in gas holdup with viscosity. Additionally, it can be seen in Table 6.3 that much of the previous work has used bubbles in the slug flow and churn-turbulent regimes. In this work however, most of the bubbles were very homogeneous and were therefore in the bubbly flow regime. This homogeneity likely reduced the amount of bubble coalescence, further enabling the bubbles to stay in the liquid for longer.

6.5. Flow Regime Transition

In most of the ionic liquids tested, bubbly flow is observed. However, in the more viscous ionic liquids, transition to the churn-turbulent regime occurs at greater flow rates. For [P_{66614}][Dec] and [P_{66614}][Cl], this transition occurs at a flow rate of about 50 mL/min, whilst for [P_{66614}][Br], the transition occurs at a flow rate of about 30 mL/min. By measuring the bubbles and calculating terminal velocities in the dry ionic liquids, the Reynolds and Eötvös numbers can be calculated. At the point of transition to the churn-turbulent regime, the bubbles which appear ellipsoidal in shape have Reynolds numbers of the order unity and Eötvös numbers between one and ten. This is in good agreement with the literature (Clift et al., 1978).

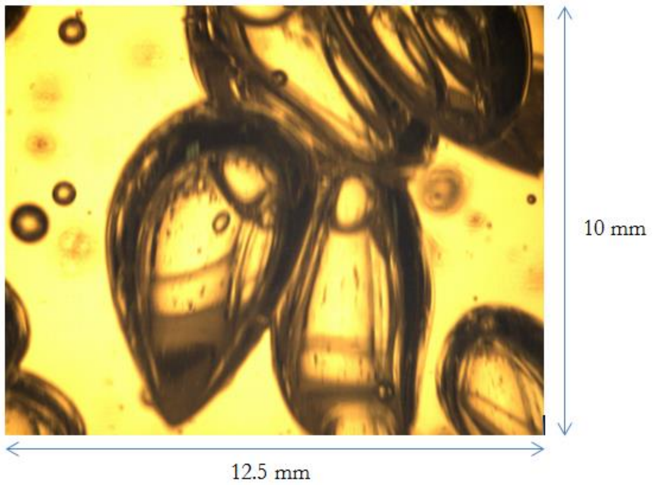

Figure 6.20. Bubbles in [P_{66614}][Br]: Flow rate = 50 mL/min

6.6. Conclusions

It is well noted in the literature that small bubbles – in particular microbubbles – have higher rates of mass transfer compared with large bubbles. Due to the physical properties of ionic liquids, in particular their high viscosities, it is more difficult to produce microbubbles in them compared with in conventional solvents.

With regard to biogas upgrading, the work undertaken in this chapter has shown that ionic liquids with a high surface tension should be considered since this parameter has a large effect on bubble size and therefore has a large influence on the rate of mass transfer. In addition to this, ionic liquids with low viscosities and high densities would also produce smaller bubbles and would therefore also enhance the rate of mass transfer. A low viscosity would also increase the diffusion coefficient of CO2 in the ionic liquid, which would further aid mass transfer.

High viscosity liquids would also be more likely to block the pores of a diffuser in a bubble column and would therefore increase the maintenance costs of running a plant. Additionally, a more powerful pump would be required with a high viscosity ionic liquid since there would be more viscous losses due to friction on the pipe walls.

It may also be useful to use wet ionic liquids for biogas upgrading in practical applications since this helps to reduce the liquid viscosity. However, it must be noted that this can also affect the CO2 absorption capacity of the ionic liquid – in some cases negatively. Therefore, using wet ionic liquids may not always be of benefit in practice.

In this work the fluidic oscillator did not have a significant effect on the bubble size due to the pressure drop across the diffuser and the high viscosity of the ionic liquids. However, further effort to improve the rig design to comply with the fluidic oscillator could potentially improve the mono-dispersity of the bubbles in ionic liquids, which could reduce the mean bubble size by reducing the amount of bubble coalescence.

The main conclusion from the work undertaken in this chapter is that [C_2mim][$EtSO_4$], [C_4mim][TFA], and [C_2mim][DCA] produce the smallest bubbles of the ionic liquids tested. The smallest bubbles produced in ionic liquids had a mean diameter of less than 100 μm, which is comparable to the bubble size produced in aqueous glycerol solutions of similar viscosity. All of the other ionic liquids produced bubbles far larger than those produced in aqueous glycerol solutions of similar viscosity.

Additionally, [C_2mim][DCA], [C_4mim][TFA], and [C_2mim][$EtSO_4$] produce large gas holdups compared with the other ionic liquids tested. Therefore, it seems that these ionic liquids are likely to be better for mass transfer applications, such as biogas upgrading.

Other conclusions of the work undertaken for this chapter are:

- When the gas supply pressure was oscillated into a single orifice bubble column containing an ionic liquid at frequencies between 70 – 770 Hz via a fluidic oscillator, no considerable reduction in bubble size was achieved. This was due to the gas not having enough inertia to break off from the orifice since the drag force acting on a bubble is far greater in ionic liquids compared with water
- In aqueous glycerol solutions, the mean bubble diameter in a bubble column was shown to be proportional to $\mu_L^{0.56}\ \gamma^{35.1}\varrho^{-0.36}$, indicating that surface tension has a much larger effect on bubble diameter than viscosity
- The viscosity of ionic liquids has a significant effect on bubble size; however, the surface tension has a comparatively more significant effect. The bubble size was shown to be approximately proportional to $\mu_L^{0.08}\ \gamma^{-2.88}\varrho^{-0.37}U_G^{0.19}$ in ionic liquids in bubble columns
- Unlike in the aqueous glycerol experiments, a lower surface tension was shown to produce larger bubbles in ionic liquids. This is thought to be due to the stabilising/de-stabilising effect that surface tension is known to have on gas holdup in bubble columns
- With the exception of [C_2mim][$EtSO_4$], gas holdup is greater in aqueous glycerol solutions than in the ionic liquids tested.
- Gas holdup is inversely proportional to liquid viscosity and surface tension in the water glycerol solutions; however, the opposite was true for ionic liquids
- Drying ionic liquids reduces the contact angle on alumina but still produces larger bubbles. This is due to the viscosity increasing upon drying the ionic liquids.
- A flow transition to the churn-turbulent regime was observed in highly viscous ionic liquids ([P_{66614}][Dec], [P_{66614}][Cl], and [P_{66614}][Br]) for Re ~ 1 and 1 < Eö < 10

7. Biogas Upgrading in MEA and Ionic Liquids

In this chapter, the capabilities of seven ionic liquids and a 30 wt. % aqueous MEA solution are investigated for the purpose of biogas upgrading in bubble columns. First, a recap of the objectives is presented; following this, the experimental results will be analysed, including a comparison of gas holdups and mass transfer coefficients observed in the ionic liquids; finally, conclusions will be drawn. Tables of the experimentally determined solubilities, bubble size, gas holdups and mass transfer coefficients can be found in Appendix G: c^*, ε, K_La, and k_L Tables.

The objectives of the work conducted in this chapter, as mentioned in Chapter 1, are to:

- Assess the capabilities of ionic liquids and a 30 wt.% aqueous MEA solution for upgrading biogas in a bubble column using microbubbles
- Determine the effect of flow rate on the capability of ionic liquids to upgrade biogas
- Determine mass transfer coefficients for CO_2 absorption in ionic liquids and compare them with correlations obtained in the literature for common solvents

The ionic liquids that will be investigated are: $[C_2mim][DCA]$, $[C_2mim][NTf_2]$, $[C_4mim][NTf_2]$, $[C_4mim][TFA]$, $[C_2mim][EtSO_4]$, $[P_{66614}][NTf_2]$, and $[P_{66614}][Cl]$. The ionic liquid with the greatest CO_2 absorption capacity will be used to determine the effect of flow rate on the mass transfer coefficients, K_La and k_L.

7.1. Preliminary Experiments

Preliminary experiments were conducted using the experimental setup and methods described in Sections 3.3.3.1 and 3.5.4.1 with $[P_{66614}][Cl]$ in order to test whether the experimental setup and methods are appropriate for achieving the objectives and to suggest improvements to the experimental setup and methods.

Figure 7.1 shows the CO_2 concentration measured in the ionic liquid between two experimental runs, each conducted at room temperature with an inlet pressure of 1.4 bar. It can be seen in Figure 7.1 that the experiment was not reproducible. This was primarily due to the large inaccuracy in the measurement of the inlet flow rate, which existed for two reasons: firstly, the water level was fluctuating in the biogas collector so there was a large amount of human error present in the gas flow rate measurement; and secondly, it could not be adequately determined when the ionic liquid became saturated.

As a result, the inlet flow rate may have been underestimated. Additionally, it was assumed that no CH_4 was absorbed in the ionic liquid since it is known that the CH_4 solubility in [P_{66614}][Cl] is less than 0.01 mol/L (Morgan et al., 2005). However, the experiments of Morgan et al. (2005) were conducted using pure gases, rather than a gas mixture. The assumption of no methane absorbing into the ionic liquid from a gas mixture could not be verified using the existing experimental setup; however, it will later be shown to be false. As a result, the observed amount of CO_2 absorbed in the ionic liquid in one of the experimental runs was greater than the saturation concentration of 0.049 mol/L as reported by (Ferguson and Scovazzo, 2007).

In addition to the experimental inaccuracies, a large time lag occurred before absorption of CO_2 was observed. This was due to a combination of the large size of the headspace in the absorption column (364 mL) and the low gas flow rate (~40 mL/min).

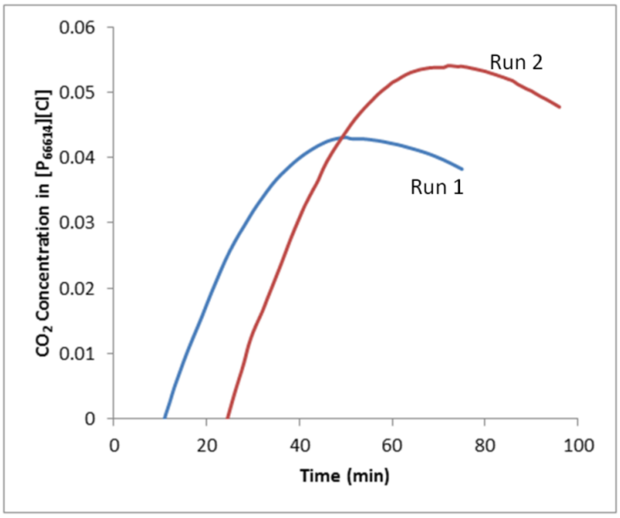

Figure 7.1. Preliminary experimental results: CO_2 concentration in [P_{66614}][Cl] (inlet pressure=1.4bar)

In order to diagnose the aforementioned problems with the experimental setup and methods, a digital mass flow controller was added to control the inlet flow rate with an accuracy of ±0.2 mL/min and the flow rate out of the column was measured by weighing the amount of water displaced in the biogas collector with an accuracy of ±0.1g (approx. 0.1 mL).

In addition to the experiment not being reproducible, the CH_4 concentration in the off-gas was relatively low, peaking at 75% after 11 minutes, as shown in Figure 7.2, which is far lower than the 95% purity requirement for injection into the gas grid. There were three main reasons for this: Firstly, the diffusivity of CO_2 in [P_{66614}][Cl] is very low –

approx. 1 order of magnitude less than in water (Morgan et al., 2005). Secondly, there was a small driving force for mass transfer due to the low solubility of CO_2 in $[P_{66614}][Cl]$ – only 0.049 mol/L according to the work of (Ferguson and Scovazzo, 2007). Thirdly, despite the mean pore size from the diffuser being 0.6 μm, the mean bubble diameter in $[P_{66614}][Cl]$ was measured to be 2,109 μm, which is relatively large; one can recall that fine bubbles – those of diameter between 1-2 mm – have a lower internal pressure, smaller surface area per unit volume, and higher rise velocities (leading to shorter residence times) than microbubbles (see Chapter 2), all of which act to reduce the rate of mass transfer. In Chapter 6, it was shown that the low surface tension and high viscosity of the ionic liquid enhances the production of larger bubbles. Therefore, in order to produce microbubbles, ionic liquids with lower viscosities, greater surface tensions and greater CO_2 solubilities were obtained.

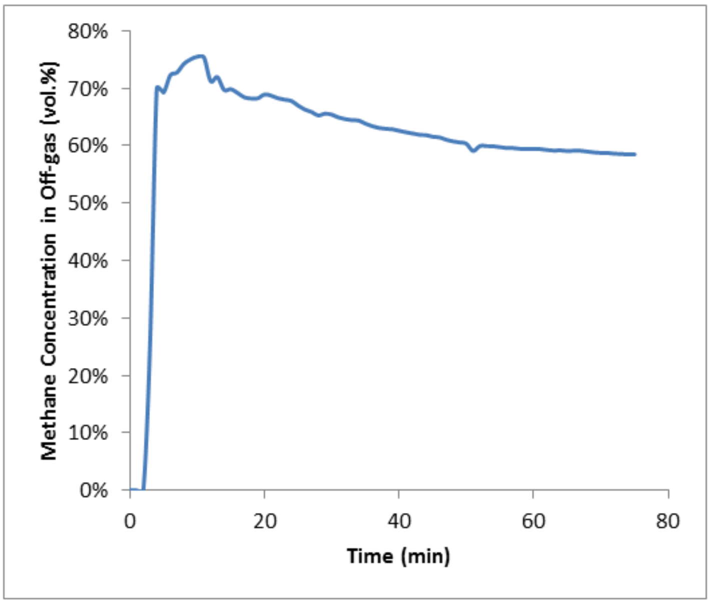

Figure 7.2. Preliminary experimental results: CH_4 concentration in off-gas (solvent = $[P_{66614}][Cl]$, gas flow rate = 36 mL/min)

Figure 7.3 and Figure 7.4 show photographs of bubbles in $[P_{66614}][Cl]$ for a flow rate of 36 mL/min. It can be seen in Figure 7.3 that due to the high viscosity of the ionic liquid and the central position of the diffuser in the column, most of the bubbles congregated in the centre of the column as they were dragged by the currents produced in the liquid; some smaller bubbles were recirculated around the edges. This led to more bubble coalescence, resulting in bubbles rising at different velocities (due to their different sizes) and thus even more bubble coalescence occurred. This was partly the cause of the relatively large bubble size.

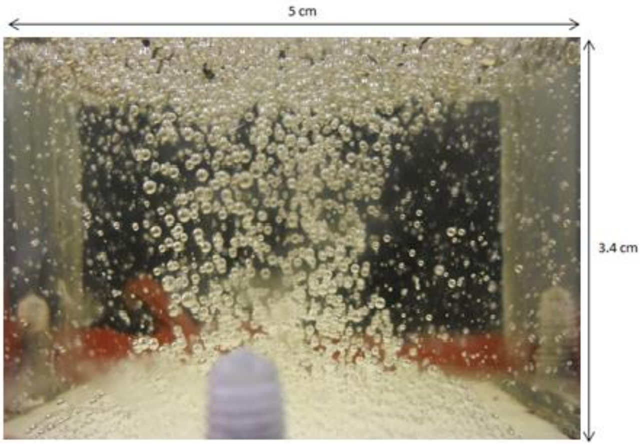

Figure 7.3. Photograph of bubble distribution in [P_{66614}][Cl] using preliminary experimental setup

Since this work aims to upgrade biogas using microbubbles, in addition to testing other ionic liquids, it was decided to re-design the absorption column such that the diffuser was placed to one side in order to reduce the amount of coalescence and make it easier to image bubbles (see Section 3.4.4.2).

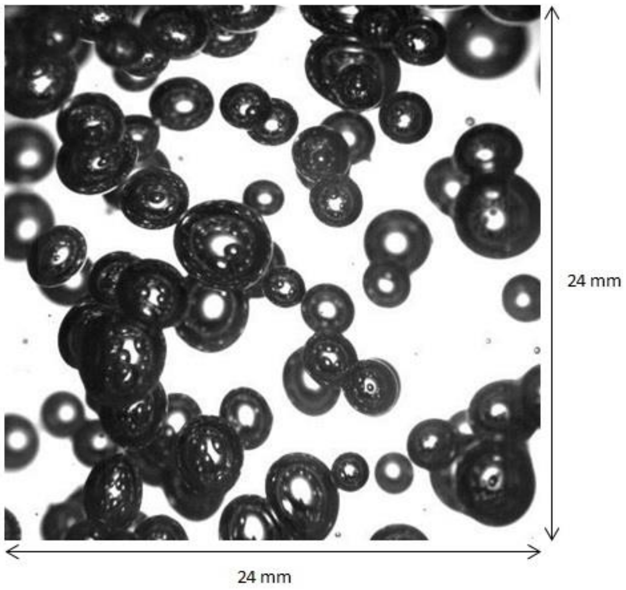

Figure 7.4. Example photograph of bubbles captured using a high-speed camera

7.2. Repeatability Checks and Uncertainties

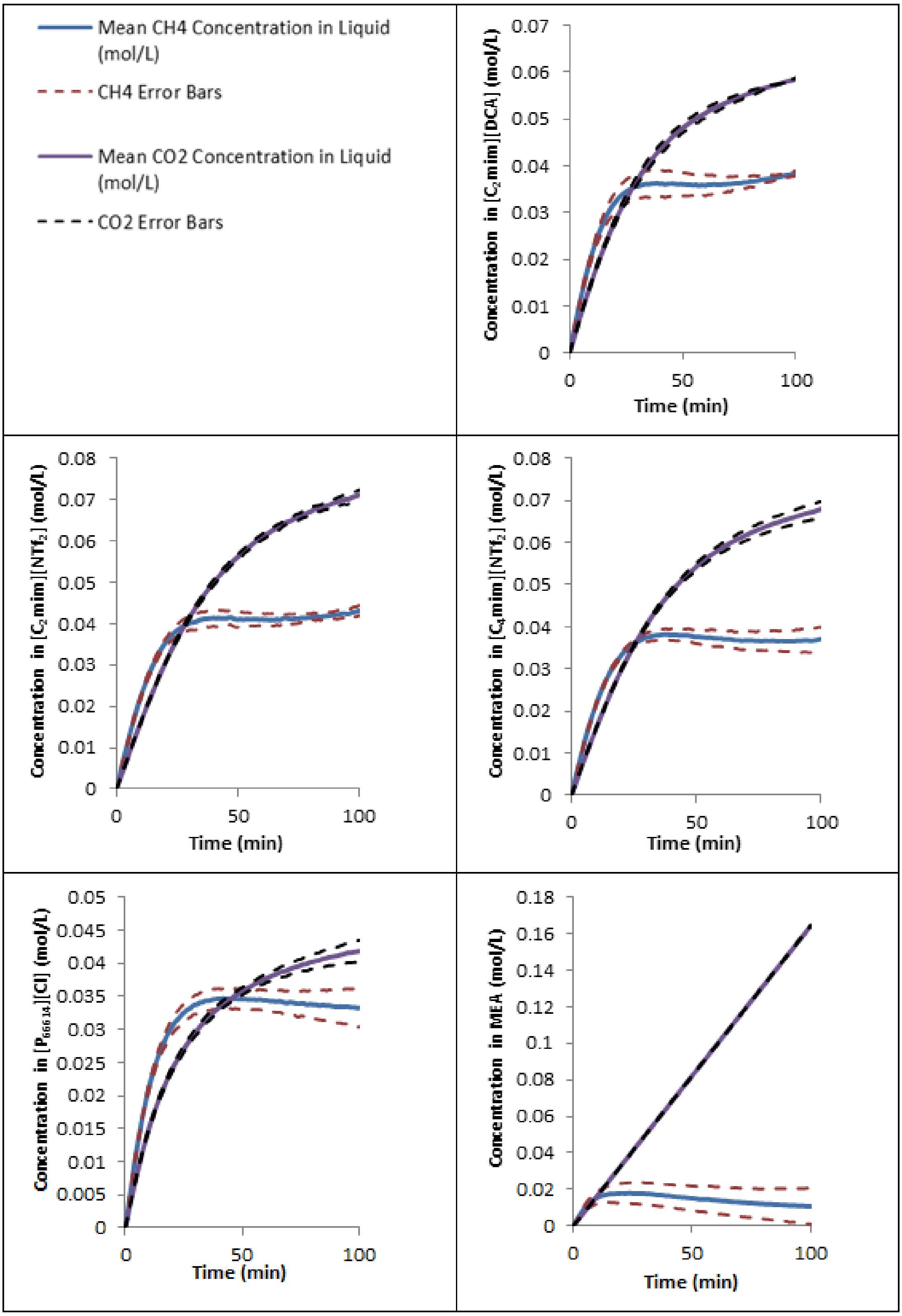

Figure 7.5. Mean concentrations of CH_4 and CO_2 in ionic liquids and MEA with error bars (±1 std. dev.); gas flow rate = 10 mL/min

Due to the difficulty in measuring the concentrations of CH_4 and CO_2 in the ionic liquids directly, these concentrations had to be inferred by measuring what was present in the gas phase. This meant that more pieces of experimental equipment had to be used, resulting in compounding errors. In order to ensure accuracy of the experimental data, each experiment was conducted three times; however, in cases where the standard deviation was greater than ±5% of the mean value, a fourth experiment was undertaken. It must be noted here that the ionic liquids [C_4mim][TFA], [C_2mim][$EtSO_4$], and [P_{66614}][NTf_2] were obtained late on in the project and thus, due to time considerations, only two experiments were undertaken. Mean CO_2 and CH_4 concentrations in the ionic liquids along with error bars of ±1 standard deviation are presented in Figure 7.5 for an inlet flow rate of 10 mL/min. Figure 7.6 presents mean concentrations of CH_4 and CO_2 in [C_2mim][NTf_2] for flow rates of 5, 15, and 20 mL/min with error bars of ±1 standard deviation.

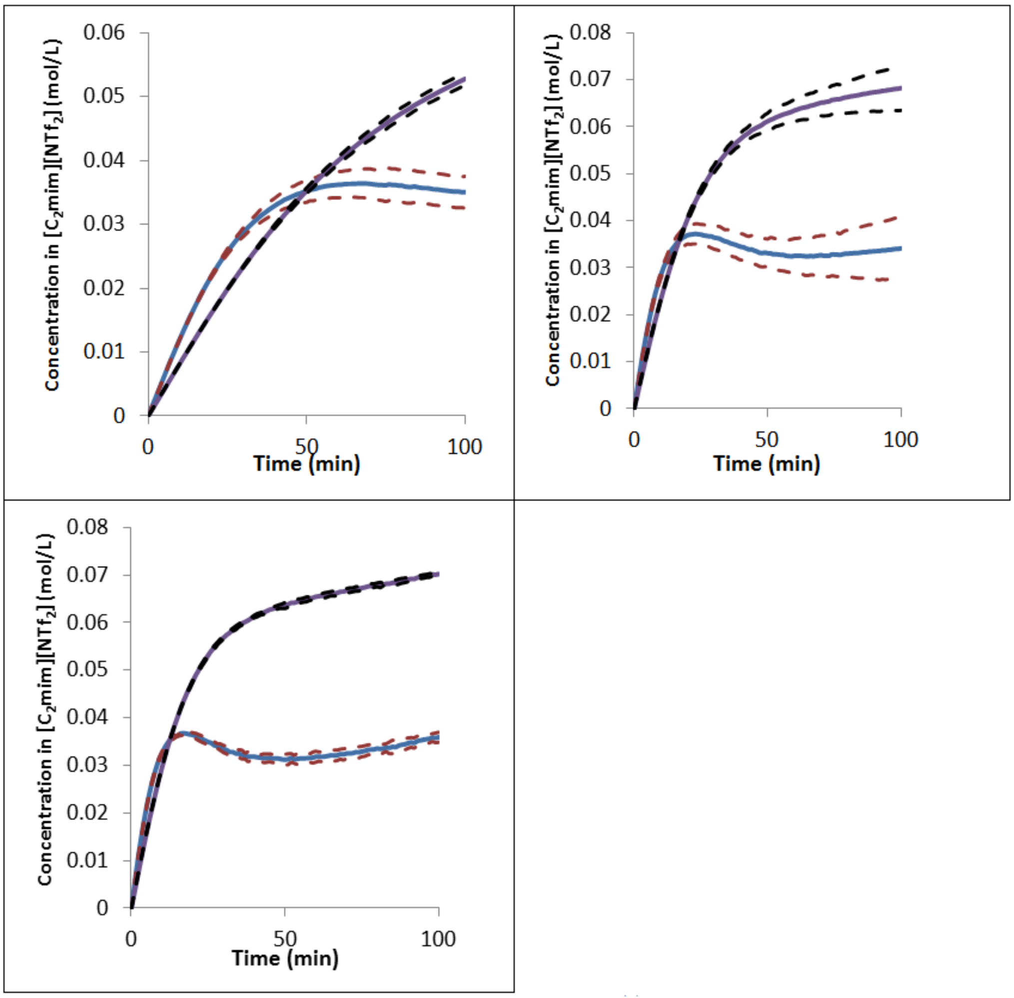

Figure 7.6. Mean concentrations of CH_4 and CO_2 in [C_2mim][NTf_2] with error bars (1 std. dev.) for gas flow rates of: (a) 5 mL/min; (b) 15 mL/min; (c) 20 mL/min

Due to the nature of the experiment, propagation of error was experienced (since the total error in the mass flow controller propagates with time); this explains why the error bars generally diverge and why the error was particularly large when measuring lower concentrations, e.g. CH_4 in MEA. Additionally, there is known to be some drift on the IR gas analyser with time (up to 1% over the course of the experiment). This was confirmed by measuring the gas composition in the cylinder after the experiment had reached completion.

Overall, the experimentally determined solubilities of CO_2 in the ionic liquids were in good agreement, differing by less than ±7.8% between experimental runs. For the purpose of calculating mass transfer coefficients, this was deemed suitable since all of the R-squared values from the K_La graphs were greater than 0.95 (see Appendix F: K_La Graphs).

7.3. Bubble Size in MEA and Ionic Liquids with Biogas Mixture

The mean diameter of bubbles in ionic liquids and a 30 wt.% aqueous MEA solution, measured using the techniques described in Section 3.5.2 with an artificial biogas mixture (60 vol.% CH_4, 40 vol.% CO_2), are presented in Figure 7.7 for a gas flow rate of 10 mL/min. It can be seen that the smallest bubbles were produced in the aqueous MEA solution with a mean diameter of 73.7 μm. This was unsurprising since this solution has the greatest surface tension and the lowest viscosity of all the liquids tested. In addition, the diffuser used has been shown to produce very small bubbles in water, which has similar properties to the MEA solution.

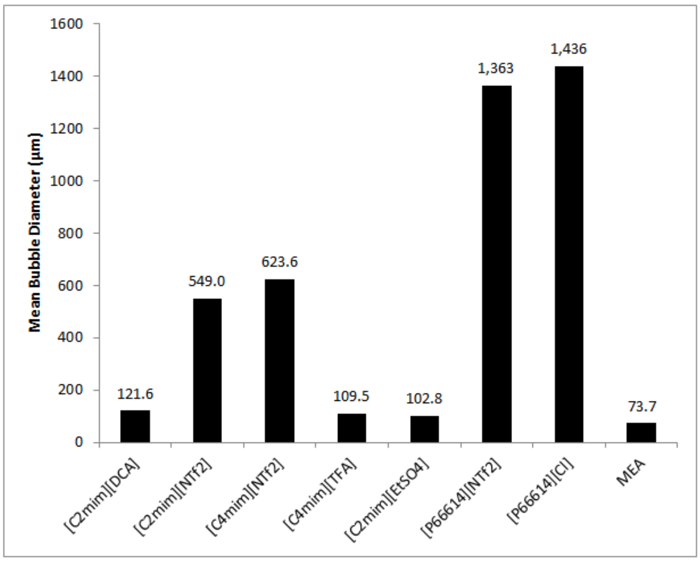

Figure 7.7. Mean diameter of biogas bubbles in MEA and ionic liquids; gas flow rate = 10 mL/min

Of the ionic liquids tested, the smallest bubbles were produced in [C_2mim][$EtSO_4$], followed by [C_4mim][TFA] and [C_2mim][DCA]. This is in agreement with the experiments conducted in Chapter 6. With the exception of [P_{66614}][NTf_2] and [P_{66614}][Cl], the mean bubble diameter in all of the liquids was in the microbubble range, i.e. between 1-1000 µm.

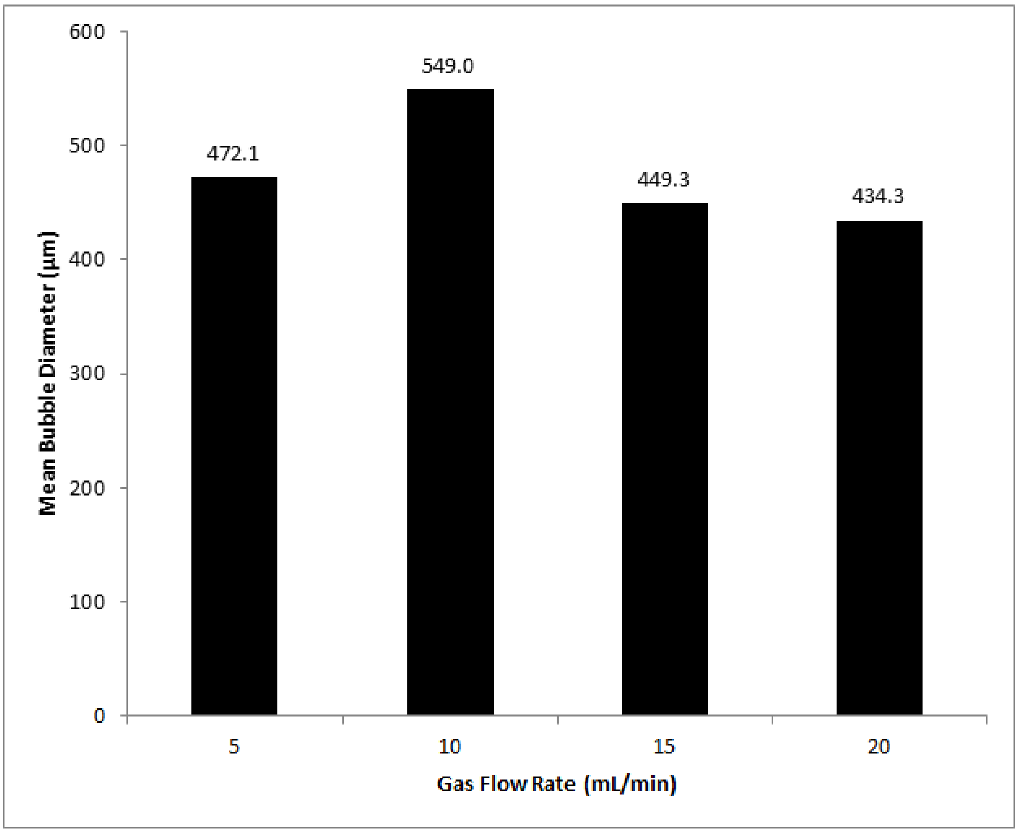

Figure 7.8. Mean diameter of biogas bubbles in [C_2mim][NTf_2] for different gas flow rates

Figure 7.8 shows the mean diameter of biogas bubbles in [C_2mim][NTf_2] for gas flow rates of 5, 10, 15, and 20 mL/min. Again, the mean bubble diameter was in the microbubble range for all flow rates investigated. However, gas flow rate appears to have little effect on mean bubble diameter, which is in agreement with the experiments conducted in Chapter 6. The bubble diameters presented in Figure 7.7 and Figure 7.8 will be used later in this chapter to calculate the individual liquid-side mass transfer coefficients.

7.4. CO_2 Uptake, CH_4 Uptake and Selectivity

The CO_2 uptake, CH_4 uptake and selectivity of the ionic liquids are presented here. In this section, the selectivity is defined as the molar ratio of CO_2 to CH_4 in the liquid at a given time.

7.4.1. CO_2 Uptake in MEA and Ionic Liquids

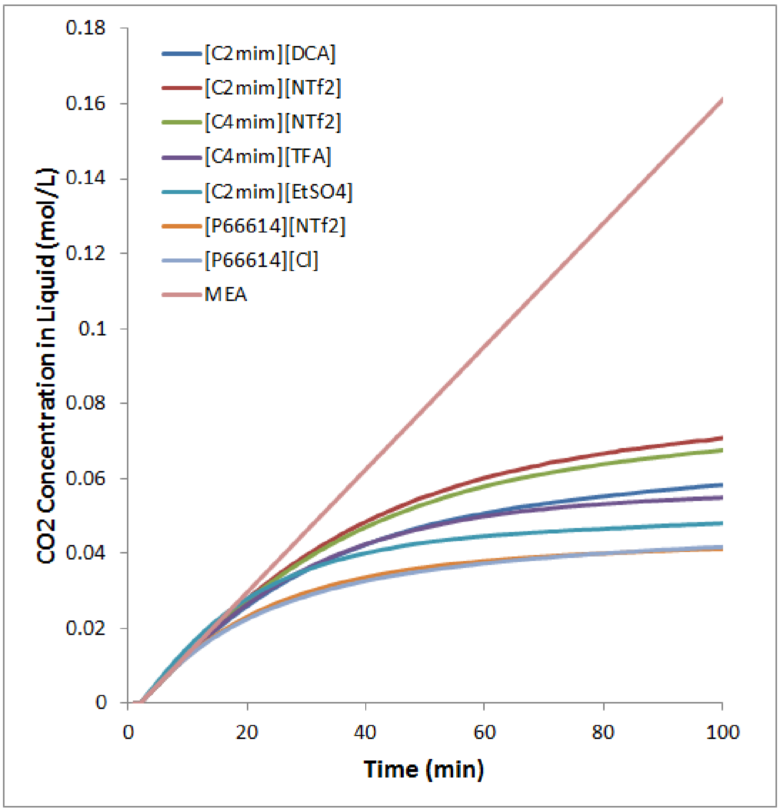

Figure 7.9. Mean CO_2 concentration in ionic liquids and aqueous MEA; flow rate=10 mL/min

Figure 7.9 shows how the mean CO_2 concentration in the MEA solution and ionic liquids varies with time for a constant biogas flow rate of 10 mL/min. The CO_2 concentration in the MEA solution was found to increase at a similar rate to that in the ionic liquids for the first five minutes but continued to increase at the same rate thereafter while the rate of absorption of CO_2 in the ionic liquids decreased. The line representing CO_2 concentration in aqueous MEA is perfectly straight since all of the CO_2 was absorbed.

By linearly interpolating the data of (Jou et al., 2009) at 25 °C, the saturation concentration at a partial pressure of 0.4 atmospheres was calculated to be 0.625 mols-CO_2/mol-MEA, which equates to:

$$c_{CO2\_sat} = \frac{0.625mol - CO_2}{mols - MEA} \cdot \frac{mol - MEA}{61.08g - MEA} \cdot \frac{0.3g - MEA}{g - MEA_{aq}} \cdot \frac{1003g - MEA_{aq}}{L - MEA_{aq}} = 3.08\frac{mol - CO_2}{L - MEA_{aq}} \tag{7.4.1}$$

This saturation concentration of CO_2 in MEA is approximately 30 times that in the ionic liquids tested, as shown in Table 7.1. The greater driving force for absorption in MEA (proportional to the difference between the CO_2 concentration in the liquid and the saturation concentration) combined with the greater CO_2 diffusivity ($1.9 \cdot 10^{-9}$ m^2/s) explain why the rate of CO_2 absorption into the MEA solution is faster than in the ionic liquids tested. Additionally, it was shown in Figure 7.7 that smaller bubbles were produced in MEA than in the ionic liquids. It is well known that smaller bubbles have greater mass transfer rates due to their greater interfacial area per unit volume, greater internal pressure, and slower rise velocities (Zimmerman et al., 2008). Additionally, since a chemical reaction takes place in the case of MEA, due to Le Chatelier's principle, as CO_2 is absorbed into the liquid, it reacts with MEA molecules further increasing the rate of absorption of CO_2. Since no chemical reaction takes place in the case of the ionic liquids tested, as the concentration of CO_2 in the ionic liquids increases, the rate of absorption is reduced.

In contrast to the MEA solution, the ionic liquids tested have absorption capacities of the order of 0.01 to 0.1 mol-CO_2/L and diffusivities between $0.2 \cdot 10^{-9}$ - $1.1 \cdot 10^{-9}$ m^2/s (see Table 7.1). The combined effect of these factors explains why the absorption curves for the ionic liquids plateau a lot sooner and at a much lower value than that for the aqueous MEA solution.

Table 7.1. CO_2 absorption capacity and diffusivity in ionic liquids and aqueous MEA

Solvent	CO_2 absorption capacity (mol/L)	Diffusivity $\cdot 10^9$ (m^2/s)
[C_2mim][DCA]	0.076 [a]	1.1 [f]
[C_2mim][NTf_2]	0.108 [a]	0.66 [g]
[C_4mim][NTf_2]	0.107 [a]	0.85 [f]
[C_4mim][TFA]	0.010 [b]	0.60 [f]
[C_2mim][$EtSO_4$]	0.055 [c]	0.22 [b]
[P_{66614}][NTf_2]	0.013 [a]	0.72 [g]
[P_{66614}][Cl]	0.049 [d]	0.22 [g]
30 wt.% MEA	3.08 [e]	1.9 [h]

(data from (Bara et al., 2009) [a], (Yokozeki et al., 2008) [b], (Jalili et al., 2010)[c], (Ferguson and Scovazzo, 2007) [d], (Jou et al., 2009) [e], (Hou and Baltus, 2007) [f], (Morgan et al., 2005) [g], (Bishnoi and Rochelle, 2000) [h])

In terms of CO_2 absorption, of the ionic liquids tested, [C_2mim][NTf_2] and [C_4mim][NTf_2] absorbed the most CO_2, followed by [C_2mim][DCA] and then [C_4mim][TFA]. It was expected that [C_2mim][DCA] would have the fastest mass transfer rate since its low viscosity and high surface tension enhances the production of microbubbles and causes the diffusivity of CO_2 to be relatively high, as can be seen in Table 7.1; however, since [C_2mim][NTf_2] and [C_4mim][NTf_2] have greater absorption capacities, the driving force was greater and so mass transfer occurred faster. As expected, the phosphonium based ionic liquids had slower rates of CO_2 absorption than the imidazolium-based ones due to their lower CO_2 diffusivities, lower absorption capacities and larger bubbles.

7.4.2. CH_4 Uptake in MEA and Ionic Liquids

For the purpose of biogas upgrading, in addition to CO_2 absorption, it is preferable to use a solvent with a low affinity to absorbing CH_4. The mean CH_4 concentration in the MEA solution and ionic liquids is presented in Figure 7.10.

It can be seen that the CH_4 concentration in the solvents initially rose at a similar rate before settling. The CH_4 saturation concentration in each of the ionic liquids was between 0.025 – 0.045 mol/L, approximately two to three times that of the aqueous MEA solution. Therefore, in addition to absorbing less CO_2, the ionic liquids also absorbed more CH_4 than the MEA solution, making them less suitable for biogas upgrading. Of the ionic liquids tested, [P_{66614}][Cl] absorbed the least CH_4 and [C_2mim][NTf_2] absorbed the most.

The next sub-section will compare the selectivity of the ionic liquids for preferentially absorbing CO_2 over CH_4.

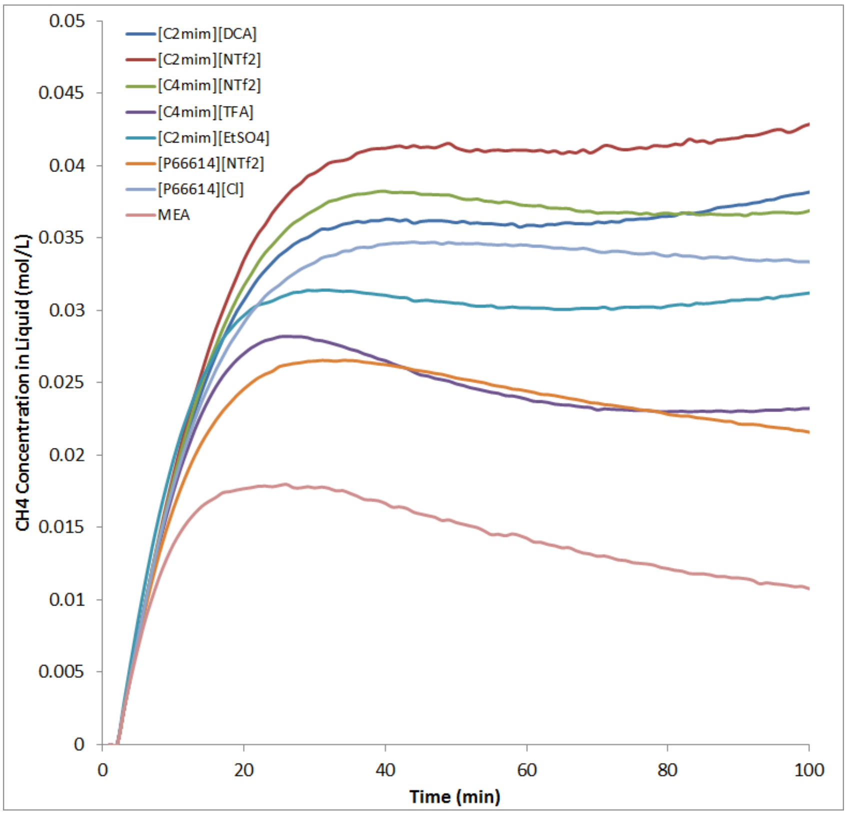

Figure 7.10. Mean CH_4 concentration in ionic liquids and aqueous MEA; flow rate = 10 mL/min

7.4.3. Ratio of CO_2 to CH_4 Absorbed in the Liquid

Figure 7.11 shows the ratio of CO_2/CH_4 in the ionic liquids studied in this work between 0 and 100 minutes. Initially, the CO_2/CH_4 ratio is less than unity since the biogas mixture contains more CH_4 than CO_2 (and most of the gas is being absorbed). However, this ratio increases as the ionic liquids becomes more saturated with CH_4 before plateauing once the CO_2 concentration nears saturation.

It can be seen from Figure 7.11 that of the ionic liquids tested, [C_4mim][TFA] possesses the greatest CO_2/CH_4 absorption ratio followed by [P_{66614}][NTf_2] and [C_4mim][NTf_2]. [P_{66614}][Cl] has the lowest CO_2/CH_4 absorption ratio of the ionic liquids.

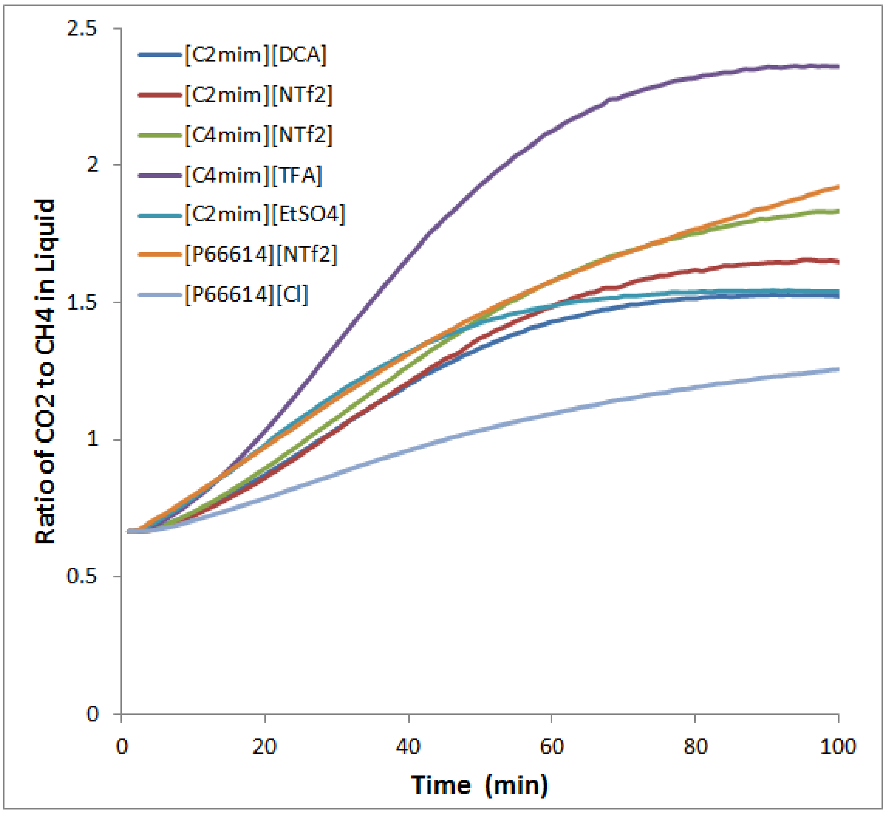

Figure 7.11. CO_2/CH_4 selectivity of ionic liquids (flow rate=10 mL/min)

The ratio of CO_2/CH_4 absorbed in the ionic liquids at t=100 minutes is compared with selectivity values obtained from literature studies; however, it must be noted that the experiments in the literature studies were conducted using pure gases, rather than a mixture. Additionally, selectivity is a measure of the ratio of solubilities of CO_2 and CH_4 in the liquid whereas the CO_2/CH_4 absorption ratio calculated in this work depends not only on solubility but also the rate of mass transfer of each species into the ionic liquid. The CO_2/CH_4 absorption ratio at t=100 minutes from this work is deemed an appropriate comparison since the ionic liquids are almost saturated with both CO_2 and methane by this time. It can be seen in Table 7.2 that the values of the ratio of CO_2/CH_4 obtained in this work are far less than the selectivity values measured in other works. One possible explanation for this is that the concentrations of both CO_2 and CH_4 in the ionic liquids are overestimated in this work due to the sensitivity of the gas analyser and the time lag before CO_2 and CH_4 were detected. However, it is also possible that the absorption of CO_2 into the ionic liquids increased the CH_4 solubility in the liquids.

Table 7.2. CO_2/CH_4 selectivities observed in the literature compared with this work

Ionic Liquid	CO_2 Capacity (mol/L/atm)	CH_4 Capacity (mol/L/atm)	CO_2/CH_4 Selectivity (Literature)	CO_2/CH_4 Ratio at t=100 min (This work)
[C$_2$mim][DCA]	0.076 [a]	0.004 [a]	21.2	1.52
[C$_2$mim][NTf$_2$]	0.108 [a]	0.007 [a]	15.4	1.65
[C$_4$mim][NTf$_2$]	0.107 [a]	0.002 [a]	50.5	1.83
[C$_4$mim][TFA]	0.101 [e]			2.36
[C$_2$mim][EtSO$_4$]	0.055 [f]		25.5 [d]	1.54
[P$_{66614}$][NTf$_2$]	0.075 [a]			1.92
[P$_{66614}$][Cl]	0.049 [b]	<0.01 [c]	>4.9	1.26

(* data from (Bara et al., 2009) [a], (Ferguson and Scovazzo, 2007) [b], (Morgan et al., 2005) [c], (Bermejo et al., 2013) at 5 bar [d], (Yokozeki et al., 2008) [e], (Jalili et al., 2010) [f])

Figure 7.12 compares the ratio of CO_2/CH_4 absorbed in the ionic liquids tested with that of the MEA solution. It is clear that 30 wt.% aqueous MEA has a greater selectivity than any of the ionic liquids tested in this work due to its greater CO_2 absorption capacity and lower CH_4 absorption capacity.

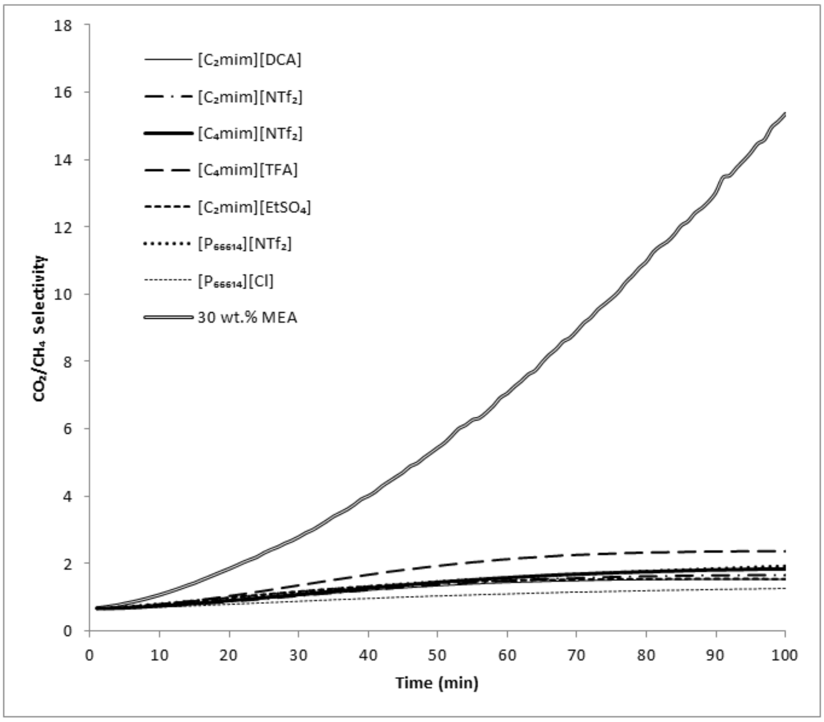

Figure 7.12. CO_2/CH_4 selectivity of ionic liquids and MEA; gas flow rate = 10 mL/min

7.5. CH_4 Concentration in Off-Gas

For the purpose of biogas upgrading, the CH_4 concentration in the off-gas is of great importance since in order to inject into the gas grid, the CH_4 concentration must have a purity between 95-97% (Ryckebosch et al., 2011).

The CH_4 concentration in the off-gas, $c_{CH4,off}$, as defined by Eqn. 3.5.8 is presented in Figure 7.13. It can be seen that for the ionic liquids, the CH_4 concentration in the off-gas peaks after about six minutes before decreasing gradually and settling at about 60% (the same as the inlet concentration). The CH_4 concentrations in the off-gas peaked at 100% for both [C_4mim][TFA] and [C_2mim][$EtSO_4$]. For [C_2mim][NTf_2], [C_4mim][NTf_2] and [P_{66614}][NTf_2], the CH_4 concentrations in the off-gas peaked at 98%, 96%, and 96% respectively. However, for [C_2mim][DCA] and [P_{66614}][Cl], the peak CH_4 concentrations in the off-gas were only 84% and 75% respectively. In the experiment undertaken with aqueous MEA, since all of the CO_2 was absorbed, the CH_4 concentration in the off-gas was 100% throughout the experiment.

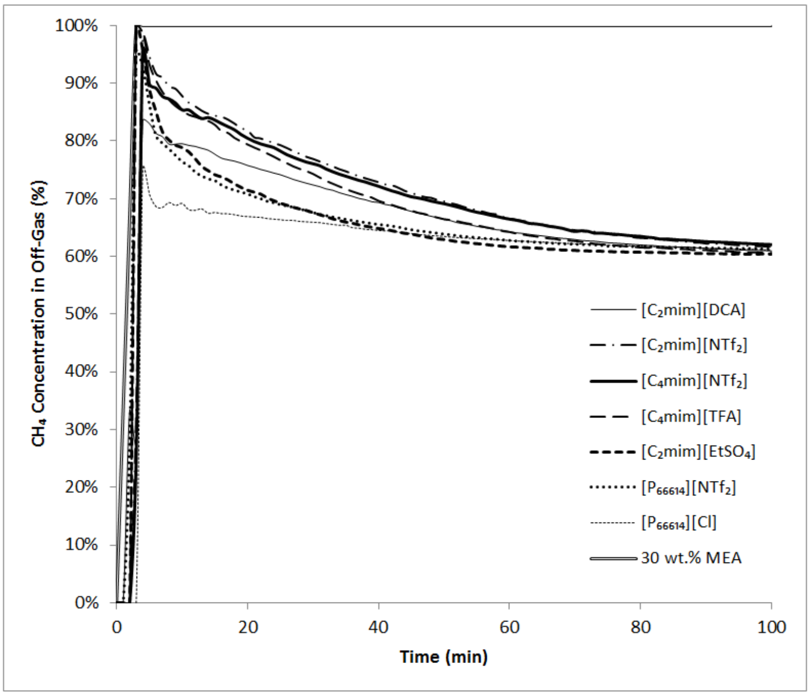

Figure 7.13. Mean CH_4 concentration in off-gas for ionic liquids and MEA; gas flow rate = 10 mL/min

7.6. Effect of Flow Rate

Since [C_2mim][NTf_2] has the greatest CO_2 absorption capacity of the ionic liquids tested, this ionic liquid was selected for investigating the effect of gas flow rate on CO_2 uptake, CH_4 uptake, and CH_4 concentration in the off-gas. Figure 7.14 and Figure 7.15 present the mean CO_2 and CH_4 concentrations in [C_2mim][NTf_2], respectively, for a range of flow rates. It can be seen that as the flow rate is increased, the rate of CO_2 and CH_4 uptake into the ionic liquid increases. This is consistent with many experimental studies on bubble columns conducted using a variety of gases and liquids by other authors, e.g. (Hikita et al., 1981, Öztürk et al., 1987), and will be discussed in more detail in Section 7.7.

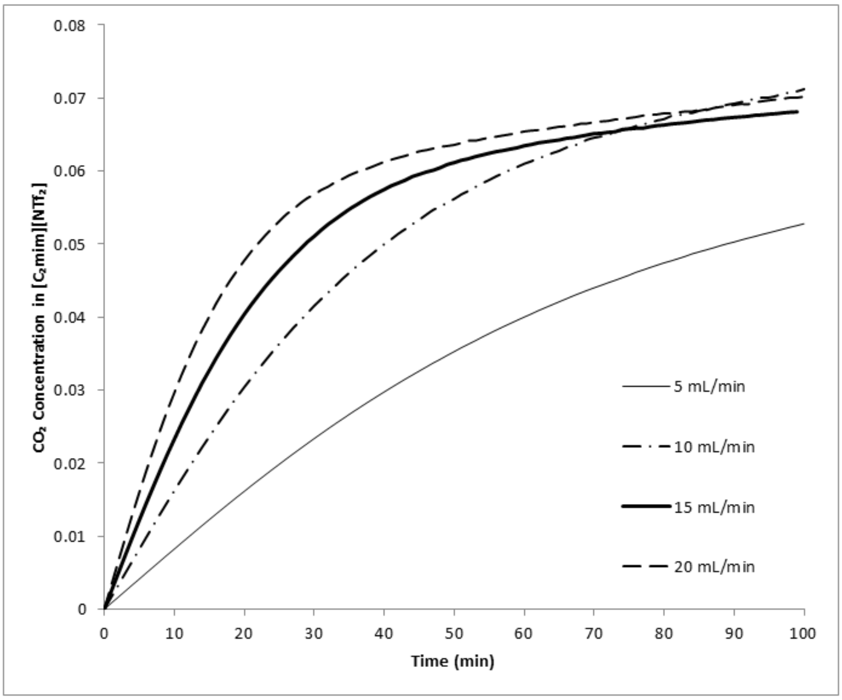

Figure 7.14. CO_2 concentration in $[C_2mim][NTf_2]$ for flow rates between 5-20 mL/min

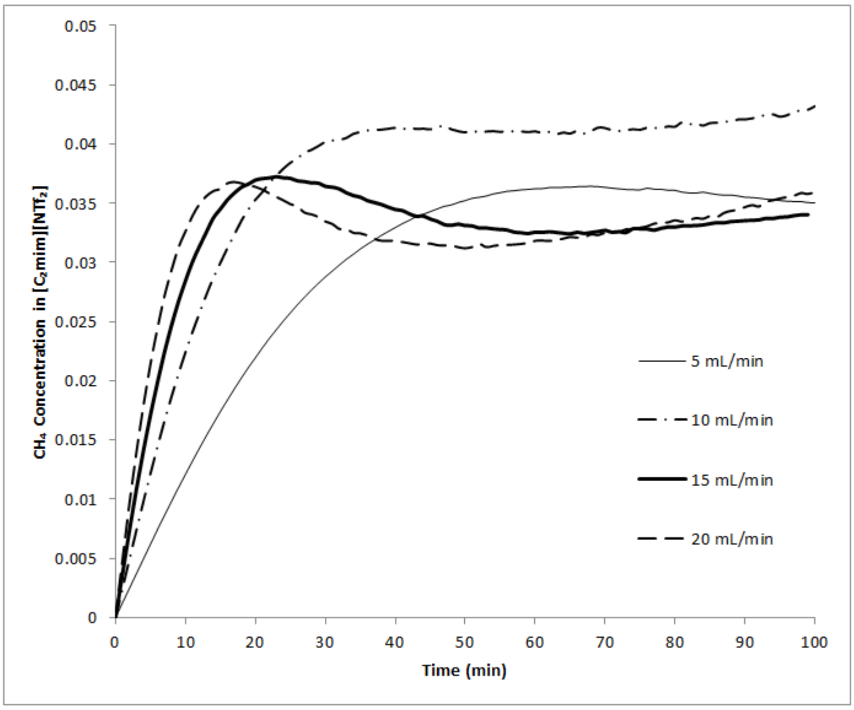

Figure 7.15. CH_4 concentration in $[C_2mim][NTf_2]$ for flow rates between 5-20 mL/min

However, although gas uptake into the liquid is faster at greater flow rates, more CO_2 passes through the liquid without being absorbed and so the CH_4 concentration in the off-gas is lower, as shown in Figure 7.16. Thus, there is a trade-off between the rate of CO_2 capture and how much CH_4 is present in the off-gas.

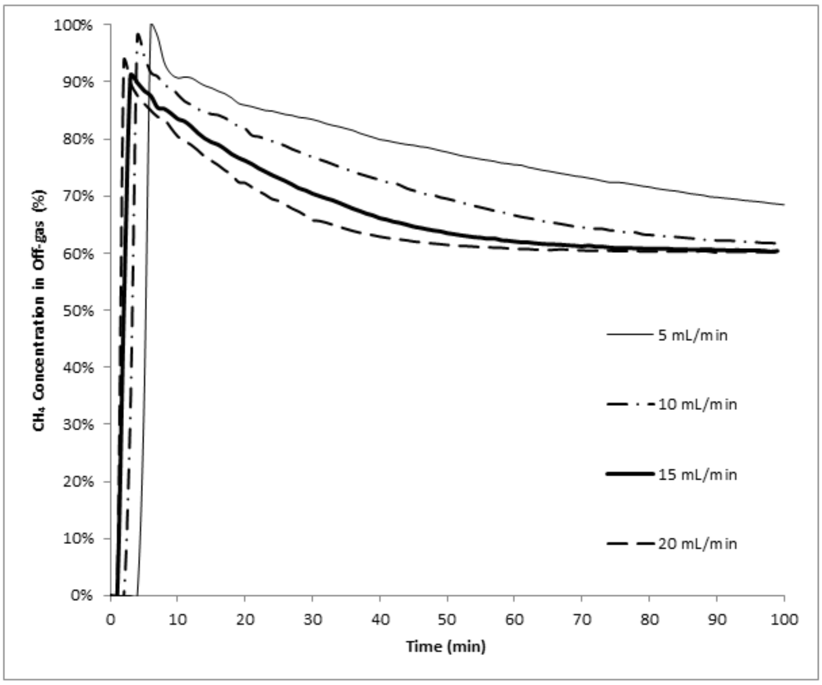

Figure 7.16. CH_4 concentration in off-gas using $[C_2mim][NTf_2]$ for flow rates between 5-20 mL/min

7.7. CO_2 Solubility, Gas Holdup and Mass Transfer Coefficients

In this section, the CO_2 solubility, gas holdup and both the volumetric and individual liquid side mass transfer coefficients are calculated from the data obtained in the biogas upgrading experiments with ionic liquids. Since the solubility of CO_2 in ionic liquids is relatively low, it can be assumed that the gas-side resistance to mass transfer is negligible, enabling simple calculation of the individual liquid-side mass transfer coefficients. This assumption is suitable when the CO_2 solubility is of the order of 0.1 mol/L (Coulson and Richardson, 1998) and has been used by other authors for CO_2 absorption in water (e.g. (Akita and Yoshida, 1973)).

7.7.1. CO_2 Solubility in Ionic Liquids

Since the solubility of CO_2 in the literature is only given for a pure CO_2 stream, the solubility from the biogas mixture had to be estimated. This was done by plotting ln((c*-c0)/(c*-c)) against time and changing the value of the saturation concentration, c*, to see which value produces the greatest R-squared value for a linear regression fit. Using this method, all of the best fit lines had an R-squared value greater than 0.95. The volumetric mass transfer coefficient is given by the gradient of the graph. The complete set of graphs from all experimental runs is provided in Appendix F: K_La Graphs.

The solubilities obtained using the above-mentioned method are presented in Figure 7.17, all of which have standard deviations of less than ±4.5% of the mean value. It can be seen that of the seven ionic liquids tested, [C_2mim][NTf_2] and [C_4mim][NTf_2] have the greatest solubilities of 0.077 and 0.073 mol/L respectively, followed by [C_2mim][DCA] and then by [C_4mim][TFA].

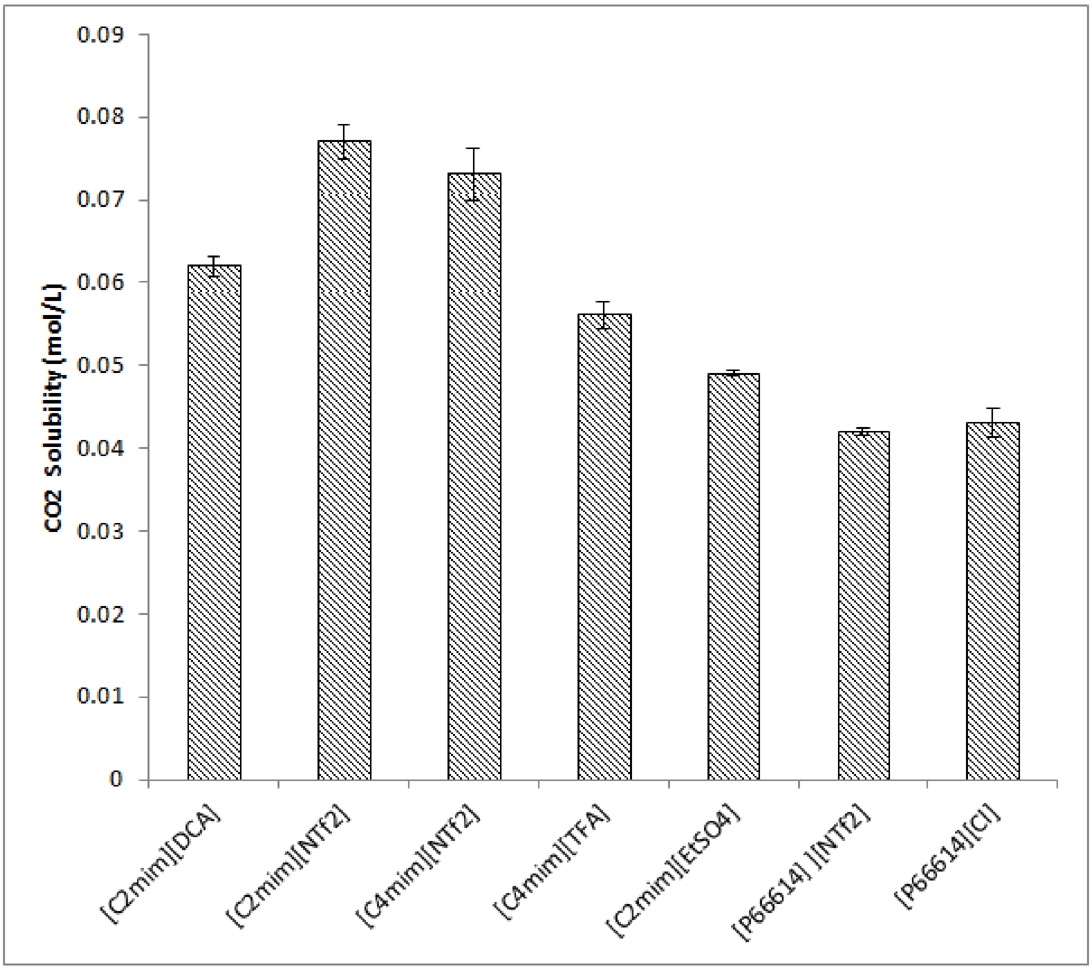

Figure 7.17. CO_2 solubility in ionic liquids from experiments conducted in this work; gas flow rate = 10 mL/min

To examine the effect of CH_4 on the CO_2 solubility in the ionic liquids, the mean values provided in Figure 7.17 are compared with solubility values reported in the literature for pure CO_2, as presented in Figure 7.18.

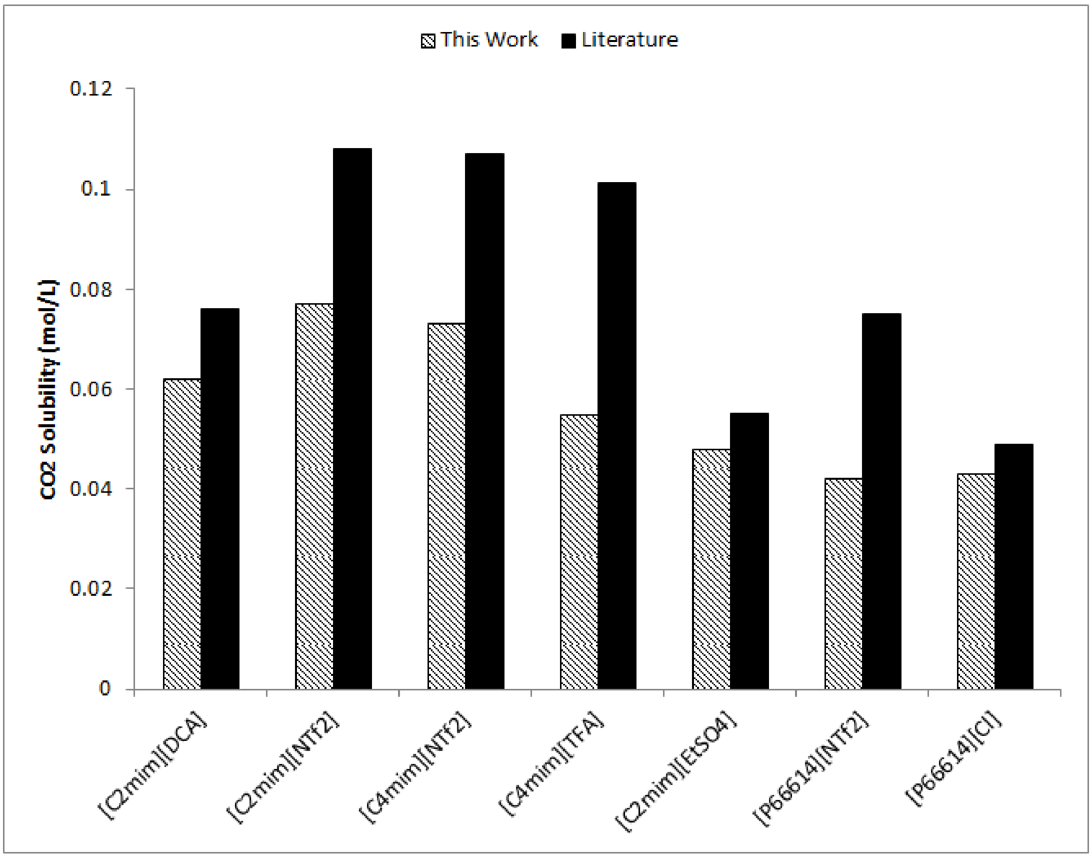

Figure 7.18. CO_2 solubility in ionic liquids: comparison between experiments and literature values for pure CO_2

It can be seen that the presence of CH_4 in the gas stream reduces the CO_2 solubility in the ionic liquid in all seven cases since the partial pressure of CO_2 in the gas stream is lower. While [C_2mim][NTf_2], [C_2mim][$EtSO_4$], and [P_{66614}][Cl] are all able to absorb more than 80% of their CO_2 capacity, [C_2mim][NTf_2] and [C_4mim][NTf_2] have their absorption capacities reduced to 71% capacity and 68% capacity respectively. The most affected ionic liquids however are [P_{66614}][NTf_2] and [C_4mim][TFA], which have their absorption capacities reduced to 56% and 54%capacity respectively.

7.7.2. Gas Holdup

Gas holdup in the ionic liquids, as presented in Figure 7.19, have been calculated using the methods described in Section 3.5.3. These gas holdups will be used to calculate the interfacial area and the individual liquid-side mass transfer coefficients in Section 7.7.4.

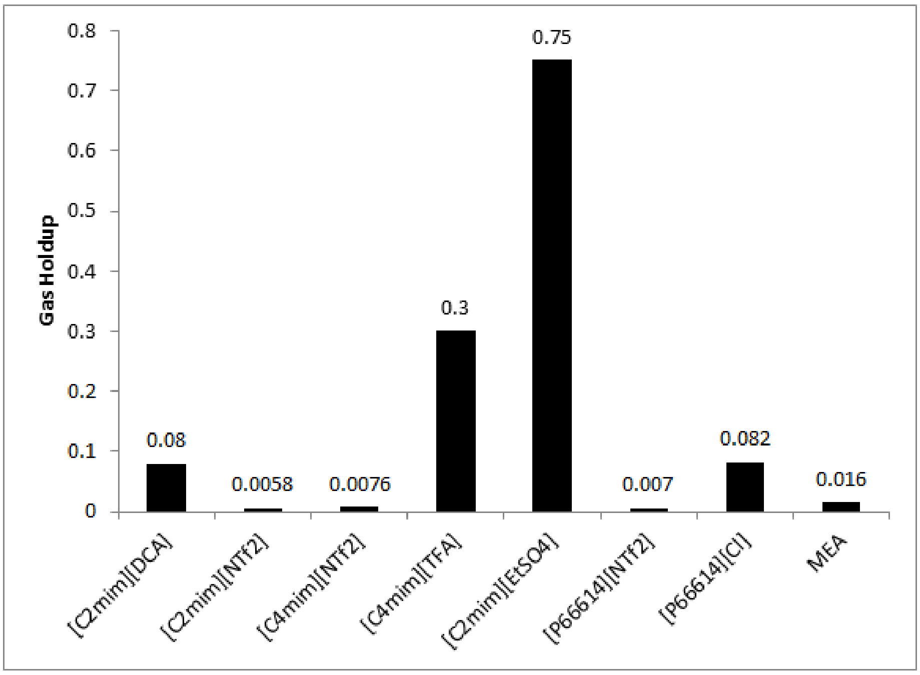

Figure 7.19. Gas holdups obtained from experiments with ionic liquids: gas flow rate = 10mL/min

Figure 7.19 shows that for a flow rate of 10 mL/min, the greatest gas holdups were obtained in [C_2mim][$EtSO_4$] and [C_4mim][TFA] since the bubble rise velocity was slowest in these liquids. This was because although these liquids are fairly viscous, they still produced very small bubbles. In [C_2mim][NTf_2], increasing the gas flow rate is shown to increase the gas holdup since the superficial gas velocity increases disproportionally more than the bubble rise velocity (see Figure 7.20).

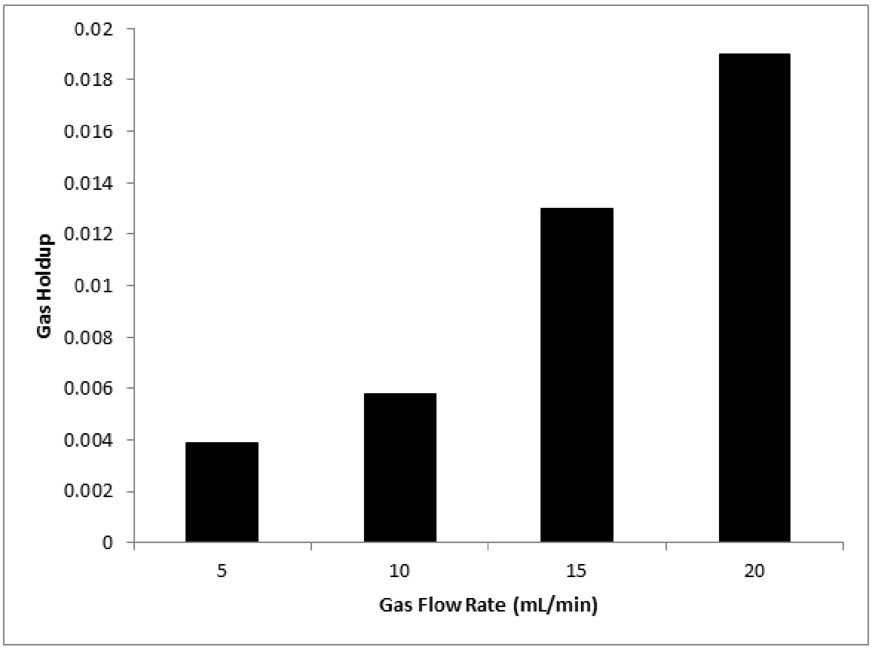

Figure 7.20. Gas holdups obtained from experiments with [C_2mim][NTf_2]

7.7.3. Volumetric Liquid-Side Mass Transfer Coefficient, K_La

K_La values obtained from the biogas upgrading experiments are presented in Figure 7.21. Between experimental runs, the K_La values showed good agreement with a maximum standard deviation of ±7.8% and all graphs having an R-squared value greater than 0.95.

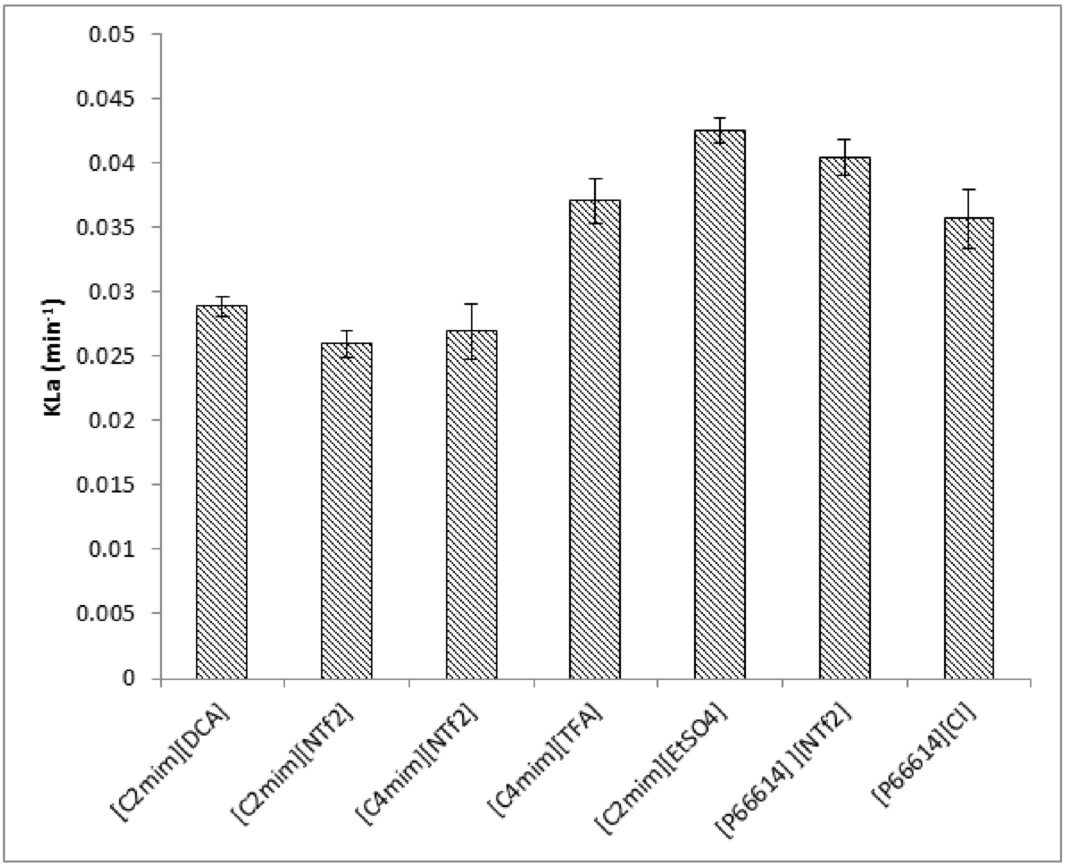

Figure 7.21. K_La values obtained in experiments with ionic liquids: gas flow rate = 10 mL/min

From Figure 7.21, it can be seen that for a flow rate of 10 mL/min, [C_2mim][$EtSO_4$] produces the greatest volumetric mass transfer coefficient of 0.0425 min^{-1}. This was followed by [P_{66614}][NTf_2], [C_4mim][TFA], and [P_{66614}][Cl]. The value of K_La was also found to increase with gas flow rate in the experiments with [C_2mim][NTf_2] having values of 0.0134, 0.0259, 0.0445, and 0.0566 min^{-1} for gas flow rates of 5, 10, 15, and 20 mL/min respectfully. Although K_La data could not be obtained for the aqueous MEA experiments since all of the CO_2 was absorbed, (Jassim et al., 2007) have reported values of 0.978 min^{-1} for a conventional absorber and up to 295 min^{-1} using a rotating packed bed, both of which are much greater than the values obtained here with ionic liquids.

In order to analyse the effects of the physical properties of the ionic liquids on the volumetric mass transfer coefficient, a multiple regression analysis has been conducted to produce the following equation with an R-squared value of 0.96:

$$K_L a = 34.13 \cdot \mu^{-0.36} \cdot \gamma^{-1.05} \cdot \rho^{-1.77} \cdot \mathrm{D}^{-0.53} \cdot \mathrm{U}_G{}^{1.05} \tag{7.7.1}$$

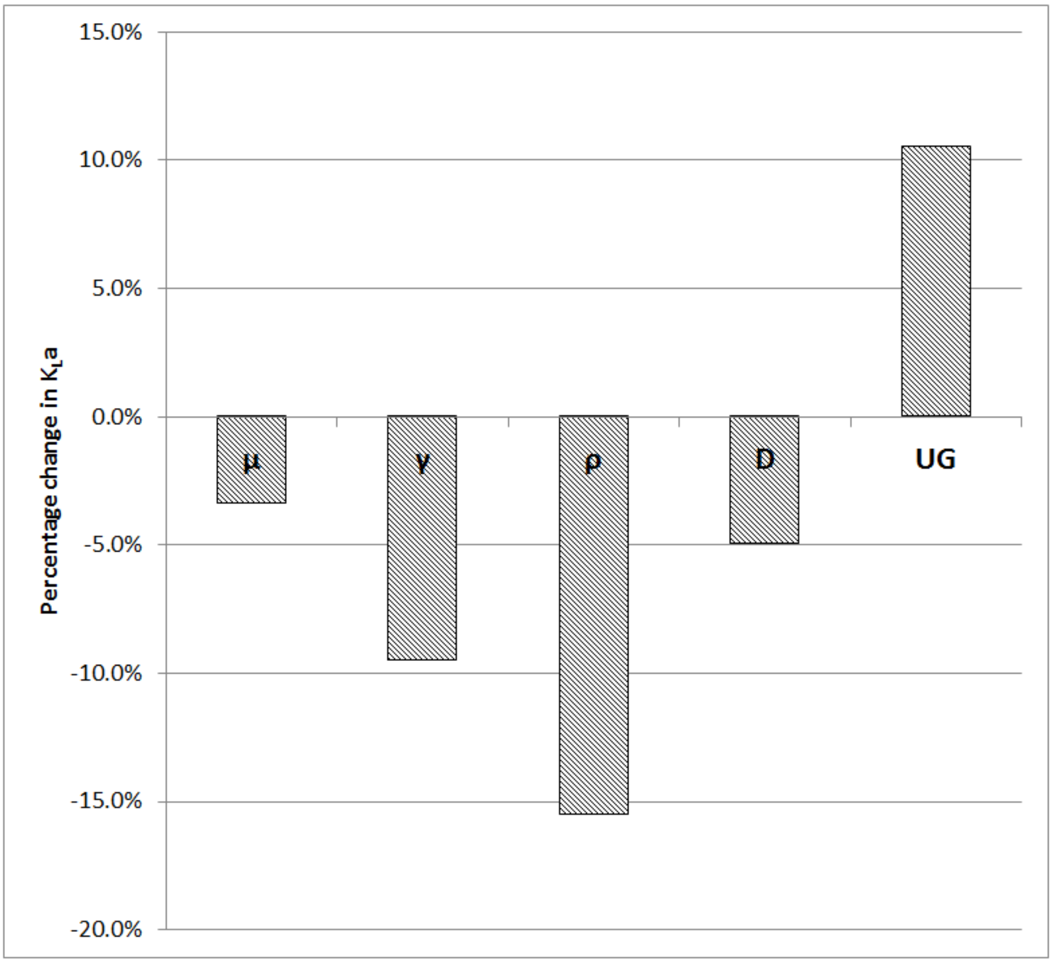

Figure 7.22. Percentage change in K_La due to a 10% increase in liquid viscosity, surface tension, density, diffusivity, and superficial gas velocity

Figure 7.22 shows the percentage change in K_La due to a 10% increase in liquid viscosity, surface tension, density, CO_2 diffusivity, and superficial gas velocity as calculated from Eqn. 7.7.1. It can be seen that liquid density has the largest effect on the volumetric mass transfer coefficient, followed by superficial gas velocity, surface tension, gas diffusivity in the liquid, and liquid viscosity. A 10% increase in viscosity, surface tension, density, and CO_2 diffusivity are found to decrease K_La by 3.4%, 9.5%, 15%, and 4.9% respectively, while a 10% increase in the superficial gas velocity is shown to increase K_La by 10.5%.

The exponential dependences of the volumetric mass transfer coefficient obtained in this work are compared with those obtained in works by other authors in Table 7.3. All of these authors have found that K_La increases with gas flow rate, which is in agreement with this work. However, the effect of gas diffusivity is shown to have the opposite effect on K_La in this work compared with other works. It is likely that this is because the gas diffusivity is not known for some of the ionic liquids that were tested and thus had to be estimated from empirical correlations for different ionic liquids. Additionally, physical properties of ionic liquids are difficult to measure, in particular, the CO_2 diffusivity, since diffusion in ionic liquids is so slow – approximately 1 order of magnitude slower than in aqueous MEA. This work has taken values of diffusivity from the literature and empirical correlations for the purpose of this multiple regression analysis, which may result in a significant error.

Table 7.3. Exponential dependences of K_La on liquid properties and gas flow rate

Reference	Viscosity	Surface tension	Density	Diffusivity	Superficial gas velocity
(Akita and Yoshida, 1973)	-0.12	-0.62	-0.5	0.5	0.0
(Hikita et al., 1981)	-0.08	-1.02	0.85	0.6	0.76
(Öztürk et al., 1987)	-0.08	-0.33	0.37	0.5	0.68
(Kawase et al., 1987)	-0.25	-0.60	0.85	0.5	0.99
(Kang et al., 1999)	-0.25	0.0	0.25	0.0	0.25
This Work	-0.36	-1.05	-1.77	-0.53	1.05

Most authors found K_La to increase with liquid density which is in disagreement with the results of this work. However, this work agrees with most other literature studies that increasing viscosity and surface tension both act in favour of reducing the volumetric mass transfer coefficient.

In order to draw firmer conclusions, more mass transfer data needs to be obtained using high viscosity liquids. However, from this work, it is clear that the correlations obtained by other authors using low viscosity liquids do not agree with that obtained in this work for ionic liquids.

7.7.4. Individual Liquid-Side Mass Transfer Coefficient, kL

In this sub-section, the individual liquid-side mass transfer coefficients are presented and compared with correlations obtained by other authors.

The individual liquid-side mass transfer coefficient, k_L, was calculated by dividing the volumetric liquid-side mass transfer coefficient, K_La, by the interfacial area, a, where a=6ε/d. The results of the k_L calculations are presented in Figure 7.23.

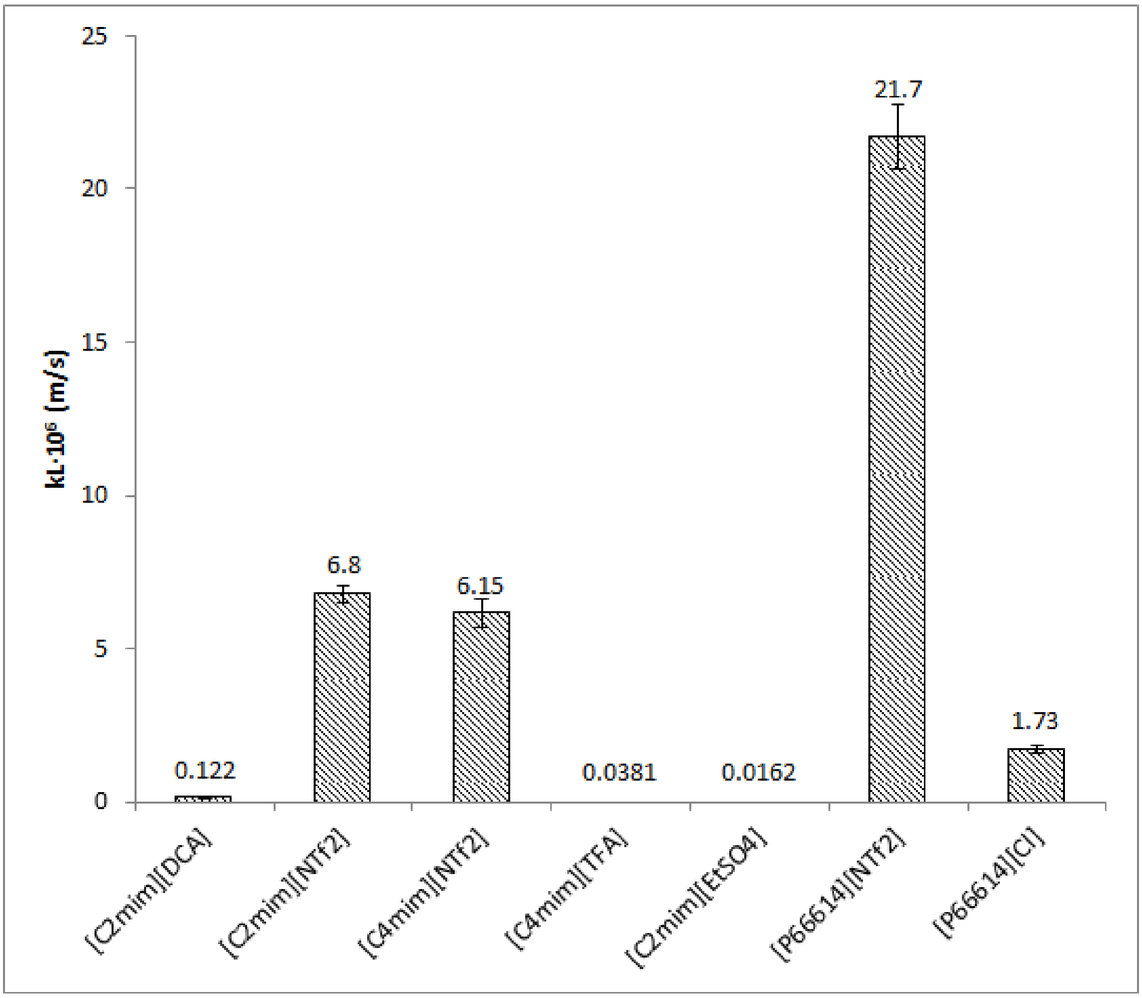

Figure 7.23. Individual liquid-side mass transfer coefficients, k_L, from experiments with ionic liquids

Of the ionic liquids, $[C_2mim][EtSO_4]$ possesses the lowest individual mass transfer coefficient and $[P_{66614}][NTf_2]$ possesses the greatest. (Dugas and Rochelle, 2009, Dugas and Rochelle, 2011) and (Dang and Rochelle, 2003) reported k_L values for MEA solutions of the order of $31\cdot10^{-6} – 160\cdot10^{-6}$ m/s using a wetted wall column, which are greater than the values obtained in this work with ionic liquids.

A multiple regression analysis on the k_L values presented in Figure 7.23 as a function of liquid physical properties and superficial gas velocity produces the following equation with an R-squared value of 0.94:

$$k_L = 4.038 \cdot 10^{15} \mu^{4.0} \cdot \gamma^{3.4} \cdot \rho^{16} \cdot D^{6.6} \cdot U_G{}^{0.12} \qquad (7.7.2)$$

Table 7.4. Exponential dependences of k_L on liquid properties and gas flow rate

Reference	Viscosity	Surface tension	Density	Diffusivity	Flow rate
(Frössling, 1938)	-0.17		0.17	0.67	0.5
(Calderbank and Moo-Young, 1961)	-0.17		0.17	0.5	
(Calderbank and Moo-Young, 1961)	-0.33		0.33	0.67	
(Hughmark, 1967)	-0.017		0.017	0.38	0.056
(Oellrich et al., 1973)				0.5	0.5
(Sherwood et al., 1975)				0.67	0.33
(Akita and Yoshida, 1974)		-0.38	0.38	0.5	
(Schumpe and Deckwer, 1982)	-0.32				0.08
(Öztürk et al., 1987)	-0.08	-0.33	0.37	0.5	0.68
This work	4.0	3.4	16	6.6	0.12

Eqn. 7.7.2 will now be compared with analytical and experimental k_L correlations obtained by other authors, which are presented in Table 7.4. All of the studies by other authors show that k_L increases with decreasing liquid viscosity, decreasing surface tension, increasing density, increasing diffusivity and increasing gas flow rate. While the k_L correlation obtained in this work agrees that k_L increases with increasing density, increasing diffusivity and increasing flow rate, the effect of liquid viscosity and gas-liquid surface tension differ from those reported. Moreover, the exponents obtained in this work are far greater than those obtained in other works. Additionally, this work showed the density to have the largest effect on k_L, whereas other authors have found the gas-liquid diffusivity to have the largest effect. One possible reason for this is because the assumption that the bubbles rise at their Hadamard-Rybczinski terminal velocities does not hold true at high gas holdups since the wakes caused by rising bubbles affect the drag on other bubbles nearby. As a result, the interfacial area is probably overestimated in this work.

None of the other studies investigated mass transfer in highly viscous liquids however. Whilst (Calderbank and Moo-Young, 1961) carried out experiments with liquids as viscous as 0.087 Pa·s, such experiments were only carried out with large bubbles (2 - 8 mm in diameter). They found in their research that large bubbles (>2.5 mm in diameter) behave differently from microbubbles since their surfaces are more mobile and so their correlation is not valid for ionic liquids using microbubbles. This is in agreement with the works of (Higbie, 1935) and (Frössling, 1938). However, their small bubble correlation on the other hand is only valid for liquid viscosities up to 0.009 Pa·s. Similarly, (Hughmark, 1967) carried out experiments with high viscosity liquids up to 0.152 Pa·s; however, the bubbles were of the order of 6 mm.

It was shown in Chapter 6 that with common solvents, bubble size increases with surface tension, however in ionic liquids, the opposite is true. This partially explains why the correlations obtained in this work differ so vastly from those of other authors for common solvents. Since increasing the surface tension reduces the bubble size in ionic liquids, the interfacial area per unit volume, a, would increase with surface tension, causing the individual mass transfer coefficient, k_L, to reduce.

7.8. Other Observations

Initially, it was intended to carry out the biogas upgrading experiments with $[P_{66614}]$[DCA] as well as the other ionic liquids tested. However, upon sparging with biogas, the microbubble dispersion produced a significant quantity of foam, making it unsuitable for obtaining results (see Figure 7.24).

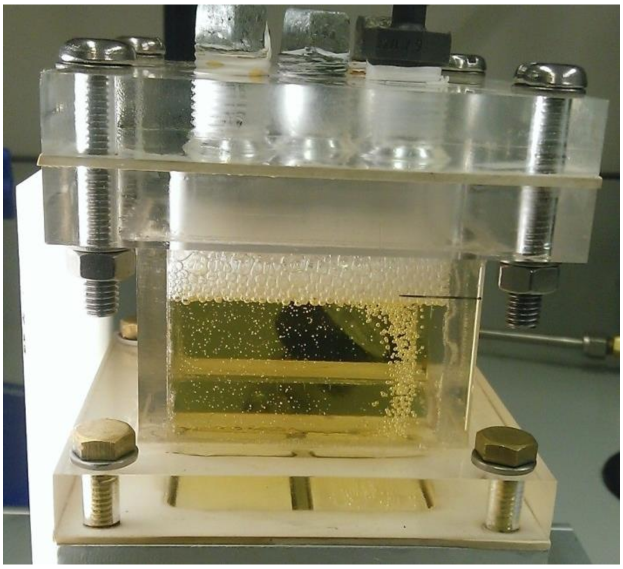

Figure 7.24. Bubble dispersion in $[P_{66614}]$[DCA] producing a foam

Another observation was that in the case of $[C_4mim][NTf_2]$, upon CO_2 capture the liquid went cloudy (see Figure 7.25). After waiting for 24 hours, the cloudiness only appeared at the bottom of the liquid implying that it was due to sedimentation of a solid that was produced.

Figure 7.25. [C$_4$mim][NTf$_2$]: Virgin sample (left) and sample which has undergone absorption (right)

7.9. Estimation of Liquid Flow Rates: MEA vs Ionic Liquids

In reality, the exact flow rate of ionic liquid and aqueous MEA would depend on the quality of CH_4 required, reactor design, and the inlet gas flow rate and composition (Treybal, 1968). However, it is still useful to estimate the liquid flow rates required to compare the two. For the purpose of this estimation, it will be assumed that the inlet gas has a CO_2 concentration of 40 vol.% and that all of the CO_2 is removed from the gas during absorption.

Here an estimation of flow rates for an MEA-based treatment plant will be compared with that for an ionic liquid-based treatment plant. Typical rich and lean loadings for an aqueous MEA solution are 0.4 and 0.2 mols-CO_2/mole-MEA respectively. The amount of aqueous MEA required to capture one tonne of CO_2 is thus equal to:

$$\begin{aligned}\dot{V}_{CO2} &= \frac{mol-MEA}{0.2mol-CO2}\cdot\frac{mol-CO_2}{44.01g-CO_2}\cdot\frac{61.08g-MEA}{mol-MEA}\\ &\quad\cdot\frac{g-MEA_{aq}}{0.3g-MEA}\cdot\frac{L-MEA_{aq}}{1003g-MEA_{aq}}\cdot\frac{1{,}000{,}000g-CO2}{tonne-CO2}\\ &= 23.1\frac{m^3-MEA_{aq}}{tonne-CO_2}\end{aligned} \tag{7.9.1}$$

For a plant using [C$_2$mim][NTf$_2$], which was shown earlier to have a saturation concentration of 0.077 mol/L at atmospheric pressure, the solvent flow rate would be:

$$\dot{V} = \frac{L-IL}{0.077mol-CO_2}\cdot\frac{mol-CO_2}{44.01g-CO_2}\cdot\frac{1{,}000{,}000g-CO2}{tonne-CO2} = 295\frac{m^3-IL}{tonne-CO_2} \tag{7.9.2}$$

In practice, it is unlikely that the ionic liquid would be fully saturated since this would significantly slow down the rate of absorption of CO_2. Assuming a concentration swing of 80% saturation between rich and lean solution loading, the amount of [C_2mim][NTf_2] required to capture one tonne of CO_2 would be 369 m^3– approximately 16 times more than the amount of aqueous MEA required.

Using the same calculation and assuming an 80% concentration swing, the flow rates required for the other ionic liquids investigated in this work are presented below:

Table 7.5. CO_2 absorption capacities of ionic liquids using physisorption (Zhang et al. (2012))

Ionic Liquid	Volume flow rate (m^3-IL/tonne-CO_2)	Volume flow rate / flow rate of aqueous MEA (23.1 m^3/tonne-CO_2)
[C_2mim][DCA]	458	19.8
[C_2mim][NTf_2]	369	16.0
[C_4mim][NTf_2]	389	16.8
[C_4mim][TFA]	507	22.0
[C_2mim][$EtSO_4$]	580	25.1
[P_{66614}][NTf_2]	676	29.3
[P_{66614}][Cl]	661	28.6

7.10. Further Discussion

From the results of work it appears that, of the ionic liquids tested here, far too much liquid would be required to capture CO_2 from biogas at atmospheric pressure since they are physical solvents with fairly low CO_2 solubilities compared with MEA. Additionally, ionic liquids with higher CO_2 absorption capacities generally have greater mass transfer rates. It would therefore be useful to conduct similar experiments with ionic liquids with higher absorption capacities than the ones used here.

(Zhang et al., 2012b) conducted a review of the CO_2 absorption capacities of ionic liquids using physisorption. The five ionic liquids with the greatest CO_2 absorption capacities have been reproduced in Table 7.6.

Table 7.6. CO_2 absorption capacities of ionic liquids using physisorption (Zhang et al. (2012))

Ionic Liquid	CO_2 Absorption Capacity		Conditions bar/K
	Mol-CO_2/mol-IL	g-CO_2/g-IL	
[C_2mim][Ac]	0.390	0.165	20/323
[C_4mim][Ac]	0.373	0.132	20/323
[C_{10}mim][NTf_2]	0.562	0.112	28.3/298
[P_{66614}][NTf_2]	0.631	0.098	27.4/313
[C_4mim][PF_6]	0.360	0.087	29.5/313

The physical properties these ionic liquids have been tabulated in Table 7.7. These values were then entered into Equations 7.7.1 and 7.7.2 from this work to determine the K_La and k_L values for a flow rate of 10 mL/min using the experimental setup in this work.

Table 7.7. Physical properties of ionic liquids in Table 7.5 with predicted K_La and k_L from Eqn. 7.7.1 and Eqn. 7.7.2 (assuming flow rate = 10 mL/min)

Ionic Liquid	Viscosity (Pa·s)	Surface Tension (N/m)	Density (kg/m3)	Diffusivity $\cdot 10^{10}$ (m2/s)	Predicted K_La (min^{-1})	Predicted $k_L \cdot 10^6$ (m/s)
[C_2mim][AcO]	0.162 ^{20} [a]	0.0381 ^{25} [c]	1101.9 ^{25} [c]	2.33 [g]	0.033	0.0170
[C_4mim][AcO]	0.485 ^{25} [b]	0.0352 ^{25} [c]	1047.4 ^{25} [c]	18.4 [h][2]	0.0284	107,000
[C_{10}mim][NTf_2]	0.100 ^{20} [a]	0.0309 ^{25} [d]	1278.8 ^{25} [d]	2.01 [i]	0.0309	0.00612
[C_4mim][PF_6]	0.308 ^{20} [a]	0.0479 ^{25} [e]	1360 ^{25} [f]	0.6 ^{25} [j]	0.041	0.0014

(data from (Zhang et al., 2006) [a], (Fendt et al., 2010) [b], (Ma et al., 2013) [c], (Oliveira et al., 2012) [d], (Kilaru et al., 2007) [e], (Huddleston et al., 2001) [f], (Albo et al., 2014) [g], (Morgan et al., 2005) [h], (Gan et al., 2011) [i], (Huang and Rüther, 2009) [j])

It can be seen that Eqn 7.7.1 predicts that the greatest volumetric mass transfer coefficient would be obtained in [C_4mim][PF_6], followed by [C_2mim][AcO] and then [C_{10}mim][NTf_2]. It would therefore be interesting to use these three ionic liquids in the future due to their high absorption capacities coupled with their high predicted mass transfer coefficients.

---

[2] Predicted using equation from Morgan et al. (2005) for other imidazolium-based ionic liquids

It is clear that Eqn. 7.7.2 cannot be used as a predictive equation for other ionic liquids however since the values of the exponents are too high. As a result, the equation is very sensitive to even a slight change in a physical property; for example, the predicted individual mass transfer coefficient of [C_4mim][AcO] is unreasonably large due to the high predicted diffusion coefficient in this liquid. Additionally, the diffusion coefficient in [C_4mim][AcO] is not known and thus had to be estimated from empirical correlations, thus increasing the error. In order to rectify this, the mass transfer coefficient of more ionic liquids needs to be tested and more data is needed regarding the physical properties of ionic liquids, in particular the diffusion coefficient of CO_2 in ionic liquids.

7.11. Conclusions

The conclusions from the experiments undertaken in this chapter are:

- 30 wt.% aqueous MEA absorbs CO_2 faster than the ionic liquids tested in this work in bubble columns, primarily due to its greater CO_2 solubility, greater diffusivity, ability to produce smaller bubbles, and Le Chatelier's principle.
- 30 wt.% aqueous MEA absorbs less CH_4 than the ionic liquids tested
- For the same liquid height, greater CH_4 concentrations are achievable in the off-gas using 30 wt.% aqueous MEA compared with the ionic liquids tested
- Of the ionic liquids tested, [C_2mim][NTf_2] has the greatest CO_2 absorption capacity; however, [C_4mim][TFA] has a greater CO_2/CH_4 selectivity
- [C_4mim][TFA] and [C_2mim][$EtSO_4$] produce the greatest CH_4 concentration in the off-gas of the ionic liquids tested
- Increasing the gas flow rate increases the rate of CO_2 absorption in ionic liquids but produces an off-gas with a greater concentration of CO_2
- Mass transfer correlations obtained using common solvents cannot be used for ionic liquids since surface tension has the opposite effect on bubble diameter in ionic liquids compared with common solvents
- Liquid density was found to have the greatest influence on K_La followed by superficial gas velocity, surface tension, CO_2 diffusivity, and liquid viscosity
- [P_{66614}][DCA] produces a foam when gas is bubbled into it
- [C_4mim][NTf_2] reacts with CO_2 to form a solid

- Approximately 16 times more [C_2mim][NTf_2] would be required to capture the same amount of CO_2 compared with using 30 wt.% aqueous MEA at atmospheric pressure. For the other ionic liquids tested, up to 29 times more liquid would be required

8. Conclusions and Future Work

8.1. Conclusions

In Chapter 2, a literature review was conducted highlighting the distinct lack of data regarding the use of ionic liquids for biogas upgrading. This was despite their increasing popularity among researchers. In particular, the review highlighted a severe lack of bubble size data, gas holdups, and mass transfer coefficients obtained in ionic liquids in bubble columns. Chapter 2 also noted that various methods have been used to reduce the high regeneration energy requirement of MEA, which was largely attributed to the sensible heat requirement, highlighting the need for a more energy efficient regeneration method.

The results of the numerical model, presented in Chapter 5, concluded that DCR with a superheated CO_2 bubble is potentially feasible in ionic liquids since the latent heat of vapourisation requirement is negligible; however, in MEA, the bubble would cool too quickly due to the evaporation of solvent, thus making the DCR technique unsuitable to be used in conjunction with CDU. If the bubble contains pure nitrogen however, then CO_2 could potentially be desorbed from the MEA solution into the bubble, although it would be more energy intensive than using temperature swing regeneration if conducted at atmospheric pressure due to the large amount of evaporation of water. Increasing the initial gas temperature, decreasing the bubble diameter, and increasing the CO_2 concentration in the liquid phase were all shown to increase the rate of desorption into the bubble as expected. The model predicted that the regeneration energy requirement of [C_2mim][NTf_2] using DCR is could be about 8% that of regenerating MEA using conventional techniques if optimised. Moreover, it is about 1% of the energy requirement of regenerating [C_2mim][NTf_2] using temperature swing regeneration. However, it must be noted that it would be very difficult to control the process accurately enough to achieve such great efficiencies. The model predicts that desorption of CO2 into the bubble only occurs within the first microsecond of the simulation time. In practice the bubble would still be forming during this time and the liquid level would have to be smaller than the bubble diameter. This indicates that DCR is not feasible.

Chapter 6 showed that [C_2mim][DCA], [C_2mim][$EtSO_4$], and [C_4mim][TFA] produced far smaller bubbles than any of the other ionic liquids tested in this work. With the exception of these three liquids, the bubble size in the ionic liquids was very large compared with that produced in aqueous glycerol mixtures of similar viscosity; this indicates that viscosity is not the only important factor for producing small bubbles. Moreover, surface tension was shown to have a comparatively greater effect on the bubble size in ionic liquids compared with the liquid viscosity and density. Unlike in aqueous glycerol mixtures, a lower surface tension was shown to produce larger bubbles in ionic liquids, primarily due to the stability of the homogeneous bubble regime in liquids with high surface tensions. The gas holdup in most of the ionic liquids was far less than that measured in aqueous glycerol mixtures and increased with increasing viscosity and surface tension. The only ionic liquid with a comparable gas holdup to the aqueous glycerol mixtures at the same flow rate was [C_2mim][$EtSO_4$] due to its small bubble size and high viscosity. Drying the ionic liquids under vacuum was shown to increase the wettability of the ionic liquid on the diffuser surface. Despite this, the bubble size increased after drying; this was due to the increase in viscosity of the ionic liquid experienced upon drying. In the more viscous ionic liquids, a transition to the churn turbulent regime was observed at superficial gas velocities of 0.0002 – 0.0003 m/s.

Chapter 7 compared a 30 wt.% aqueous MEA solution and ionic liquids for biogas upgrading. MEA was shown to absorb CO_2 much more rapidly than the ionic liquids. Additionally, the CO_2 solubility in MEA was a lot higher than in the ionic liquids tested and the CH_4 solubility was lower. This makes it much more suitable for biogas upgrading from an absorption perspective. As a result of the above, greater CH_4 concentrations were achieved in the off-gas using MEA compared with the ionic liquids. Increasing the gas flow rate was found to increase the rate of desorption of CO_2 and CH_4 into the ionic liquid; however, a lower concentration of CH_4 was observed in the off-gas since more CO_2 passed through the liquid. [C_2mim][$EtSO_4$] was found to have the greatest volumetric mass transfer coefficient due to its high viscosity and small bubbles, promoting a long residence time for mass transfer. Of the ionic liquids tested, [C_2mim][NTf_2] had the greatest CO_2 absorption capacity; however, [C_4mim][TFA] was found to have a greater CO_2/CH_4 selectivity. Decreasing the liquid viscosity and surface tension were found to increase the volumetric mass transfer coefficient in ionic liquids, which is in agreement with the works of many other authors using bubble columns. Increasing viscosity and surface tension were found to increase the individual liquid-side mass transfer coefficient in ionic liquids, which disagrees with previous works; however, more data is needed in order to reduce the value of the exponents. Additionally, better diffusivity data is required so as to obtain a more accurate correlation. Based on calculations from the solubility of CO_2 in MEA and ionic liquids, it is estimated that, by volume, approximately 16-29 times as much ionic liquid is required to capture the same amount of CO_2 as a 30 wt.% aqueous MEA solution at atmospheric pressure assuming a concentration swing of 80% saturation in the ionic liquids.

8.2. Future Work

From the numerical model presented in Chapter 4, DCR seems like a promising technique for regenerating ionic liquids. It is recommended that the technique is investigated experimentally. This author recommends carrying out DCR experiments from a single orifice initially in order to accurately determine whether CO_2 can be desorbed from the ionic liquid. If these experiments are successful then DCR experiments could be carried out in bubble columns to investigate whether they would be suitable on a larger scale. As suggested by the model, a very thin layer of liquid should be used and the gas temperature required is approximately 400-600 K.

An investigation into the bubble size, gas holdups and mass transfer coefficients in bubble columns in a wider range of ionic liquids should be carried out to investigate to what extent they agree with the results presented here. Additionally, it would be useful to investigate biogas upgrading in ionic liquids with higher CO_2 solubilities than the ones used in this work. In particular, $[C_2mim][AcO]$, $[C_{10}mim][NTf_2]$, and $[C_4mim][PF_6]$ appear to be good candidates due to their high absorption capacities and high predicted mass transfer coefficients.

Additionally, it would be useful to test absorption into ionic liquids from biogas at higher pressures. This was not possible in this work due to the materials used in constructing the absorption column. Absorbing at greater pressures is known to increase the absorption capacity of the ionic liquids (e.g. (Carvalho et al., 2010)), meaning that the capture plant would not need to be as big and less ionic liquid would be required, which would make ionic liquids more competitive with MEA. Additionally, operating at a greater pressure is known to produce smaller bubbles (Urseanu et al., 2003), thus increasing the rate of mass transfer.

References

ABU-ZAHRA, M. R., SCHNEIDERS, L. H., NIEDERER, J. P., FERON, P. H. & VERSTEEG, G. F. 2007a. CO< sub> 2</sub> capture from power plants: Part I. A parametric study of the technical performance based on monoethanolamine. *International journal of greenhouse gas control,* **1**, 37-46.

ABU-ZAHRA, M. R. M., NIEDERER, J. P. M., FERON, P. H. M. & VERSTEEG, G. F. 2007b. CO2 capture from power plants. Part II. A parametric study of the economical performance based on mono-ethanolamine. *International journal of greenhouse gas control,* **1**, 135-142.

AKI, S. N., MELLEIN, B. R., SAURER, E. M. & BRENNECKE, J. F. 2004. High-pressure phase behavior of carbon dioxide with imidazolium-based ionic liquids. *The Journal of Physical Chemistry B,* **108**, 20355-20365.

AKITA, K. & YOSHIDA, F. 1973. Gas holdup and volumetric mass transfer coefficient in bubble columns. Effects of liquid properties. *Industrial & Engineering Chemistry Process Design and Development,* **12**, 76-80.

AKITA, K. & YOSHIDA, F. 1974. Bubble size, interfacial area, and liquid-phase mass transfer coefficient in bubble columns. *Industrial & Engineering Chemistry Process Design and Development,* **13**, 84-91.

AL-MASHHADANI, M. K., BANDULASENA, H. & ZIMMERMAN, W. B. 2011. CO2 mass transfer induced through an airlift loop by a microbubble cloud generated by fluidic oscillation. *Industrial & Engineering Chemistry Research.*

ALBO, J., YOSHIOKA, T. & TSURU, T. 2014. Porous Al2O3/TiO2 tubes in combination with 1-ethyl-3-methylimidazolium acetate ionic liquid for CO2/N2 separation. *Sep. Purif. Technol,* **122**, 440-448.

ALIE, C., BACKHAM, L., CROISET, E. & DOUGLAS, P. L. 2005. Simulation of CO< sub> 2</sub> capture using MEA scrubbing: a flowsheet decomposition method. *Energy conversion and Management,* **46**, 475-487.

ALMEIDA, H. F., LOPES-DA-SILVA, J. A., FREIRE, M. G. & COUTINHO, J. A. 2013. Surface tension and refractive index of pure and water-saturated tetradecyltrihexylphosphonium-based ionic liquids. *The Journal of Chemical Thermodynamics,* **57**, 372-379.

ARESTA, M. 2007. In Greenhouse gases: Mitigation and utilisation.

BARA, J. E., CARLISLE, T. K., GABRIEL, C. J., CAMPER, D., FINOTELLO, A., GIN, D. L. & NOBLE, R. D. 2009. Guide to CO2 separations in imidazolium-based room-temperature ionic liquids. *Industrial & engineering chemistry research,* **48**, 2739-2751.

BEHKISH, A., MEN, Z., INGA, J. R. & MORSI, B. I. 2002. Mass transfer characteristics in a large-scale slurry bubble column reactor with organic liquid mixtures. *Chemical Engineering Science,* **57**, 3307-3324.

BERMEJO, M. D., FIEBACK, T. M. & MARTÍN, Á. 2013. Solubility of gases in 1-alkyl-3methylimidazolium alkyl sulfate ionic liquids: Experimental determination and modeling. *The Journal of Chemical Thermodynamics,* **58**, 237-244.

BIDART, C., JIMÉNEZ, R., CARLESI, C., FLORES, M. & BERG, Á. 2011. Synthesis and usage of common and functionalized ionic liquids for biogas upgrading. *Chemical Engineering Journal,* **175**, 388-395.

BIRD, R. B., STEWART, W. E. & LIGHTFOOT, E. N. 2007. *Transport phenomena*, John Wiley & Sons.

BISHNOI, S. & ROCHELLE, G. T. 2000. Absorption of carbon dioxide into aqueous piperazine: reaction kinetics, mass transfer and solubility. *Chemical Engineering Science,* **55**, 5531-5543.

BLATH, J., CHRIST, M., DEUBLER, N., HIRTH, T. & SCHIESTEL, T. 2011. Gas solubilities in room temperature ionic liquids–Correlation between RTiL-molar mass and Henry's law constant. *Chemical Engineering Journal,* **172**, 167-176.

BOC GASES., 2015, Telephone Conversation on 20/06/2015.

BREDWELL, M. D. & WORDEN, R. M. 1998. Mass - Transfer Properties of Microbubbles. 1. Experimental Studies. *Biotechnology progress,* **14**, 31-38.

BRENNECKE, J. F. & MAGINN, E. J. 2001. Ionic liquids: innovative fluids for chemical processing. *AIChE Journal,* **47**, 2384-2389.

BRITTLE, S. 2014. *RE: Private communication with author.*

CADENA, C., ANTHONY, J. L., SHAH, J. K., MORROW, T. I., BRENNECKE, J. F. & MAGINN, E. J. 2004. Why is CO2 so soluble in imidazolium-based ionic liquids? *Journal of the American Chemical Society,* **126**, 5300-5308.

CALDERBANK, P. & MOO-YOUNG, M. 1961. The continuous phase heat and mass-transfer properties of dispersions. *Chemical Engineering Science,* **16**, 39-54.

CAMPER, D., BECKER, C., KOVAL, C. & NOBLE, R. 2006. Diffusion and solubility measurements in room temperature ionic liquids. *Industrial & engineering chemistry research,* **45**, 445-450.

CARROLL, J. J., JOU, F. Y., MATHER, A. E. & OTTO, F. D. 1998. The solubility of methane in aqueous solutions of monoethanolamine, diethanolamine and triethanolamine. *The Canadian Journal of Chemical Engineering,* **76**, 945-951.

CARVALHO, P. J., ALVAREZ, V. H., MARRUCHO, I. M., AZNAR, M. & COUTINHO, J. A. 2010. High carbon dioxide solubilities in trihexyltetradecylphosphonium-based ionic liquids. *The Journal of Supercritical Fluids,* **52**, 258-265.

CARVALHO, P. J., FREIRE, M. G., MARRUCHO, I. M., QUEIMADA, A. J. & COUTINHO, J. A. 2008. Surface tensions for the 1-alkyl-3-methylimidazolium bis (trifluoromethylsulfonyl) imide ionic liquids.

CHAKMA, A. 1997. CO< sub> 2</sub> capture processes—Opportunities for improved energy efficiencies. *Energy conversion and Management,* **38**, S51-S56.

CHAPEL, D. G., MARIZ, C. L. & ERNEST, J. 1999. Recovery of CO2 from flue gases: commercial trends. *Aliso Viejo.*

CHAUMAT, H., BILLET, A.-M. & DELMAS, H. 2007. Hydrodynamics and mass transfer in bubble column: Influence of liquid phase surface tension. *Chemical Engineering Science,* **62**, 7378-7390.

CHENG, N.-S. 2008. Formula for the viscosity of a glycerol-water mixture. *Industrial & engineering chemistry research,* **47,** 3285-3288.

CLIFT, R., GRACE, J. R. & WEBER, M. E. 1978. *Bubbles, drops, and particles*, Academic press New York.

COMSOL 2013. COMSOL Multiphysics v4.3b Materials Library.

CORNING, D. 1991. Foam and Anti-Foam Theory.

COULSON, J. & RICHARDSON, J. 1998. Chemical engineering-Particle technology and separation processes, Vol. 2, RK Butterworth. Heinemann, Oxford.

CREMER, T., STARK, M., DEYKO, A., STEINRUCK, H.-P. & MAIER, F. 2011. Liquid/solid interface of ultrathin ionic liquid films:[C1C1Im][Tf2N] and [C8C1Im][Tf2N] on Au (111). *Langmuir,* **27,** 3662-3671.

CYTEC 2008a. Product data sheet - Cyphos 102.

CYTEC 2008b. Product data sheet - Cyphos IL 101.

CYTEC 2008c. Product data sheet - Cyphos IL 103.

CYTEC 2008d. Product data sheet - Cyphos IL 105.

DANG, H. & ROCHELLE, G. T. 2003. CO2 absorption rate and solubility in monoethanolamine/piperazine/water. *Separation science and technology,* **38,** 337-357.

DAVIDSON, J. & SCHÜLER, B. 1960. Bubble formation at an orifice in a viscous liquid. *Trans. Instn Chem. Engrs,* **38,** S105-S115.

DECKWER, W. D. 1991. *Bubble Column Reactors.*

DESAI, P. 2014. *RE: Personal communication with the author.*

DONG, H., WANG, X., LIU, L., ZHANG, X. & ZHANG, S. 2010. The rise and deformation of a single bubble in ionic liquids. *Chemical Engineering Science,* **65,** 3240-3248.

DTI 2007. Meeting the Energy Challenge - A White Paper on Energy.

DUGAS, R. & ROCHELLE, G. 2009. Absorption and desorption rates of carbon dioxide with monoethanolamine and piperazine. *Energy Procedia,* **1,** 1163-1169.

DUGAS, R. E. 2006. Pilot plant study of carbon dioxide capture by aqueous monoethanolamine. *MSE Thesis, University of Texas at Austin.*

DUGAS, R. E. & ROCHELLE, G. T. 2011. CO2 Absorption Rate into Concentrated Aqueous Monoethanolamine and Piperazine. *Journal of Chemical & Engineering Data,* **56,** 2187-2195.

FENDT, S., PADMANABHAN, S., BLANCH, H. W. & PRAUSNITZ, J. M. 2010. Viscosities of acetate or chloride-based ionic liquids and some of their mixtures with water or other common solvents. *Journal of Chemical & Engineering Data,* **56,** 31-34.

FERGUSON, L. & SCOVAZZO, P. 2007. Solubility, diffusivity, and permeability of gases in phosphonium-based room temperature ionic liquids: data and correlations. *Industrial & engineering chemistry research,* **46,** 1369-1374.

FINOTELLO, A., BARA, J. E., CAMPER, D. & NOBLE, R. D. 2008. Room-temperature ionic liquids: temperature dependence of gas solubility selectivity. *Industrial & engineering chemistry research,* **47,** 3453-3459.

FRASER, K. J. & MACFARLANE, D. R. 2009. Phosphonium-based ionic liquids: An overview. *Australian journal of chemistry,* **62,** 309-321.

FREIRE, M. G., CARVALHO, P. J., FERNANDES, A. M., MARRUCHO, I. M., QUEIMADA, A. J. & COUTINHO, J. A. 2007. Surface tensions of imidazolium based ionic liquids: anion, cation, temperature and water effect. *Journal of colloid and interface science,* **314,** 621-630.

FRÖSSLING, N. 1938. bber die verdünstung fallenden tropfen (Evaporation of falling drops). *Gerlands Beitage Geophys.,* **52,** 170-216.

GAD-EL-HAK, M. 2001. *The MEMS handbook*, CRC press.

GADDIS, E. & VOGELPOHL, A. 1986. Bubble formation in quiescent liquids under constant flow conditions. *Chemical Engineering Science,* **41,** 97-105.

GALÁN SÁNCHEZ, L., MEINDERSMA, G. & DE HAAN, A. 2011. Kinetics of absorption of CO< sub> 2</sub> in amino-functionalized ionic liquids. *Chemical Engineering Journal,* **166,** 1104-1115.

GALLAGHER, S., KAVANAGH, A., ZÍOŁKOWSKI, B., FLOREA, L., MACFARLANE, D. R., FRASER, K. & DIAMOND, D. 2014. Ionic liquid modulation of swelling and LCST behavior of N-isopropylacrylamide polymer gels. *Physical Chemistry Chemical Physics,* **16,** 3610-3616.

GAN, Q., ZOU, Y., ROONEY, D., NANCARROW, P., THOMPSON, J., LIANG, L. & LEWIS, M. 2011. Theoretical and experimental correlations of gas dissolution, diffusion, and thermodynamic properties in determination of gas permeability and selectivity in supported ionic liquid membranes. *Advances in colloid and interface science,* **164,** 45-55.

GE, R., HARDACRE, C., JACQUEMIN, J., NANCARROW, P. & ROONEY, D. W. 2008. Heat capacities of ionic liquids as a function of temperature at 0.1 MPa. Measurement and prediction. *Journal of Chemical & Engineering Data,* **53,** 2148-2153.

GE, R., HARDACRE, C., NANCARROW, P. & ROONEY, D. W. 2007. Thermal conductivities of ionic liquids over the temperature range from 293 K to 353 K. *Journal of Chemical & Engineering Data,* **52,** 1819-1823.

GNYLOSKURENKO, S., BYAKOVA, A., RAYCHENKO, O. & NAKAMURA, T. 2003. Influence of wetting conditions on bubble formation at orifice in an inviscid liquid. Transformation of bubble shape and size. *Colloids and Surfaces A: Physicochemical and Engineering Aspects,* **218,** 73-87.

GODBOLE, S., HONATH, M. & SHAH, Y. 1982. Holdup structure in highly viscous Newtonian and non-Newtonian liquids in bubble columns. *Chemical Engineering Communications,* **16,** 119-134.

GOODRICH, B. F., DE LA FUENTE, J. C., GURKAN, B. E., LOPEZ, Z. K., PRICE, E. A., HUANG, Y. & BRENNECKE, J. F. 2011. Effect of water and temperature on absorption of CO2 by amine-functionalized anion-tethered ionic liquids. *The Journal of Physical Chemistry B,* **115,** 9140-9150.

HANOTU, J., BANDULASENA, H. & ZIMMERMAN, W. B. 2012. Microflotation performance for algal separation. *Biotechnology and Bioengineering.*

HAQUE, M., NIGAM, K. & JOSHI, J. 1986. Hydrodynamics and mixing in highly viscous pseudo-plastic non-Newtonian solutions in bubble columns. *Chemical Engineering Science,* 41, 2321-2331.

HIGBIE, R. 1935. The rate of absorption of a pure gas into a still liquid during a short time of exposure. *Transactions of the American Institute of Chemical Engineers,* 31, 365-389.

HIKITA, H., ASAI, S., TANIGAWA, K., SEGAWA, K. & KITAO, M. 1980. Gas hold-up in bubble columns. *the chemical Engineering Journal,* 20, 59-67.

HIKITA, H., ASAI, S., TANIGAWA, K., SEGAWA, K. & KITAO, M. 1981. The volumetric liquid-phase mass transfer coefficient in bubble columns. *the chemical Engineering Journal,* 22, 61-69.

HILLIARD, M. D. 2008. *A predictive thermodynamic model for an aqueous blend of potassium carbonate, piperazine, and monoethanolamine for carbon dioxide capture from flue gas.*

HOU, Y. & BALTUS, R. E. 2007. Experimental measurement of the solubility and diffusivity of CO2 in room-temperature ionic liquids using a transient thin-liquid-film method. *Industrial & engineering chemistry research,* 46, 8166-8175.

HUANG, J. & RÜTHER, T. 2009. Why are ionic liquids attractive for CO2 absorption? An overview. *Australian journal of chemistry,* 62, 298-308.

HUDDLESTON, J. G., VISSER, A. E., REICHERT, W. M., WILLAUER, H. D., BROKER, G. A. & ROGERS, R. D. 2001. Characterization and comparison of hydrophilic and hydrophobic room temperature ionic liquids incorporating the imidazolium cation. *Green chemistry,* 3, 156-164.

HUGHMARK, G. 1967. Holdup and mass transfer in bubble columns. *Industrial & Engineering Chemistry Process Design and Development,* 6, 218-220.

IDEM, R., WILSON, M., TONTIWACHWUTHIKUL, P., CHAKMA, A., VEAWAB, A., AROONWILAS, A. & GELOWITZ, D. 2006. Pilot plant studies of the CO2 capture performance of aqueous MEA and mixed MEA/MDEA solvents at the University of Regina CO2 capture technology development plant and the boundary dam CO2 capture demonstration plant. *Industrial & engineering chemistry research,* 45, 2414-2420.

IEA. 2013. *Plant Lists* [Online]. Available: http://www.iea-biogas.net/plant-list.html.

INCROPERA, F. P. 2011. *Fundamentals of heat and mass transfer,* John Wiley & Sons.

IPCC 2005. Special report on carbon dioxide capture and storage. Intergovernmental Panel on Climate Change, Geneva (Switzerland). Working Group III.

JALILI, A. H., MEHDIZADEH, A., SHOKOUHI, M., AHMADI, A. N., HOSSEINI-JENAB, M. & FATEMINASSAB, F. 2010. Solubility and diffusion of CO< sub> 2</sub> and H< sub> 2</sub> S in the ionic liquid 1-ethyl-3-methylimidazolium ethylsulfate. *The Journal of Chemical Thermodynamics,* 42, 1298-1303.

JAMIALAHMADI, M., ZEHTABAN, M., MÜLLER-STEINHAGEN, H., SARRAFI, A. & SMITH, J. 2001. Study of bubble formation under constant flow conditions. *Chemical Engineering Research and Design,* 79, 523-532.

JASSIM, M. S. & GARY, T. 2006. Innovative absorber/stripper configurations for CO2 capture by aqueous monoethanolamine. *Industrial & Engineering Chemistry Research,* 45, 2465-2472.

JASSIM, M. S., ROCHELLE, G., EIMER, D. & RAMSHAW, C. 2007. Carbon dioxide absorption and desorption in aqueous monoethanolamine solutions in a rotating packed bed. *Industrial & Engineering Chemistry Research,* 46, 2823-2833.

JOU, F. Y., MATHER, A. E. & OTTO, F. D. 2009. The solubility of CO2 in a 30 mass percent monoethanolamine solution. *The Canadian Journal of Chemical Engineering,* 73, 140-147.

KAJI, R., ZHAO, D., LICENCE, P. & AZZOPARDI, B. 2009. Studies of the interaction of ionic liquid and gas in a small-diameter bubble column. *Industrial & engineering chemistry research,* 48, 7938-7944.

KANG, Y., CHO, Y., WOO, K. & KIM, S. 1999. Diagnosis of bubble distribution and mass transfer in pressurized bubble columns with viscous liquid medium. *Chemical Engineering Science,* 54, 4887-4893.

KANTARCI, N., BORAK, F. & ULGEN, K. O. 2005. Bubble column reactors. *Process Biochemistry,* 40, 2263-2283.

KAWASE, Y., HALARD, B. & MOO-YOUNG, M. 1987. Theoretical prediction of volumetric mass transfer coefficients in bubble columns for Newtonian and non-Newtonian fluids. *Chemical Engineering Science,* 42, 1609-1617.

KAWASE, Y. & MOO-YOUNG, M. 1987. Theoretical prediction of gas hold-up in bubble columns with Newtonian and non-Newtonian fluids. *Industrial & engineering chemistry research,* 26, 933-937.

KERLÉ, D., LUDWIG, R., GEIGER, A. & PASCHEK, D. 2009. Temperature dependence of the solubility of carbon dioxide in imidazolium-based ionic liquids. *The Journal of Physical Chemistry B,* 113, 12727-12735.

KESKIN, S., KAYRAK-TALAY, D., AKMAN, U. & HORTAÇSU, Ö. 2007. A review of ionic liquids towards supercritical fluid applications. *The Journal of Supercritical Fluids,* 43, 150-180.

KHOSSRAVI, D. & CONNORS, K. A. 1993. Solvent effects on chemical processes. 3. Surface tension of binary aqueous organic solvents. *Journal of solution chemistry,* 22, 321-330.

KHURANA, A. & KUMAR, R. 1969. Studies in bubble formation—III. *Chemical Engineering Science,* 24, 1711-1723.

KILARU, P., BAKER, G. A. & SCOVAZZO, P. 2007. Density and surface tension measurements of imidazolium-, quaternary phosphonium-, and ammonium-based room-temperature ionic liquids: data and correlations. *Journal of Chemical & Engineering Data,* 52, 2306-2314.

KIM, I. & SVENDSEN, H. F. 2007. Heat of absorption of carbon dioxide (CO2) in monoethanolamine (MEA) and 2-(Aminoethyl) ethanolamine (AEEA) solutions. *Industrial & Engineering Chemistry Research,* 46, 5803-5809.

KLOMFAR, J., SOUČKOVÁ, M. & PÁTEK, J. 2011. Temperature dependence of the surface tension and density at 0.1 MPa for 1-ethyl-and 1-butyl-3-methylimidazolium dicyanamide. *Journal of Chemical & Engineering Data,* 56, 3454-3462.

KOHL, A. L. & NIELSEN, R. B. 1997. *Gas purification*, Gulf Professional Publishing.

KULKARNI, A. A. & JOSHI, J. B. 2005. Bubble formation and bubble rise velocity in gas-liquid systems: a review. *Industrial & Engineering Chemistry Research,* 44**,** 5873-5931.

KUMAR, A., DEGALEESAN, T., LADDHA, G. & HOELSCHER, H. 1976. Bubble swarm characteristics in bubble columns. *The Canadian Journal of Chemical Engineering,* 54**,** 503-508.

LANGE, V., AZZOPARDI, B. J. & LICENCE, P. 2013. Hydrodynamics of ionic liquids in bubble columns.

LAPLACE, P. S. 1805. *Traité de mécanique céleste/par PS Laplace...; tome premier [-quatrieme]*, de l'Imprimerie de Crapelet.

LEWIS, W. & WHITMAN, W. 1924. Principles of gas absorption. *Industrial & Engineering Chemistry,* 16**,** 1215-1220.

LI, M.-H. & LIE, Y.-C. 1994. Densities and viscosities of solutions of monoethanolamine+ N-methyldiethanolamine+ water and monoethanolamine+ 2-amino-2-methyl-1-propanol+ water. *Journal of Chemical and Engineering Data,* 39**,** 444-447.

MA, X. X., WEI, J., ZHANG, Q., TIAN, F., FENG, Y. & GUAN, W. 2013. Prediction of thermophysical properties of acetate-based ionic liquids using semiempirical methods. *Industrial & engineering chemistry research,* 52**,** 9490-9496.

MACKAY, D. 2008. *Sustainable Energy-without the hot air*, UIT Cambridge.

MIKKELSEN, M., JØRGENSEN, M. & KREBS, F. C. 2010. The teraton challenge. A review of fixation and transformation of carbon dioxide. *Energy & Environmental Science,* 3**,** 43-81.

MIMURA, T., SIMAYOSHI, H., SUDA, T., IIJIMA, M. & MITUOKA, S. 1997. Development of energy saving technology for flue gas carbon dioxide recovery in power plant by chemical absorption method and steam system. *Energy conversion and Management,* 38**,** S57-S62.

MOKHATAB, S., POE, W. A., ZATZMAN, G. C., ISLAM, M. C. & VAN WASSENHOVE, W. C. 2006. *Handbook of natural gas transmission and processing*, Gulf Professional Publishing.

MORGAN, D., FERGUSON, L. & SCOVAZZO, P. 2005. Diffusivities of gases in room-temperature ionic liquids: data and correlations obtained using a lag-time technique. *Industrial & engineering chemistry research,* 44**,** 4815-4823.

MOTARJEMI, M. & JAMESON, G. 1978. Mass transfer from very small bubbles--the optimum bubble size for aeration. *Chemical Engineering Science,* 33**,** 1415-1423.

MOUZA, A., DALAKOGLOU, G. & PARAS, S. 2005. Effect of liquid properties on the performance of bubble column reactors with fine pore spargers. *Chemical Engineering Science,* 60**,** 1465-1475.

NIGMATULIN, R.I., KHABEEV, N.S., NAGIEV, F.B., Dynamics, heat and mass transfer of vapour-gas bubbles in a liquid, 1981. Int. Journal of Heat and Mass Transfer

OELLRICH, L., SCHMIDT-TRAUB, H. & BRAUER, H. 1973. Theoretische berechnung des stofftransports in der umgebung einer einzelblase. *Chemical Engineering Science,* 28**,** 711-721.

OLIVEIRA, M., DOMÍNGUEZ-PÉREZ, M., FREIRE, M., LLOVELL, F., CABEZA, O., LOPES-DA-SILVA, J., VEGA, L. & COUTINHO, J. 2012. Surface tension of binary mixtures of 1-alkyl-3-methylimidazolium bis (trifluoromethylsulfonyl) imide ionic liquids: experimental measurements and Soft-SAFT modeling. *The Journal of Physical Chemistry B,* 116**,** 12133-12141.

OYENEKAN, B. A. & ROCHELLE, G. T. 2007. Alternative stripper configurations for CO2 capture by aqueous amines. *AIChE Journal,* 53**,** 3144-3154.

ÖZTÜRK, S. S., SCHUMPE, A. & DECKWER, W. D. 1987. Organic liquids in a bubble column: holdups and mass transfer coefficients. *AIChE Journal,* 33**,** 1473-1480.

PALGUNADI, J., KIM, H. S., LEE, J. M. & JUNG, S. 2010. Ionic liquids for acetylene and ethylene separation: Material selection and solubility investigation. *Chemical Engineering and Processing: Process Intensification,* 49**,** 192-198.

PALMERI, N., CAVALLARO, S. & BART, J. C. 2008. Carbon dioxide absorption by MEA. *Journal of Thermal Analysis and Calorimetry,* 91**,** 87-91.

PANT, K. & SRIVASTAVA, V. 2007. Carbon dioxide absorption into monoethanolamine in a continuous film contactor. *Chemical Engineering Journal,* 133**,** 229-237.

PARK, Y., LAMONT TYLER, A. & DE NEVERS, N. 1977. The chamber orifice interaction in the formation of bubbles. *Chemical Engineering Science,* 32**,** 907-916.

PERRY, R. H. & GREEN, D. W. 2008. *Perry's chemical engineers' handbook*, McGraw-Hill New York.

PETERSSON, A. & WELLINGER, A. 2009. Biogas upgrading technologies–developments and innovations. *IEA Bioenergy***,** 12-15.

POHORECKI, R., MONIUK, W., BIELSKI, P., SOBIESZUK, P. & DĄBROWIECKI, G. 2005. Bubble diameter correlation via numerical experiment. *Chemical Engineering Journal,* 113**,** 35-39.

PRIVALOVA, E., RASI, S., MÄKI-ARVELA, P., ERÄNEN, K., RINTALA, J., MURZIN, D. Y. & MIKKOLA, J.-P. 2013a. CO 2 capture from biogas: absorbent selection. *RSC Advances,* 3**,** 2979-2994.

PRIVALOVA, E. I., MÄKI - ARVELA, P., ERÄNEN, K., AVETISOV, A. K., MIKKOLA, J. P. & MURZIN, D. Y. 2013b. Amine Solutions for Biogas Upgrading: Ideal versus Non - Ideal Absorption Isotherms. *Chemical Engineering & Technology,* 36**,** 740-748.

RAMAKRISHNAN, S., KUMAR, R. & KULOOR, N. 1969. Studies in bubble formation—I bubble formation under constant flow conditions. *Chemical Engineering Science,* 24**,** 731-747.

RAO, A. B. & RUBIN, E. S. 2002. A technical, economic, and environmental assessment of amine-based CO2 capture technology for power plant greenhouse gas control. *Environmental Science & Technology,* 36**,** 4467-4475.

REHMAN, F. 2014. Personal communication with the author.

RESTOLHO, J., MATA, J. L. & SARAMAGO, B. 2009a. Electrowetting of ionic liquids: Contact angle saturation and irreversibility. *The Journal of Physical Chemistry C,* 113**,** 9321-9327.

RESTOLHO, J., MATA, J. L. & SARAMAGO, B. 2009b. On the interfacial behavior of ionic liquids: Surface tensions and contact angles. *Journal of colloid and interface science,* 340, 82-86.

RIBEIRO, C. & LAGE, P. L. 2005. Gas ‐ Liquid Direct ‐ Contact Evaporation: A Review. *Chemical Engineering & Technology,* 28, 1081-1107.

RUZICKA, M., DRAHOŠ, J., MENA, P. & TEIXEIRA, J. 2003. Effect of viscosity on homogeneous–heterogeneous flow regime transition in bubble columns. *Chemical Engineering Journal,* 96, 15-22.

RUZICKA, M., VECER, M., ORVALHO, S. & DRAHOŠ, J. 2008. Effect of surfactant on homogeneous regime stability in bubble column. *Chemical Engineering Science,* 63, 951-967.

RUZICKA, M., ZAHRADNıK, J., DRAHOŠ, J. & THOMAS, N. 2001. Homogeneous–heterogeneous regime transition in bubble columns. *Chemical Engineering Science,* 56, 4609-4626.

RYCKEBOSCH, E., DROUILLON, M. & VERVAEREN, H. 2011. Techniques for transformation of biogas to biomethane. *Biomass and bioenergy,* 35, 1633-1645.

SARDEING, R., PAINMANAKUL, P. & HÉBRARD, G. 2006. Effect of surfactants on liquid-side mass transfer coefficients in gas–liquid systems: a first step to modeling. *Chemical Engineering Science,* 61, 6249-6260.

SATYANARAYAN, A., KUMAR, R. & KULOOR, N. 1969. Studies in bubble formation—II bubble formation under constant pressure conditions. *Chemical Engineering Science,* 24, 749-761.

SCHÄFER, R., MERTEN, C. & EIGENBERGER, G. 2002. Bubble size distributions in a bubble column reactor under industrial conditions. *Experimental Thermal and Fluid Science,* 26, 595-604.

SCHUMPE, A. & DECKWER, W. D. 1982. Gas holdups, specific interfacial areas, and mass transfer coefficients of aerated carboxymethyl cellulose solutions in a bubble column. *Industrial & Engineering Chemistry Process Design and Development,* 21, 706-711.

SCHUMPE, A. & DECKWER, W. D. 1987. Organic liquids in a bubble column: holdups and mass transfer coefficients. *AIChE Journal,* 33, 1473-1480.

SEDEV, R. 2011. Surface tension, interfacial tension and contact angles of ionic liquids. *Current Opinion in Colloid & Interface Science,* 16, 310-316.

SHAH, Y., KELKAR, B. G., GODBOLE, S. & DECKWER, W. D. 1982. Design parameters estimations for bubble column reactors. *AIChE Journal,* 28, 353-379.

SHERWOOD, T. K., PIGFORD, R. L. & WILKE, C. R. 1975. *Mass transfer*, McGraw-Hill New York.

SHIFLETT, M. B. & YOKOZEKI, A. 2005. Solubilities and diffusivities of carbon dioxide in ionic liquids:[bmim][PF6] and [bmim][BF4]. *Industrial & engineering chemistry research,* 44, 4453-4464.

SIGMA-ALDRICH 2012a. Safety Data Sheet - 1-Butyl-3-methylimidazolium bis(trifluoromethylsulfonyl)imide.

SIGMA-ALDRICH 2012b. Safety Data Sheet - 1-Ethyl-3-methylimidazolium bis(trifluoromethylsulfonyl)imide.

SIGMA-ALDRICH 2012c. Safety Data Sheet - Ethanolamine.

SIGMA ALDRICH 2015a. http://www.sigmaaldrich.com/chemistry/chemistry-products.html?TablePage=16255914, accessed on 07/06/2015

SIGMA ALDRICH 2015b. http://www.sigmaaldrich.com/chemistry/chemistry-products.html?TablePage=16255998, accessed on 07/06/2015

SIGMA ALDRICH 2015b. http://www.sigmaaldrich.com/chemistry/chemistry-products.html?TablePage=16255998, accessed on 07/06/2015

SIGMA ALDRICH 2015c. http://www.sigmaaldrich.com/catalog/product/sial/e9508?lang=en&region=GB, accessed on 07/06/2015

SINGH, D., CROISET, E., DOUGLAS, P. L. & DOUGLAS, M. A. 2003. Techno-economic study of CO< sub> 2</sub> capture from an existing coal-fired power plant: MEA scrubbing vs. O< sub> 2</sub>/CO< sub> 2</sub> recycle combustion. *Energy conversion and Management,* 44, 3073-3091.

SONG, H.-J., LEE, S., PARK, K., LEE, J., CHAND SPAH, D., PARK, J.-W. & FILBURN, T. P. 2008. Simplified estimation of regeneration energy of 30 wt% sodium glycinate solution for carbon dioxide absorption. *Industrial & engineering chemistry research,* 47, 9925-9930.

STERN, N. 2007. *The economics of climate change: the Stern review*, Cambridge University Press.

STEVANOVIC, S. P., PODGORŠEK, A., PÁDUA, A. A. & COSTA GOMES, M. F. 2012. Effect of water on the carbon dioxide absorption by 1-alkyl-3-methylimidazolium acetate ionic liquids. *The Journal of Physical Chemistry B,* 116, 14416-14425.

STYRING, P., JANSEN, D., DE CONINCK, H., REITH, H. & ARMSTRONG, K. 2011. Carbon Capture and Utilisation in the Green Economy: Using CO2 to manufacture fuel, chemicals and materials. The Centre for Low Carbon Futures 2011. Report.

SUDA, T., FUJII, M., YOSHIDA, K., IIJIMA, M., SETO, T. & MITSUOKA, S. 1992. Development of flue gas carbon dioxide recovery technology. *Energy conversion and Management,* 33, 317-324.

SUNG, J., JEON, Y., KIM, D., IWAHASHI, T., IIMORI, T., SEKI, K. & OUCHI, Y. 2005. Air–liquid interface of ionic liquid+ H< sub> 2</sub> O binary system studied by surface tension measurement and sum-frequency generation spectroscopy. *Chemical physics letters,* 406, 495-500.

SWOPE, R. D. 1971. Single bubble formation at orifices submerged in viscous liquids. *The Canadian Journal of Chemical Engineering,* 49, 169-174.

TAYLOR, R., MCCRELLIS, C., JACQUEMIN, J. & HARDACRE, C. 2014. CO2 Capture in wet and dry superbase ionic liquids. *4CU Project Team Meeting.*

TERASAKA, K., HIRABAYASHI, A., NISHINO, T., FUJIOKA, S. & KOBAYASHI, D. 2011. Development of microbubble aerator for waste water treatment using aerobic activated sludge. *Chemical Engineering Science.*

TERASAKA, K. & TSUGE, H. 1990. Bubble formation at a single orifice in highly viscous liquids. *Journal of Chemical Engineering of Japan,* 23, 160-165.

TESAŘ, V. 2007. *Pressure-driven microfluidics*, Artech House.

TESAŘ, V. & BANDALUSENA, H. C. H. 2010. Bistable diverter valve in microfluidics. *Experiments in fluids*, 1-9.

TESAŘ, V., HUNG, C. H. & ZIMMERMAN, W. B. 2006. No-moving-part hybrid-synthetic jet actuator. *Sensors and Actuators A: Physical,* 125, 159-169.

TREYBAL, R. E. 1968. *Mass-transfer operations*, McGraw-Hill New York.

UNGER, E. C., HERSH, E., VANNAN, M., MATSUNAGA, T. O. & MCCREERY, T. 2001. Local drug and gene delivery through microbubbles. *Progress in cardiovascular diseases,* 44, 45-54.

URSEANU, M., GUIT, R., STANKIEWICZ, A., VAN KRANENBURG, G. & LOMMEN, J. 2003. Influence of operating pressure on the gas hold-up in bubble columns for high viscous media. *Chemical Engineering Science,* 58, 697-704.

VAN DIERENDONCK, L. L. 1970. *Vergrotingsregels voor Gasbelwassers.* University Twente.

VATAI, G. & TEKIĆ, M. 1989. Gas hold-up and mass transfer in bubble columns with pseudoplastic liquids. *Chemical Engineering Science,* 44, 2402-2407.

VAZQUEZ, G., ALVAREZ, E., NAVAZA, J. M., RENDO, R. & ROMERO, E. 1997. Surface tension of binary mixtures of water+ monoethanolamine and water+ 2-amino-2-methyl-1-propanol and tertiary mixtures of these amines with water from 25 C to 50 C. *Journal of Chemical & Engineering Data,* 42, 57-59.

WANG, X., DONG, H., ZHANG, X., XU, Y. & ZHANG, S. 2010a. Numerical simulation of absorbing CO2 with ionic liquids. *Chemical Engineering & Technology,* 33, 1615-1624.

WANG, X., DONG, H., ZHANG, X., YU, L., ZHANG, S. & XU, Y. 2010b. Numerical simulation of single bubble motion in ionic liquids. *Chemical Engineering Science,* 65, 6036-6047.

WEILAND, R. H., DINGMAN, J. C. & CRONIN, D. B. 1997. Heat capacity of aqueous monoethanolamine, diethanolamine, N-methyldiethanolamine, and N-methyldiethanolamine-based blends with carbon dioxide. *Journal of Chemical & Engineering Data,* 42, 1004-1006.

WILKINSON, P. M., HARINGA, H. & VAN DIERENDONCK, L. L. 1994. Mass transfer and bubble size in a bubble column under pressure. *Chemical Engineering Science,* 49, 1417-1427.

WILKINSON, P. M., SPEK, A. P. & VAN DIERENDONCK, L. L. 1992. Design parameters estimation for scale‐up of high‐pressure bubble columns. *AIChE Journal,* 38, 544-554.

WU, B., LIU, W.W., ZHANG, Y., WANG, H., 2009. Do we understand the recyclability of ionic liquids?, Chemistry - A European Journal.

XIE, Y., ZHANG, Y., LU, X., JI, X., 2014. Energy Consumption analysis for CO2 separation using imidazolium-based ionic liquids, Applied Energy

XU, Q., NAKAJIMA, M., ICHIKAWA, S., NAKAMURA, N. & SHIINA, T. 2008. A comparative study of microbubble generation by mechanical agitation and sonication. *Innovative Food Science & Emerging Technologies,* 9, 489-494.

YOKOZEKI, A., SHIFLETT, M. B., JUNK, C. P., GRIECO, L. M. & FOO, T. 2008. Physical and chemical absorptions of carbon dioxide in room-temperature ionic liquids. *The Journal of Physical Chemistry B,* 112, 16654-16663.

YOUNG, T. 1805. An essay on the cohesion of fluids. *Philosophical Transactions of the Royal Society of London,* 95, 65-87.

ZHANG, L.-L., WANG, J.-X., XIANG, Y., ZENG, X.-F. & CHEN, J.-F. 2011. Absorption of carbon dioxide with ionic liquid in a rotating packed bed contactor: Mass transfer study. *Industrial & engineering chemistry research,* 50, 6957-6964.

ZHANG, S., SUN, N., HE, X., LU, X. & ZHANG, X. 2006. Physical properties of ionic liquids: database and evaluation. *Journal of physical and chemical reference data,* 35, 1475-1517.

ZHANG, X., BAO, D., HUANG, Y., DONG, H., ZHANG, X. & ZHANG, S. 2014. Gas-Liquid Mass-Transfer Properties in CO2 Absorption System with Ionic Liquids. *AIChE Journal,* 60, 2929-2939.

ZHANG, X., DONG, H., BAO, D., HUANG, Y., ZHANG, X. & ZHANG, S. 2013. Effect of small amount of water on CO2 bubble behavior in ionic liquid systems. *Industrial & engineering chemistry research,* 53, 428-439.

ZHANG, X., DONG, H., HUANG, Y., LI, C. & ZHANG, X. 2012a. Experimental study on gas holdup and bubble behavior in carbon capture systems with ionic liquid. *Chemical Engineering Journal,* 209, 607-615.

ZHANG, X., ZHANG, X., DONG, H., ZHAO, Z., ZHANG, S. & HUANG, Y. 2012b. Carbon capture with ionic liquids: overview and progress. *Energy & Environmental Science,* 5, 6668-6681.

ZHU, L., SCHADE, G. W. & NIELSEN, C. J. 2013. Real-Time Monitoring of Emissions from Monoethanolamine-Based Industrial Scale Carbon Capture Facilities. *Environmental Science & Technology,* 47, 14306-14314.

ZIMMERMAN, W. B., AL-MASHHADANI, M. K. H. & BANDULASENA, H. C. H. 2013. Evaporation dynamics of microbubbles.

ZIMMERMAN, W. B., HEWAKANDAMBY, B. N., TESAR, V., BANDULASENA, H. C. H. & OMOTOWA, O. A. 2009a. On the design and simulation of an airlift loop bioreactor with microbubble generation by fluidic oscillation. *Food and Bioproducts Processing,* 87, 215-227.

ZIMMERMAN, W. B., TESAŘ, V. & BANDULASENA, H. 2011. Towards energy efficient nanobubble generation with fluidic oscillation. *Current Opinion in Colloid & Interface Science,* 16, 350-356.

ZIMMERMAN, W. B., TESAŘ, V. & BANDULASENA, H. C. H. 2009b. Efficiency of an aerator driven by fluidic oscillation. Part I: Laboratory bench scale studies.

ZIMMERMAN, W. B., TESAŘ, V., BANDULASENA, H. C. H. & OMOTOWA, O. A. 2009c. Efficiency of an aerator driven by fluidic oscillation. Part II: Pilot scale trials with flexible membrane diffusers.

ZIMMERMAN, W. B., TESAR, V., BUTLER, S. & BANDULASENA, H. C. H. 2008. Microbubble generation. *Recent Patents on Engineering,* 2, 1-8.

Appendix A: List of Dimensionless Numbers

Engineers often non-dimensionalise equations so that predictions can be made if one or more of the parameters were varied. They do this using dimensionless quantities, which usually have some physical meaning with regard to what they represent. For completeness, a list of the relevant dimensionless numbers used in this work and their meanings are mentioned here.

Dimensionless Numbers Regarding Heat and Mass Transfer

The dimensionless numbers used in this work with regard to heat and mass transfer between gaseous bubbles and liquids are provided in Eq. 3.1.1:

$$\begin{aligned}
Reynolds\ Number\ (Re) &= \frac{Inertial\ Forces}{Viscous\ Forces} = \frac{\rho_L u d}{\mu_L} \\
Nusselt\ Number\ (Nu) &= \frac{Convective\ Heat\ Transfer}{Conductive\ Heat\ Transfer} = \frac{hd}{\kappa_L} \\
Sherwood\ Number\ (Sh) &= \frac{Advective\ Mass\ Transfer}{Diffusive\ Mass\ Transfer} = \frac{k_L d}{D} \\
Prandtl\ Number\ (Pr) &= \frac{Momentum\ Diffusivity}{Thermal\ Diffusivity} = \frac{\mu_L c_{p,L}}{\kappa_L} \\
Schmidt\ Number\ (Sc) &= \frac{Momentum\ Diffusivity}{Mass\ Diffusivity} = \frac{\mu_L}{\rho_L D} \\
Péclet\ Number\ (Heat)(Pe_H) &= \frac{Advective\ Heat\ Transfer}{Conductive\ Heat\ Transfer} \\
&= \frac{\rho_L u d c_{p,L}}{\kappa_L} \\
Péclet\ Number\ (Mass)(Pe_M) &= \frac{Advective\ Mass\ Transfer}{Diffusive\ Mass\ Transfer} = \frac{ud}{D} \\
Rayleigh\ Number\ (Heat)(Ra_H) &= \frac{d^3(\rho_L - \rho_G) g \rho_L c_{p,L}}{\mu_L \kappa_L} \\
Rayleigh\ Number\ (Mass)(Ra_M) &= \frac{d^3(\rho_L - \rho_G) g}{\mu_L D}
\end{aligned} \tag{3.1.1}$$

where ρ_L, μ_L, κ_L, and $c_{p,L}$ are the density [kg/m^3], viscosity [Pa·s], thermal conductivity [W/m/K], and specific heat capacity [J/kg/K] of the liquid respectively, u and d represent the velocity [m/s] and diameter [m] of the bubble respectively, h denotes the heat transfer coefficient [W/m^2/K] between the bubble and the liquid, D denotes the diffusivity of the gas in the liquid [m^2/s], k_L is the liquid-side mass transfer coefficient [m/s], and g represents the acceleration due to gravity [m/s^2].

Since the equations that govern heat and mass transfer are similar in nature, there are analogies that can be drawn between these dimensionless numbers; some of these are listed below:

$$\begin{gathered} Nu \equiv Sh \\ Pr \equiv Sc \\ Pe_H \equiv Pe_M \\ Ra_H \equiv Ra_M \end{gathered} \tag{3.1.2}$$

Dimensionless Numbers Regarding Bubble Formation

$$\begin{gathered} Bond\ Number = \frac{Buoyancy\ force}{Surface\ tension\ force} = \frac{\rho g d^2}{\gamma} \\ Capillary\ Number = \frac{Viscous\ force}{Surface\ tension\ force} = \frac{\mu u}{\gamma} \\ \text{Eötvös}\ Number = \frac{Buoyancy\ force}{Surface\ tension\ force} = \frac{\Delta\rho g d^2}{\gamma} \\ Morton\ Number = \frac{g {\mu_L}^4 \Delta\rho}{{\rho_L}^2 \gamma^3} \\ Froude\ Number = \frac{Inertial\ force}{Gravitational\ force} = \frac{U_G}{\sqrt{gd}} \\ Galilei\ Number = \frac{Gravitational\ \ force}{Viscous\ force} = \frac{{\rho_L}^2 g d^3}{{\mu_L}^2} \\ Weber\ Number = \frac{Inertial\ force}{Surface\ tension\ force} = \frac{\rho_L u^2 d}{\gamma} \end{gathered} \tag{3.1.1}$$

Appendix B: MEA-CO_2 Reaction

The reaction between MEA and ionic liquids is a two-step reaction which occurs via a zwitterion mechanism (Caplow (1968), Danckwerts (1979)):

$$RNH_2 + CO_2 \rightarrow RNH_2{}^{+}COO^{-} \tag{3.1.1}$$

The zwitterion then reacts with another MEA molecule forming protonated MEA and MEA carbamate:

$$RNH_2{}^{+}COO^{-} + RNH_2 \rightarrow RNH_3{}^{+} + RNHCOO^{-} \tag{3.1.1}$$

At high CO_2 loadings ($\alpha > 0.5$ mol-CO_2/mol-MEA), the zwitterion can also react with water molecules to form more protonated MEA and bicarbonate:

$$RNH_2{}^{+}COO^{-} + H_2O \rightarrow RNH_3{}^{+} + HCO_3{}^{-} \tag{3.1.1}$$

This reaction mechanism suggests that two moles of MEA are used to capture one mole of CO_2

Appendix C: Stokes Flow Inside and Outside of a Bubble

Stokes Flow can be applied when the drag force is very large relative to the inertia. Typically it is used when the Reynolds number is less than unity. Such is the case for microbubbles travelling in a liquid. The velocity vectors for the flow of fluid inside and outside of a bubble will be derived here in cylindrical coordinates.

For a fluid moving horizontally, from right to left, over a spherical fluid region, such as a droplet or a bubble, the fluid stream functions inside and outside of the spherical region are given by:

$$\varphi^i = \frac{1}{4} U r^2 sin^2(\theta)\left(1 - \left(\frac{r}{R}\right)^2\right) \tag{A.1}$$

$$\varphi^o = -\frac{1}{2} U r^2 sin^2(\theta)\left(1 - \frac{R}{r}\right) \tag{A.2}$$

where U is the velocity of the outer fluid region far from the sphere, r is the radial distance from the centre of the sphere, theta represents the angle from the horizontal axis which goes through the centre of the sphere, and R is the radius of the spherical region.

The velocity vectors of the fluid in spherical coordinates (r, θ) can be calculated from:

$$v_r = \frac{1}{r^2 \sin(\theta)} \frac{\partial \varphi}{\partial \theta} \tag{A.3}$$

$$v_\theta = -\frac{1}{r \sin(\theta)} \frac{\partial \varphi}{\partial r} \tag{A.4}$$

and applying the appropriate boundary conditions.

When the flow is horizontal, the solution is simple as much of the complexity in the calculation conveniently cancels out. The solutions in this case are:

$$v_r{}^o = \frac{U}{r}(R - r)\cos(\theta) \tag{A.5}$$

$$v_\theta{}^o = -\frac{U}{2r}(R - 2r)\sin(\theta) \tag{A.6}$$

$$v_r{}^i = \frac{U}{2}\left(1 - \left(\frac{r}{R}\right)^2\right)\cos(\theta) \tag{A.7}$$

$$v_{\theta}{}^{i} = -\frac{U}{2}\left(1 - 2\left(\frac{r}{R}\right)^{2}\right)\sin(\theta) \tag{A.8}$$

However, when the flow is vertical, as in the case of a bubble rising in a liquid, the solutions cannot be determined by this method.

A simple solution can be found by transforming to cylindrical coordinates (ϱ, z) using the following transformation:

$$u_{\rho} = u_{r}\cos(\theta) - u_{\theta}\sin(\theta) \tag{A.9}$$

$$u_{z} = u_{r}\sin(\theta) + u_{\theta}\cos(\theta) \tag{A.10}$$

Using this transformation, the following velocity vectors are obtained:

$$u_{\rho}{}^{o} = \frac{U}{2r}(Rcos^{2}(\theta) + R - 2r) \tag{A.11}$$

$$u_{z}{}^{o} = \frac{UR}{2r}\sin(\theta)\cos(\theta) \tag{A.12}$$

$$u_{\rho}{}^{i} = \frac{U}{2}\left(1 - \left(\frac{r}{R}\right)^{2} - \left(\frac{r}{R}\right)^{2}\sin^{2}(\theta)\right) \tag{A.13}$$

$$u_{z}{}^{i} = \frac{U}{2}\left(\frac{r}{R}\right)^{2}\sin(\theta)\cos(\theta) \tag{A.14}$$

Now, in order to translate the flow so that it is travelling in the vertical direction relative to the spherical fluid region, one can simply switch the ϱ and z velocity vectors and change the switch the sines and cosines to obtain the following solutions:

$$u_{\rho}{}^{o} = \frac{UR}{2r}\sin(\theta)\cos(\theta) \tag{A.15}$$

$$u_{z}{}^{o} = \frac{U}{2r}(Rsin^{2}(\theta) + R - 2r) \tag{A.16}$$

$$u^{i} = \frac{U}{2}\left(\frac{r}{R}\right)^{2}\sin(\theta)\cos(\theta) \tag{A.17}$$

$$u_{z}{}^{i} = \frac{U}{2}\left(1 - \left(\frac{r}{R}\right)^{2} - \left(\frac{r}{R}\right)^{2}\cos^{2}(\theta)\right) \tag{A.18}$$

There are two simple checks that can be made to ensure these solutions are reliable. Firstly, since $\sin(\theta) = y/\rho$ and $\cos(\theta) = x/\rho$, one can see that the velocity field inside the bubble is equal to:

$$u^i = \frac{U\rho z}{2R^2} \tag{A.19}$$

$$u_z{}^i = \frac{U}{2}\left(1 - 2\left(\frac{\rho}{R}\right)^2 - \left(\frac{z}{R}\right)^2\right) \tag{A.20}$$

which is equal to the solution to Hill's spherical vortex.

Secondly, by substituting r=R into Equations A.15-A.18, one can confirm that the velocity vectors on the interface are equal to one another.

The solution to this velocity vector appears as follows:

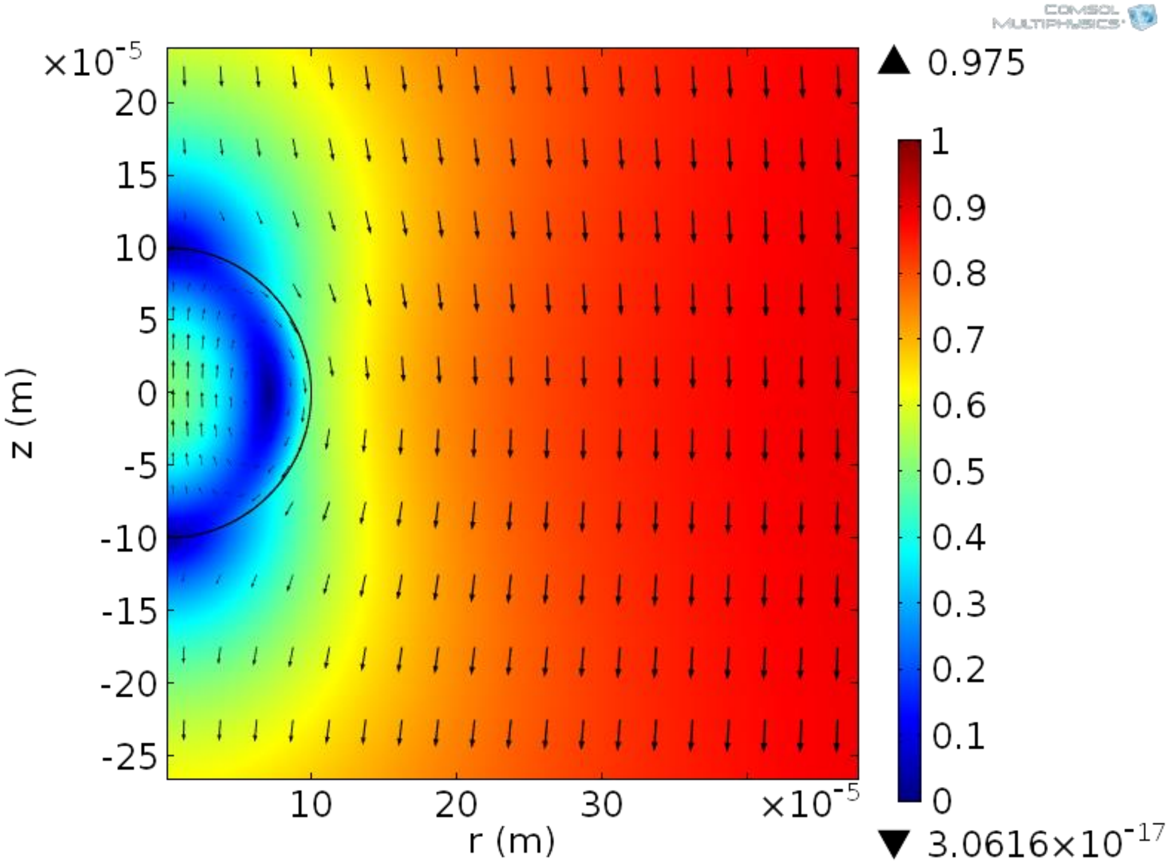

Figure C.0.1. Normalised velocity field inside and outside of a fluid sphere

Appendix D: Bubble Sizing Software

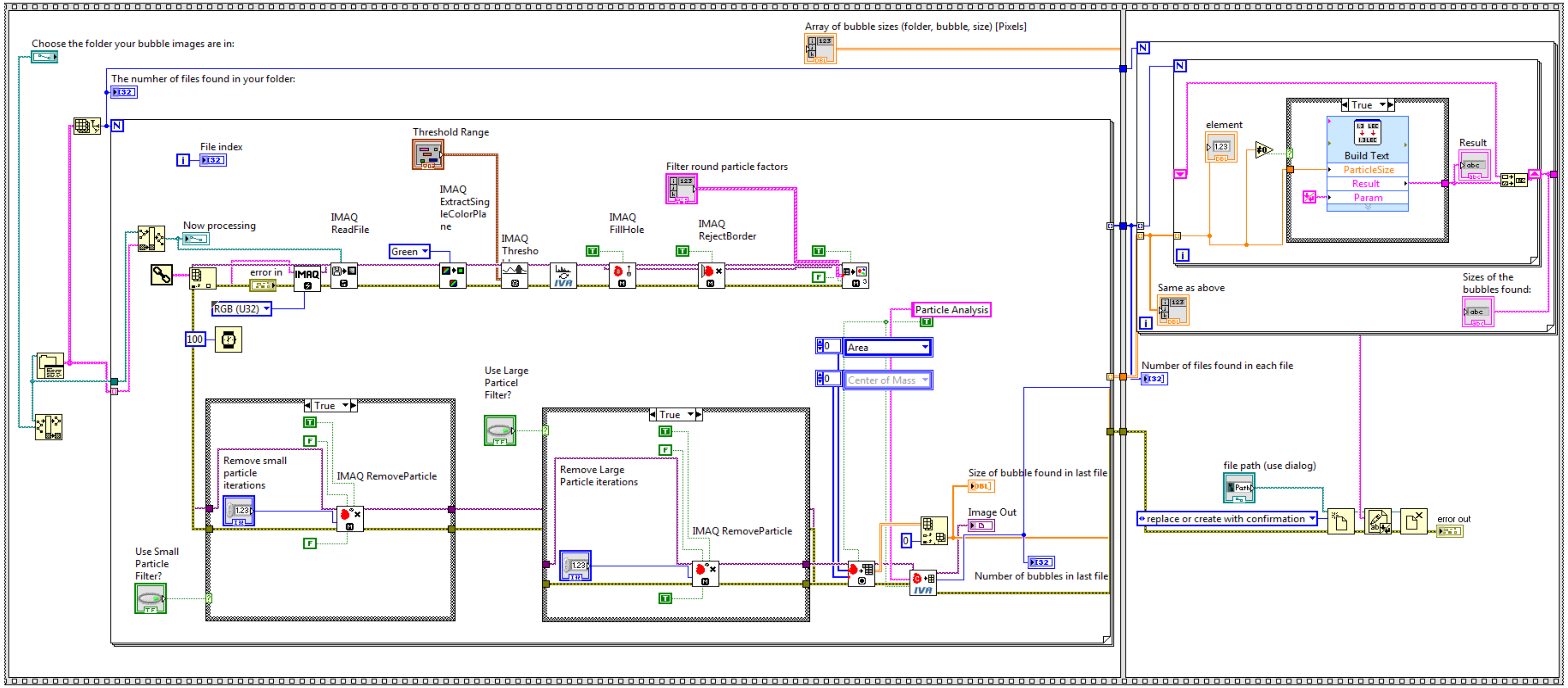

Figure E.0.1. LabVIEW program used for sizing bubbles

Appendix E: Mean Bubble Diameters

Aqueous Glycerol Mixtures

Mixture #	Viscosity (Pa-s)	Surface Tension (N/m)	Density (kg/m3)	Mean Bubble Diameter (μm)	Gas Holdup
1	1.412	0.064	1261.0	207.67	0.4239
2	1.202	0.064	1259.7	182.66	0.4670
3	1.001	0.064	1258.1	167.04	0.4655
4	0.842	0.064	1256.6	170.80	0.3749
5	0.714	0.065	1255.0	159.77	0.3640
6	0.611	0.065	1253.5	155.74	0.3283
7	0.527	0.065	1252.0	163.45	0.2574
8	0.418	0.065	1249.5	169.53	0.1902
9	0.338	0.065	1247.0	176.62	0.1418
10	0.230	0.066	1242.0	167.30	0.1081
11	0.141	0.066	1234.8	193.82	0.0498
12	0.094	0.066	1227.7	134.95	0.0690
13	0.067	0.067	1220.9	115.33	0.0676
14	0.050	0.067	1214.3	118.99	0.0477
15	0.039	0.067	1207.9	117.27	0.0383
16	0.031	0.067	1201.6	104.47	0.0387
17	0.023	0.067	1191.5	99.20	0.0314
18	0.017	0.068	1182.0	96.99	0.0253
19	0.011	0.068	1163.8	105.68	0.0139
20	0.006	0.068	1131.0	112.59	0.0067
21	0.004	0.069	1104.8	88.65	0.0072
22	0.002	0.070	1062.9	93.66	0.0038
23	0.001	0.072	1000.0	214.50	0.0004

Ionic Liquids

[C2mim][DCA]

Mean Bubble Diameter (μm)

FR	Run 1	Run 2	Run 3	Mean	SD
3	121.856	111.9861	112.4398	115.4273	5.572014
5	127.568	150.5696	115.2985	131.1454	17.90562
7	138.04	138.3358	118.1571	131.511	11.56573
10	137.088	145.8643	122.9215	135.2913	11.57644
15	154.224	140.2179	121.9686	138.8035	16.17413
20	164.696	157.157	139.1205	153.6578	13.14192
30	162.792	164.6855	151.5079	159.6618	7.124657

[C2mim][NTf2]

Mean Bubble Diameter (μm)

FR	Run 1	Run 2	Run 3	Mean	SD
3	555.0448	552.16	556.92	557.9024	2.397778
5	571.1194	574.056	590.24	581.5197	10.29679
7	567.3372	569.296	594.048	573.5942	14.88828
10	552.2082	569.296	604.52	578.305	26.67473
15	568.2828	554.064	577.864	569.6792	11.97507
20	554.0994	576.912	596.904	578.8142	21.41778
30	573.0106	550.256	573.104	568.3424	13.16442
50	560.7182	571.2	586.432	575.5995	12.92982
80	544.6438	508.368	560.728	535.8448	26.82103

[C4mim][NTf2]

Mean Bubble Diameter (μm)

FR	Run 1	Run 2	Run 3	Mean	SD
3	587.079	600.98	569.098	585.719	15.98445
5	630.9906	588.045	548.2774	589.1043	41.36677
7	615.717	600.98	560.175	592.2907	28.7725
10	636.7182	618.89	570.0896	608.5659	34.49322
15	686.3574	650.73	629.5772	655.5549	28.69595
20	735.9966	689.535	654.3636	693.2984	40.94642
30	804.7278	732.32	699.9708	745.6729	53.63983
50	875.3682	816.895	774.3302	822.1978	50.7273
80	918.3252	568.145	845.7154	777.3952	184.8169

[C4mim][TFA]

Mean Bubble Diameter (μm)

FR	Run 1	Run 2	Run 3	Mean	SD
3	142.8391	120.0161	125.7888	129.548	5.93339
5	143.6863	121.2413	111.3839	125.4372	8.277465
7	133.9425	116.3406	112.3476	120.8769	5.74496
10	132.8128	115.8811	109.3044	119.3328	6.064173
15	132.25	114.1455		123.1977	
20	146.14			146.14	

[C2mim][EtSO4]

Mean Bubble Diameter (μm)

FR	Run 1	Run 2	Run 3	Mean	SD
3	98.23887	95.88517	102.2284	98.78416	1.603297
5	97.65429	91.47233	103.6126	97.57973	3.035233
7	91.60387	90.80612	99.08083	93.83028	2.282288
10	100.7526	102.8659	109.492	104.3701	2.279878
15	94.70215	104.1298	110.5005	103.1108	3.974156
20	97.62506	109.744	106.0778	104.4823	3.107511

[P66614][NTf2]

Mean Bubble Diameter (µm)

FR	Run 1	Run 2	Run 3	Mean	SD
3	689.1662	630.5665	784.2282	701.3203	38.77425
5	736.298	737.6351	872.6403	782.1911	39.16708
7	778.8411	783.1566	894.2748	818.7575	32.71774
10	845.4166	854.226	1037.905	912.516	54.33986
15	891.2262	925.9147	1035.406	950.849	37.62729
20	899.7815	1048.389	1084.611	1010.927	48.972
30	764.4526	788.8855	878.9667	810.7683	30.15587
50	678.8999	417.1261	531.0196	542.3485	65.62704
80	625.7016	432.2226	374.6582	477.5275	65.75543

[P66614][DCA]

Mean Bubble Diameter (µm)

FR	Run 1	Run 2	Run 3	Mean	SD
3	511.2934	454.5138		482.9036	40.14924
5	487.5582	445.5822		466.5702	29.68151
7	497.4478	433.6736		465.5607	45.09517
10	472.7238	440.6202		456.672	22.70067

[P66614][Dec]

Mean Bubble Diameter (µm)

FR	Run 1	Run 2	Run 3	Mean	SD
3	1030.828	1014.272		1022.55	5.853253
5	1094.503	1073.419		1083.961	7.454143
7	1232.182	1266.142		1249.162	12.00667
10	1389.106	1409.199		1399.152	7.103948
15	1406.51	1629.231		1517.871	78.74376
20	1059.835	1398.02		1228.928	119.5665
30	768.911	750.516		759.7135	6.503615
50	491.854	510.9565		501.4053	6.753754

[P66614][Cl]

Mean Bubble Diameter (µm)

FR	Run 1	Run 2	Run 3	Mean	SD
3	1479.309	1351.295	1263.381	1364.661	108.5828
5	1522.537	1359.057	1256.967	1379.52	133.9624
7	1758.89	1436.389	1223.757	1473.012	269.4393
10	1579.379	1388.38	1207.509	1391.756	185.9582
15	1661.766	1464.993	1232.737	1453.165	214.759
20	1446.747	1631.012	1218.056	1431.939	206.8759

[P66614][Br]

Mean Bubble Diameter (µm)

FR	Run 1	Run 2	Run 3	Mean	SD
3	846.736	833.8595	899.5155	860.037	17.39515
5	905.6	833.0105	867.112	868.5742	18.15842
7	794.947	765.0905	1068.184	876.0737	83.5202
10	972.8125	895.5535	901.638	923.3347	21.47846
15	990.0755	1040.733	1207.561	1079.456	56.89824
20	942.956	1175.441	974.7935	1031.063	63.02178

Appendix F: K_La Graphs

$[C_2mim][NTf_2]$ – 5 mL/min

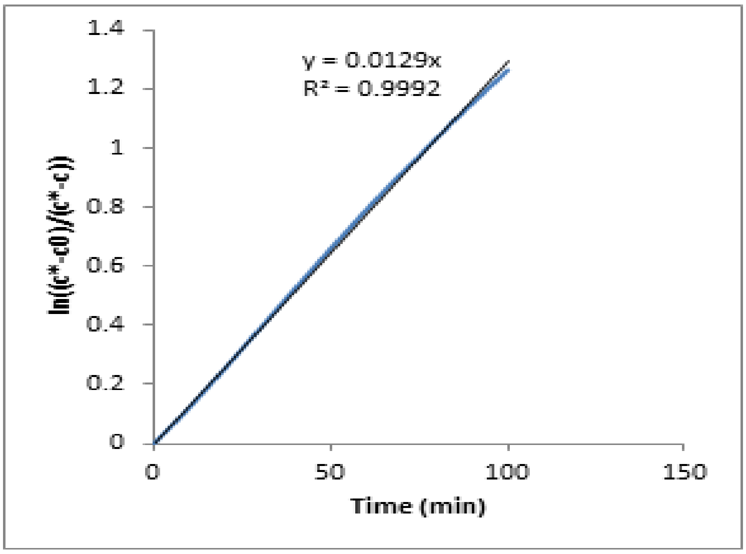

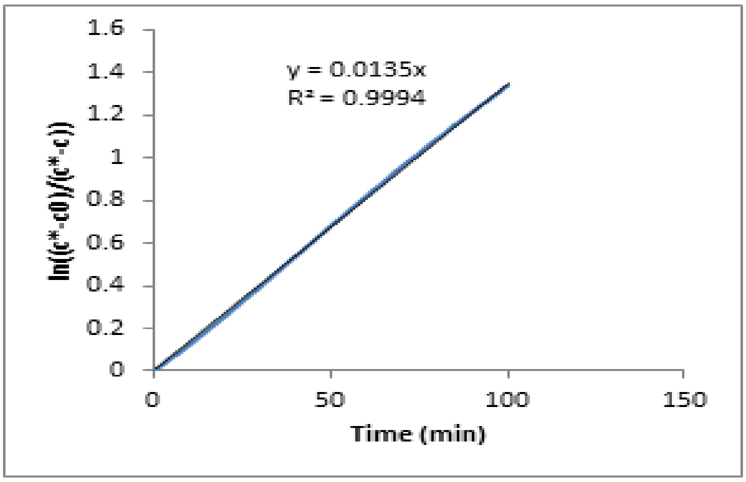

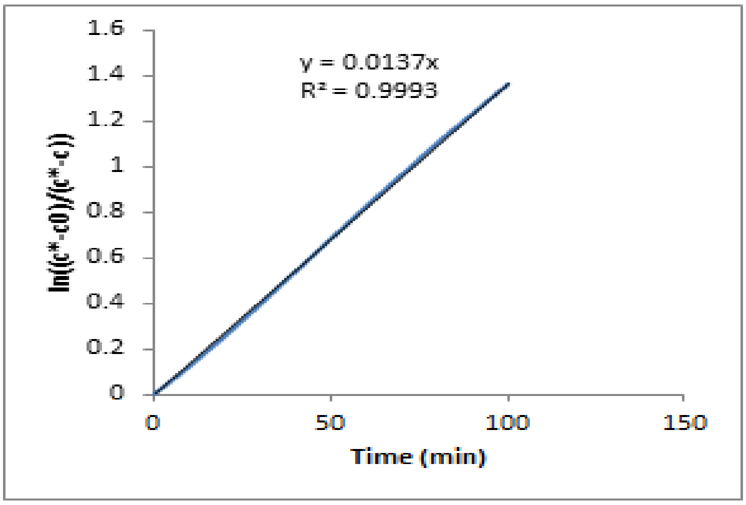

[C_2mim][NTf_2] **– 10 mL/min**

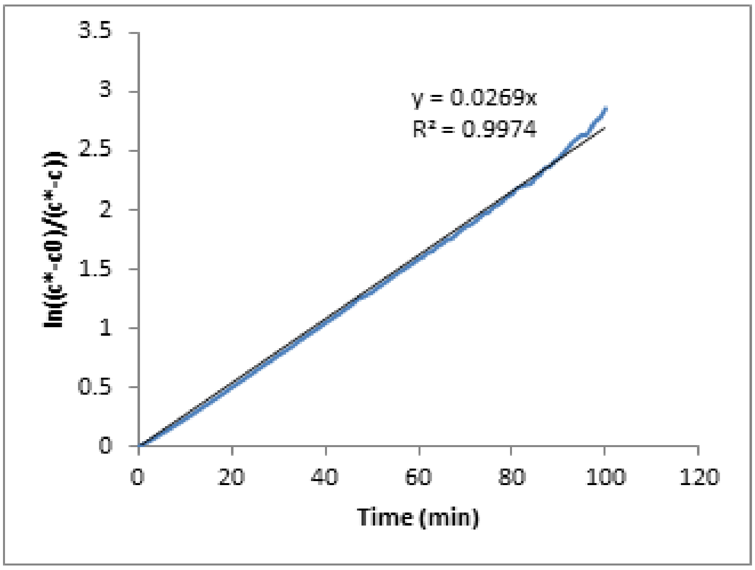

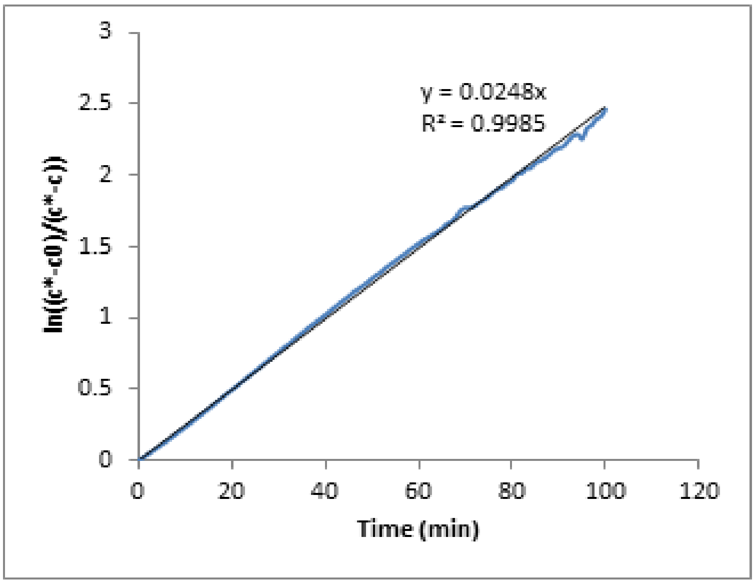

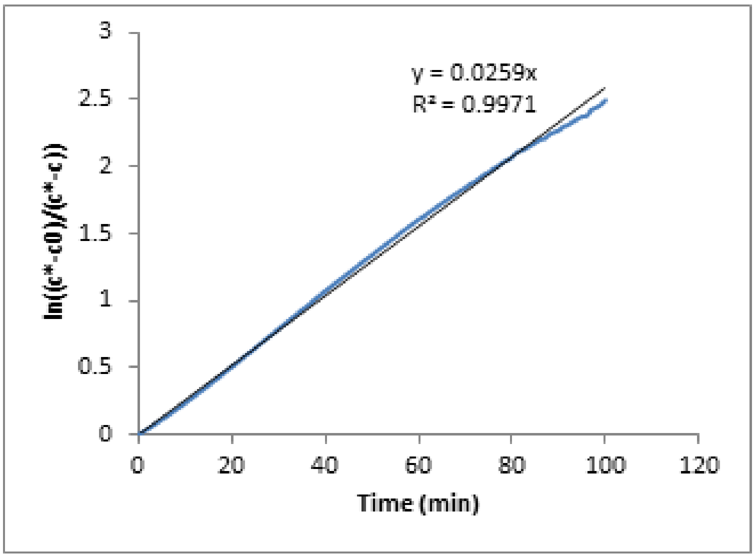

[C$_2$mim][NTf$_2$] – 15 mL/min

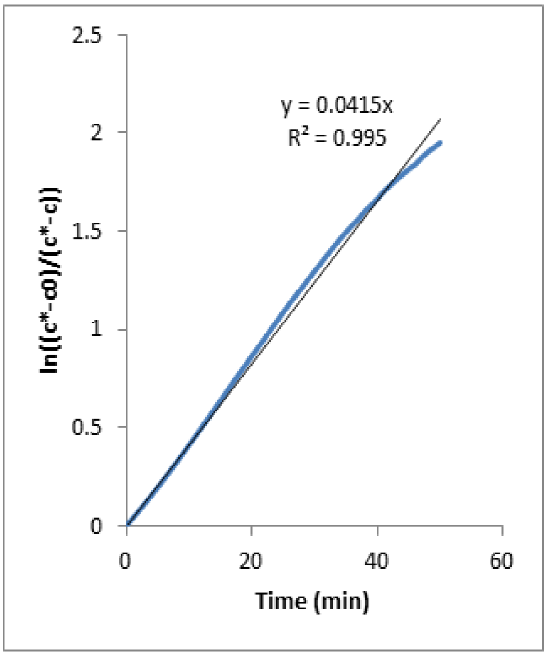

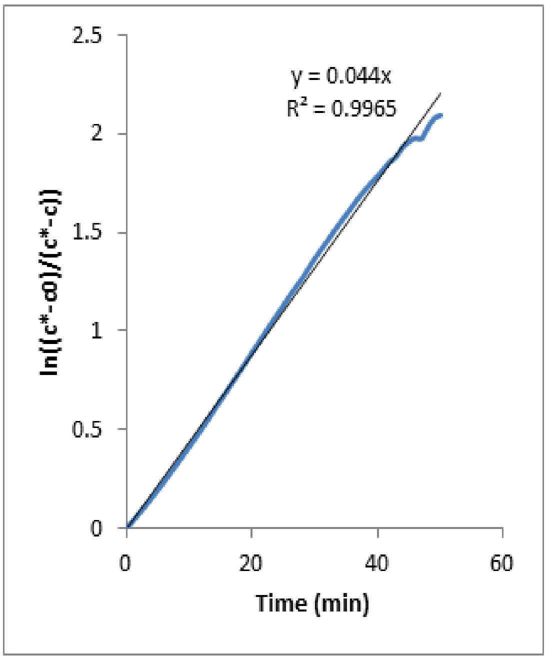

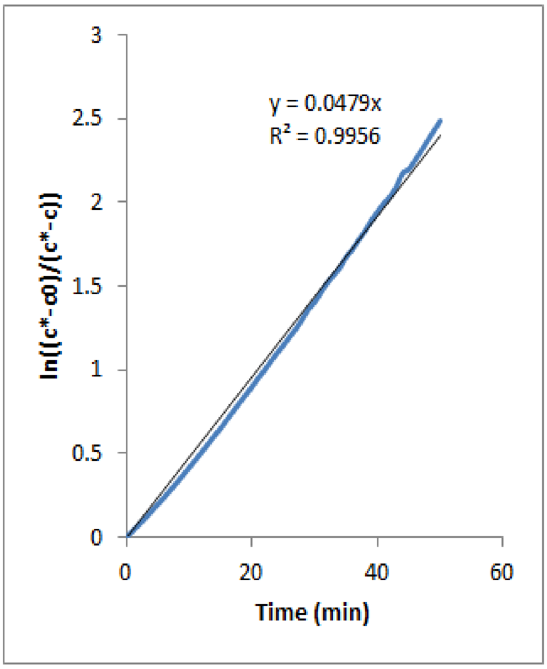

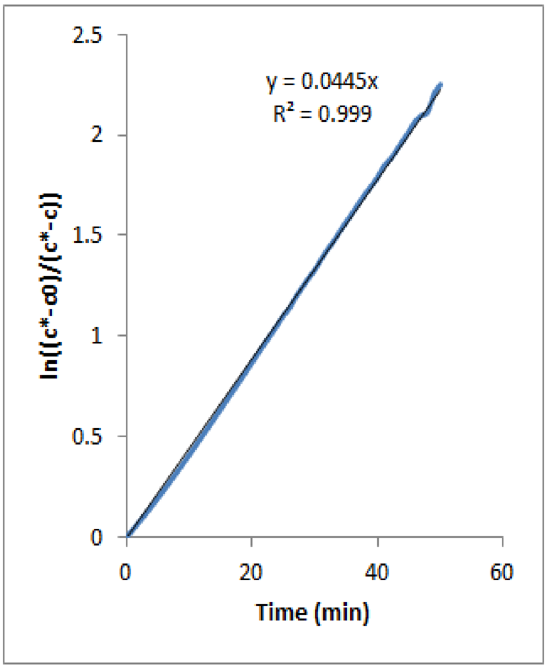

[C$_2$mim][NTf$_2$] – 20 mL/min

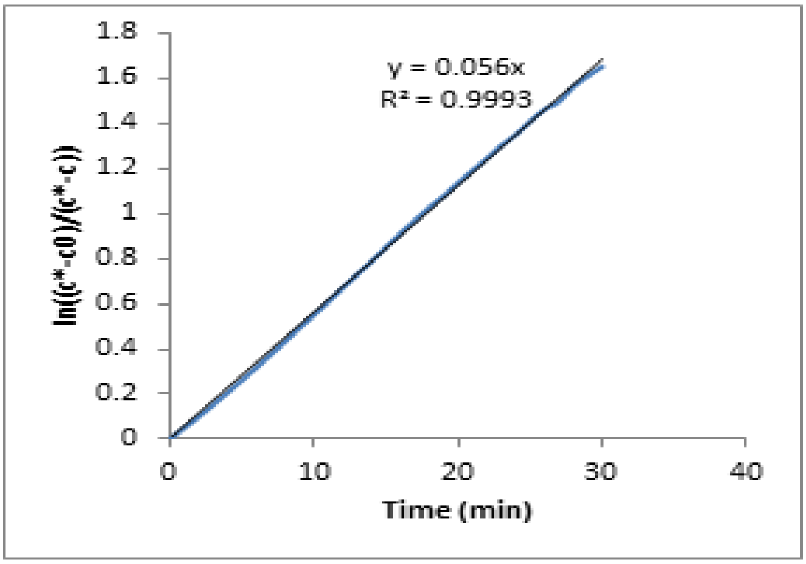

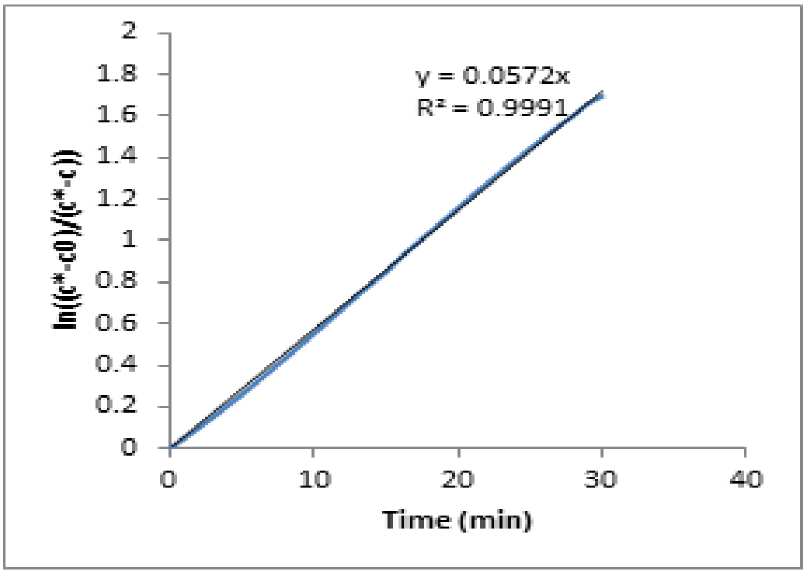

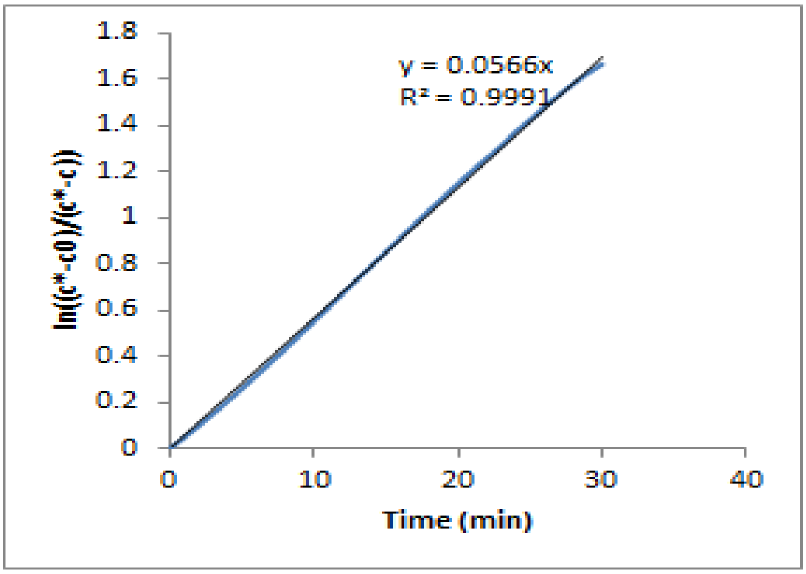

[C_2mim]**[DCA] – 10 mL/min**

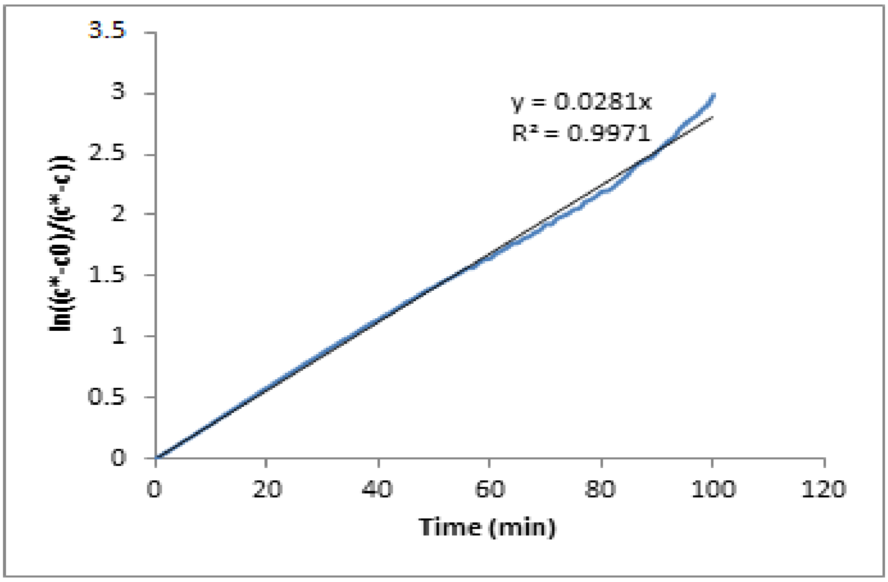

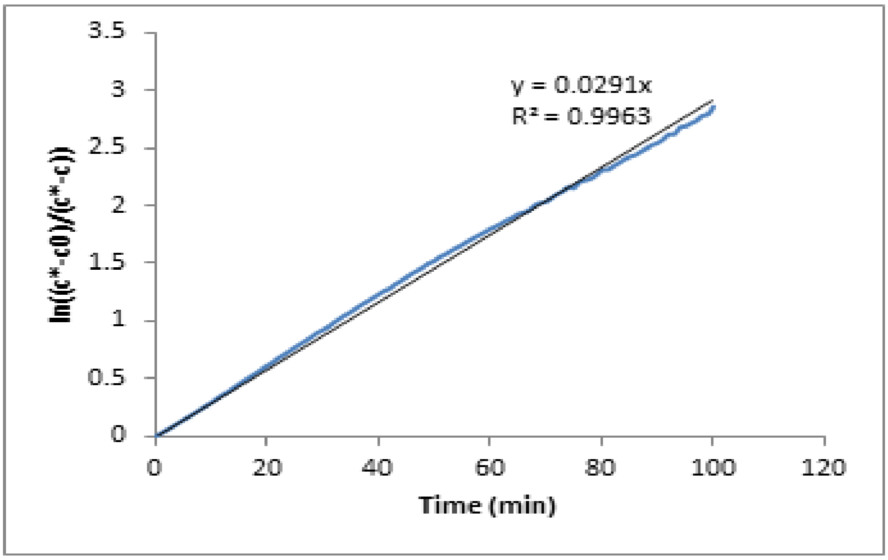

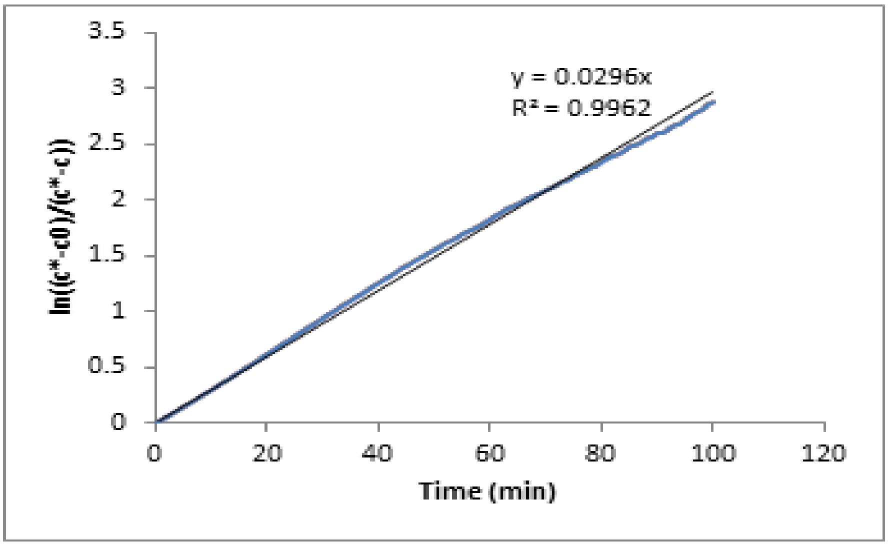

[C$_4$mim][NTf$_2$] – 10 mL/min

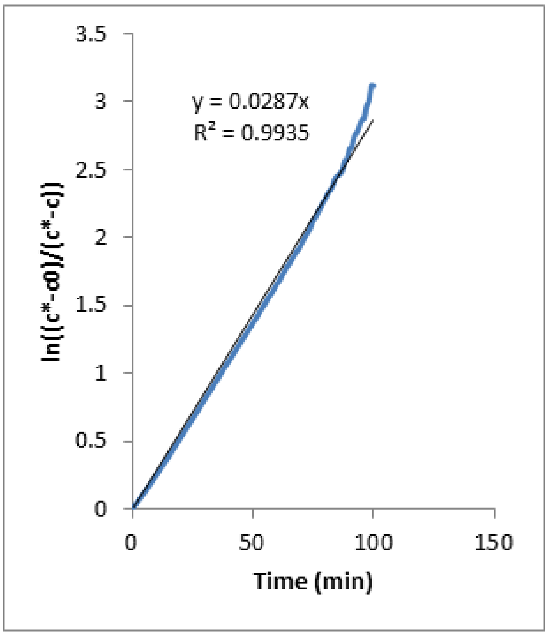

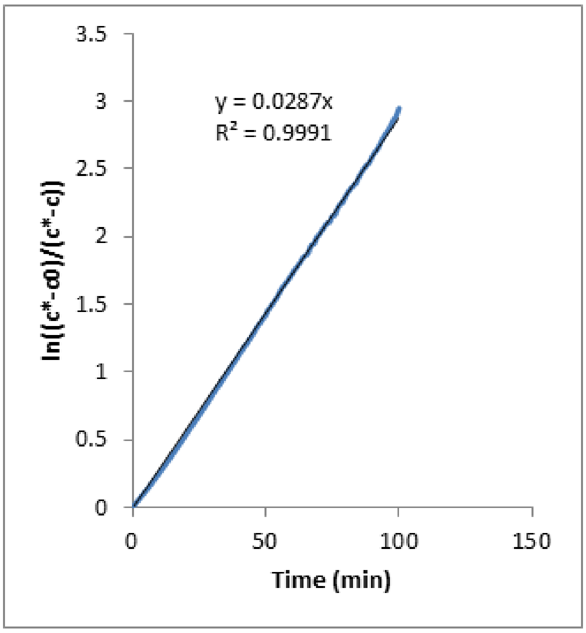

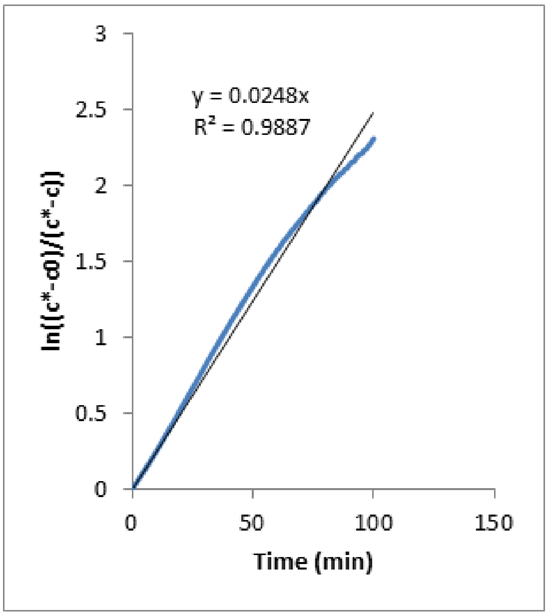

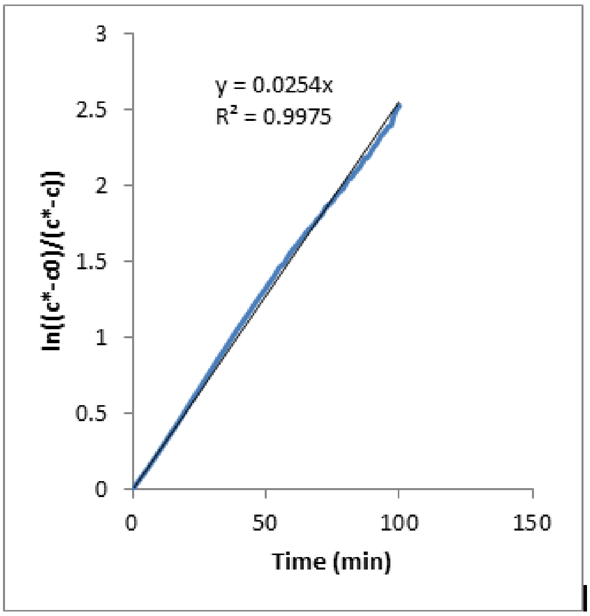

$[P_{66614}][Cl]$ – 5 mL/min

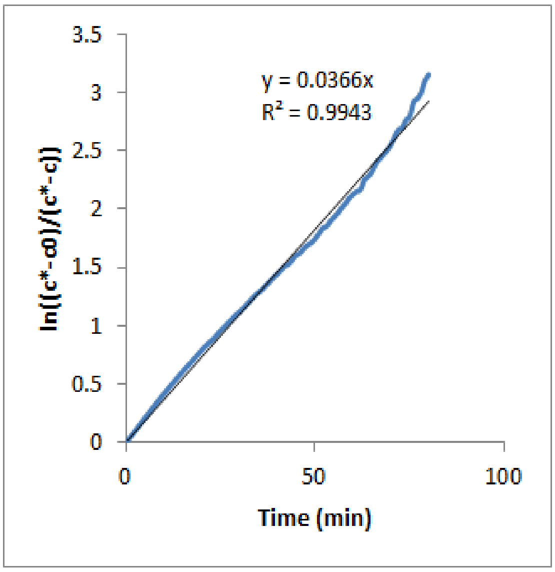

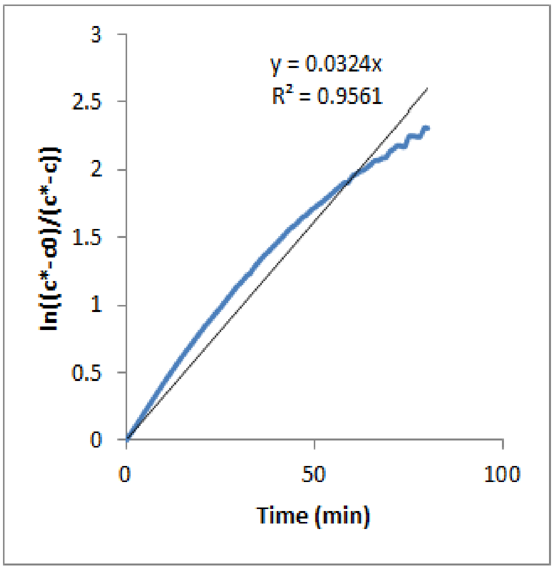

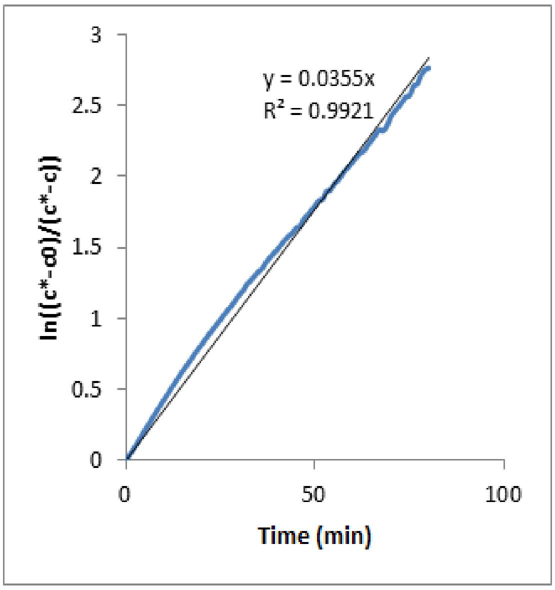

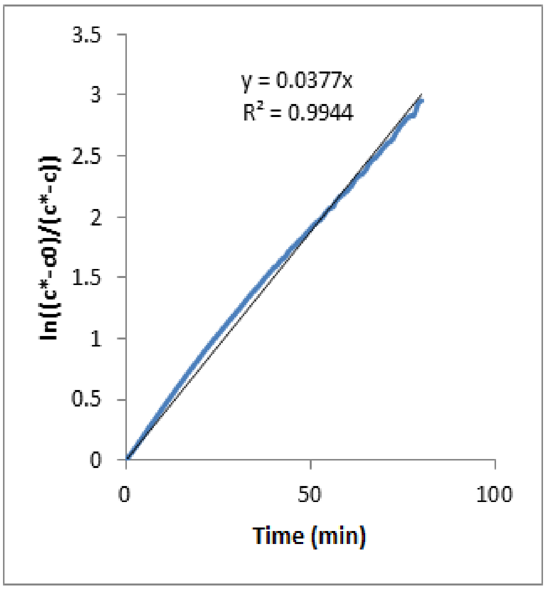

Appendix G: c^*, ε, K_La, and k_L Tables

Table G.0.1. Estimated solubility of CO_2 in the ionic liquids obtained by curve fitting

Ionic Liquid	Gas Flow Rate (mL/min)	Solubility (mol/L)					
		Run 1	Run 2	Run 3	Run 4	Mean (mol/L)	St. Dev. (+/- %)
[C$_2$mim][DCA]	10	0.063	0.061	0.061		0.062	1.87%
[C$_2$mim][NTf$_2$]	10	0.079	0.076	0.075		0.077	2.72%
[C$_4$mim][NTf$_2$]	10	0.076	0.074	0.069	0.071	0.073	4.29%
[C$_4$mim][TFA]	10	0.055	0.058			0.056	3.01%
[C$_2$mim][EtSO$_4$]	10	0.048	0.049			0.049	0.73%
[P$_{66614}$]][NTf$_2$]	10	0.042	0.043	0.042		0.042	1.09%
[P$_{66614}$][Cl]	10	0.044	0.04	0.043	0.043	0.043	4.08%
[C$_2$mim][NTf$_2$]	5	0.069	0.072	0.074		0.072	3.51%
[C$_2$mim][NTf$_2$]	15	0.0655	0.067	0.0725	0.07	0.069	4.54%
[C$_2$mim][NTf$_2$]	20	0.0695	0.071	0.07		0.070	1.09%

Table G.0.2. Solubility obtained from experiments compared with literature values for pure CO_2

Ionic Liquid	Experimental Mean CO_2 Solubility (mol/L)	Solubility of Pure CO_2 (mol/L) (Literature)	Percentage of Max. Solubility (%)
[C$_2$mim][DCA]	0.062	0.076 [a]	81%
[C$_2$mim][NTf$_2$]	0.077	0.108 [a]	71%
[C$_4$mim][NTf$_2$]	0.073	0.107 [a]	68%
[C$_4$mim][TFA]	0.055	0.101	54%
[C$_2$mim][EtSO$_4$]	0.048	0.055	87%
[P$_{66614}$][NTf$_2$]	0.042	0.075	56%
[P$_{66614}$][Cl]	0.043	0.049 [b]	87%

(* data from (Bara et al., 2009) [a], (Ferguson and Scovazzo, 2007) [b])

Table G.0.3. Gas holdup obtained from experiments with ionic liquids

Solvent	**Gas Flow Rate (mL/min)**	**Mean bubble diameter, d (µm)**	**Density, ρ (kg/m^3)**	**Viscosity, µ (Pa·s)**	**Hadamard-Rybczinski terminal velocity, $U_T \cdot 10^4$ (m/s)**	**Superficial gas velocity, $U_G \cdot 10^4$ (m/s)**	**Gas Holdup, $\varepsilon = U_G/U_T$**
[C$_2$mim][DCA]	10	121.6	1095 [a]	0.016 [a]	8.30	0.667	0.080
[C$_2$mim][NTf$_2$]	10	549.0	1515 [a]	0.032 [a]	115	0.667	0.0058
[C$_4$mim][NTf$_2$]	10	623.6	1440 [b]	0.052 [d]	88.0	0.667	0.0076
[C$_4$mim][TFA]	10	109.5	1220	0.053	2.25	0.667	0.30
[C$_2$mim][EtSO$_4$]	10	102.8	1241	0.12	0.893	0.667	0.75
[P$_{66614}$][NTf$_2$]	10	1,363	1064	0.17	95.0	0.667	0.0070
[P$_{66614}$][Cl]	10	1,436	881.9 [c]	1.8 [c]	8.14	0.667	0.082

Solvent	Gas Flow Rate (mL/min)	Mean bubble diameter, d (µm)	Density, ρ (kg/m^3)	Viscosity, µ (Pa·s)	Hadamard-Rybczinski terminal velocity, $U_T \cdot 10^4$ (m/s)	Superficial gas velocity, $U_G \cdot 10^4$ (m/s)	Gas Holdup, $\varepsilon = U_G/U_T$
MEA	10	73.2	1003	0.0021 [e]	40.8	0.667	0.016
[C$_2$mim][NTf$_2$]	5	472.1	1515 [a]	0.032 [a]	84.9	0.333	0.0039
[C$_2$mim][NTf$_2$]	15	449.3	1515 [a]	0.032 [a]	76.9	1.00	0.013
[C$_2$mim][NTf$_2$]	20	434.3	1515 [a]	0.032 [a]	71.9	1.33	0.019

(* data from (Gallagher et al., 2014) [a], (Sigma-Aldrich, 2012a) [b], (Cytec, 2008b) [c], (Zhang et al., 2006) [d], (Li and Lie, 1994) [e])

Table G.0.4. K_La values obtained in experiments with ionic liquids

Ionic Liquid	Flow Rate (mL/min)	Solubility (mol/L)	K_La (1/min)					
			Run 1	Run 2	Run 3	Run 4	Mean	St. Dev. (+/- %)
[C$_2$mim][DCA]	10	0.062	0.0281	0.0291	0.0296		0.0289	2.64%
[C$_2$mim][NTf$_2$]	10	0.077	0.0269	0.0248	0.0259		0.0259	4.06%
[C$_4$mim][NTf$_2$]	10	0.073	0.0287	0.0287	0.0248	0.0254	0.0269	7.78%
[C$_4$mim][TFA]	10	0.056	0.0382	0.0358			0.0370	4.59%
[C$_2$mim][EtSO$_4$]	10	0.049	0.0418	0.0432			0.0425	2.33%
[P$_{66614}$]][NTf$_2$]	10	0.042	0.0417	0.0389			0.0404	3.51%
[P$_{66614}$][Cl]	10	0.043	0.0366	0.0324	0.0355	0.0377	0.0356	6.42%
[C$_2$mim][NTf$_2$]	5	0.072	0.0129	0.0135	0.0137		0.0134	3.11%
[C$_2$mim][NTf$_2$]	15	0.069	0.0415	0.044	0.0479	0.0445	0.0445	5.92%
[C$_2$mim][NTf$_2$]	20	0.07	0.056	0.0572	0.0566		0.0566	1.06%

Table G.0.5. k_L values obtained in experiments with ionic liquids

Ionic Liquid	Flow Rate (mL/min)	a (1/m)	$k_L \cdot 10^6$ (m/s)					
			Run 1	Run 2	Run 3	Run 4	Mean	St. Dev. (+/- %)
[C$_2$mim][DCA]	10	3,960	0.118	0.122	0.125		0.122	2.64
[C$_2$mim][NTf$_2$]	10	63.4	7.07	6.52	6.81		6.80	4.06
[C$_4$mim][NTf$_2$]	10	72.9	6.56	6.56	5.67	5.81	6.15	7.78
[C$_4$mim][TFA]	10	16,200	0.0393	0.0368			0.0381	4.59
[C$_2$mim][EtSO$_4$]	10	43,700	0.0159	0.0165			0.0162	2.33
[P$_{66614}$][NTf$_2$]	10	30.9	22.5	21.0			21.7	4.91
[P$_{66614}$][Cl]	10	342	1.78	1.58	1.73	1.84	1.73	6.42
[C$_2$mim][NTf$_2$]	5	49.8	4.32	4.52	4.59		4.47	3.11
[C$_2$mim][NTf$_2$]	15	173.7	3.98	4.22	4.60	4.27	4.27	5.92
[C$_2$mim][NTf$_2$]	20	255.6	3.65	3.73	3.69		3.69	1.06